Multi-scale structural response of the lead-free perovskite-type ferroelectric solid solution (1-x)$Na_{0.5}Bi_{0.5}TiO_3$-$x$$BaTiO_3$ to high pressures

Dissertation

Zur Erlangung des Doktorgrades
an der Fakultät für Mathematik, Informatik und Naturwissenschaften
Fachbereich Erdsystemwissenschaften
der Universität Hamburg

vorgelegt von
Constanze Rösche

Hamburg, 2025

Fachbereich Erdsystemwissenschaften

Datum der Disputation:	10.11.2025
Gutachter/innen der Dissertation:	Prof. Dr. Boriana Mihailova Dr. Tiziana Boffa Ballaran Prof. Dr. Mike Glazer
Zusammensetzung der Prüfungskommission:	Prof. Dr. Boriana Mihailova Dr. Tiziana Boffa Ballaran Prof. Dr. Christian Schroer Prof. Dr. Ulrich Bismayer Prof. Dr. Gerhard Schmiedl
Vorsitzender des Fach-Promotionsausschusses Erdsystemwissenschaften:	Prof. Dr. Hermann Held
Dekan der Fakultät MIN:	Prof. Dr.-Ing. Norbert Ritter

Contents

Abstract **3**

Zusammenfassung **5**

1 Motivation **8**

2 Objectives **12**

3 Results and Discussion **13**

3.1 In-house single crystal x-ray diffraction 14

3.2 Synchrotron single crystal x-ray diffraction 15

3.2.1 Crystal structure and x-ray diffuse scattering at ambient pressure . 15

3.2.2 High-pressure diffuse scattering analyses 17

3.2.3 The high-pressure structure of NBT-xBT 20

3.3 Raman spectroscopy 21

3.3.1 Raman scattering at ambient pressure 21

3.3.2 Raman scattering at high pressure 22

4 Conclusions **28**

Bibliography **31**

Acknowledgments **39**

Appendix **42**

A.1 Pressure-induced structural transformations in (1-x)$Na_{0.5}Bi_{0.5}TiO_3$-$x$$BaTiO_3$ at the morphotropic phase boundary 42

A.2 Supplementary Material 72

B.1 The high-pressure structure of (1-x)$Na_{0.5}Bi_{0.5}TiO_3$-$x$$BaTiO_3$ at the morphotropic phase boundary 82

B.2 Supplementary Material 92

C.1 Structural transformations in the (1-x)$Na_{0.5}Bi_{0.5}TiO_3$-$x$$BaTiO_3$ solid solution under high pressure: comparison between x below and above the morphotropic phase boundary 99

C.2 Supplementary Material 116

Eidesstattliche Versicherung **127**

Abstract

The perovskite-type (ABO_3) solid solution (1-x)$Na_{0.5}Bi_{0.5}TiO_3$-$x$$BaTiO_3$ (NBT-xBT) is a promising environmentally friendly alternative to the lead-containing ferroelectric materials that currently dominate the market. NBT-xBT exhibits a morphotropic phase boundary (MPB) at $x_{MPB} \approx 0.05 - 0.06$, which is a transition region where the symmetry of the ferroelectric phase changes and the material properties are enhanced. However, the piezoelectric and dielectric responses of NBT-x_{MPB}BT still remain insufficient to compete with the lead-based ferroelectric compounds currently in industrial use. The material performance may be improved by tuning the local ferroic atomic clustering via additional A- or B-site doping, but for an effective modification a better understanding of the relationship between the chemical composition, nanoscale structural features and the macroscopic properties is required. Previous studies of Pb-based ferroelectrics have demonstrated that analyzing the response of the structure to high pressures can reveal subtle features of the structure, which ultimately elucidates the structural features at ambient conditions.

This thesis is the first high-pressure structural study of NBT-xBT across the MPB. The high-pressure behavior of single crystals with x below (x = 0.013), near (x = 0.048) and above (x = 0.074) the MPB has been studied thoroughly via x-ray diffraction (XRD) and x-ray diffuse scattering (XDS), informative of long- and intermediate-range order, and complementary Raman spectroscopy, giving a deeper insight into the local structure and phonons that trigger the structural transformations.

Own Raman-scattering data on pure NBT as well as x-ray and neutron diffraction data from literature were used as reference to follow the effect of Ba^{2+} substitution for A-site Na^{+} and Bi^{3+}.

The comprehensive analyses show that, similarly to pure NBT, NBT-xBT with x = 0.013, 0.048 and 0.074 undergo a reversible pressure-induced phase transition to an orthorhombic structure with symmetry *Pnma*, independently of the corresponding ambient-pressure symmetry. The high-pressure structure is characterized by antipolar A-cation displacements and a mixed octahedral tilt pattern ($a^-b^+a^-$). Polar B-cation shifts still persist above the phase-transition pressure, but they are uncorrelated and strongly reduced in magnitude compared to the low-pressure structure. The phase transition is preceded by multistep structural alterations, comprising the reduction of polar B-cation shifts, suppression of the Ba-induced local B-site anisotropy due to in-

creased orientation disorder of B-site dipoles, the development of antipolar A-cation shifts and enhancement of octahedral tilting. With increasing x the structural transformations are shifted to higher pressures. The critical phase-transition pressures p_c are ∼3.5(5), ∼4.3(6) and ∼4.9(5) GPa for x = 0.013, 0.048 and 0.074, respectively. The presence of Ba in the structure hinders the suppression of off-centered A- and B-cation shifts and consequently, their fraction in the high-pressure phase is increased compared to pure NBT.

Furthermore, the combined analyses of the XRD and Raman scattering data show how Ba^{2+} cations are incorporated in the NBT structure at ambient conditions. For x = 0.013, Ba^{2+} cations are preferentially embedded in the pre-existing tetragonal *P*4*bm*-type nanoregions, where they disturb the correlation length of in-phase BO_6 tilts with pattern $a^0a^0c^+$. The pseudorhombohedral matrix, which is characterized by an anti-phase octahedral tilt pattern, resembles that of pure NBT. For NBT-xBT with x = 0.048 and 0.074, Ba^{2+} cations are dispersed in both the tetragonal nanoregions with in-phase BO_6 tilts ($a^0a^0c^+$) and the pseudorhombohedral matrix with anti-phase BO_6 tilts, disturbing the correlation length of coherent A-cation shifts in both the tetragonal and pseudorhombohedral fraction. This is revealed by the fact that the application of an external pressure of ∼0.7 GPa (for x = 0.048) and ∼2.3 GPa (for x = 0.074) reinforces a structural state similar to pure NBT at ambient conditions, indicating that the Ba-induced internal "chemical pressure" and the applied external pressure have an opposing effect.

At ambient pressure the dominant octahedral tilt pattern of NBT-0.013BT and NBT-0.048BT consists of anti-phase BO_6 tilts. For x = 0.048, there are additional subordinate in-phase octahedral tilts of type $a^0a^0c^+$, indicating that near the MPB Ba restores the correlation of in-phase BO_6 tilts to a certain degree. For NBT-0.074BT, $a^0a^0c^+$ is the prevailing octahedral tilt pattern, but streak-like appearance of the Bragg reflections that are indicative of in-phase BO_6 tilts shows that their long-range correlation is disturbed. To some extent, this should be due to remaining regions with anti-phase octahedral tilts, as deduced from the presence of weak Bragg scattering characteristic of anti-phase BO_6 tilting.

Additionally, satellite peaks are observed for x = 0.048 and 0.074 below p_c, which suggest the presence of a modulated structure due to self-organized extended defects with mixed BO_6 tilts and antipolar shifts of A-cations, resembling *Pnma*-type layers.

Zusammenfassung

(1-x)$Na_{0.5}Bi_{0.5}TiO_3$-$x$$BaTiO_3$ (NBT-xBT) Mischkristalle mit Perowskitstruktur (ABO_3) sind eine vielversprechende umweltfreundliche Alternative zu den bleihaltigen ferroelektrischen Materialien, die gegenwärtig den Markt beherrschen. NBT-xBT hat eine morphotrope Phasengrenze (MPG) bei $x_{MPG} \approx 0.05 - 0.06$, was eine Übergangsregion ist, in der sich die Symmetrie der ferroelektrischen Phase ändert und die Materialeigenschaften verbessert sind. Allerdings sind die piezoelektrischen und dielektrischen Eigenschaften von NBT-x_{MPG}BT noch unzureichend, um mit den aktuell industriell verwendeten Blei-basierten ferroelektrischen Verbindungen zu konkurrieren. Die Leistungsfähigkeit des Materials könnte durch Justierung der lokalen ferroischen atomaren Clusterbildung durch zusätzliche Dotierung der A- oder B- Gitterplätze verbessert werden. Aber für eine effektive Anpassung ist ein besseres Verständnis der Zusammenhänge zwischen der chemischen Zusammensetzung, den nanoskaligen Eigenschaften der Struktur und den makroskopischen Eigenschaften erforderlich. Vorherige Studien mit Pb-basierten Ferroelektrika haben gezeigt, dass eine Untersuchung des Hochdruckverhaltens der Struktur subtile Merkmale der Struktur enthüllen kann, was letztlich Aufschluss über die strukturellen Merkmale bei Umgebungsbedingungen gibt.

Diese Dissertation ist die erste Hochdruck-Strukturstudie mit NBT-xBT im Bereich der MPG. Das Hochdruckverhalten von Einkristallen mit x unterhalb (x = 0.013), nahe (x = 0.048) und oberhalb (x = 0.074) der MPG wurde gründlich mit Hilfe von Röntgenbeugung und diffuser Streuung untersucht, wodurch Informationen über die Fernordnung und intermediäre Ordnung erhalten wurden. Ergänzende Raman-Spektroskopie Experimente geben einen tieferen Einblick in die lokale Struktur und Phononen, die die Veränderungen der Struktur hervorrufen.

Eigene Raman-Streuungsdaten von reinem NBT sowie Röntgen- und Neutronenbeugungsdaten aus der Literatur wurden als Referenz verwendet, um den Effekt von Ba^{2+} Substitution für Bi^{3+} und Na^{+} auf dem A-Gitterplatz zu untersuchen.

Die umfassenden Analysen zeigen, dass NBT-xBT mit x = 0.013, 0.048 und 0.074, ähnlich zu reinem NBT, eine umkehrbare druckinduzierte Phasenumwandlung zu einer orthorhombischen Struktur mit *Pnma* Symmetrie durchläuft, unabhängig von der entsprechenden Symmetrie bei Umgebungsdruck. Die Hochdruckstruktur ist von antipolaren A-Kationen-Auslenkungen und einem gemischten Oktaeder-Verkippungsmuster ($a^-b^+a^-$) gekennzeichnet. Die polaren B-Kationen-Auslenkungen bleiben auch

oberhalb des Phasenübergangsdrucks bestehen, sind jedoch unkorreliert und ihre Auslenkung ist im Vergleich zur Niederdruckstruktur stark reduziert.

Der Phasenumwandlung gehen mehrstufige strukturelle Veränderungen voraus, die die Reduktion von polaren B-Kationen-Auslenkungen, eine Unterdrückung der Ba-induzierten lokalen Anisotropie des B-Gitterplatzes aufgrund erhöhter Unordnung der B-Gitterplatz Dipol-Orientierung, die Entwicklung von antipolaren A-Kationen-Auslenkungen und die Verstärkung von Oktaeder-Verkippungen umfassen. Mit zunehmendem x werden die strukturellen Umwandlungen zu höheren Drucken verschoben. Die kritischen Phasenübergangsdrucke p_c sind jeweils ∼3.5(5), ∼4.3(6) und ∼4.9(5) GPa für x = 0.013, 0.048 und 0.074. Die Anwesenheit von Ba in der Struktur hemmt die Unterdrückung der Auslenkung von A- und B-Kationen und folglich ist deren Anteil in der Hochdruckphase im Vergleich zu reinem NBT erhöht.

Darüberhinaus zeigen die kombinierten Analysen der XRD- und Ramanstreuungsdaten, wie Ba^{2+} Kationen bei Umgebungsbedingungen in die NBT-Struktur eingebaut werden. Für x = 0.013 werden Ba^{2+} Kationen bevorzugt in bereits vorhandene tetragonale $P4bm$-artige Nanoregionen eingebettet, wo sie die Korrelationslänge zwischen gleichphasig verkippten BO_6-Oktaedern mit $a^0a^0c^+$ Muster stören. Die pseudorhomboedrische Matrix, die von einem gegenphasigen Oktaeder-Verkippungsmuster gekennzeichnet ist, ähnelt der von reinem NBT. Für NBT-xBT mit x = 0.048 und 0.074 sind die Ba^{2+}-Kationen sowohl in den tetragonalen Nanoregionen mit gleichphasigen BO_6-Verkippungen ($a^0a^0c^+$) als auch in der pseudorhomboedrischen Matrix mit gegenphasigen BO_6-Verkippungen verteilt, wodurch die Korrelationslänge der kohärenten A-Kationen-Auslenkungen sowohl in der tetragonalen als auch in der pseudorhomboedrischen Phase gestört wird. Dies wird dadurch deutlich, dass die Ausübung eines externen Drucks von ∼0.7 GPa (für x = 0.048) und ∼2.3 GPa (für x = 0.074) einen Strukturzustand herbeiführt, der dem von reinem NBT bei Umgebungsbedingungen ähnelt, was darauf hindeutet, dass der Ba-induzierte interne „chemische Druck“ und der ausgeübte externe Druck eine entgegengesetzte Wirkung haben.

Bei Umgebungsdruck besteht das vorherrschende oktaedrische Verkippungsmuster von NBT-0.013BT und NBT-0.048BT aus gegenphasigen Verkippungen der BO_6-Oktaeder. Für x = 0.048 existieren zusätzlich untergeordnete gleichphasige BO_6-Verkippungen des Typs $a^0a^0c^+$, was darauf hinweist, dass Ba in der Nähe der MPG die Korrelation der gleichphasigen BO_6-Verkippungen bis zu einem gewissen Grad wiederherstellt. Für NBT-0.074BT ist $a^0a^0c^+$ das vorherrschende Oktaeder-Verkippungsmuster,

aber das streifenartige Erscheinungsbild der Bragg-Reflexe, die auf gleichphasige BO_6-Verkippungen hindeuten, zeigt, dass ihre Fernordnung gestört ist. Bis zu einem gewissen Grad dürfte dies auf die verbleibenden Regionen mit gegenphasigen verkippten BO_6-Oktaedern zurückzuführen sein, was aus dem Vorhandensein von schwacher für gegenphasige BO_6-Verkippungen charakteristischer Bragg-Streuung abgeleitet werden kann.

Darüber hinaus werden für $x = 0.048$ und 0.074 unterhalb von p_c Satellitenreflexe beobachtet, die auf das Vorhandensein einer modulierten Struktur aufgrund von selbstorganisierten ausgedehnten Defekten mit gemischten BO_6-Verkippungen und antipolar ausgelenkten A-Kationen hindeuten, die vergleichbar mit *Pnma*-artigen Ebenen sind.

1 Motivation

Ferroelectric materials exhibit spontaneous electric polarization below a certain temperature, called the Curie temperature (T_c), which can be reversed by the application of an external electric field. They possess piezoelectric and pyroelectric properties, which means they can transform mechanical stress and temperature variations into electrical energy and vice versa. Applications range from capacitors, sensors, actuators and ultrasonic devices to non-volatile ferroelectric random access memory. In today's world, where life without electronic devices is hardly imaginable in industry, medicine and research as well as in private everyday life, it is not only important to find materials with excellent properties, but also to ensure that the environment is harmed as little as possible. Currently the most widely used ferroelectric materials are lead-based, e.g. $PbZr_xTi_{1-x}O_3$ (PZT) (Bell et al., 2021). Unfortunately, the mining, manufacture and waste disposal of Pb compounds bares considerable environmental and health risks (Bell and Deubzer, 2018). For this reason, there are regulations like the Restriction of Hazardous Substances Directive (RoHS) by the European Union (RoHS, 2011), which restricts the use of lead and other harmful substances in various electronic devices. Due to lack of suitable Pb-free replacements, piezoelectric materials are so far exempt from these restrictions (RoHS, 2011). However, these exemptions have expired in 2021-2024 and even if an extension has been requested (RoHS2, 2024), it is urgent to further explore environmentally friendly alternatives.

The ferroelectric solid solution (1-x)$Na_{0.5}Bi_{0.5}TiO_3$-$x$$BaTiO_3$ (NBT-xBT) is a promising candidate for replacement (Takenaka et al., 1991). Potential applications include actuators (Takenaka et al., 1991, Fan et al., 2021), ultrasonic transducers (Takenaka et al., 1991, Zhou et al., 2012) and energy storage (Lu et al., 2016, Lee and Son, 2024).

NBT-xBT is a perovskite-type oxide with the general chemical formula ABO_3, similar to PZT. The idealized perovskite structure consists of a framework of corner-sharing BO_6 octahedra with cavities that are filled by 12-fold coordinated A cations (Fig. 1a). The symmetry is cubic with space group $Pm\bar{3}m$, where $a = b = c \approx 4$Å. The A and B site can be occupied by various cations with different ionic radii and valences, which leads to composition-induced distortions of the structure. The tolerance factor $t = \frac{r_A + r_O}{\sqrt{2}(r_B + r_O)}$ (Goldschmidt, 1926) indicates whether the perovskite structure is stable, depending on the ionic radii r_A and r_B of the A- and B-site cations as well as the ionic radius of O^{2-} anions r_O. For NBT the average size of the A-site cations ($r_{XII_{Bi^{3+}}} = 1.45$ Å (Okawa et al.,

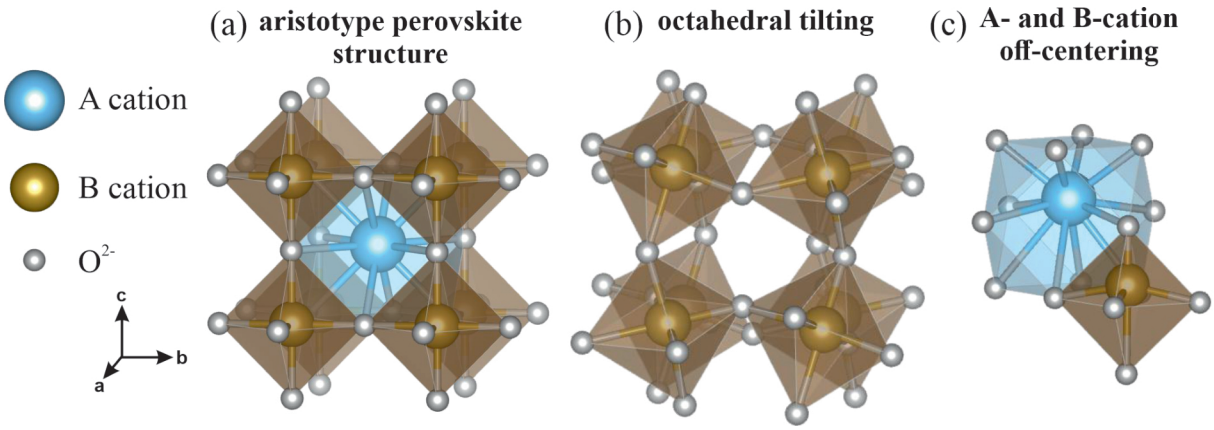


Figure 1: Sketches of (a) the aristotype ABO_3 perovskite structure, (b) exemplary tilted BO_6 octahedra and (c) and exemplary off-centered A- and B-cations. The figures were prepared using VESTA (Momma and Izumi, 2011). The **a**, **b** and **c** axes correspond to cubic symmetry.

2002), $r_{XII_{Na^+}}$ = 1.39 Å (Shannon, 1976)) is relatively small ($t < 1$) and therefore tilting of the BO_6 octahedra (Fig. 1b) is favored in order to reduce the size of the cavities (Reaney et al., 1994). The incorporation of larger Ba^{2+} cations ($r_{XII_{Ba^{2+}}}$ = 1.61 Å (Shannon, 1976)) on the other hand suppresses octahedral tilts. Similar to Pb^{2+}, Bi^{3+} cations in 12-fold coordination form stereochemically active lone pair electrons (Schütz et al., 2012), which promotes displacements of Bi^{3+} from the centers of the AO_{12} polyhedra (Fig. 1c). The Ti^{4+} cations are also off-set from the BO_6 centers (Fig.1c), due to the second-order Jahn-Teller effect (Bersuker, 2018).

The structure of NBT-*x*BT single crystals appears pseudocubic in x-ray diffraction (XRD) experiments with subtle ferroic distortions of the unit cell (Gorfman and Thomas, 2010, de La Flor et al., 2017). The description of the structure is complicated by nanoscale structural inhomogeneities, which can be described as being due to the presence of dynamic polar and/or antipolar nanoregions that have a symmetry different from the surrounding matrix (Kreisel et al., 2003, Ma et al., 2010, Ge et al., 2013). However, it is clear that with increasing x the unit-cell volume increases (de La Flor et al., 2017, Trujillo et al., 2005) (Fig. 2a) and in the vicinity of the morphotropic phase boundary (MPB) the average unit-cell angle becomes 90° within uncertainties (Ranjan and Dviwedi, 2005, de La Flor et al., 2017) (Fig. 2b). Interestingly, the unit-cell angle distortion from cubic metrics does not decrease gradually with increasing x, but it is maximal for x = 0.013 (de La Flor et al., 2017).

In spite of ongoing debates on the nanoscale structural features (Beanland and

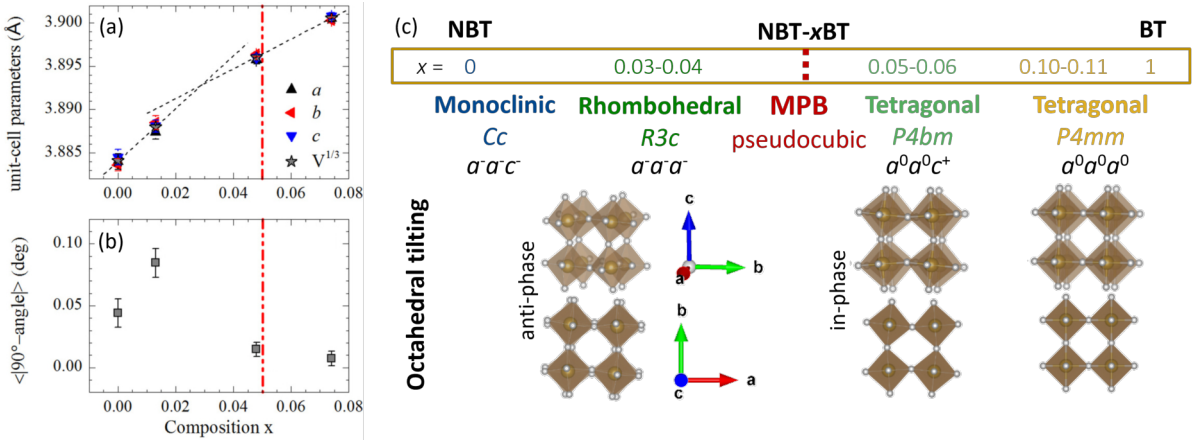


Figure 2: (a) The pseudocubic unit-cell parameters of NBT-xBT with $0 \leq x \leq 0.074$, (b) the deviation of the average unit-cell angle from 90° and (c) overview of the composition-induced changes of the average symmetry of NBT-xBT and the corresponding octahedral tilt patterns (based on Ma et al., 2013). The plots in (a) and (b) are after de La Flor et al., 2017. The figures of tilted octahedra in (c) were prepared using VESTA (Momma and Izumi, 2011). The **a**, **b** and **c** axes correspond to cubic symmetry.

Thomas, 2011, Levin and Reaney, 2012, Ma et al., 2013, Meyer et al., 2015, Fetzer et al., 2022), it is commonly accepted that the average structure of unpoled NBT-xBT with $x \leq 0.03$ has monoclinic Cc symmetry (Gorfman and Thomas, 2010, Aksel et al., 2011, Das Adhikary et al., 2023) and it is characterized by anti-phase octahedral tilts with pattern $a^-a^-c^-$ (Glazer notation (Glazer, 1972)) (Fig. 2c). For $0.03 < x < 0.05$ the symmetry of the structure is rhombohedral $R3c$ with tilt pattern $a^-a^-a^-$ and at $x > 0.05 - 0.06$ it changes to tetragonal $P4bm$ characterized by in-phase tilts of type $a^0a^0c^+$ (Ma et al., 2013). For $x > 0.10 - 0.11$ octahedral tilting is completely suppressed and the symmetry is tetragonal $P4mm$ (Ma et al., 2013), similar to pure $BaTiO_3$ (Buttner and Maslen, 1992). Compositions with $x \approx 0.05$ (for single crystals (Zhang et al., 2011, Kang et al., 2015)) or $x \approx 0.06$ (for ceramics (Takenaka et al., 1991)) correspond to the MPB, which is a transition region where the material properties are strongly enhanced. The characteristics of the structure at the MPB are still controversial. The symmetry is either described as cubic-like (Das Adhikary et al., 2023), rhombohedral with BO_6 tilt-free space group $R3m$ (Jo et al., 2011) or as a mixture of rhombohedral ($R3c$) and tetragonal ($P4bm$) phases (Ma and Tan, 2011, Liu et al., 2022, Fetzer et al., 2022).

The material properties of NBT-xBT are promising, but they still need to be improved to be suitable for industrial application. In order to go beyond the trial-and-error

approach to optimize the material performance, it is required to improve the knowledge about the relation between chemical composition, nanoscale structural features and macroscopic properties of NBT-*x*BT. A deeper understanding of the structure can be gained by analyzing the response of the structure to changes in temperature, pressure or to the application of an external electric field. The high- and low-temperature behavior and electric-field-induced changes of NBT-*x*BT have been already extensively studied (e.g. Daniels et al., 2012, Luo et al., 2017, de La Flor et al., 2017, de La Flor et al., 2019, Das Adhikary et al., 2023). In contrast, high-pressure (HP) studies are still scarce, although comprehending the HP behavior of a structure is essential to fully understand its characteristics. Up to now, HP x-ray and neutron diffraction data are only available for pure NBT. HP analyses on NBT-*x*BT are limited to Raman spectroscopy under non-hydrostatic conditions (Kreisel et al., 2001, Trujillo et al., 2005, Zheng et al., 2021). However, performing HP experiments under hydrostatic conditions is essential to get reliable results and to be able to compare the experimental data with theoretical calculations (Takemura, 2021). Besides, so far no HP Raman scattering data on any NBT-*x*BT compound have been collected in the spectral range below 80 cm^{-1}, which is dominated by the off-centering vibrations of A-site cations.

In this doctoral thesis high-pressure XRD and Raman scattering experiments have been performed on NBT-*x*BT single crystals with the aim to elucidate the pressure-induced structural changes depending on *x* and to better understand how exactly Ba^{2+} cations modify the nanoscale NBT structure below, at and above the MPB.

2 Objectives

Despite various studies on different compounds of NBT-*x*BT, the chemically-induced structural changes with different Ba content have still not been satisfactorily clarified. Since the macroscopic properties of a material strongly depend on the micro- and nano-scale structure, the aim of this doctoral thesis is to elucidate how the incorporation of different amounts of Ba^{2+} cations influences the structure of NBT-*x*BT at different length scales. Exposing a material to external stimuli, such as temperature, pressure or an electric field, enhances or suppresses certain structural features, which may help to draw conclusions on the ambient pressure structure. The application of pressure, in particular, is known to favor antiferrodistortive order in relaxor ferroelectrics, meaning octahedral tilting and antipolar cation displacements are enhanced, while polar order is suppressed (Mihailova et al., 2011).

The pressure evolution of the long-range order was examined via synchrotron XRD as well as via in-house XRD. The former experiments were carried out with the aim to determine the symmetry of the high-pressure structure, while the latter were performed using the eight-position diffracted beam centering technique (King and Finger, 1979) in order to follow the pressure-dependence of the unit-cell parameters with high precision and to determine the bulk modulus, which is a measure of the compressibility of a material. Pressure-induced mesoscopic scale transformation processes have been studied via polarized Raman scattering experiments as well as via analyses of the x-ray diffuse scattering (XDS) derived from synchrotron XRD.

The focus of the work was to better understand the structural features across the morphotropic phase boundary, and thus to elucidate the underlying physical phenomena, which are responsible for the enhanced properties at the MPB.

3 Results and Discussion

This section is based on the following articles:

a. **C. Rösche**, T. Boffa Ballaran, and B. Mihailova. Pressure-induced structural transformations in (1-x)$Na_{0.5}Bi_{0.5}TiO_3$-$x$$BaTiO_3$ at the morphotropic phase boundary. *Physical Review B* **108**, 094110 (2023).
B.M. and T.B. developed the original project. ***C.R.*** *carried out the Raman measurements and analyzed the Raman data.* ***C.R.*** *and T.B.B. carried out the XRD experiments and* ***C.R.*** *analyzed the XRD data.* ***C.R.*** *and B.M. wrote the manuscript. All authors reviewed and edited the manuscript.*

b. **C. Rösche**, T. Boffa Ballaran, T. Malcherek, C. Paulmann, R.J. Angel, S. Gorfman, and B. Mihailova. The high-pressure structure of (1-x)$Na_{0.5}Bi_{0.5}TiO_3$-$x$$BaTiO_3$ at the morphotropic phase boundary. *Scientific Reports* **14**, 18799 (2024)
B.M. and T.B. developed the original project. S.G. provided the single crystals. ***C.R.****, T.B., T.M., C.P., R.J.A. and B.M. carried out the single-crystal X-ray diffraction experiments.* ***C.R.*** *evaluated the data.* ***C.R.*** *and B.M. wrote the manuscript. All authors reviewed and edited the manuscript.*

c. **C. Rösche**, T. Boffa Ballaran, T. Malcherek, C. Paulmann, R.J. Angel, S. Gorfman, and B. Mihailova. Structural transformations in the (1-x)$Na_{0.5}Bi_{0.5}TiO_3$-$x$$BaTiO_3$ solid solution under high pressure: comparison between x below and above the morphotropic phase boundary. *Physical Review B* **112**, 184102 (2025)
B.M. and T.B. developed the original project. S.G. provided the single crystals. ***C.R.****, T.B., T.M., C.P., R.J.A. and B.M. carried out the single-crystal X-ray diffraction experiments.* ***C.R.*** *carried out the Raman measurements.* ***C.R.*** *evaluated the XRD and Raman data.* ***C.R.*** *and B.M. wrote the manuscript. All authors reviewed and edited the manuscript.*

Single crystals of (1-x)$Na_{0.5}Bi_{0.5}TiO_3$-$x$$BaTiO_3$ with x = 0, 0.013, 0.048 and 0.074 were synthesized by the top-seeded-solution-growth method (Woll et al., 2014). The chemical composition and homogeneity were verified by wavelength-dispersive x-ray emission spectroscopy (de La Flor et al., 2017). For the high-pressure experiments the samples were cut parallel to one of the pseudocubic {100} planes.

All high-pressure experiments were conducted using diamond anvil cells (DACs). For measurements up to 10 GPa methanol : ethanol 4:1 or methanol : ethanol : H_2O 16 : 3 : 1 mixtures were used as pressure-transmitting media, since both ensure hydrostatic conditions in this pressure range (Klotz et al., 2009, Angel et al., 2007). In experiments up to 12.3 GPa helium was used instead, which is hydrostatic at least up to $\sim$20 GPa (Klotz et al., 2009).

In the following, the results on the pressure-induced structural changes in the analyzed NBT-*x*BT compounds are presented, starting with alterations observed at the long-range scale via high-precision in-house XRD, followed by structural changes at intermediate- to long-range scale derived from x-ray diffuse scattering analyses and structure refinements based on synchrotron XRD data. At the end of the chapter, the local scale transformations of the structure observed by Raman spectroscopy are summarized.

3.1 In-house single crystal x-ray diffraction

The accurate determination of the unit-cell parameters of a crystal measured in a DAC is challenging because the optical alignment is restricted by the cell. The effect of crystal offsets and diffractometer aberrations can be overcome by measuring a set of reflections, each centered in eight positions (King and Finger, 1979).

In-house HP XRD experiments were performed only on NBT-0.048BT. For pure NBT the ferroic distortion of the unit cell at ambient pressure was too large to determine the lattice constants in terms of cubic metrics, but too small to detect any lower symmetry. The same is expected to be the case for NBT-0.013BT (de La Flor et al., 2017). For NBT-0.074BT initial HP experiments were carried out only up to 0.5 GPa, because HP synchrotron XRD data collected meanwhile indicated similar compressional to that of NBT-0.048BT.

The pseudocubic unit-cell parameters ($a \approx 3.9$ Å) of NBT-0.048BT were determined with high accuracy at increasing pressures up to 5.4 GPa. Above 4 GPa there is evidence that the structure significantly deviates from cubic symmetry, since the unconstrained lattice constants a_1 and a_2 become unequal (Rösche et al., 2023, Fig. 8a) and the Bragg reflections strongly broaden (Rösche et al., 2023, Fig. 8d). This broadening hindered the determination of the high-pressure symmetry from in-house XRD.

To determine the bulk modulus K_0 ($K_0 = -V_0(\delta P/\delta V)$) of NBT-0.048BT, the unit-

cell parameters were constrained to cubic symmetry at all pressures. The data points of the volume normalized to the volume at ambient pressure (V/V_0) as a function of pressure have been fitted up to 3.3 GPa using a third-order Birch-Murnaghan equation of state (EoS) (Rösche et al., 2023, Fig. 8b). The resulting bulk modulus is K_0 = 83.5 ± 1.7 GPa, which is smaller than that of the end members of the solid solution series $Na_{0.5}Bi_{0.5}TiO_3$ (K_0 = 95.2 GPa (Suchanicz, 2002)) and $BaTiO_3$ ($K_0 \approx$ 130 GPa (Zhang et al., 2016)), indicating that adding $BaTiO_3$ to NBT at level of the MPB softens the material.

Moreover, the normalized pressure $F = p/[3f(1+2f)^{5/2}]$ and Eulerian strain $f_E = [(V_0/V)^{2/3} - 1]/2$ (Angel, 2000) were calculated and plotted against each other (Rösche et al., 2023, Fig. 8c). Anomalous trends of $F(f_E)$ reveal discontinuities in the bulk modulus and/or its derivative, which indicate changes in the elastic properties and may point to alteration of the compression mechanism or a phase transition (Mihailova et al., 2008, Maier et al., 2011, Welsch et al., 2011). The $F(f_E)$ plot of NBT-0.048BT reveals that there are changes in the elastic behavior already at 0.5 and 0.9 GPa. Furthermore, it is indicated that the compressibility remains constant with increasing pressure in the range ∼2-4 GPa. This suggests that above 2 GPa a new compression mechanism allows the structure to better adapt to decreasing volume.

3.2 Synchrotron single crystal x-ray diffraction

3.2.1 Crystal structure and x-ray diffuse scattering at ambient pressure

At ambient pressure the diffraction pattern of NBT-*x*BT shows strong XDS around the Bragg reflections due to mesoscopically correlated structural distortions. If the pattern is analyzed in terms of a primitive cubic cell with $a \approx$ 3.9 Å, typical of the aristotype perovskite structure, superstructure reflections are observed at $\frac{1}{2}(hkl)$, indicating that the structure is actually doubled and it is best indexed in a double cubic perovskite cell with $a \approx$ 7.8 Å.

Reconstructed $hk0$ and $hk1$ reciprocal-space layers of NBT-*x*BT with x = 0.013, 0.048 and 0.074 are shown here in Figs. 3 and 4, in Rösche et al., 2024 Figs. 1 and 2 and in Rösche et al. 2025 Figs. 1-4. The shape of the XDS is asymmetric due to the difference of the charge environments of Bi^{3+} and Na^{+} that causes a transfer of XDS intensity from one side of a Bragg peak to another (Kreisel et al., 2003). This phenomenon is

similar to the atomic size effect in disordered alloys, which is observed if there is a large difference in scattering power of two types of atoms and low degree of chemical order (Warren et al., 1951, Welberry, 1986).

For NBT-0.013BT, XDS in the *hk*0 plane extends along pseudocubic $\langle 100 \rangle^*_{pc}$, similar to pure NBT (Kreisel et al., 2003, Thomas et al., 2010, Tung et al., 2018). Streak-like appearance of the XDS indicates that there are mesoscopically correlated deviations from the average structure along the direction of the streak, while the long-range order is undisturbed in directions perpendicular to the streaks. These structural distortions can be interpreted as subordinate platelet-like tetragonal nanoregions (Beanland and Thomas, 2011, Thomas et al., 2010). In the *hk*1 plane relatively weak but sharp reflections are observed at *hkl* with three odd indices (*ooo*), which are indicative of the existence of octahedral tilts with a pure anti-phase pattern (Woodward and Reaney, 2005) and may be either of type $a^-a^-c^-$ or $a^-a^-a^-$ (Ma et al., 2013). Contrary to the diffraction pattern of pure NBT, there is no sign of x-ray scattering at *hkl* with two odd and one even indices (*ooe*), which would indicate the presence of in-phase BO_6 tilting of type $a^0a^0c^+$ (see Fig. 1b) in the tetragonal nanoplatelets (Woodward and Reaney, 2005, Dorcet and Trolliard, 2008, Beanland and Thomas, 2011). Thus, the addition of 0.013 apfu of Ba^{2+} to NBT, does not significantly change the monoclinic/pseudorhombohedral matrix, but destroys the intermediate range correlation of the in-phase tilts in the platelet-like tetragonal nanoregions, indicating that this is where the Ba^{2+} cations are preferentially incorporated.

For NBT-0.048BT and NBT-0.074BT, XDS in the *hk*0 plane extends along pseudocubic $\langle 110 \rangle^*_{pc}$. This indicates the presence of subordinate nanoregions with polar cation shifts that correlate within $\{110\}_{pc}$ planes (Paściak et al., 2007), which are surrounded by a pseudocubic polarizable matrix for the case of $x = 0.048$, and a tetragonal matrix for the case of $x = 0.074$. In the *hk*1 plane sharp reflections are observed at *ooo* and broad and diffuse reflections at *eoo*, which also appear as sharp spots at *ooe* in the *hk*0 layer. For $x = 0.048$ the *ooo*-type reflections appear with significantly higher intensity than *ooe*-type reflections, while for $x = 0.074$ it is the other way around. Accordingly, the prevailing BO_6 tilt pattern is anti-phase at the MPB and in-phase for NBT-0.074BT, but the respective other type of tilting also exists in both, even if it is only subordinate. These observations show, that while the addition of $x = 0.013$ disturbs the correlation length of in-phase BO_6 tilts in tetragonal nanoregions, increasing the Ba content up to $x = 0.074$ leads to an overall increased fraction of in-phase tilted tetragonal material.

A further feature of the Bragg diffraction pattern of NBT-0.048BT and NBT-0.074BT is the occurrence of satellite peaks (Rösche et al., 2024, Fig. 1b, Rösche et al. 2025, Fig. S3). The satellites are off-set along $\langle 100 \rangle^*_{pc}$ towards the lower angle side of *eee* Bragg reflections by ∼0.3 and ∼0.6 reciprocal lattice units (r.l.u.) for x = 0.048, and by ∼0.15, ∼0.3, ∼0.45, ∼0.6 and ∼0.75 r.l.u for x = 0.074. In the XRD pattern of NBT-0.048BT they are only observed next to {220} reflections, while in that of NBT-0.074BT satellite peaks also appear in the vicinity of {240},{440} {020} and {040} reflections. The appearance of satellites has also been observed for pure NBT and NBT-0.04BT (Balagurov et al., 2006, Thomas et al., 2010, Daniels et al., 2012, Tung, 2014, Tung et al., 2018) and has been ascribed to a modulation of the structure. For pure NBT a modulated structure exists at ambient pressure between the depoling temperature T_d and the temperature at which the dielectric permittivity exhibits a maximum (T_m) (Trolliard and Dorcet, 2008, Aktas et al., 2018). The modulation of the NBT structure has been attributed to self-organized extended defects (*Pnma*-like layers) comprising mixed BO_6 tilts and antipolar A-cation shifts (Dorcet et al., 2008), which can relax the BO_6 tilt system between two opposing *R*3*c*-type domains. The same type of modulation can also relax the structure between two *P*4*bm*-type domains. The observation of satellite reflections in the XRD pattern of NBT-0.048BT and NBT-0.074BT at ambient pressure and temperature suggests that the modulated structure observed in pure NBT at elevated temperature is stabilized already at room temperature for these Ba-doped compounds.

3.2.2 High-pressure diffuse scattering analyses

Upon pressure increase XDS extending along $\langle 110 \rangle^*_{pc}$ is suppressed, while XDS extending along $\langle 100 \rangle^*_{pc}$ is enhanced. For NBT-0.013BT this change is not observed, since, as described above, XDS extends only along $\langle 100 \rangle^*_{pc}$ already at ambient pressure. For x = 0.048 and 0.074, however, the $\langle 100 \rangle^*_{pc}$ XDS becomes dominant only at 0.7 GPa and 2.3 GPa, respectively. Moreover, in the XRD pattern of NBT-0.074BT the *ooo* reflections become dominant with respect to the *ooe* reflections, indicating a change from a dominant in-phase BO_6 tilt pattern to a dominant anti-phase BO_6 tilt pattern. For NBT-0.048BT anti-phase octahedral tilting already prevails at ambient pressure. Accordingly, at 0.7 and 2.3 GPa, respectively, NBT-0.048BT and NBT-0.074BT adopt a structural state similar to that of pure NBT at ambient conditions, which means that the effect of added Ba^{2+} is overcome by the application of external pressure. In general hydrostatic pressure is isotropic and therefore cannot change the preferred direction of the polar cation

shifts in the tetragonal nanoregions and simultaneously the polar long-range order of the matrix. It is more likely that for x = 0.048 and 0.074 the Ba^{2+} cations are incorporated in both the pseudorhombohedral matrix and tetragonal nanoregions, disturbing the correlation length in both these fractions of the structure. For NBT-0.048BT this results in a pseudocubic polarizable matrix interspersed with rhombohedral polar clusters, which give rise to the $\langle 110 \rangle^*_{pc}$ XDS. For NBT-0.074BT the matrix has tetragonal symmetry, since Ba facilitates the expansion of tetragonal distortions, but the presence of $\langle 110 \rangle^*_{pc}$ XDS likewise indicates the existence of subordinate rhombohedral entities.

With further increase in pressure the $\langle 100 \rangle^*_{pc}$ XDS streaks increase in length and intensity. At a certain pressure, precursors for new developing Bragg reflections appear at *oee*. For x = 0.013 this happens at 1.8 GPa, along with the appearance of precursor reflections at *ooe*. For x = 0.048 and x = 0.074, where diffuse *ooe* reflections already exist at ambient pressure, enhanced XDS at *oee* is first observed at 2.8 and 3.3 GPa, respectively. As pressure increases, these precursors for Bragg reflections of the high-

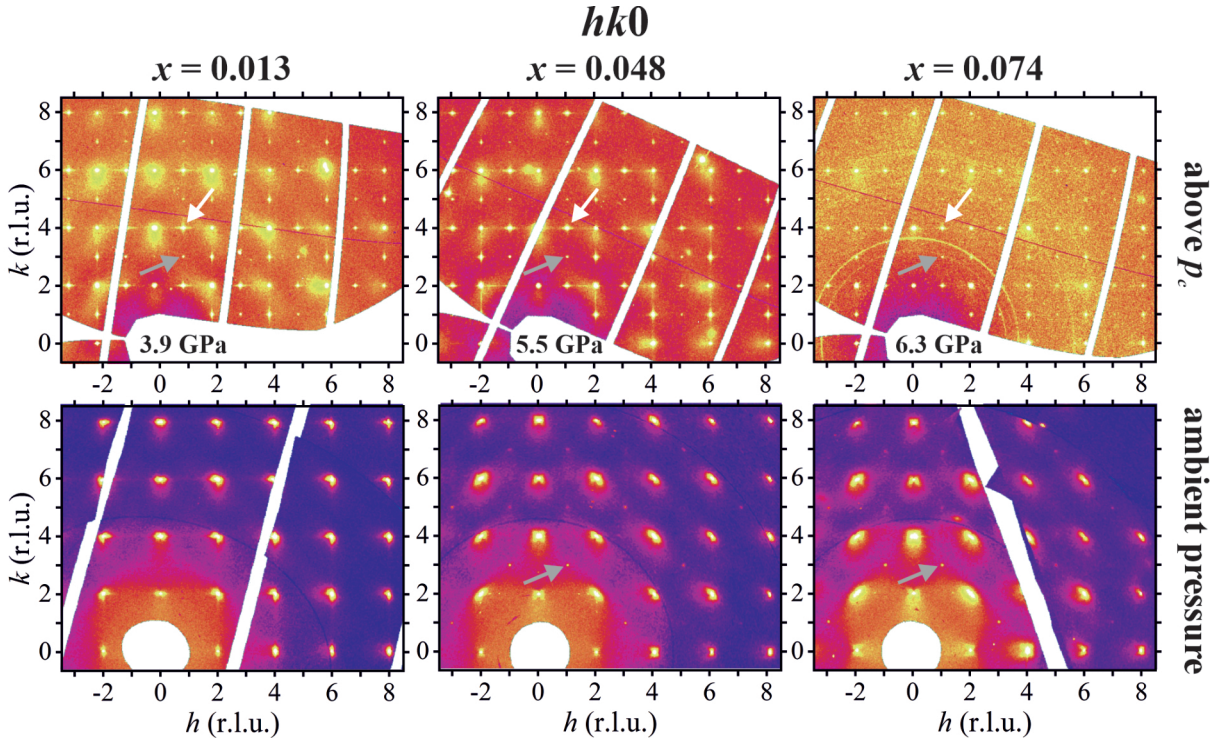


Figure 3: *hk*0 reciprocal space layers of NBT-*x*BT with x = 0.013, 0.048 and 0.074 at ambient pressure and above the phase transition pressure p_c. The indices refer to a doubled cubic perovskite cell. Representative *ooe* and *oee* reflections are marked by gray and white arrows, respectively.

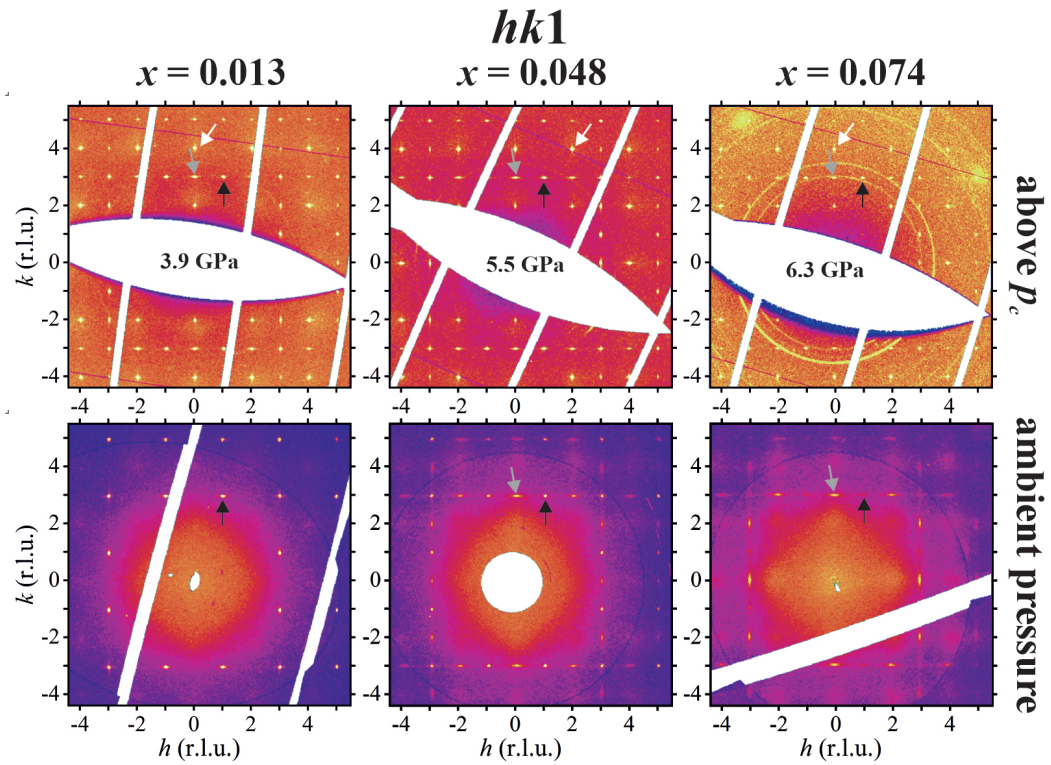


Figure 4: *hk*1 reciprocal space layers of NBT-*x*BT with x = 0.013, 0.048 and 0.074 at ambient pressure and above the phase transition pressure p_c. The indices refer to a doubled cubic perovskite cell. Representative *ooo*, *ooe* and *oee* reflections are marked by black, gray and white arrows, respectively.

pressure phase sharpen and increase in intensity, until a phase transition takes place. For x = 0.013 the critical phase transition pressure p_c has been crossed at 3.9 GPa, for x = 0.048 at 5.0 GPa and for x = 0.074 at 6.3 GPa (Figs. 3 and 4). In the XRD pattern of the high-pressure phase the XDS along $\langle 100 \rangle^*_{pc}$ is strongly reduced and there are new sharp Bragg reflections at *oee* and *ooe*. The co-existence of *ooo*, *ooe* and *oee* type reflections, characteristic of distortions driven by phonon modes at the *R*-, *M*- and *X*-point of the first Brillouin zone of the primitive cubic perovskite cell, respectively, indicates that the high-pressure phase of NBT-*x*BT is characterized by a mixed octahedral tilt pattern and antipolar A-cation shifts (Woodward and Reaney, 2005, Maier et al., 2011). The evolution of Bragg peak full widths at half maximum (FWHMs) of *ooe* reflections indicates that the development of the new tilt pattern is predominantly realized via rearrangement of the $a^0a^0c^+$ in-phase tilts (Rösche et al. 2025, Fig. 5). In the high-pressure phase the *ooo*-type reflections have a higher intensity than the *ooe*-type reflections, indicating that the anti-phase tilt component of the mixed BO_6 tilt pattern is stronger than the

in-phase component (Rösche et al., 2024, Fig. 3 a and b, Rösche et al. 2025, Fig. S2).

For NBT-0.074BT, satellite reflections were observed up to the last pressure measured below the phase transition (4.5 GPa). Their distance to the Bragg reflections remained constant, indicating that pressure does not change the periodicity of the modulation of the structure. However, in the high-pressure phase the modulation has disappeared.

3.2.3 The high-pressure structure of NBT-*x*BT

The symmetry of the high-pressure phase of NBT-*x*BT with x = 0.013 - 0.074 is orthorhombic with space group *Pnma* (see Rösche et al., 2024 Fig. 4), similar to pure NBT (Thomas et al., 2005). The orthorhombic **a** axis is oriented parallel to the cubic [110] direction and the **b** axis along the cubic [001] direction, meaning that the orthorhombic unit cell is rotated by 45° with respect to the cubic unit cell. In symmetry *Pnma* the B-site cations are constrained to be located at the centers of BO_6 octahedra and the A-site cations are only allowed to be shifted from the centers of AO_{12} polyhedra along **a** and **c**. Analyses of the atomic positions of the refined structure have revealed that the A cations are predominantly off-centered along **a** (Rösche et al., 2024 Fig. 5a, Rösche et al. 2025, Fig. 6a). While the A-cation off-centering $\vec{\delta}_A$ of NBT-0.048BT and NBT-0.074BT is the same within uncertainties and comparable to that of pure NBT (Thomas et al., 2005, Rösche et al., 2024, Rösche et al., 2025), $\vec{\delta}_A$ along **a** of NBT-0.013BT is significantly higher (Rösche et al. 2025).

The octahedral tilt pattern in the high-pressure *Pnma* phase is of type $a^-b^+a^-$. The BO_6 tilt angle φ of pure NBT (Thomas et al., 2005) and NBT-0.013BT tends to be higher than that of NBT-0.048BT and NBT-0.074BT at comparable pressures (Rösche et al., 2024 Fig. 5b, Rösche et al. 2025, Fig. 6b), indicating that the presence of a high enough amount of Ba^{2+} in the structure reduces not only the correlation length of BO_6 octahedral tilting at low pressure, but also diminishes the degree of tilting in the high-pressure phase.

3.3 Raman spectroscopy

3.3.1 Raman scattering at ambient pressure

Group theory analyses predict 27, 13, and 16 Raman active modes for NBT-xBT with monoclinic (Cc), rhombohedral ($R3c$), or tetragonal ($P4bm$) symmetry, respectively. When considering longitudinal optical (LO)-transverse optical (TO) effects, which occur for polar Raman active modes, the number of expected phonon modes even increases to 54 (Cc), 26 ($R3c$), or 28 ($P4bm$) (Datta et al., 2014). However, strong overlapping (Niranjan et al., 2013, Datta et al., 2014) hinders the distinction of such a high number of peaks in the Raman spectra of NBT-xBT. Therefore, the distinguishable peaks are discussed in terms of the dominant types of atomic vibrations that comprise a certain phonon mode.

Raman scattering at ∼30-60 cm^{-1} arises from vibrational modes comprising A-site cation displacements. The Raman signal is dominated by Bi^{3+} cation vibrations, due to their stronger affinity to off-center compared to Na^{+} and Ba^{2+} cations (Schütz et al., 2012, Keeble et al., 2013) as well as due to the higher degree of covalency of Bi^{3+}-O bonds with respect to Na^{+}-O and Ba^{2+}-O bonds (Datta et al., 2014).

At ∼115-160 cm^{-1} A-BO_3 translation modes are observed, which involve out-of-phase TiO_3 and Bi^{3+} cation vibrations, and thus are sensitive to the coupling of dipoles at adjacent A- and B-sites (Datta et al., 2014, Mihailova et al., 2008).

The Raman scattering at ∼240-325 cm^{-1} is dominated by B-cation localized modes comprising vibrations of off-centered Ti^{4+} cations. For pure NBT only one broad peak is resolved in this spectral region, whereas in the spectra of NBT-xBT a second peak is observed (Rösche et al., 2023 Fig. 1, Rösche et al. 2025, Fig. 7). This additional peak appears at lower wavenumbers and its intensity is enhanced in the cross polarized ($\bar{Z}(XY)Z$) Raman spectra, indicating that it is associated with vibrations of B-cations within planes perpendicular to the polar axis. The higher-wavenumber component appears stronger in the parallel polarized ($\bar{Z}(XX)Z$) spectra and is therefore related to B-cation vibrations along the polar axis. The existence of the additional lower-wavenumber peak indicates that the presence of Ba^{2+} in the structure induces a uniaxial local anisotropy of the BO_6 octahedra (de La Flor et al., 2017).

BO_6 tilting modes contribute to the Raman spectra in the range ∼370-420 cm^{-1}. These vibrations can also be regarded as A-O bond stretching vibrations within the pseudocubic {111} planes (Mihailova et al., 2002, Welsch et al., 2011). However, at ambient pressure these modes are difficult to be detected, because they appear with very

low intensity and overlap with the neighboring modes (see Fig. 5). In the $\bar{Z}(XX)Z$ ambient pressure Raman spectra of pure NBT and NBT-0.013BT two peaks can be resolved near 376 cm^{-1} and 407 cm^{-1} (Rösche et al., 2023, Fig. 1, Rösche et al. 2025, Fig. 7), while for NBT-0.074BT only one can be distinguished at ∼398 cm^{-1} (Rösche et al. 2025, Fig. 7) and none is detectable for NBT-0.048BT (Rösche et al., 2023, Fig. 1).

Raman scattering in the range from ∼470 - 860 cm^{-1} stems from internal BO_6 vibrational modes (Schütz et al., 2012, Mihailova et al., 2002, Welsch et al., 2011).

3.3.2 Raman scattering at high pressure

Parallel polarized ($\bar{Z}(XX)Z$) and cross polarized ($\bar{Z}(XY)Z$) Raman spectra were analyzed for all four compounds. Even though there are variations in the pressure trends of the peak wavenumbers (ω), full widths at half maximum (FWHMs, Γ) and fractional intensities ($I_n(s) = I(s)/\sum_s I(s)$, where $I(s)$ is the integrated intensity of a phonon mode (s)) derived from the Raman spectra measured in different scattering geometries, in general the trends give the same information. The focus of this work lies on the trends derived from the $\bar{Z}(XX)Z$ spectra.

The overall changes in the Raman spectra of NBT-xBT upon pressure increase are comparable to those observed for Pb-based perovskite-type ferroelectrics (Mihailova et al., 2011, Maier et al., 2011, Waeselmann et al., 2012, Welsch et al., 2009, Mihailova et al., 2013): The phonon modes related to off-center shifts of B-site cations strongly decrease in intensity, while octahedral tilting modes are amplified (Fig. 5, Rösche et al., 2023, Fig. 2, Rösche et al. 2025, Fig. 7), showing that polar order is suppressed, whereas antiferrodistortive order is enhanced by increasing pressure.

The evolution of the Raman peaks in the spectral range up to ∼450 cm^{-1} upon pressure increase was analyzed regarding anomalous behavior. Any deviation from linear increase of $\omega(p)$ and constant $\Gamma(p)$ and $I_n(p)$ trends is indicative of a structural alteration.

The B-cation localized modes of NBT-xBT soften, i. e. they are shifted to lower wavenumbers, as polar B-cation shifts are suppressed upon pressure increase (Rösche et al., 2023, Fig. 6, Rösche et al. 2025, Fig. 8b and d). The Ba-induced lower-wavenumber component (ω_{240}, ω_{250}, ω_{269}) strongly decreases in intensity and cannot be distinguished anymore above ∼0.2 GPa for x = 0.013, 1.0 GPa for x = 0.048 and 3.5 GPa for x = 0.074, although there is no preceding reduction of the wavenumber differ-

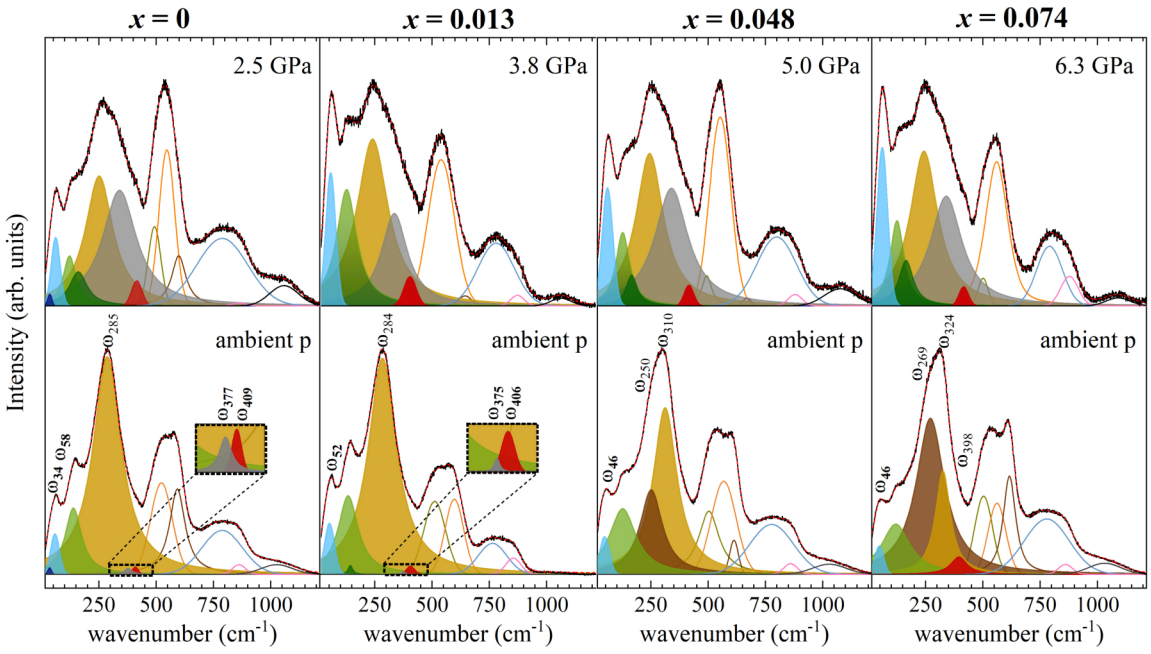


Figure 5: $\bar{Z}(XX)Z$ Raman spectra of NBT-xBT with x = 0, 0.013, 0.048 and 0.074 (solid black line) along with the fitted pseudo-Voigt functions and the resultant spectrum profiles (red dashed lines) at ambient pressure and above the phase transition pressure p_c.

ence of the two peaks. This indicates that the Ba-induced uniaxial local B-site anisotropy is reduced due to increased orientation disorder of local B-site dipoles. For x = 0.048 and 0.074, the disappearance of the lower-wavenumber peak (ω_{250}, ω_{269}) is preceded by a $\omega(p)$ minimum at ∼0.5 and ∼1.6 GPa, respectively, further confirming the occurrence of a structural rearrangement. These characteristic pressures of NBT-0.048BT (0.5 and 1.0 GPa) match the pressures at which discontinuities in the bulk modulus have been detected (0.5 and 0.9 GPa), indicating that the changes in the elastic properties are triggered by rearrangements in the B-site subsystem.

The phase transition detected by XRD can be also deduced from the Raman spectra considering the $\omega(p), \Gamma(p)$ and $I_n(p)$ trends. The A-cation localized mode (Rösche et al., 2023, Fig. 3, Rösche et al. 2025, Fig. 8a and c) exhibits plateau-like $\omega(p)$ behavior at 1.4(7) - 3.5(5) GPa for x = 0.013 (ω_{52}), at 1.9(1) - 4.3(6) GPa for x = 0.048 (ω_{46}) and at 2.5(2) - 4.9(5) GPa for x = 0.074 (ω_{46}), while for pure NBT $\omega_{\langle 34,58 \rangle}$ is shifted to lower wavenumbers at ∼1.5-2.2 GPa. At pressures above it shows normal behavior again by being shifted to higher wavenumbers. The beginning of anomalous $\omega(p)$ behavior indicates the onset of development of antipolar order of A-cation shifts, whereas the end of

the constant $\omega(p)$ trend for the NBT-xBT compounds and the minimum for pure NBT approximately correspond to the critical phase transition pressures deduced from XRD. The observation of a $\omega(p)$ plateau for the Ba-doped compounds instead of mode softening and a minimum as for pure NBT, indicates that the presence of Ba-induced local strains in NBT-xBT hinders the development of antipolar order of A-site cations. Similar behavior has been observed in Ba-doped lead-based relaxor ferroelectrics (Welsch et al., 2009).

The BO_6 tilt modes (Rösche et al., 2023, Fig. 7, Rösche et al. 2025, Fig. 8b and d) already existing at ambient pressure increase in intensity and width upon pressure increase, indicating an enhancement of octahedral tilting and local disorder in the BO_6 tilt pattern. In the spectra of pure NBT and NBT-0.013BT the I_n and Γ increase of the lower-wavenumber component near 376 cm^{-1} is significantly higher than that of the higher-wavenumber component at $\omega_{406-409}$. Near the phase transition pressure, $I_{n(376)}$ and Γ_{376} show a maximum and $d\omega/dp$ of both tilt modes changes abruptly, mirroring the change in the octahedral tilt pattern. In the spectra of NBT-0.048BT the lower-wavenumber component is only distinguishable above ∼2.7 GPa at ∼326 cm^{-1} and the higher-wavenumber component above ∼4.0 GPa at ∼412 cm^{-1}. For NBT-0.074BT ω_{398} is observable already at ambient pressure and has a minimum near 3 GPa, which is followed by the appearance of the lower-wavenumber tilt mode component at ∼310 cm^{-1}. At ∼4.5 GPa $\omega_{326}(p)$ exhibits a kink for NBT-0.048BT, marking the pressure at which the mixed octahedral tilt pattern is fully developed at a local scale. The same is observed for NBT-0.074BT at ∼5.6 GPa. The lower-wavenumber tilt mode is dominant in the high-pressure phase of all four compounds. In general, the existence of two octahedral tilt modes indicates the existence of tilts with unequal magnitudes (Maier et al., 2011) and does not give explicit information on the type of tilting. However, the comparison of the Raman peak evolutions with the information on octahedral tilt species in NBT-xBT at ambient and high-pressure derived from synchrotron XRD indicates that the lower-wavenumber component is related to anti-phase octahedral tilting and the higher-wavenumber component to in-phase octahedral tilting. Accordingly, the presence of a peak at ∼407 cm^{-1} in the ambient pressure Raman spectra of NBT-0.013BT shows that at a local scale in-phase octahedral tilts still exists, only their length of coherence is too small to be detected via XRD.

A further structural alteration at pressures above the phase transition is indicated in the Raman spectra of pure NBT and NBT-0.013BT by a minimum of the wavenumber of

the B-cation localized mode (ω_{285}) at 5 GPa and 5.7-8.0 GPa, respectively, which is accompanied by maxima in Γ and I_n of the A-cation and BO_6 tilting modes in the $\bar{Z}(XX)Z$ spectra. Additionally, for NBT-0.013BT a change in $d\omega_{52}/dp$ of the A cation localized mode is observed at $\sim$8 GPa. Moreover, a third BO_6 tilt mode becomes distinguishable in the $\bar{Z}(XX)Z$ spectra of pure NBT and the $\bar{Z}(XY)Z$ spectra of NBT-0.013BT at $\sim$390-395 cm^{-1}, indicating a further adjustment of the BO_6 tilt pattern. For pure NBT and NBT-0.013BT the fractional intensity of the B-cation localized mode $I_{n(285)}$ stops to decrease above the same pressures where $\omega_{285}(p)$ has a minimum, which suggests that above this pressure B-cation off-center shifts are not further reduced. The FWHM Γ_{285} is overall reduced, indicating that the order within the B-site subsystem is increased with pressure. For NBT-0.048BT and NBT-0.074BT on the other hand, no $\omega(p)$ minimum is observed for ω_{310} and ω_{324} up to 10 GPa, overall $\Gamma_{310}(p)$ and $\Gamma_{324}(p)$ are not reduced and $I_{n(310)}$ and $I_{n(324)}$ decrease slightly in the whole pressure range measured. For NBT-0.11BT a $\omega(p)$ minimum of the B-cation localized mode has been observed at 9-10 GPa (Trujillo et al., 2005), showing that the pressure-induced structural transformations are not simply gradually shifted to higher pressure with increasing Ba content, but there is an anomaly for compounds close to the morphotropic phase boundary. It is unclear, whether a $\omega(p)$ minimum of the B-cation localized mode exists at pressures above 10 GPa for NBT-0.048BT and NBT-0.074BT, or if the corresponding structural alteration is completely suppressed. However, it can be concluded that Ba-doping at MPB levels leads to a higher degree of disorder within the B-site subsystem in the high-pressure phase compared to pure NBT and NBT-xBT away from the MPB and transformations involving the B-site cations are hampered.

The persistence of Raman scattering arising from the B-cation localized modes in the high-pressure phase of all four compounds studied indicates that Ti^{4+} polar shifts still exist. However, their correlation length and/or life time is below the detection limit of XRD, since the XRD data indicate long-range *Pnma* symmetry, for which the B-site cations are constrained to the octahedral centers.

The fraction of off-centered A- and B-cations is related to the total fractional intensity of the corresponding modes $I_{n(XX+XY)}(s) = [I_{XX}(s) + I_{XY}(s)]/\sum_s[I_{XX}(s) + I_{XY}(s)]$, where $I_{XX}(s)$ and $I_{XY}(s)$ are the integrated Raman intensities of a phonon mode (s) measured in $\bar{Z}(XX)Z$ and $\bar{Z}(XY)Z$ scattering geometry (Fig. 6). In the low-pressure phase $I_{n(XX+XY)}$ of the B-cation localized modes (near 240 - 325 cm^{-1}) is the same within the uncertainties for all four compounds. For the A-cation localized modes

(near 30 - 60 cm^{-1}) $I_{n(XX+XY)}$ is significantly higher for NBT-0.013BT, which indicates that the large distortion from the idealized cubic perovskite cell observed for this compound (de La Flor et al., 2017) may be related to an increased fraction of off-centered A-cations. A possible explanation is related to the assumption that for x = 0.013 Ba^{2+} cations are preferably incorporated in the tetragonal nanoregions. Consequently, the volume of the Ba^{2+}-containing tetragonal nanoregions is enlarged, which in turn generates elastic stress on the boundary between the nanoregions and the surrounding pseudorhombohedral matrix, similar to phenomena at the boundary of a mineral inclusion-host system. The resultant strain accumulated in the pseudorhombohedral matrix is relaxed via a larger fraction of off-centered A-site cations, which ultimately leads to an increased unit-cell non-orthogonality.

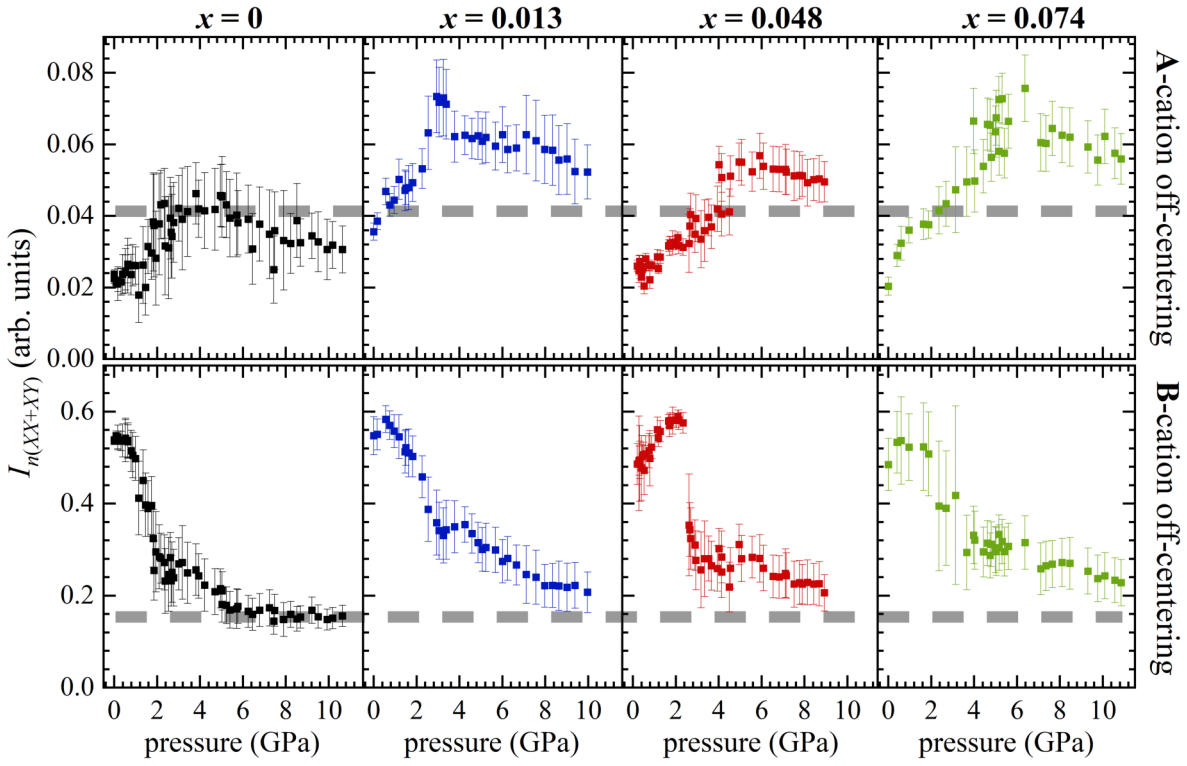


Figure 6: Pressure dependence of the total fractional intensity $I_{n(XX+XY)}(s) = [I_{XX}(s) + I_{XY}(s)] / \sum_i [I_{XX}(s) + I_{XY}(s)]$ of the A-cation localized modes (∼30-60 cm^{-1}) and B-cation localized modes (∼240-325 cm^{-1}) in NBT-xBT with x = 0, 0.013, 0.048 and 0.074, where $I_{XX}(s)$ and $I_{XY}(s)$ are the integrated Raman intensities of a phonon mode (s) measured in $\bar{Z}(XX)Z$ and $\bar{Z}(XY)Z$ scattering geometry. The gray dashed lines are a guide for the eye for better comparability of the intensities.

In the high-pressure phase $I_{n(XX+XY)}$ of A- and B-cation localized modes is higher for the Ba-doped compounds than for pure NBT. This shows that the presence of Ba^{2+} cations in the structure favors the off-centering of the dominant A-site cations at high pressures and hinders the reduction of polar B-cation shifts. The latter was also observed for Ba-doped relaxor ferroelectric $PbSc_{0.5}Ta_{0.5}O_3$ and $PbSc_{0.5}Nb_{0.5}O_3$ (Welsch et al., 2009, Maier et al., 2010).

4 Conclusions

Upon pressure increase, NBT-xBT with x = 0.013 - 0.074 undergo a reversible phase transition of predominant order-disorder character. The phase transition is preceded by structural alterations involving the reduction of B-cation off-center displacements, suppression of the Ba-induced local BO_6 anisotropy due to increased orientation disorder of local B-site dipoles and enhancement of octahedral tilting. The effect of Ba^{2+}-induced local internal stress fields is counterbalanced by an external hydrostatic pressure of ∼0.7 GPa for NBT-0.048BT and ∼2.3 GPa for NBT-0.074BT, at which the structural features resemble those of pure NBT at ambient pressure.

The symmetry of the high-pressure phase of NBT-xBT with x = 0.013 - 0.074 is orthorhombic *Pnma*, similar to that of pure NBT. The high-pressure structure is characterized by antipolar order of A-cation displacements, predominantly shifted along the **a**-axis ($\parallel [110]_{cubic}$), a mixed octahedral tilt pattern of type $a^-b^+a^-$ and uncorrelated polar B-cation shifts that are strongly reduced in magnitude compared to the low-pressure structure. The characteristic pressures of structural transformations are shifted to higher pressures with increasing amount of Ba. The critical phase-transition pressures p_c are ∼3.5(5), ∼4.3(6) and ∼4.9(5) GPa for x = 0.013, 0.048 and 0.074, respectively. The presence of Ba^{2+} in the structure hinders the pressure-induced reduction of cation shifts and consequently, the fraction of off-centered A- as well as B-cations is enhanced in the high-pressure phase of NBT-xBT with x = 0.013 - 0.074 compared to pure NBT.

The results furthermore indicate that at low levels of x, the Ba^{2+} cations are preferably incorporated in tetragonal (*P*4*bm*-type) nanoregions existing in the structure of pure NBT (Fig. 7). For x = 0.013 this leads to a disturbance of the correlation length of the in-phase octahedral tilts within the nanoregions, while the ⟨001⟩ cation shifts in the nanoregions as well as the pseudorhombohedral matrix comprising an anti-phase BO_6 tilt pattern remain undisturbed. At the morphotropic phase boundary (x = 0.048) Ba^{2+} cations are embedded in both the tetragonal nanoregions and the pseudorhombohedral matrix (Fig. 7), disrupting the coherence of A-cation off-center shifts. This results in a pseudocubic polarizable matrix interspersed with rhombohedral polar clusters. The dominant octahedral tilt pattern is anti-phase, but there is also subordinate in-phase tilted material, due to Ba-induced increase of the *P*4*bm* fraction. For x = 0.074 the predominant structural distortion is tetragonal with in-phase octahedral tilts of type

$a^0a^0c^+$. However, the long-range correlation of in-phase tilts is disturbed by the presence of subordinate rhombohedral regions and Ba-induced tetragonal BO_6 tilt-free defects.

For NBT-0.013BT the fraction of off-centered A-cations in the low-pressure phase and their displacement amplitude in the high-pressure phase are increased compared to the other compounds. This might be due to internal stresses imposed by Ba-containing tetragonal nanoregions on the pseudorhombohedral matrix.

The bulk modulus of NBT-0.048BT is reduced compared to pure NBT, indicating an increased elastic response of the material, which is in accordance with the enhanced macroscopic properties observed at the MPB. The nanoscale origin for the outstanding material properties is most likely a result of the optimal balance between nanoscale polar, antipolar and antiferrodistortive structural distortions, since there is no indication for any unique feature only present for this compound.

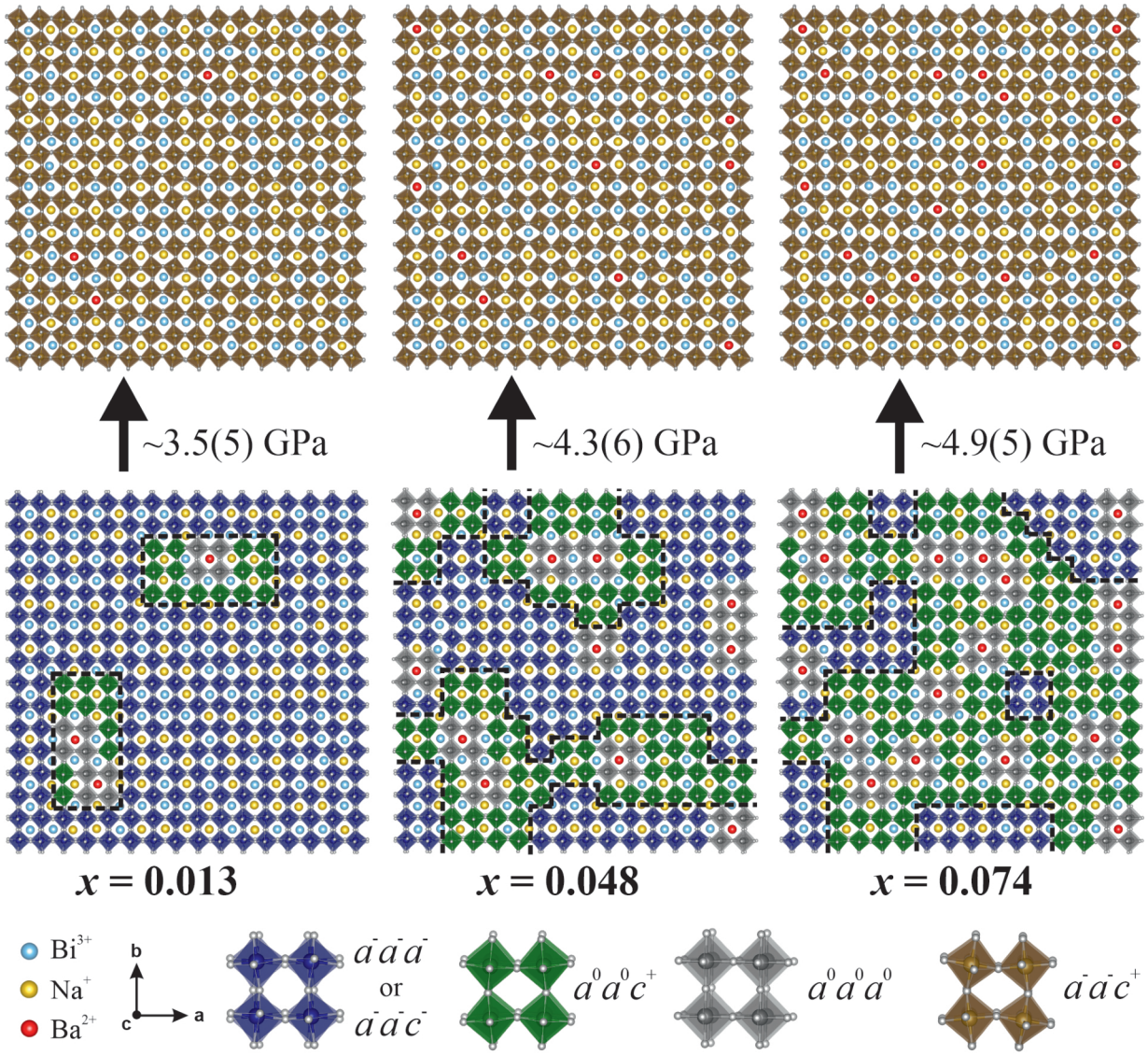


Figure 7: Sketch of the octahedral tilt patterns and Ba^{2+} cation distribution in NBT-xBT with x below (x = 0.013), near (x = 0.048) and above (x = 0.074) the morphotropic phase boundary at ambient and high pressure. A-site Ba^{2+} is assumed to locally suppress the BO_6 titling (Das Adhikary et al., 2021, Fetzer et al., 2022). The **a**, **b** and **c** axes correspond to cubic symmetry. The figures of tilted octahedra were prepared using VESTA (Momma and Izumi, 2011).

Bibliography

Aksel, E., Forrester, J. S., Jones, J. L., Thomas, P. A., Page, K., and Suchomel, M. R. (2011). Monoclinic crystal structure of polycrystalline $Na_{0.5}Bi_{0.5}TiO_3$. *Applied Physics Letters*, 98(15).

Aktas, O., Duclère, J. R., Quignon, S., Trolliard, G., and Salje, E. K. H. (2018). Polarity of modulated $Na_{0.5}Bi_{0.5}TiO_3$ and its slow structural relaxation. *Applied Physics Letters*, 113:032901.

Angel, R. J. (2000). Equations of state. *Reviews in Mineralogy and Geochemistry*, 41(1):35–59.

Angel, R. J., Bujak, M., Zhao, J., Gatta, G. D., and Jacobsen, S. D. (2007). Effective hydrostatic limits of pressure media for high-pressure crystallographic studies. *Journal of applied crystallography*, 40(1):26–32.

Balagurov, A. M., Koroleva, E. Y., Naberezhnov, A. A., Sakhnenko, V. P., Savenko, B. N., Ter-Oganessian, N. V., and Vakhrushev, S. B. (2006). The rhombohedral phase with incommensurate modulation in $Na_{1/2}Bi_{1/2}TiO_3$. *Phase Transitions*, 79(1-2):163–173.

Beanland, R. and Thomas, P. A. (2011). Imaging planar tetragonal sheets in rhombohedral $Na_{0.5}Bi_{0.5}TiO_3$ using transmission electron microscopy. *Scripta Materialia*, 65(5):440–443.

Bell, A. J., Comyn, T. P., and Stevenson, T. J. (2021). Expanding the application space for piezoelectric materials. *APL Materials*, 9(1).

Bell, A. J. and Deubzer, O. (2018). Lead-free piezoelectrics - the environmental and regulatory issues. *MRS Bulletin*, 43(8):581–587.

Bersuker, I. B. (2018). Vibronic (pseudo Jahn-Teller) theory of ferroelectricity: Novel aspects and applications. *Ferroelectrics*, 536(1):1–59.

Buttner, R. H. and Maslen, E. N. (1992). Structural parameters and electron difference density in $BaTiO_3$. *Acta Crystallographica Section B*, 48(6):764–769.

Daniels, J. E., Jo, W., and Donner, W. (2012). High-energy synchrotron x-ray diffraction for in situ diffuse scattering studies of bulk single crystals. *JOM*, 64(1):174–180.

Das Adhikary, G., Mahale, B., Rao, B. N., Senyshyn, A., and Ranjan, R. (2021). Depoling phenomena in $Na_{0.5}Bi_{0.5}TiO_3$-$BaTiO_3$: A structural perspective. *Physical Review B*, 103:184106.

Das Adhikary, G., Muleta, G. J., and Ranjan, R. (2023). Composition–electric field phase diagram of the Pb-free piezoelectric system $Na_{0.5}Bi_{0.5}TiO_3-BaTiO_3$. *Physical Review B*, 108(22).

Datta, K., Richter, A., Göbbels, M., Neder, R. B., and Mihailova, B. (2014). Atomistic origin of huge response functions at the morphotropic phase boundary of $(1-x)Na_{0.5}Bi_{0.5}TiO_3-xBaTiO_3$. *Physical Review B*, 90(6).

de La Flor, G., Gorfman, S., and Mihailova, B. (2019). Local-scale structural response of (1-x)$Na_{0.5}Bi_{0.5}TiO_3 - xBaTiO_3$ to external electric fields. *Applied Physics Letters*, 114(4).

de La Flor, G., Malcherek, T., Gorfman, S., and Mihailova, B. (2017). Structural transformations in (1-x)$Na_{0.5}Bi_{0.5}TiO_3 - xBaTiO_3$ single crystals studied by Raman spectroscopy. *Physical Review B*, 96(21).

Dorcet, V. and Trolliard, G. (2008). A transmission electron microscopy study of the A-site disordered perovskite $Na_{0.5}Bi_{0.5}TiO_3$. *Acta Materialia*, 56(8):1753–1761.

Dorcet, V., Trolliard, G., and Boullay, P. (2008). Reinvestigation of phase transitions in $Na_{0.5}Bi_{0.5}TiO_3$ by tem. part i: First order rhombohedral to orthorhombic phase transition. *Chemistry of Materials*, 20:5061–5073.

Fan, P., Liu, K., Ma, W., Tan, H., Zhang, Q., Zhang, L., Zhou, C., Salamon, D., Zhang, S.-T., Zhang, Y., Nan, B., and Zhang, H. (2021). Progress and perspective of high strain NBT-based lead-free piezoceramics and multilayer actuators. *Journal of Materiomics*, 7(3):508–544.

Fetzer, A.-K., Wohninsland, A., Lalitha, K. V., and Kleebe, H.-J. (2022). Nanoscale polar regions embedded within ferroelectric domains in $Na_{1/2}Bi_{1/2}TiO_3-BaTiO_3$. *Physical Review Materials*, 6(6).

Ge, W., Luo, C., Devreugd, C. P., Zhang, Q., Ren, Y., Li, J., Luo, H., and Viehland, D. (2013). Direct evidence of correlations between relaxor behavior and polar nano-regions in relaxor ferroelectrics: A case study of lead-free piezoelectrics $Na_{0.5}Bi_{0.5}TiO_3 - x\%BaTiO_3$. *Applied Physics Letters*, 103(24).

Glazer, A. M. (1972). The classification of tilted octahedra in perovskites. *Acta Crystallographica Section B Structural Crystallography and Crystal Chemistry*, 28(11):3384–3392.

Goldschmidt, V. (1926). Die gesetze der krystallochemie. *Naturwissenschaften*, 14:477–485.

Gorfman, S. and Thomas, P. A. (2010). Evidence for a non-rhombohedral average structure in the lead-free piezoelectric material $Na_{0.5}Bi_{0.5}TiO_3$. *Journal of Applied Crystallography*, 43(6):1409–1414.

Jo, W., Daniels, J. E., Jones, J. L., Tan, X., Thomas, P. A., Damjanovic, D., and Rödel, J. (2011). Evolving morphotropic phase boundary in lead-free $(Bi_{1/2}Na_{1/2})TiO_3$-$BaTiO_3$ piezoceramics. *Journal of Applied Physics*, 109(1).

Kang, S.-J. L., Park, J.-H., Ko, S.-Y., and Lee, H.-Y. (2015). Solid–state conversion of single crystals: The principle and the state–of–the–art. *Journal of the American Ceramic Society*, 98(2):347–360.

Keeble, D. S., Barney, E. R., Keen, D. A., Tucker, M. G., Kreisel, J., and Thomas, P. A. (2013). Bifurcated polarization rotation in bismuth-based piezoelectrics. *Advanced Functional Materials*, 23(2):185–190.

King, H. E. and Finger, L. W. (1979). Diffracted beam crystal centering and its application to high-pressure crystallography. *Journal of Applied Crystallography*, 12(4):374–378.

Klotz, S., Chervin, J.-C., Munsch, P., and Le Marchand, G. (2009). Hydrostatic limits of 11 pressure transmitting media. *Journal of Physics D: Applied Physics*, 42(7):075413.

Kreisel, J., Bouvier, P., Dkhil, B., Thomas, P. A., Glazer, A. M., Welberry, T. R., Chaabane, B., and Mezouar, M. (2003). High-pressure x-ray scattering of oxides with a nanoscale local structure: Application to $Na_{0.5}Bi_{0.5}TiO_3$. *Physical Review B*, 68(1).

Kreisel, J., Glazer, A. M., Bouvier, P., and Lucazeau, G. (2001). High-pressure raman study of a relaxor ferroelectric: The $Na_{0.5}Bi_{0.5}TiO_3$ perovskite. *Physical Review B*, 63(17).

Lee, E. and Son, J. Y. (2024). Energy storage and ferroelectric properties of flexible 1-x($Na_{0.5}Bi_{0.5}TiO_3$)-x$BaTiO_3$ thin films on Pt/mica substrates. *Journal of Energy Storage*, 77:109945.

Levin, I. and Reaney, I. M. (2012). Nano– and mesoscale structure of $Na_{0.5}Bi_{0.5}TiO_3$: A TEM perspective. *Advanced Functional Materials*, 22(16):3445–3452.

Liu, H., Zhang, Q., Luo, H., and Zhu, J. (2022). Direct observations of electric-field-induced domain switching and phase transition in $0.95Na_{0.5}Bi_{0.5}TiO_3$-$0.05BaTiO_3$ single crystals using in situ transmission electron microscopy. *Applied Physics Letters*, 120(7).

Lu, X., Xu, J., Yang, L., Zhou, C., Zhao, Y., Yuan, C., Li, Q., Chen, G., and Wang, H. (2016). Energy storage properties of $(Bi_{0.5}Na_{0.5})_{0.93}Ba_{0.07}TiO_3$ lead-free ceramics modified by La and Zr co-doping. *Journal of Materiomics*, 2(1):87–93.

Luo, C., Bansal, D., Li, J., Viehland, D., Winn, B., Ren, Y., Li, X., Luo, H., and Delaire, O. (2017). Neutron and x-ray scattering study of phonon dispersion and diffuse scattering in (Na,Bi)$TiO_3 - x BaTiO_3$ single crystals near the morphotropic phase boundary. *Physical Review B*, 96(17).

Ma, C., Guo, H., and Tan, X. (2013). A new phase boundary in $(Bi_{1/2}Na_{1/2})TiO_3$ - $BaTiO_3$ revealed via a novel method of electron diffraction analysis. *Advanced Functional Materials*, 23(42):5261–5266.

Ma, C. and Tan, X. (2011). In situ transmission electron microscopy study on the phase transitions in lead-free (1-x)$(Bi_{1/2}Na_{1/2})TiO_3$-$x BaTiO_3$ ceramics. *Journal of the American Ceramic Society*, 94(11):4040–4044.

Ma, C., Tan, X., Dul'kin, E., and Roth, M. (2010). Domain structure-dielectric property relationship in lead-free (1-x)$(Bi_{1/2}Na_{1/2})TiO_3$-$x BaTiO_3$ ceramics. *Journal of Applied Physics*, 108(10).

Maier, B. J., Waeselmann, N., Mihailova, B., Angel, R. J., Ederer, C., Paulmann, C., Gospodinov, M., Friedrich, A., and Bismayer, U. (2011). Structural state of relaxor ferroelectrics $PbSc_{0.5}Ta_{0.5}O_3$ and $PbSc_{0.5}Nb_{0.5}O_3$ at high pressures up to 30 GPa. *Physical Review B*, 84(17).

Maier, B. J., Welsch, A.-M., Angel, R. J., Mihailova, B., Zhao, J., Engel, J. M., Schmitt, L. A., Paulmann, C., Gospodinov, M., Friedrich, A., and Bismayer, U. (2010). A -site doping-induced renormalization of structural transformations in the $PbSc_{0.5}Nb_{0.5}O_3$ relaxor ferroelectric under high pressure. *Physical Review B*, 81(17).

Meyer, K.-C., Gröting, M., and Albe, K. (2015). Octahedral tilt transitions in the relaxor ferroelectric $Na_{1/2}Bi_{1/2}TiO_3$. *Journal of Solid State Chemistry*, 227:117–122.

Mihailova, B., Angel, R. J., Maier, B. J., Welsch, A.-M., Zhao, J., Gospodinov, M., and Bismayer, U. (2011). The structural state of lead-based relaxor ferroelectrics under pressure. *IEEE Transactions on Ultrasonics, Ferroelectrics, and Frequency Control*, 58(9):1905–1913.

Mihailova, B., Angel, R. J., Welsch, A.-M., Zhao, J., Engel, J., Paulmann, C., Gospodinov, M., Ahsbahs, H., Stosch, R., Güttler, B., and Bismayer, U. (2008). Pressure-induced phase transition in $PbSc_{0.5}Ta_{0.5}O_3$ as a model Pb-based perovksite-type relaxor ferroelectric. *Physical Review Letters*, 101(1):017602.

Mihailova, B., Bismayer, U., Güttler, B., Gospodinov, M., and Konstantinov, L. (2002). Local structure and dynamics in relaxor-ferroelectric $PbSc_{1/2}Nb_{1/2}O_3$ and $PbSc_{1/2}Ta_{1/2}O_3$ single crystals. *Journal of Physics: Condensed Matter*, 14(5):1091–1105.

Mihailova, B., Waeselmann, N., Maier, B. J., Welsch, A.-M., Angel, R. J., and Bismayer, U. (2013). Pressure-induced structural transformations in advanced ferroelectrics with relaxor behaviour. *High Pressure Research*, 33(3):595–606.

Momma, K. and Izumi, F. (2011). Vesta 3 for three-dimensional visualization of crystal, volumetric and morphology data. *Journal of Applied Crystallography*, 44(6):1272–1276.

Niranjan, M. K., Karthik, T., Asthana, S., Pan, J., and Waghmare, U. V. (2013). Theoretical and experimental investigation of Raman modes, ferroelectric and dielectric properties of relaxor $Na_{0.5}Bi_{0.5}TiO_3$. *Journal of Applied Physics*, 113(19).

Okawa, T., Imaeda, M., and Ohsato, H. (2002). Site occupancy of Bi ions and microwave dielectric properties in $Ba_{6-3x}Nd_{8+2x}Ti_{18}O_{54}$ solid solutions. *Materials Science and Engineering: B*, 88(1):58–61.

Paściak, M., Wołcyrz, M., and Pietraszko, A. (2007). Interpretation of the diffuse scattering in Pb-based relaxor ferroelectrics in terms of three-dimensional nanodomains of the $\langle 110 \rangle$-directed relative interdomain atomic shifts. *Physical Review B*, 76(1).

Ranjan, R. and Dviwedi, A. (2005). Structure and dielectric properties of $(Na_{0.50}Bi_{0.50})_{1-x}Ba_xTiO_3$: $0 \leq x \leq 0.10$. *Solid State Communications*, 135(6):394–399.

Reaney, I. M., Enrico L. Colla, E. L. C., and Nava Setter, N. S. (1994). Dielectric and structural characteristics of ba- and sr-based complex perovskites as a function of tolerance factor. *Japanese Journal of Applied Physics*, 33(7R):3984.

RoHS (2011). Directive 2011/65/EU of the European Parliament and of the Council of 8 june 2011 on the restriction of the use of certain hazardous substances in electrical and electronic equipment. *Official Journal of the European Union*, L 174/88.

RoHS2 (2024). Directive 2011/65/EU (RoHS2) exemptions list - validity and rolling plan December 2024. *https://environment.ec.europa.eu/topics/waste-and-recycling/rohs-directive/implementation-rohs-directive_en*.

Rösche, C., Boffa Ballaran, T., Malcherek, T., Paulmann, C., Angel, R. J., Gorfman, S., and Mihailova, B. (2024). The high-pressure structure of (1-x)$Na_{0.5}Bi_{0.5}TiO_3$ -x$BaTiO_3$ at the morphotropic phase boundary. *Scientific reports*, 14(1):18799.

Rösche, C., Boffa-Ballaran, T., and Mihailova, B. (2023). Pressure-induced structural transformations in (1-x)$Na_{0.5}Bi_{0.5}TiO_3$-$x$$BaTiO_3$ at the morphotropic phase boundary. *Physical Review B*, 108(9).

Schütz, D., Deluca, M., Krauss, W., Feteira, A., Jackson, T., and Reichmann, K. (2012). Lone–pair–induced covalency as the cause of temperature– and field–induced instabilities in bismuth sodium titanate. *Advanced Functional Materials*, 22(11):2285–2294.

Shannon, R. D. (1976). Revised effective ionic radii and systematic studies of interatomic distances in halides and chalcogenides. *Acta Crystallographica Section A*, 32(5):751–767.

Suchanicz, J. (2002). Elastic constants of $Na_{0.5}Bi_{0.5}TiO_3$ single crystal. *Journal of Materials Science*, 37(3):489–491.

Takemura, K. (2021). Hydrostaticity in high pressure experiments: some general observations and guidelines for high pressure experimenters. *High Pressure Research*, 41(2):155–174.

Takenaka, T., Kei-ichi Maruyama, K.-i. M., and Koichiro Sakata, K. S. (1991). ($Bi_{1/2}Na_{1/2}$)TiO_3-$BaTiO_3$ system for lead-free piezoelectric ceramics. *Japanese Journal of Applied Physics*, 30(9S):2236.

Thomas, P. A., Kreisel, J., Glazer, A. M., Bouvier, P., Jiang, Q., and Smith, R. (2005). The high-pressure structural phase transitions of sodium bismuth titanate. *Zeitschrift für Kristallographie - Crystalline Materials*, 220(8):717–725.

Thomas, P. A., Trujillo, S., Boudard, M., Gorfman, S., and Kreisel, J. (2010). Diffuse X-ray scattering in the lead-free piezoelectric crystals $Na_{1/2}Bi_{1/2}TiO_3$ and Ba-doped $Na_{1/2}Bi_{1/2}TiO_3$. *Solid State Sciences*, 12(3):311–317.

Trolliard, G. and Dorcet, V. (2008). Reinvestigation of phase transitions in $Na_{0.5}Bi_{0.5}TiO_3$ by TEM. part ii: Second order orthorhombic to tetragonal phase transition. *Chemistry of Materials*, 20:5074–5082.

Trujillo, S., Kreisel, J., Jiang, Q., Smith, J. H., Thomas, P. A., Bouvier, P., and Weiss, F. (2005). The high-pressure behaviour of Ba-doped $Na_{1/2}Bi_{1/2}TiO_3$ investigated by Raman spectroscopy. *Journal of Physics: Condensed Matter*, 17(41):6587–6597.

Tung, P. (2014). Modelling of disorder in lead-free sodium bismuth titanate ferroelectric single crystals using diffuse x-ray scattering. *PhD thesis, UNSW Sydney*.

Tung, P. K., Major, M., Hudspeth, J., and Daniels, J. E. (2018). Compositional dependence of disordered structures in $Na_{1/2}Bi_{1/2}TiO_3$-$BaTiO_3$ solid solutions. *Materials Research Bulletin*, 106:301–306.

Waeselmann, N., Maier, B. J., Mihailova, B., Angel, R. J., Zhao, J., Gospodinov, M., Paulmann, C., Ross, N., and Bismayer, U. (2012). Pressure-induced structural transformations in pure and Ru-doped $0.9PbZn_{1/3}Nb_{2/3}O_3$-$0.1PbTiO_3$ near the morphotropic phase boundary. *Physical Review B*, 85(1).

Warren, B. E., Averbach, B. L., and Roberts, B. W. (1951). Atomic size effect in the x-ray scattering by alloys. *Journal of Applied Physics*, 22(12):1493–1496.

Welberry, T. R. (1986). Multi-site correlations and the atomic size effect. *Journal of Applied Crystallography*, 19(5):382–389.

Welsch, A.-M., Maier, B. J., Engel, J. M., Mihailova, B., Angel, R. J., Paulmann, C., Gospodinov, M., Friedrich, A., Stosch, R., Güttler, B., Petrova, D., and Bismayer, U. (2009). Effect of Ba incorporation on pressure-induced structural changes in the relaxor ferroelectric $PbSc_{0.5}Ta_{0.5}O_3$. *Physical Review B*, 80(10).

Welsch, A.-M., Maier, B. J., Mihailova, B., Angel, R. J., Zhao, J., Paulmann, C., Engel, J. M., Gospodinov, M., Marinova, V., and Bismayer, U. (2011). Transformation processes in relaxor ferroelectric $PbSc_{0.5}Ta_{0.5}O_3$ heavily doped with Nb and Sn. *Zeitschrift für Kristallographie*, 226(2):126–137.

Woll, M., Burianek, M., Klimm, D., Gorfman, S., and Mühlberg, M. (2014). Characterization of $(Bi_{0.5}Na_{0.5})_{1-x}BaTiO_3$ grown by the TSSG method. *Journal of Crystal Growth*, 401:351–354.

Woodward, D. I. and Reaney, I. M. (2005). Electron diffraction of tilted perovskites. *Acta Crystallographica. Section B, Structural Science*, 61(Pt 4):387–399.

Zhang, H.-Y., Zeng, Z.-Y., Zhao, Y.-Q., Lu, Q., and Cheng, Y. (2016). First-principles study of lattice dynamics, structural phase transition, and thermodynamic properties of barium titanate. *Zeitschrift für Naturforschung A*, 71(8):759–768.

Zhang, Q., Zhao, X., Sun, R., and Luo, H. (2011). Crystal growth and electric properties of lead–free NBT–BT at compositions near the morphotropic phase boundary. *Physica Status Solidi (a)*, 208(5):1012–1020.

Zheng, Q., Li, Q., Xue, S., Wu, Y., Wang, L., Zhang, Q., Qin, X., Zhao, X., Wang, F., and Yang, W. (2021). Pressure driven structural evolutions of $0.935(Na_{0.5}Bi_{0.5})TiO_3$-$0.065BaTiO_3$ lead-free ferroelectric single crystal through raman spectroscopy. *Chinese Physics Letters*, 38(2):026102.

Zhou, D., Lam, K. H., Chen, Y., Zhang, Q., Chiu, Y. C., Luo, H., Dai, J., and Chan, H. L. W. (2012). Lead-free piezoelectric single crystal based 1–3 composites for ultrasonic transducer applications. *Sensors and Actuators A: Physical*, 182:95–100.

Acknowledgments

I am very grateful to my supervisor Prof. Dr. Boriana Mihailova for all that she has taught me and for all the guidance, enthusiasm, patience and support throughout my studies. Likewise, I am thankful to my other supervisor Dr. Tiziana Boffa Ballaran, especially for teaching me how to perform and evaluate XRD experiments and for helping with the in-house XRD experiments carried out at BGI in Bayreuth.

In addition to my supervisors, I would also like to thank the other scientists who were involved in the beamtime at DESY and ensured that the experiments could be realized. Special thanks go to Dr. Thomas Malcherek for teaching me a lot about structure refinements, to Dr. Carsten Paulmann for the technical support during the experiments at DESY and to Dr. Ross Angel for sharing his expertise.

I would like to thank everyone mentioned so far as well as Dr. Semën Gorfman for reviewing the papers related to this thesis and for always giving constructive feedback.

Furthermore, I thank Peter Stutz for preparing the samples for the high-pressure experiments, and Dr. Alexander Kurnosov for being a great support in preparing the high-pressure experiments during my stays in Bayreuth.

I am thankful to all the current and former members of the institute and participants of our Crystal Coffee meetings. Special thanks go to Dr. Irina Schablack for being a great company in the office and over lunch, to Dr. Stylianos Aspiotis, who always did his best to help me with various problems, and to Dr. Nicola Campomenosi, for making sure I eat enough cookies.

Many thanks go to the Deutsche Forschungsgemeinschaft (DFG) for financial support through the projects MI 1127/12-1 and BO 255/10.

Last but not least, I am truly thankful to my partner Elias and all my friends and family for all their support and encouragement.

List of publications

Publications related to the doctoral thesis:

- **Rösche, C.**, Boffa Ballaran, T., and Mihailova, B. Pressure-induced structural transformations in (1-x)$Na_{0.5}Bi_{0.5}TiO_3$-$x$$BaTiO_3$ at the morphotropic phase boundary. *Physical Review B* **108**, 094110 (2023).

- **Rösche, C.**, Boffa Ballaran, T., Malcherek, T., Paulmann, C., Angel, R.J., Gorfman, S., and Mihailova, B. The high-pressure structure of (1-x)$Na_{0.5}Bi_{0.5}TiO_3$-$x$$BaTiO_3$ at the morphotropic phase boundary. *Scientific Reports* **14**, 18799 (2024).

- **Rösche, C.**, Boffa Ballaran, T., Malcherek, T., Paulmann, C., Angel, R.J., Gorfman, S., and Mihailova, B. Structural transformations in the (1-x)$Na_{0.5}Bi_{0.5}TiO_3$-$x$$BaTiO_3$ solid solution under high pressure: comparison between x below and above the morphotropic phase boundary. *Physical Review B* **112**, 184102 (2025)

Other publications:

- **Rösche, C.**, Waeselmann, N., Petrova, N., Malcherek, T., Schlüter, J., Mihailova, B. Oxidation processes and thermal stability of actinolite. *Physics and Chemistry of Minerals* **49**, 47 (2022)

Contributions to conferences related to this doctoral thesis:

- **Rösche, C.**, Boffa Ballaran, T., and Mihailova, B. Pressure-induced structural transformations in (1-x)$Na_{0.5}Bi_{0.5}TiO_3$-$x$$BaTiO_3$ at the morphotropic phase boundary. *Poster presentation* at the joint conference of the International Symposium on Applications of Ferroelectrics, the Piezoresponse Force Microscopy International Workshop series and the European Conference on Applications of Polar Dielectrics (ISAF-PFM-ECAPD), Tours, France, 27 June - 1 July, 2022

- **Rösche, C.**, Boffa Ballaran, T., and Mihailova, B. Pressure-induced structural transformations in (1-x)$Na_{0.5}Bi_{0.5}TiO_3$-$x$$BaTiO_3$ single crystals. IMA2022, *Poster presentation* at the 23rd General Meeting of the International Mineralogical Association (IMA2022), Lyon, France, 18-22 July, 2022.

- **Rösche, C.**, Boffa Ballaran, T., and Mihailova, B. The high-pressure structural behaviour of (1-*x*)$Na_{0.5}Bi_{0.5}TiO_3$-*x*$BaTiO_3$: insights from single-crystal Raman spectroscopy and XRD. *Oral presentation* at the 15th International Meeting on Ferroelectricity (IMF2023), Tel Aviv, Israel, 26-30 March, 2023

- **Rösche, C.**, Boffa Ballaran, T., Malcherek, T., Paulmann, C., Angel, R.J., and Mihailova, B. Structural peculiarities in (1-*x*)$Na_{0.5}Bi_{0.5}TiO_3$-*x*$BaTiO_3$ at the morphotropic phase boundary studied by high-pressure XRD and Raman spectroscopy. *Oral presentation* at the joint meeting of the Mineralogical Societies of Austria, Germany, and Slovakia (MinWien2023), Wien, Austria, 17-23 September, 2023

- **Rösche, C.**, Boffa Ballaran, T., Malcherek, T., Paulmann, C., Angel, R.J., and Mihailova, B. Multi-scale analysis of the high-pressure behaviour of (1-*x*)$Na_{0.5}Bi_{0.5}TiO_3$-*x*$BaTiO_3$ at the morphotropic phase boundary. *Poster presentation* at the 32nd annual meeting of the German Crystallographic Society (DGK), Bayreuth, Germany, 18-21 March, 2024

- **Rösche, C.**, Boffa Ballaran, T., Malcherek, T., Paulmann, C., Angel, R.J., and Mihailova, B. Multi-scale structural response of (1-*x*)$Na_{0.5}Bi_{0.5}TiO_3$-*x*$BaTiO_3$ single crystals to high pressures. *Oral presentation* at the European Conference on Applications of Polar Dielectrics (ECAPD2024), Trondheim, Norway, 16-19 June, 2024

Pressure-induced structural transformations in (1-*x*)$Na_{0.5}Bi_{0.5}TiO_3$-*x*$BaTiO_3$ at the morphotropic phase boundary

Constanze Rösche[1,*], Tiziana Boffa Ballaran[2], Boriana Mihailova[1]

[1]*Department of Earth System Sciences, Universität Hamburg, Grindelallee 48, 20146 Hamburg, Germany*

[2]*Bayerisches Geoinstitut, Universität Bayreuth, Universitätsstraße 30, 95440 Bayreuth, Germany*

Abstract

Pressure-induced structural transformations up to 8.9 GPa in the perovskite-type (ABO_3) (1-*x*)$Na_{0.5}Bi_{0.5}TiO_3$-*x*$BaTiO_3$ (NBT-*x*BT) at the morphotropic phase boundary (MPB), x_{MPB} = 0.048, were studied by means of polarized Raman spectroscopy and single-crystal x-ray diffraction (XRD). Raman spectroscopic analysis was performed also on reference undoped NBT to reveal the effect of chemical composition on the response of the atomic dynamics to isotropic elastic stress. Our results demonstrate that similar to Pb-based relaxors and pure NBT, NBT-0.048BT undergoes multistep structural alteration to a high-pressure state consisting of reduced off-centered displacements of B-site cations, enhanced antipolar order of off-centered shifts of A-site cations, and induced BO_6 tilt order. The comparison between NBT and NBT-0.048BT reveals that Ba-doping at the level of the morphotropic phase boundary composition smears out the pressure range of ongoing structural transformations, slows down the suppression of off-centering for both A-site and B-site cations, and hardens the A-cation subsystem, but softens the B-cation subsystem. The larger volume compressibility of NBT-0.048BT with respect to NBT suggests that the softening of the B-cation subsystem due to the substitution of Ba controls the bulk compressibility at the MBP.

Keywords: NBT-xBT, lead-free ferroelectrics, morphotropic phase boundary, Raman spectroscopy, single-crystal XRD, high pressure

*constanze.roesche@uni-hamburg.de

I. INTRODUCTION

Perovskite-type (ABO_3) ferroelectrics are widely used functional materials, which have found numerous applications in electronic devices, such as sensors, actuators and capacitors [1]. Currently, mainly Pb-based perovskite-type ferroelectric materials are in industrial use, but due to continuously growing concerns related to the toxicity of lead, they should be replaced by ecologically friendly alternatives in the near future. Solid solutions exhibiting a morphotropic phase boundary (MPB), where the symmetry of the ferroelectric phase changes upon compositional variations and the material properties are enhanced, are of particular interest, as small changes in the composition affect the nanoscale structure, which in turn allows for tuning the properties [2–4]. The ferroelectric solid solution $(1\text{-}x)Na_{0.5}Bi_{0.5}TiO_3\text{-}xBaTiO_3$ (NBT-xBT) is a promising candidate as a lead-free functional material, because it exhibits heavy nanoscale structural inhomogeneities [5–8] and a MPB at x = 0.05-0.06, where the dielectric permittivity, piezoelectric coefficient, and electromechanical coupling factor are strongly boosted [9–12]. The existence of polar nanoregions (PNR), consisting of cationic off-center displacements with a coherence length of only a few nm, was suggested for NBT-xBT with $0 \leq x \leq x_{MPB}$ [13,14], similar to the structural state of Pb-based relaxor ferroelectrics [15], while the occurrence of nanoregions comprising polar shifts of A-site cations that are antiparallel to those of the B-site cations was proposed for compositions with $x_{MPB} \leq x \leq 0.11$, giving rise to the so-called relaxor antiferroelectric state [16]. Further studies have indicated that for Ba-doped NBT with $0.013 \leq x \leq 0.074$ mesoscopic-scale antiferroelectric order in the A-cation subsystem coexists with mesoscopic-scale ferroelectric order within the B-cation subsystem between the temperature of the dielectric-permittivity maximum T_m and the depoling temperature T_d [17,18]. Pure NBT is characterized by local-scale A-site chemical order [19–23] and octahedral tilting [24]. The addition of $BaTiO_3$ to NBT induces extra local strains in the structure [17,25], which suppress the octahedral tilts while favoring polar Ti displacements from the BO_6 centers [17]. Furthermore, doping with $BaTiO_3$ reduces the average size of PNRs, but increases their fraction [26,27]. At ambient conditions, with the increase of Ba-content, NBT-xBT undergoes a series of composition-induced phase transitions, involving transformations of the BO_6-tilt pattern. The end member NBT was assumed to exhibit rhombohedral symmetry (*R*3*c)* for a long time, but meanwhile it has been proven this is only true for poled samples [28]. The structure of unpoled NBT is in fact monoclinic (*Cc*) [29] with tilt pattern $a^-a^-c^-$ [8] (Glazer notation [30]). Only at x = 0.03-0.04 the symmetry transforms to

rhombohedral *R*3*c* with tilt pattern $a^-a^-a^-$ also in the absence of an electric field [31]. Near x_{MPB} = 0.05-0.06 $a^0a^0c^+$ in-phase tilting occurs, changing the symmetry to *P*4*bm*, and at x = 0.10-0.11 the structure adopts the same BO_6 tilt-free tetragonal *P*4*mm* symmetry as $BaTiO_3$ [31]. The MPB is at $x \sim 0.05$ for unpoled single crystals [32,33] ($x \sim 0.06$ for unpoled ceramics [9]) and the structure becomes pseudocubic [34]. At this composition NBT-*x*BT shows an enhanced flexibility of the local dipoles, which may be caused by increasing decoupling of strain and polarization as well as reduced competing local correlations, leading to reduced local strains [23,35]. Moreover, an increased self-organization between PNRs along the ⟨110⟩ direction has been observed by means of piezoresponse force microscopy (PFM), polarized light microscopy (PLM) and transmission electron microscopy (TEM) for compositions approaching the MPB [26,27], which is consistent with the shape and abnormally large correlation length of the neutron diffuse scattering observed for NBT-0.05BT [36].

Despite the similarities between NBT-*x*BT and Pb-based ferroelectric perovskites, the properties of NBT-*x*BT are somehow inferior [37]. Chemical variations can tune the local ferroic atomic clustering [38], therefore the properties could be improved by additional A- or B-site doping [39]. Knowledge of the relation between chemical composition and structural features is key for efficiently designing novel high-performance functional materials and thus, deeper understanding of the complex nanoscale structure of NBT-*x*BT is required. This can be reached by studying the response of the structure to external stimuli such as temperature, elastic stress or electric field at different length scales. Several studies examining the effect of temperature and electric field have been conducted [17,18,35], but high-pressure studies on NBT-*x*BT are still scarce, although essential, since the application of pressure can help revealing subtle structural features, which are hard to be detected at ambient pressure [40,41].

Previous high-pressure studies combining x-ray diffraction (XRD) and Raman scattering, i.e. probing long-range and short-rang order, respectively, have revealed that Pb^{2+}-based ABO_3-type relaxor ferroelectrics undergo two pressure-induced phase transitions in the range up to ~25 GPa, whose critical pressures p_{c1} and p_{c2} strongly depend on the chemical composition, and each phase transition is preceded by local-scale structural transformations at characteristic pressures $p_1^* < p_{c1}$ and $p_2^* < p_{c2}$. [41–43]. The first phase transition at p_{c1} consists of a change from relaxor cubic to a rhombohedral non-polar state with long-range order of antiphase octahedral tilts, which is preceded by the suppression of dynamical coupling between off-centered A- and B-site cations at p_1^*. At the second phase-transition pressure p_{c2}, long-range order of antipolar A-cation displacements together with $a^-a^-c^+$ octahedral tilts is developed or a

sole long-range order of $a^-a^-c^-$ tilt ($0 \leq c < a$) order occurs. This second transition is preceded by the formation of unequal octahedral tilts on the local scale at p_2^* [41,42]. From these observations it could be deduced that at ambient conditions ferroelectric and antiferrodistortive order coexist on the mesoscopic scale in ABO_3-type relaxors, indicating that the nature of the polar nanoregions is ferrielectric [41,42,44–46]. Since the structure of NBT-*x*BT near MBP is rather similar to that of perovskite-type Pb^{2+}-based relaxors [47], high-pressure structural analysis are needed to shed further light into the nanoscale structural inhomogeneities of Pb-free ferroelectric solid solutions.

So far only the high-pressure behavior of pure NBT has been extensively studied by various analytical methods including powder synchrotron x-ray diffraction and neutron diffraction [48,49], single-crystal x-ray diffraction [19,48] and x-ray diffuse scattering [19], powder Raman spectroscopy [50] and differential thermal analysis [51]. The results obtained from the methods sensitive to long-range order suggest that multiple structural transformations take place from 0.7 to 4 GPa, which are mostly interpreted as a phase transition from rhombohedral *R3c* to orthorhombic *Pnma* symmetry through a state of phase coexistence [48,49]. This assumption is supported by *ab initio* calculations [21]. In particular, single-crystal synchrotron x-ray diffraction analysis revealed a transition at 1.6 – 2.0 GPa to a lower symmetry phase, followed by gradual structural changes on the short-range scale between 2.8 - 3.7 GPa, where the ferroic distortions in PNRs are synchronized with those in the matrix [19]. Furthermore, the data imply a second phase transition between 9.9 and 11.1 GPa to a non-cubic phase [19], whose true symmetry has not been determined yet [49]. Powder Raman spectroscopic data on the other hand indicate that structural transformations proceed from 2.7 - 5 GPa [50]. The available high-pressure data of NBT-*x*BT are limited to Raman spectroscopic studies on NBT [50] and NBT-0.11BT powders [52] as well as on NBT-0.065BT single crystals [53], neither of which however consider the important spectral range below 80 cm^{-1}, dominated by atomic vibrations of off -centered A-site cations [54]. Moreover, the use of powder, as in the case of NBT and NBT-0.11BT, or non-hydrostatic pressure-transmitting media, as in the case of NBT-0.065BT may give rise to undesired non-hydrostatic stresses during the high-pressure experiments, which undermines the quantitative analysis of intrinsic material properties [55,56]. Nevertheless, it has been shown that NBT-*x*BT ferroelectrics with $x = 0.065$ and 0.11 undergo similar pressure-induced transformations as undoped NBT, but the presence of Ba shifts the structural alterations to higher pressures [52]. No data exist for compositions close to the MPB, though.

Here we report the results of high-pressure Raman spectroscopy of single crystals of NBT-xBT at the MPB (x = 0.048 [17]) and pure NBT in the entire spectral range of fundamental phonons (15-1215 cm^{-1}) up to 10 GPa as well as high-precision single-crystal XRD data on NBT-0.048BT up to 6.1 GPa. All measurements have been conducted under hydrostatic conditions using a methanol:ethanol or methanol:ethanol:water pressure-transmitting medium. The goal of our study was to analyze the composition-related difference between the pressure-induced structural transformations in NBT-xBT for $x = x_{MPB}$ and $x = 0$ to give further insights into the MPB structure.

II. Experimental details

A. Samples

Single crystals of (1-x)NBT-xBT with x = 0 and x = 0.048 were synthesized by the top seeded solution growth method [57]. The chemical composition was verified by wavelength-dispersive x-ray emission spectroscopy and the unit-cell parameters at ambient conditions were determined by single-crystal x-ray diffraction (XRD) [17]. Both single-crystal compounds are chemically homogeneous and appear pseudocubic under in-house XRD examination. At room temperature and atmospheric pressure the unit-cell parameters best match rhombohedral metrics, with $a = b = c$ = 3.884 Å and 90° - α_{rh} = 0.045° for x = 0 , and $a = b = c$ = 3.896 Å and 90° - α_{rh} = 0.015° for x = 0.048 [17]. For the high-pressure experiments ~40 µm thick specimens cut parallel to one of the pseudocubic {100} planes were prepared using a diamond wire.

B. High-pressure Raman spectroscopy

In situ high-pressure Raman-scattering experiments were conducted in a Boehler-Almax diamond anvil cell [58] with a culet diameter of 600 µm. The sample chamber was prepared by pre-indenting a stainless-steel gasket to ~92 µm and drilling a 300-µm hole with a Boehler microDriller spark erosion device. Hydrostatic conditions up to 10.5 GPa were ensured by using a 16:3:1 methanol-ethanol-water mixture as a pressure transmitting medium [55]. The pressure in the sample chamber was determined with an uncertainty of ~0.05 GPa using the ruby-line photoluminescence method [59].

The Raman spectra were measured with a Horiba Jobin-Yvon T64000 triple-grating spectrometer equipped with an Olympus BH41 microscope and a 50x long-working-distance

objective, using the 514.5 nm line of a Coherent Innova 90C FreD Ar^+ laser. The spectrometer operated in a subtractive regime to ensure maximum suppression of the Rayleigh scattering without artificially distorting the Raman signal [60]. The spectral resolution was ~2 cm^{-1} and the accuracy of the peak position was 0.35 cm^{-1}. Parallel polarized ($\mathbf{E}_i \parallel \mathbf{E}_s$, $\mathbf{E}_i$ and $\mathbf{E}_s$ represent the polarization of the incident and scattered light) and cross polarized ($\mathbf{E}_i \perp \mathbf{E}_s$) Raman spectra in the range 15-1215 cm^{-1} were collected in backscattering geometry, resulting in the scattering geometries $\bar{Z}(XX)Z$ and $\bar{Z}(XY)Z$ (Porto's notation) with X, Y, Z parallel to the three pseudocubic $\langle 100 \rangle$ directions. Reproducibility of the spectra was proven by collecting data from at least two different spatial points at every pressure.

For NBT-0.048BT two different pressure runs were conducted with the same specimen: up to 4.5 GPa and up to 8.9 GPa. Note that the orientation of the sample during the first run was slightly different (rotated by ~10°) from that during the second run. This was due to the subtle depolarizing effect of diamond anvils, which hindered to find the crystal orientation yielding the strongest difference between $\bar{Z}(XX)Z$ and $\bar{Z}(XY)Z$ spectra. For pure NBT a single pressure run was conducted up to 10.6 GPa. In all experiments the pressure was increased in small steps (~0.2–0.3 GPa) and after each pressure change the sample was given time to relax before data acquisition. Additional spectra were recorded on decompression after reaching the highest pressure to verify reversibility of the pressure-induced changes. Furthermore, at each pressure the Raman signal of the diamond anvils was measured in the range 1050-1610 cm^{-1} to track the changes in diamond optical properties due to the stress-induced morphic effect, which leads to an increasing degree of depolarization of the Raman spectra [61].

To remove the contribution from the diamond anvils and the pressure transmitting medium to the Raman spectrum of the sample, a background spectrum was collected from an area next to the crystal using the same experimental conditions, normalized to the height of the Raman peaks generated by the pressure medium that could be resolved in the spectrum collected from the sample, and subsequently subtracted. The Raman intensities of the background-corrected spectra were temperature reduced by the Bose-Einstein phonon occupation factor and then fitted with pseudo-Voigt functions to determine the phonon wave numbers (ω), full widths at half maximum (FWHMs, Γ) and integrated intensities (I). The data evaluation was performed with the OriginPro 2021 software package [62].

C. High-pressure single-crystal x-ray diffraction

Two sets of high-pressure XRD experiments were performed up to 6.1 GPa and 1.6 GPa using two different specimens of approximately 60×60×40 μm dimensions from the same bulk crystal. The purpose of the second experiment was to collect additional points in the low-pressure range and confirm the reproducibility of the data. In the first run a BX90 diamond anvil cell [63] with 500-μm culets was used, while the second run was conducted using a Boehler-Almax diamond anvil cell [58] with 600-μm culets. Stainless steel gaskets were pre-indented to 70 μm and 96 μm, respectively, and 280-μm holes were generated by laser drilling. The pressure transmitting medium was a 16:3:1 methanol-ethanol-water mixture in the first and a 4:1 methanol-ethanol mixture in the second experiment, which are hydrostatic up to 10.5 and 9.8 GPa, respectively [55,64]. In the first run the fluorescence spectra of ruby measured before and after the x-ray measurements were used for determining pressure [59], whereas in the second run the unit-cell volume of quartz [65] loaded together with the NBT-0.048BT crystal was used instead, allowing to determine the pressure with accuracy less than 0.01 GPa.

High-pressure single-crystal x-ray diffraction was performed using a four circle Huber Eulerian goniometer coupled with an ultra-high intensity rotating anode x-ray source with Mo $K\alpha$ radiation equipped with a multilayer VaryMax™ focusing optic and a point detector [66]. The rotating anode was operated at 45 kV and 55 mA, and the diffractometer was driven by the SINGLE software [67]. Unit-cell lattice parameters were determined by the vector least-squares method [68], using up to 12 unique reflections centered in eight positions [69] to eliminate the effect of crystal offsets and diffractometer aberrations. Because of the specific orientation of the single-crystal cuts, being parallel to one of the pseudocubic {100} crystallographic planes only two of the three unconstrained unit-cell lattice parameters could be determined with high accuracy and precision at all pressure points with uncertainties smaller than 0.0002 Å. The uncertainties on the third unit-cell parameter were instead larger than 0.001 Å.

III. Results and discussion

A. Raman spectroscopy

1. Spectra at ambient conditions: symmetry considerations and peak assignment

The Raman spectra of NBT and NBT-0.048BT measured at ambient conditions are shown in Fig. 1. A detailed group-theory analysis for NBT-*x*BT is given by Datta *et al*. [70]. For NBT-*x*BT with monoclinic (*Cc*), rhombohedral (*R3c*) or tetragonal (*P4bm*) symmetry 27,

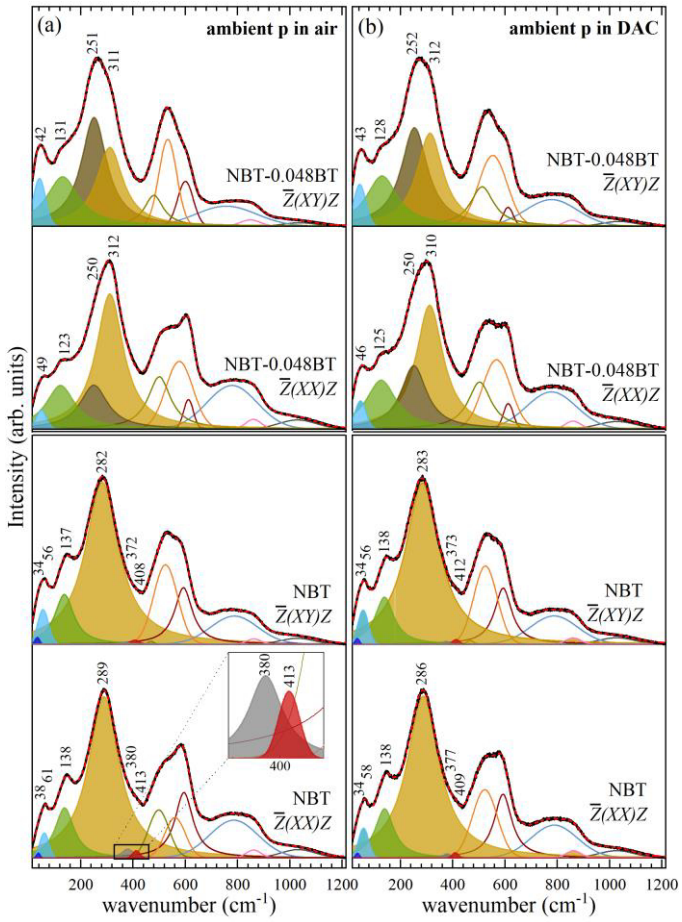


FIG. 1. *(color online)* Polarized $\bar{Z}(XX)Z$ and $\bar{Z}(XY)Z$ Raman spectra (solid black lines) of NBT-0.048BT and NBT measured at ambient conditions in air (a) and inside the diamond anvil cell without pressure transmitting medium (b), along with the fitting pseudo-Voigt functions and the resultant spectrum profiles (red dashed lines). The insert in (a) shows the tilt modes in an enlarged scale.

13 and 16 Raman-active modes are predicted, respectively. If LO-TO effects for polar Raman active modes are taken into account, the number of observable Raman peaks is 54 (*Cc*), 26 (*R3c*) or 28 (*P4bm*). However, a considerably smaller number of peaks could be resolved for both pure NBT and NBT-0.048BT. Thus, the spectra were fitted using the model presented by de la Flor *et al*. [17], which was developed analyzing samples from the same synthesis batch as in this study at different temperatures as well as under an external electric field [17,18,35]. Peaks were added or removed in the high-pressure spectra following the standard goodness-of-fit criteria, including $\Delta I/I < 0.5$ for all peaks, where ΔI is the absolute error in the integrated intensity I [17,70]. The fitting procedure is described in detail in the Supplemental Material, Text SI [71].

The Raman scattering at 30-60 cm^{-1} and 240-310 cm^{-1} is associated with the A-site and B-site cation shifts from the centers of the AO_{12} dodecahedra and BO_6 octahedra, respectively [54,70,72]. The range 120-160 cm^{-1} is dominated by the A-BO_3 translation modes, which are sensitive to the coupling between the dipoles at adjacent A- and B-sites [70,73]. The Raman scattering arising from A-cation vibrations is most likely dominated by Bi vibrations due to the more covalent character of the Bi-O bonds as compared to the Na-O and Ba-O bonds as well as the large off-centered displacement of Bi^{3+} [70,74] related to its affinity to form stereochemically active electronic lone pairs in 12^{th} coordination [54]. The TiO_6 octahedral tilting modes, which can be considered also as A-O bond stretching vibrations within pseudocubic ⟨111⟩ planes, are located at ~320-420 cm^{-1} [17,75,76]. The Raman peaks in the range 470-820 cm^{-1} arise from internal BO_6 vibrations [54,75,76]. Due to the larger partition of oxygen vibrations, these peaks are broader than the peaks below 470 cm^{-1} and consequently, the peak overlapping is stronger, which results in larger dispersions of the fitted wave numbers, FWHMs, and relative intensities. Hence, we will not consider in detail the pressure evolution of BO_6-internal modes.

The substitution of Ba into the NBT structure in sample with $x = 0.048$ slightly changes the Raman spectrum (see Fig. 1(a)). Within the range 30-60 cm^{-1} only one peak (light blue), instead of two (see Supplemental Material Text SI [71]), can be distinguished for the NBT-0.048BT, which most probably results from the increased disorder within the subsystem of A-site dipoles due to Ba-doping. The peak associated with the A-BO_3 translation mode (in green, Fig. 1(a)), which appears in the range 120-160 cm^{-1}, exhibits a lower wave number and larger FWHM as compared to pure NBT due to composition-induced softening of this mode caused by the increased coupling between the adjacent off-centered A- and B-site cations at the MPB [23,70]. Furthermore, two Raman peaks related to off-centered B-site cations (brown and yellow, in the range 240-310 cm^{-1}) can be resolved for NBT-0.048BT, whereas only one peak is visible for NBT, indicating the presence of a uniaxial local anisotropy of the BO_6 octahedra. The higher-wave number component is associated with B-cation vibrations along the polar axis, whereas the lower wave number component represents B-cation vibrations within the perpendicular planes [35]. The sole broad peak observed for NBT in both scattering geometries (Fig. 1(a) bottom) most probably results from overlapping of the multiple B-cation-related Raman peaks expected in monoclinic perovskite-type oxides [77], contributing with similar weights to $\bar{Z}(XX)Z$ and $\bar{Z}(XY)Z$ polarized spectra. The BO_6 tilting modes in the range 370-420

cm^{-1} appear only with a very weak intensity in pure NBT (see the insert in Fig. 1(a)) and are not observed at all in NBT-0.048BT.

The comparison of the polarized Raman spectra of the NBT and NBT-0.048BT samples obtained inside (Fig. 1(b)) and outside (Fig. 1(a)) of a diamond anvil cell shows that the optical properties of the diamond anvils interfere with the polarization of the incident and scattering light, reducing the difference between the $\bar{Z}(XX)Z$ and $\bar{Z}(XY)Z$ spectra already at ambient conditions. As pressure increases, the depolarizing effect of the stressed diamonds also increases [61]. However, a clear distinction between the two scattering geometries was still maintained at the highest pressure measured.

2. Spectra at high pressures

In general, the Raman spectra of NBT-0.048BT and pure NBT (Fig. 2) show a pressure evolution similar to that of Pb-based perovskite-type ferroelectrics [40,43,45,46,78]. First of all, the intensity of the phonon modes associated with off-centering of the B-site cations (near 240-310 cm^{-1}) is strongly reduced. Simultaneously, the intensity in the spectral region from 300-400 cm^{-1}, where octahedral tilting modes are observed is enhanced. In other words, pressure suppresses the polar order, while it promotes the antiferrodistortive order in NBT-*x*BT, as in the case of Pb-based ferroelectrics [40]. These structural changes are fully reversible on decompression. Qualitatively, our results are in a good agreement with previous studies of NBT [50] and NBT-0.11BT [52].

Below we analyze in detail the pressure dependencies of the wave numbers ω (values are listed in Tables SI, SII and SIII [71]), full widths at half maximum, FWHM, or Γ, and fractional intensities $I_n(s) = I(s)/\sum_s I(s)$ of the Raman peaks in the range 15-450 cm^{-1}. The trends of NBT-0.048BT derived from the spectra measured in different scattering geometries reveal the same pressure evolution, therefore only the $\bar{Z}(XX)Z$ data are shown. In contrast, for pure NBT the pressure evolutions of the peaks corresponding to the same type of vibration measured with $\mathbf{E}_i \parallel \mathbf{E}_s$ or $\mathbf{E}_i \perp \mathbf{E}_s$ significantly deviate from each other. This difference mirrors the lower symmetry of the average structure of undoped NBT as compared to the pseudocubic NBT-0.048BT at MPB [17,34].

(a) A-cation localized mode. The pressure evolutions of ω, Γ, and I_n of the A-cation localized modes near 30-60 cm^{-1} are shown in Fig. 3. As mentioned above, only one peak related to the A-cation vibrations is distinguished for NBT-0.048BT at ~46 cm^{-1}, while for pure NBT two components can be resolved at ~34 and ~58 cm^{-1} in the parallel polarized spectra and

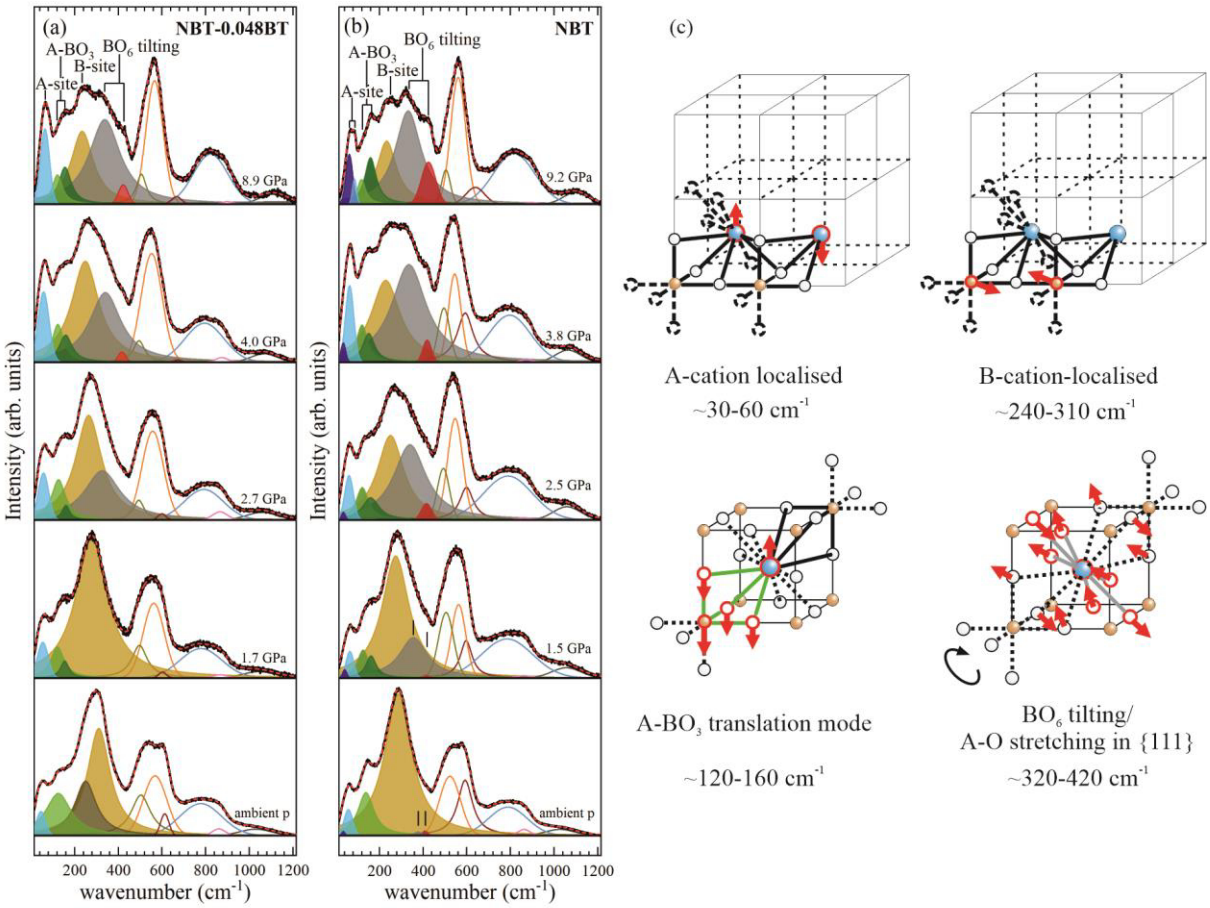


FIG. 2. *(color online)* Selected polarized $\bar{Z}(XX)Z$ Raman spectra of NBT-0.048BT (a) and NBT (b) measured at different pressures (solid black line), along with the fitting pseudo-Voigt functions and the resultant spectrum profiles (red dashed lines). For each compound a comprehensive set of spectra measured at approximately every 0.5 GPa is given in supplemental Fig. S2 [71]. Sketches of atomic vibrations for the modes generating the shaded peaks are given in (c) (after [17,40,75]).

at ~34 and ~56 cm^{-1} in the cross-polarized spectra. Thus, to compare the trends for both compounds, the square root of the average square wave number $\omega_{34,58} = \sqrt{(\omega_{34}^2 + \omega_{58}^2)/2}$, an effective FWHM $\Gamma_{34,58} = (\omega_{58} - \omega_{34}) + \frac{\Gamma_{34}+\Gamma_{58}}{2}$ (see also the sketch in supplemental Fig. S3 [71]), and the sum of the fractional intensities $I_{\mathrm{n}\,34,58} = I_{\mathrm{n}\,34} + I_{\mathrm{n}\,58}$ of the two peaks in NBT, were considered as a function of pressure and compared with the corresponding trends for NBT-0.048BT (see Fig. 3). The pressure dependences of the two individual components at ω_{34} and ω_{58} for NBT are given in supplemental Fig. S4 [71].

For NBT-0.048BT the wave number of the A-cation mode (Fig. 3(a)) gradually increases with pressure up to 1.9±0.1 GPa and above ~4.3±0.6 GPa, with a plateau-like feature in between, which indicates ongoing structural transformations driven by rearrangements within the A-site sublattice. To better reveal the trends of the FWHM and fractional intensity,

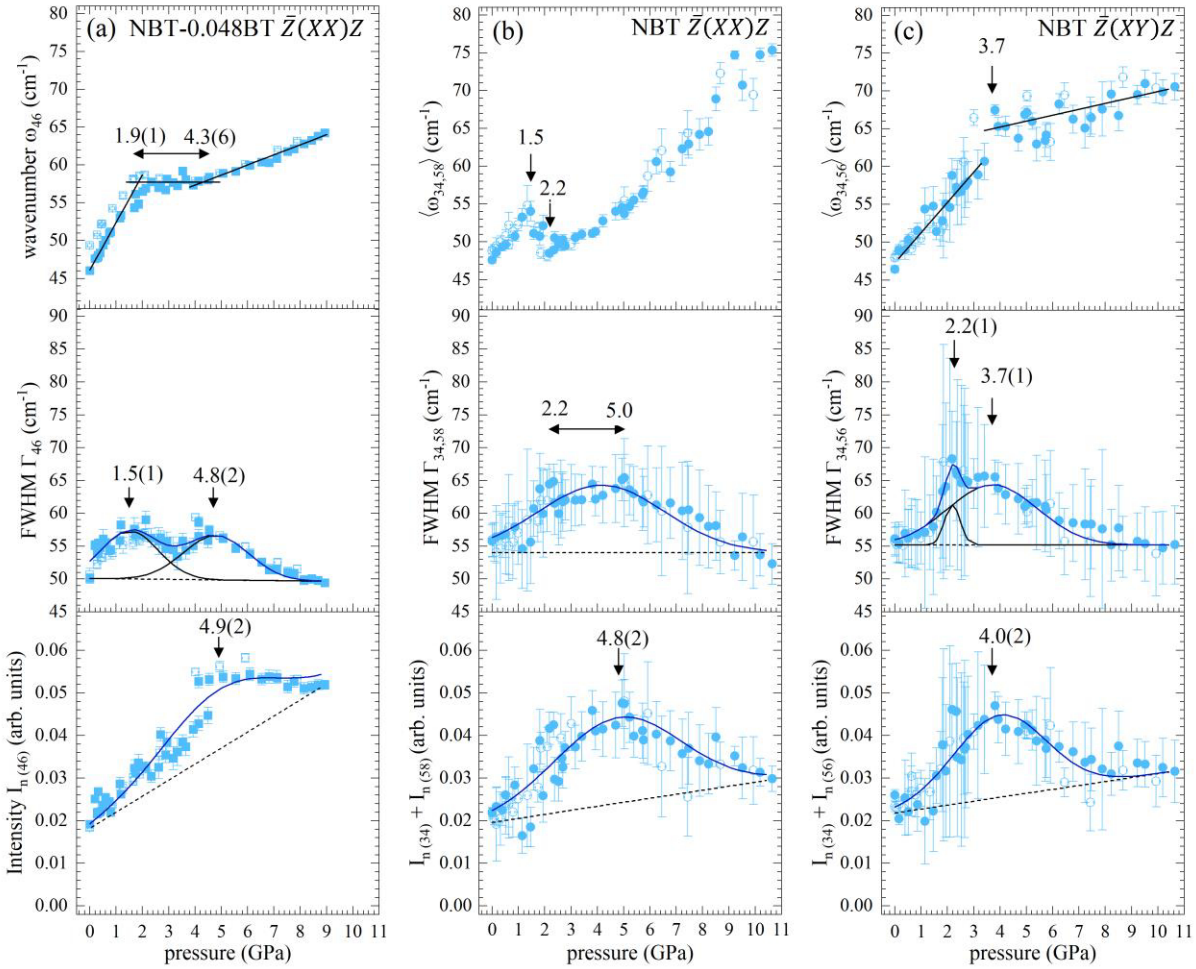


FIG. 3. *(color online)* Pressure dependence of the Raman peak positions (ω), FWHMs (Γ) and fractional intensities (I_n) of the A-cation localized mode in parallel polarized spectra of NBT-0.048BT (a) and NBT (b) as well as in cross polarized spectra of NBT (c). For NBT-0.048BT the trends in the cross polarized spectra are the same as in the parallel polarized spectra shown here. For better comparability the average square wave number $\langle\omega_{1,2}\rangle = \sqrt{(\omega_1^2 + \omega_2^2)/2}$, an effective FWHM $\Gamma_{1,2} = (\omega_2 - \omega_1) + \frac{\Gamma_1+\Gamma_2}{2}$, and the sum of the fractional intensities of the two peaks in NBT positioned at ω_1 ~34 cm^{-1} and ω_2 ~58 cm^{-1}, were considered. Open symbols correspond to data measured on decompression. Lines in the $\omega(p)$ plots in (a) and (c) are linear fits to the data points in the corresponding pressure ranges. The solid lines in the $\Gamma(p)$ and $I_n(p)$ plots are Gaussian fits to the data points with polynomial baselines (dashed lines). The errors in the individual data points stem from the corresponding spectral fit. The errors in the characteristic pressures are derived from the Gaussian fits or from the intersection points of the linear fits. The offset between ω_{46} in NBT-0.048BT measured upon compression and decompression below 2.3 GPa results from the slightly different orientation of the crystal as described in section II.B.

the variations with pressure of $\Gamma(p)$ and $I_n(p)$ were fitted with Gaussian functions using polynomial baselines to account for the anharmonic background [79]. The start and endpoint of the wave number plateau are accompanied by maxima in the FWHM at 1.5±0.1 GPa and

4.8±0.2 GPa, whereas the fractional intensity considerably increases and exhibits a maximum at 4.9±0.2 GPa. In general pressure does not change the phonon decay and therefore $\Gamma(p)$ should remain constant as a function of pressure. Hence, following the concept of hard-mode spectroscopy [79], the excess FWHM as well as the non-linear behavior of the fractional intensity (Fig. 3) confirm the pressure range of ongoing structural transformations indicated by $\omega(p)$. The overall increase in intensity, as demonstrated by the slope of the $I_n(p)$ baseline indicates that the fraction of off-centered A-cations increases with increasing pressure.

For pure NBT, $\omega_{34,58}(p)$ derived from parallel polarized spectra anomalously softens in the pressure range 1.5-2.2 GPa (Fig. 3 (b)). This softening confirms that there is a progressing phase transition to a lower symmetry phase as suggested by synchrotron XRD [19], which starts at 1.6 GPa and is complete at ~2.0 GPa, resulting in a long-range order of antiphase A-site cationic displacements and mixed BO_6 tiling [19,49]. The $\omega_{34,56}(p)$ derived from the cross polarized Raman spectra of pure NBT shows a change in $d\omega/dp$ at 3.7±0.7 GPa (Fig. 3(c)), indicating a reduction of the phonon compressibility (defined as $\beta_\omega = \frac{1}{\omega_0}\frac{d\omega}{dp}$ [80]) and hence, the A-site-cation subsystem becoming "stiffer", i.e. more resistant to a pressure increase. Since such a kink is not observed for $\omega_{34,58}(p)$ derived from parallel polarized spectra, the phenomenon at ~3.7 GPa cannot be related to an overall reduction of the volume compressibility. However, this characteristic pressure perfectly matches the disappearance of the asymmetric x-ray diffuse scattering [19], due to PNRs with polar atomic displacements deviating from those in the matrix. Hence, the presence of a kink in $\omega_{34,56}(p)$ from cross polarized Raman data can be interpreted as an improvement of the local orientation order of A-cation off-center shifts at 3.7 GPa. This assumption is supported by the continuously decreasing FWHM above 3.7 GPa and 5 GPa. In spite of the large uncertainties in FWHMs due to peak overlapping, two distinct maxima can be identified at 2.2±0.1 GPa and 3.7±0.1 GPa for $\Gamma(p)$ derived from the cross polarized spectra from NBT–(Fig. 3(c)) and in the parallel polarized spectra $\Gamma_{34,58}(p)$ exhibits a broad plateau-like maximum between 2.2 and 5.0 GPa (Fig. 3(b)). Thus, the $\Gamma(p)$ trends confirm the occurrence of structural transformations in NBT at ~2.2 GPa and ~3.7 GPa, but furthermore suggest that there are ongoing structural changes at least up to 5.0 GPa.

The comparison between the $\omega(p)$, $\Gamma(p)$ and $I_n(p)$ of pure NBT and NBT-0.048BT suggests that the latter also develops antiphase A-site cationic displacements between 1.9±0.1 GPa and 4.3±0.6 GPa, the mutual alignment of which increases above 4.8±0.2 GPa.

However, the presence of a wave number plateau in the Ba-doped compound (~1.9-4.3 GPa) compared to the softening in pure NBT (1.5-2.2 GPa) indicates that Ba-doping hinders pressure-induced structural alterations and smears out the structural changes over a broader pressure range. This effect has also been observed for Ba-doped $PbSc_{0.5}Ta_{0.5}O_3$ and assumed to be caused by Ba-induced local strains [25]. The increase in the baseline of $I_n(p)$ is much steeper in NBT-0.048BT than in pure NBT (Fig. 3), indicating a stronger pressure-induced increase in the fraction of off-centered A-cations. This is supported by the total fractional intensity $I_{n(XX+XY)}(s) = (I_{XX}(s) + I_{XY}(s))/\sum_s(I_{XX}(s) + I_{XY}(s))$, where $I_{XX}(s)$ and $I_{XY}(s)$ are the integrated intensities obtained from the Raman spectra measured in $\bar{Z}(XX)Z$ and $\bar{Z}(XY)Z$ scattering geometry for a phonon mode s. For the A-site localized modes $I_{n(XX+XY)}$ has approximately the same value in both compounds up to ~ 4 GPa, but above 4 GPa it is higher in the Ba-doped composition (Fig. 4(a)). This indicates that the presence of Ba^{2+} cations facilitates the A-site Bi^{3+} off-centering upon elastic stress, thus causing a higher fraction of off-centered A-site cations in the NBT-0.048BT sample with respect to the end-member.

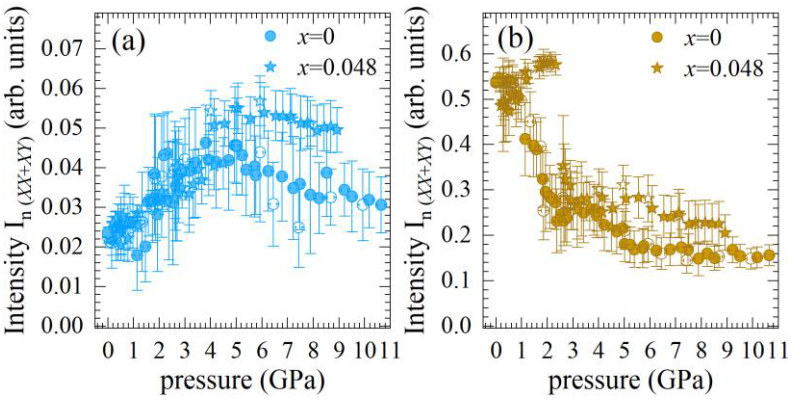


FIG. 4. *(color online)* Pressure dependence of the total fractional intensity $I_{n(XX+XY)}$ of the A-cation (a) and B-cation (b) localized modes in pure NBT (circles) and NBT-0.048BT (stars). $I_{n(XX+XY)}(s) = (I_{XX}(s) + I_{XY}(s))/\sum_s(I_{XX}(s) + I_{XY}(s))$, where $I_{XX}(s)$ and $I_{XY}(s)$ are the integrated intensities obtained from the Raman spectra measured in $\bar{Z}(XX)Z$ and $\bar{Z}(XY)Z$ scattering geometry for a phonon mode s. Open symbols correspond to data measured on decompression. The errors in the individual data points stem from the corresponding spectral fit.

(b) A-BO_3 translation mode. The A-BO_3 translation mode (120-160 cm^{-1}) involves out-of-phase A-cation and BO_3 vibrations (see Fig. 2(c)) and is sensitive to the coupling between adjacent A- and B-site dipole subsystems [23,76]. In Pb-based perovskite-type relaxors this mode splits at a pressure ranging from 0.1 to 2.5 GPa (depending on the chemistry), preceding the phase transition, due to decoupling between dipoles at adjacent A- and B-sites, thus allowing

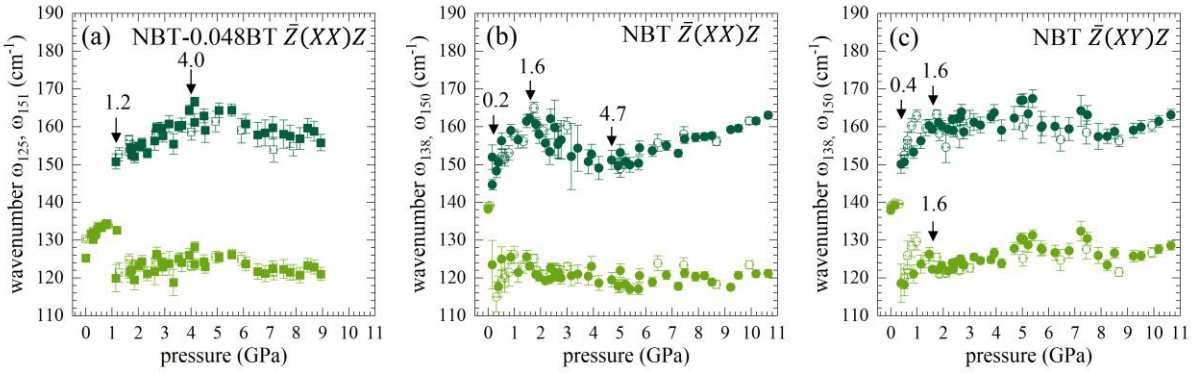


FIG. 5. *(color online)* Pressure dependence of the Raman peak positions (ω) of the A-BO_3 translation mode in parallel polarized spectra of NBT-0.048BT (a) and NBT (b) as well as in cross polarized spectra of NBT (c). For NBT-0.048BT the trends in the cross polarized spectra are the same as in the parallel polarized spectra shown here. Open symbols correspond to data measured on decompression. The errors in the individual data points stem from the corresponding spectral fit.

for suppression of B-cation off-centering and antipolar ordering of the A-site cations at higher pressures [73,78]. A splitting of the A-BO_3 translation mode is observed at ~1.2 GPa for NBT-0.048BT and at 0.3 ± 0.1 GPa for NBT (see supplemental Fig. S5 [71] and Fig. 5), indicating the occurrence of a decoupling between dipoles at adjacent A- and B-sites, allowing for suppression of B-cation off-centering and antipolar ordering of the A-site cations at higher pressures. This decoupling occurs at higher pressure for NTB-0.048BT than for pure NBT, which is consistent with the proposed strengthened coupling between the dipoles at adjacent A- and B-sites at MPB [23]. High-pressure differential thermal analysis of pure NBT [51] has revealed that at pressures below ~0.7 GPa NBT may undergo two temperature-induced phase transitions, similar to those occurring at ambient pressure, whereas at pressures above ~0.7 GPa no phase transitions are observed upon temperature increase. Our results imply that the reason for the suppression of temperature-induced phase transitions is the reduced coupling of the subsystems of off-centered A- and B-site cations.

In NBT-0.048BT the onset of the structural transformations at 1.9±0.1 GPa does not affect $\omega(p)$ of the A-BO_3 mode, but above 4.0 GPa the slope of $\omega_{151}(p)$ changes from trivially positive to anomalously negative (see Fig. 5(a)), indicating a further change in the dynamical coupling between adjacent A- and B-site dipoles due to the ordering processes within the A-site subsystem revealed by the phonon mode at ~46 cm^{-1} (see Fig. 3 (a)). In pure NBT, at ~1.6 GPa, both $d\omega_{138}(p)/dp$ and $d\omega_{150}(p)/dp$ derived from the cross polarized spectra become approximately zero (see Fig. 5(c)), indicating a reduction of the respective phonon compressibilities as the structure starts undergoing a phase transition. In the parallel polarized

spectra $\omega_{138}(p)$ is almost constant, while $\omega_{150}(p)$ softens from 1.6 to ~4.5-5 GPa, thus reflecting the beginning of A-cation arrangements and completion of B-cation rearrangements (see the following discussion).

(c) B-cation localized mode. In the range 240-310 cm^{-1} both modes associated with off-centered B-site Ti^{4+} in NBT-0.048BT soften upon pressure increase (Fig. 6(a)), but they exhibit different behavior in terms of $\Gamma(p)$, and $I_n(p)$. The lower-energy component ω_{250} decreases in both intensity and FWHM. Moreover, at ~0.5 GPa $\omega_{250}(p)$ reaches a minimum and then remains constant until it cannot be distinguished anymore above ~1 GPa. These trends reveal subtle structural transformations in the B-site dipole system already between 0.5-1.0 GPa. The higher-energy component ω_{310} also considerably softens but without an apparent minimum. However, $|d\omega_{310}(p)/dp|$ decreases above 1.2 GPa and then even further at ~4.5 GPa. Interestingly $\Gamma_{310}(p)$ and $I_{n(310)}(p)$ exhibit a maximum at ~1.7 GPa. This might be partially related to an evolving BO_6 tilting mode (see next subsection), which at low pressures cannot be energetically resolved from the B-cation mode at ~310 cm^{-1}. However, the corresponding baseline within the entire pressure range (10^{-4} – 9 GPa) clearly shows that $I_{n(310)}$ decreases, while Γ_{310} remains constant. The former further indicates that pressure suppresses the off-centering of the B-site cations, while the latter suggests that no ordering process in the B-cation subsystem takes place.

For pure NBT the B-cation localized mode shows considerable softening up to 5 GPa (Figs. 6(b) and 6(c)), with an abrupt drop of $\omega(p)$ at 1.6 GPa in both parallel and cross polarized spectra. The FWHM in the $\bar{Z}(XX)Z$ spectra shows an excess between 1.6 and 5.0 GPa, with a maximum of $\Gamma(p)$ at 3.7±0.1 GPa, but overall, $\Gamma(p)$ in both $\bar{Z}(XX)Z$ and $\bar{Z}(XY)Z$ anomalously decreases with pressure. At the same time the Raman intensity of the B-localized modes strongly decreases up to 2.2 GPa in the $\bar{Z}(XY)Z$ spectra and up to 5 GPa in $\bar{Z}(XX)Z$ spectra. The trends in $\omega(p)$ and $I_n(p)$ that we have detected in the parallel polarized spectra are in full accordance with the Raman analysis on powders by Kreisel *et al*. [50]. The minimum in $\omega(p)$ at 5 GPa along with the constant $I_n(p)$ at pressures above suggest that the reduction of B-cation off-center shifts does not further proceed above 5 GPa. This stabilization of the remaining B-site Ti^{4+} off-centering might be caused by the pressure-induced correlation of the A-site subsystem, indicated by the decrease in the effective $\Gamma(p)$ in both parallel and cross polarized spectra (Figs. 3(b) and 3(c)). In contrast to the observations made in NBT-0.048BT, pressure in pure NBT also increases the order within the B-site subsystem, as deduced from the decrease in FWHM (see Figs. 6(b) and 6(c)). This indicates that the presence of Ba at the A-site in the

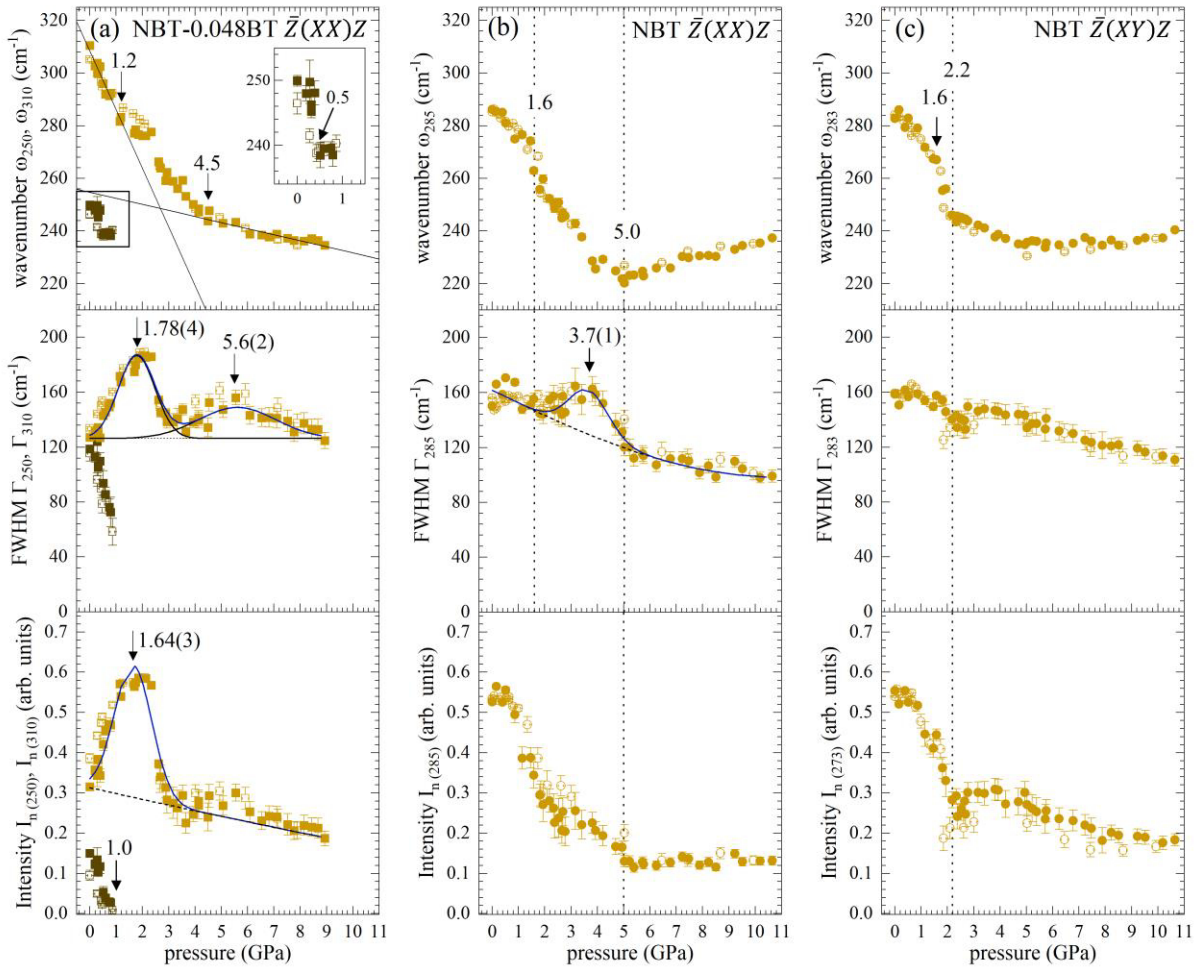


FIG. 6. *(color online)* Pressure dependence of the Raman peak positions (ω), FWHMs (Γ) and fractional intensities (I_n) of the B-cation localized mode in parallel polarized spectra of NBT-0.048BT (a) and NBT (b) as well as in cross polarized spectra of NBT (c). For NBT-0.048BT the trends in the cross polarized spectra are the same as in the parallel polarized spectra shown here. Open symbols correspond to data measured on decompression. Lines in the $\omega(p)$ plot in (a) are linear fits to the data points in the corresponding pressure ranges. The solid lines in the $\Gamma(p)$ and $I_n(p)$ plots in (a) and (b) are Gaussian fits to the data points with polynomial baselines (dashed lines). The errors in the individual data points stem from the corresponding spectral fit. The errors in the characteristic pressures are derived from Gaussian or linear fits to the data points.

NBT structure hinders any possible ordering in the B-cation subsystem. Besides, also the presence of a $\omega(p)$ minimum at 5 GPa for NBT in contrast to merely a subtle kink in $\omega_{310}(p)$ at ~4.5 GPa in NBT-0.048BT demonstrates that Ba-doping hinders not only the structural transformations involving the A-site cations, but also those concerning the B-site cations. Furthermore, at pressures above 2.7 GPa, where ω_{310} in the Ba-doped compound can be unambiguously ascribed to B-cation off-centering vibrations the total fractional intensity $I_{n(XX+XY)}$ is larger for NBT-0.048BT than for pure NBT (Fig. 4(b)), indicating that Ba-doping

prevents the pressure-induced suppression of polar B-cation displacements, similar to Pb-based relaxors [81].

(d) BO_6 tilting. The tilting vibrations of BO_6 octahedra (between 320 and 420 cm^{-1}) involve also A-O bond stretching within the pseudocubic ⟨111⟩ planes [75,76]. At ambient pressure NBT-0.048BT does not exhibit any BO_6 tilting detectable by Raman spectroscopy (Fig. 1), which is consistent with the Ba-induced suppression of tilts deduced from neutron total scattering [23]. This is most probably related to the disturbance in coherent off-centered shifts of A-site cations in the presence of Ba, which in turns hinders tilt development. Only above 2.7 GPa can a new peak be identified at ~326 cm^{-1} (Fig. 7(a)). At 4 GPa a second minor peak at ~412 cm^{-1} is resolved, followed up by a kink in $\omega_{326}(p)$ at ~4.5 GPa. Although the spectral range and the increase in intensity with increasing pressure of the peak at ~326 cm^{-1} indicate that it originates from BO_6 tilting vibrations, it might also be influenced by B-cation off-centering vibrations, since at the same pressure at which it appears the wave number of the B-localized mode $\omega_{310}(p)$ drops abruptly, and both $\omega_{310}(p)$ and $\omega_{326}(p)$ exhibit a kink at ~4.5 GPa. The appearance and pressure dependence of $\omega_{326}(p)$ and $\omega_{412}(p)$ reveal the occurrence of evolving octahedral tilt pattern between 2.7 GPa and 4.5 GPa, alongside the antipolar order in the A-cation subsystem, which occurs already at ~1.9 GPa. The presence of two Raman signals suggests the existence of octahedral tilts with unequal magnitudes, independently of whether these are antiphase or in-phase tilts [43]. Previous density-functional simulations on Pb-based perovskite-type relaxors have revealed that antiphase $a^-a^-c^-$ ($c < a$) and mixed $a^-a^-c^+$ tilt patterns are thermodynamically preferred at high pressures [43]. Neutron and x-ray diffraction experiments on Pb-based relaxors have confirmed that if no tilting is observed at ambient conditions, pressure first induces antiphase $a^-a^-a^-$ order, which upon a further pressure increase transforms into $a^-a^-c^-$ ($c < a$) or mixed $a^-a^-c^+$ [41,43]. On the other hand, transmission electron microscopy at ambient conditions suggests a co-presence of local antiphase $a^-a^-a^-$ and in-phase $a^0a^0c^+$ tilt order in NBT-x_{MPB}BT [82,83]. As the $a^0a^0c^+$ tilt order is the thermodynamically most unstable tilt pattern in perovskite oxides at high pressures [43], we can speculate that the appearance of new Raman peaks for $x = 0.048$ indicates a development of an $a^-a^-a^-$ pattern at 2.7 GPa (a single peak at 326 cm^{-1}), which transforms into a mixed $a^-a^-c^+$ tilt pattern at 4.0 GPa (a second Raman peak at 412 cm^{-1}).

For pure NBT at ambient pressure there are two weak Raman peaks generated by BO_6 tilting, near 375 and 409 cm^{-1} (Fig. 1, inset). It is worth noting that for pure NBT a nanoscale

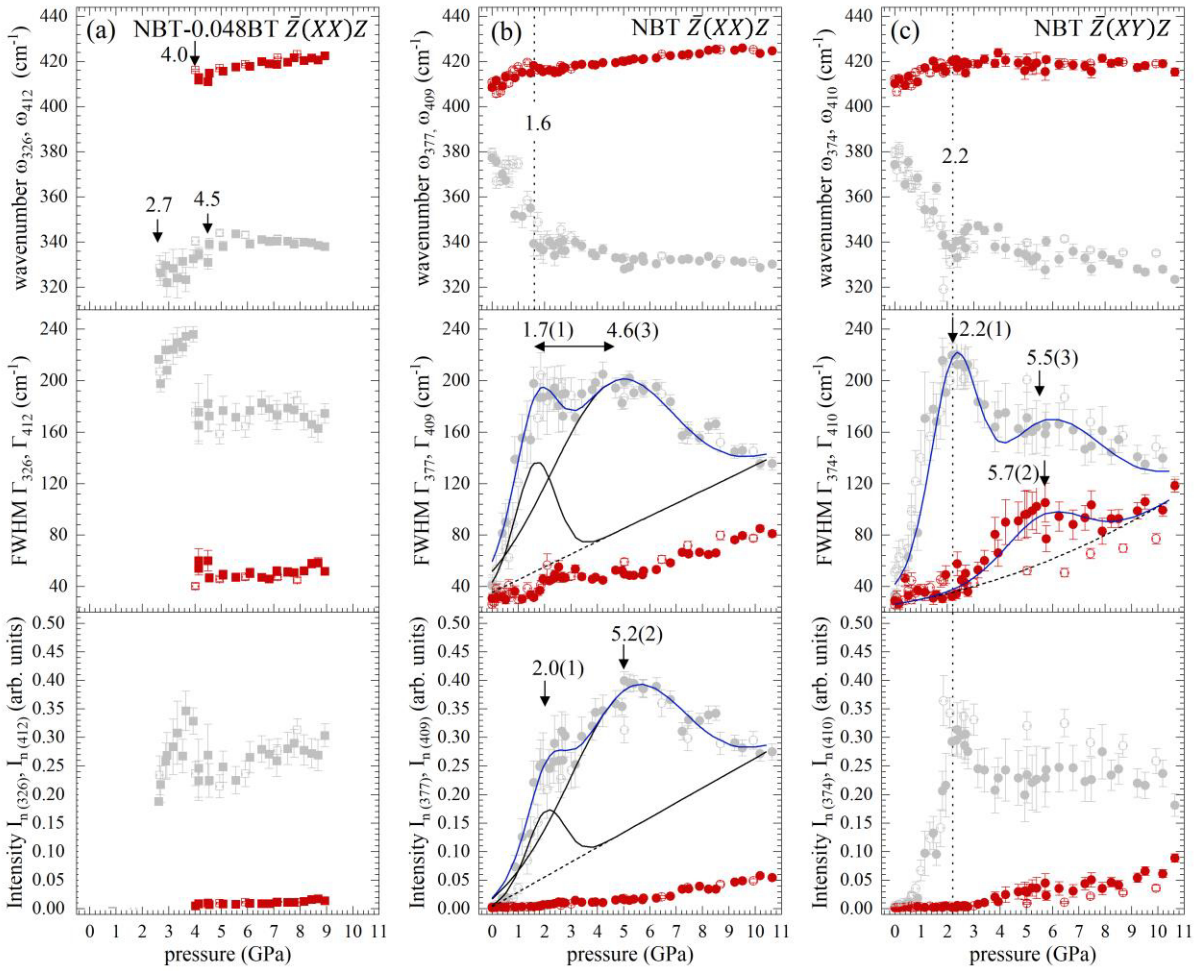


FIG. 7. *(color online)* Pressure dependence of the Raman peak positions (ω), FWHMs (Γ) and fractional intensities (I_n) of the octahedral tilting modes in parallel polarized spectra of NBT-0.048BT (a) and NBT (b) as well as in cross polarized spectra of NBT (c). For NBT-0.048BT the trends in the cross polarized spectra are the same as in the parallel polarized spectra shown here. Open symbols correspond to data measured on decompression. The solid lines in the $\Gamma(p)$ and $I_n(p)$ plots in (b) and (c) are Gaussian fits to the data points with polynomial baselines (dashed lines). For the sake of limited space, the baseline and individual Gaussian functions are not displayed for Γ_{374} in the $\bar{Z}(XY)Z$ spectra of NBT. The errors in the individual data points stem from the corresponding spectral fit. The errors in the characteristic pressures are derived from Gaussian or linear fits to the data points.

$a^-a^-c^+$ BO_6 tilting pattern was suggested, but with a coherence length of the in-phase tilt component significantly shorter than that of the antiphase tilting, resulting in an average tilt pattern $a^-a^-c^-$ typical of *Cc* [8,84]. The lower-energy peak (at ~375 cm^{-1}) strongly softens up to 1.6 GPa and 2.2 GPa in $\bar{Z}(XX)Z$ and $\bar{Z}(XY)Z$ spectra, respectively, and keeps softening above these charactering pressures but with a considerably lower rate (Figs. 7(b) and 7(c)). Likewise, the $d\omega(p)/dp$ of the higher-energy peak (at ~409 cm^{-1}) of NBT slightly changes at the abovementioned characteristic pressures. This indicates significant changes in the octahedral

tilt pattern at 1.6 and 2.2 GPa, which most probably is due to a pressure-induced transformation of the dominant antiphase tilt pattern into a mixed tilt pattern [49], to facilitate the rearrangements of the off-centered A-site cations, as deduced from the Raman scattering near 50 cm^{-1} (Fig. 3) and synchrotron XRD [19]. The alterations in $\omega(p)$ are accompanied by maxima in the FWHM and fractional intensity of the tilt modes. The $\Gamma(p)$ and $I_{n(377)}(p)$ trends were fitted with Gaussian functions using polynomial functions as baselines. In both parallel and cross polarized spectra, $\Gamma(p)$ and $I_n(p)$ for the lower-energy peak show a well pronounced maximum at a pressure where $d\omega(p)/dp$ considerably changes, and a second very broad maximum at ~5.0 GPa. The latter pressure is in excellent agreement with that at which the off-center shift of the B-site cations stops reducing (see Fig. 6). The $I_{n(409)}(p)$ trend as well as the gradually increasing baseline of $I_{n(375)}(p)$ indicate that pressure enhances the BO_6 tilting in NBT, similar to Pb-based relaxors [43,73,76,78,81], while the corresponding $\Gamma(p)$ trends suggest increasing disorder in the tilting patterns. The latter may be related to the ongoing development of unequal tilts around the cubic [100], [010], and [001] directions, which has been detected for Pb-based relaxors via resolved splitting of the corresponding Raman peak [41,43]. Kreisel *et al*. [50] report the occurrence of four new Raman peaks in the range 250-420 cm^{-1} at 5 GPa in NBT powders. Two of those peaks correspond to the peaks at ~375 and ~409 cm^{-1}, which are already included in our starting model at ambient pressure. Although the goodness of fit did not require the use of additional peaks, we tried to include two more peaks, at ~260 and ~395 cm^{-1}, above 5 GPa. The uncertainties in the integrated intensity however indicate only an extra peak at ~395 cm^{-1} in the parallel polarized spectra could be acceptable, which has negligible effect on the trends of the other modes and does not provide new information about characteristic pressures (see supplemental Fig. S6 [71]).

B. In-house single crystal x-ray diffraction

The variation of the two unconstrained unit-cell parameters that were determined with high accuracy in the single-crystal high-pressure x-ray diffraction measurements (referred to hereafter as a_1 and a_2) is reported in Fig. 8(a). These two lattice parameters are identical up to 4 GPa. At this pressure the a_1 and a_2 axes start to differ from each other, and the difference is above the 2σ standard deviation at 5.4 GPa. The unit-cell lattice parameters were, therefore, constrained to the cubic symmetry (Table SIV [71]) at all pressures, being this a good approximation for the data points below 4 GPa and a fair approximation for the two highest data points for sake of comparison. The variation with pressure of the pseudocubic unit-cell

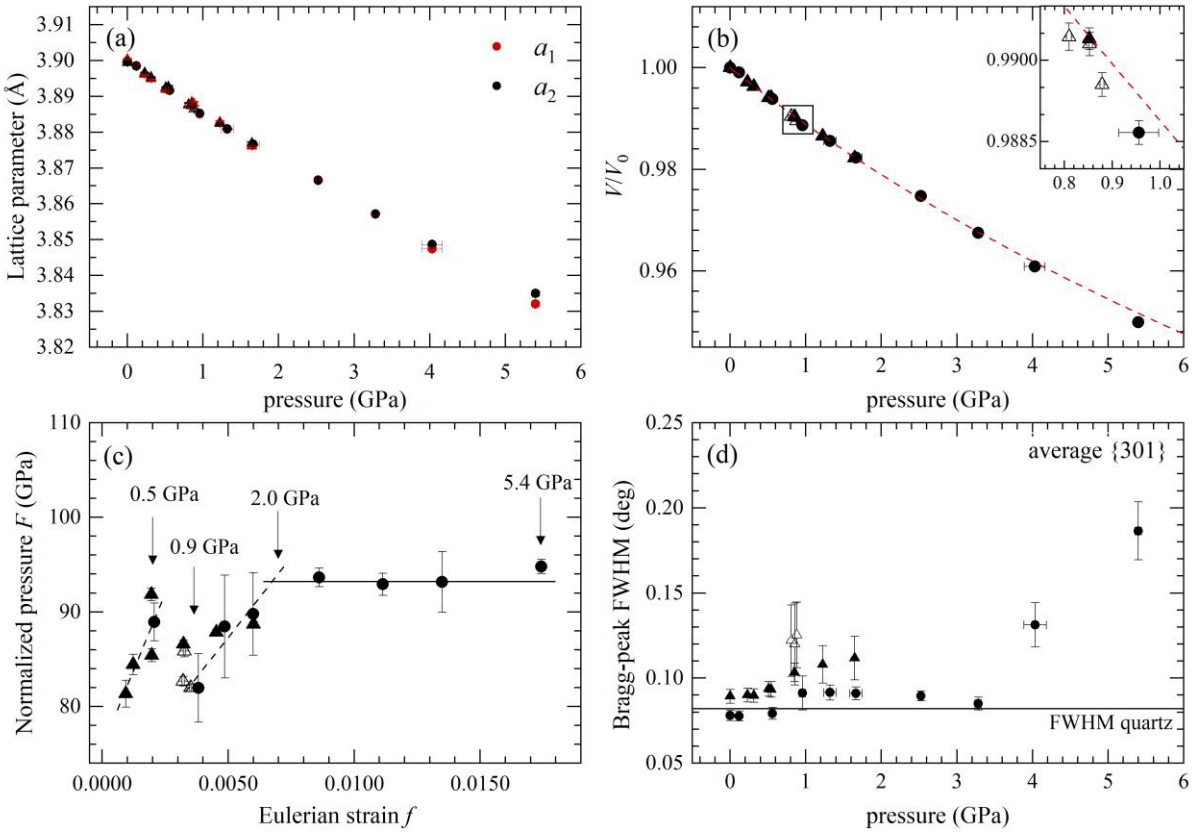


FIG. 8 *(color online)* Pressure dependence of the unconstrained lattice parameters a_1 and a_2 (a); pseudocubic unit-cell volume of NBT-0.048BT normalized to the volume V_0 measured at ambient pressure (b); the normalized pressure $F = p/[3f(1+2f)^{5/2}]$ plotted against the Eulerian strain $f = [(V_0/V)^{2/3}-1]/2$ (c) with propagating errors calculated according to [85]; and pressure evolution of the average FWHM of pseudocubic{301} Bragg reflections as representative for the broadening of the diffraction peaks (d). Vertical error bars in (a) are smaller than the size of the symbols. The red dashed line in (b) is 3rd-order Birch-Murnaghan EoS fitted to the data points up to 3.3 GPa. The lines in (c) show the linear fits of the data from 0.23-0.56 GPa, 0.88-1.68 GPa (black, dotted) and 2.5-4.0 GPa (black, solid). The horizontal solid line in (d) at 0.082° represents the instrumental resolution via the average FWHM of quartz Bragg reflections. Circles correspond to data points measured in the first pressure run, while triangles to data points measured in the second run. Data points measured on decompression are given by open symbols.

volume of NBT-0.048BT, normalized with respect to the respective value at ambient pressure is shown in Fig. 8(b). Since above 4 GPa the unconstrained unit-cell lattice parameters start deviating from the cubic symmetry, the *P*-*V* data have been fitted using a 3rd-order Birch-Murnaghan equation of state (EoS) only up to 3.3 GPa. The resulting bulk modulus is $K_0 = 83.5 \pm 1.7$ GPa with a pressure derivative $K' = 11.4 \pm 2.0$. However, the weighted chi-squared of the fitting, $\chi_w^2 = 2.42$, is quite large, indicating that such EoS may not be representative for the entire data set [85]. Near 0.9 ±0.1 GPa, V/V_0 significantly deviates from the equation of state in a few points (see insert in Fig. 8(b)), indicating complex compressional

behavior. Pressure-induced phase transitions as well as changes in compressional mechanism can be better revealed if the p-V data are recalculated in terms of normalized pressure $F = p/[3f(1+2f)^{5/2}]$ versus Eulerian strain $f = [(V_0/V)^{2/3}-1]/2$ [85]. $F(f)$ data which, when lying either on an horizontal or on a straight line with a positive slope, indicate the absence of a phase transition and can be appropriately fitted using a 2nd- or a 3rd-order Birch-Murnaghan EoS [85], whereas points in $F(f)$ at which $dF/df = 3K_0(K_0' - 4)f/2 = 0$ are indicative of discontinuity in the bulk modulus or its derivative, or both, which in turn points out to a phase transition [43,73,76]. In the pressure range between 0.23 and 1.68 GPa, the $F((f)$ plot of NBT-0.048BT shows three discontinuities at 0.5, 0.9 and near 2 GPa (Fig. 8(c)). The maximum at ~0.5 GPa as well as the minimum at ~0.9 GPa has been observed for data collected in separate experiments both on compression and decompression and thus likely indicate changes in the elasticity triggered by structural transformations. The feature at ~0.5 GPa matches the kink in $\omega(p)$ of the lower-energy B-cation mode (see insert in Fig. 6(a)), whereas the feature at ~0.9 GPa corresponds to the pressure at which this mode disappears (1.0±0.1 GPa). Therefore, the rearrangements in the B-cation subsystem at low pressures, occurring in NBT-0.048BT but not in NBT, appear to affect also the macroscopic elastic strain, likely because of the enhanced elastoelectric response of NBT-xBT at the MPB, although it does not appear to affect the overall pseudocubic symmetry. Above 2 GPa the $F(f)$ remains constant and the intercept with the F-axis of a horizontal lines through the data suggest a K_0=93.2 GPa (with K'=4), indicating a stiffer structure than that at atmospheric pressure. However, the decrease in compressibility with pressure of this high-pressure structure is not as pronounced as that occurring at low pressures (0.23-0.56 GPa and 0.88 – 1.68 GPa), where the $F(f)$ data lie on very steep straight lines. According to the Raman data, the A-cation and B-cation subsystems rearrange between ~1.7 and ~4.5 GPa. Moreover, at 2.7±0.1 and 4.0±0.1 GPa there is the appearance of tilt modes (see Fig. 7(a)). The tilting may, therefore, act as a new compression mechanism allowing the structure to better accommodate at larger pressures, giving rise to a smaller K'. The data point corresponding to 5.4 GPa is slightly above the constant trend in the f-F plot (Fig. 8(b)). This pressure matches the second maximum (5.6±0.2 GPa) in the $\Gamma_{250}(p)$ of the B-cation mode (see Fig. 6(a)), implying a possible phase transition due to further rearrangements of the B-cation subsystem at ~5.5 GPa. At this pressure the violation of the pseudocubic symmetry starts to be significative, as indicated by the unconstrained unit-cell parameters (Fig. 8(a)) as well as by the extensive broadening of the Bragg reflections (Fig. 8(d)). Such broadening is unlikely to be due to non-hydrostatic stresses, given the small crystal dimensions and the hydrostaticity of the

pressure medium used [64]. The broadening, however, hindered the determination of the symmetry of the evolving high-pressure phase, which might be orthorhombic *Pnma* or a non-centrosymmetric subgroup of *Pnma*, as it was proposed to develop in pure NBT already above 2 GPa [49]. At 4.0 GPa a second tilt mode occurs in NBT-0.048BT, followed up by a kink at 4.5 GPa of $\omega(p)$ of the primary tilt mode that appeared at 2.7 GPa (see Fig. 7(a)). Moreover, the evolving antipolar order of off-center shifts of the A-site cations is completed at ~4.5 GPa (Fig. 3(a)). Therefore, the anomalous broadening of the Bragg peaks may indicate an increase in the ferroic distortion of the atomic structure and a consequent development of ferroic domains, i.e. enhanced mosaicity. Variation in mosaicity should be responsible for the slight difference between the Bragg-peak FWHMs of the two specimens analyzed in the two runs (triangles and circles in Fig. 8) as well as for the subtly incomplete recovery of the Bragg-peak widths on decompression (open symbols in Fig. 8(d)). However, the broadening of the Bragg-peak observed at high pressures recovers on decompression, in full accordance with the Raman data that indicate reversibility of all atomic-scale structural changes induced by pressure.

The bulk modulus of NBT-0.048BT (K_0 = 83.5 ±1.7 GPa) is smaller than that of pure NBT (K_0 = 95.2 GPa [86]). $BaTiO_3$ exhibits a bulk modulus around 130 GPa [87], which is also considerably larger than that of NBT-0.048BT. Therefore, Ba doping of NBT to the level of MPB significantly softens the material. The bulk modulus of NBT-0.048BT is also smaller than that of Pb-based relaxor ferroelectrics and ferroelectric solid solutions, which typically exhibit a bulk modulus in the range 92-110 GPa [25,81,88,89].

IV. Summary and conclusions

The characteristic pressures of structural transformations in NBT and NBT-0.048BT revealed by Raman scattering and XRD analyses are summarized in Table I.

Similar to Pb-based relaxor ferroelectrics [40,41,43,73], decoupling of dipoles at adjacent A- and B-sites takes place in NBT-*x*BT at a characteristic pressure p_1^* in the range 0.3-1.2 GPa [40,73] and a development or change of existing BO_6 tilt pattern occurs at a higher characteristic pressure p_2^* in the range 1.6-2.7 GPa. Another common feature for both Pb-based and Bi-based perovskite-type ferroelectrics is that pressure hinders the off-centering of the B-site cations, while enhancing antipolar order of A-site-cation displacements.

TABLE I. Characteristic pressures/pressure ranges (in GPa) of structural transformations for NBT-0.048BT and pure NBT.

NBT-0.048BT		NBT		Structural transformation
Raman	XRD	Raman	XRD/XDS [19]	
0.5–1.0	0.5–0.9			Rearrangements of the B-site cations, suppression of the Ba-induced uniaxial local octahedral anisotropy.
1.2[a]		~0.3[a]		Decoupling of adjacent A-site and B-site dipoles
1.9–4.3		1.5-2.2	1.6–2.0	Antipolar order of A-cation off-center shifts
		1.6[b]–2.2	1.6–2.0	Change in the BO_6-tilt order pattern
2.7[b]–4.0	2.5–4.0			Development of BO_6 tilt order
4.8		3.7	2.8-3.7	Suppression of the directional dispersion of A-cation off-center shifts and increasing of the length of coherence of correlated antiphase A-cation shifts
4.5		5.0		Slowdown of the suppression of B-cation off-centering; further readjustment in the BO_6 tilt pattern
5.6	5.4			Possible further rearrangement in the B-cation subsystem?
			9.9-11.1	Phase transition to a another ferroic phase

[a] analogue of p_1* in Pb-based relaxor ferroelectrics [40,73]
[b] analogue of p_2* in Pb-based relaxor ferroelectrics [41,43]

The comparison between NBT and NBT-0.048BT reveals that Ba-doping at the level of MBP composition affects the structural response to pressure as follows:

- The substitution of Ba^{2+} shifts the rearrangements of the A-site cations towards higher pressures, i.e. it hardens the A-cation subsystem, most probably via the intrinsic local stresses around Ba^{2+} [25,81] due to its larger ionic radius as compared to Na^{+} and Bi^{3+} [90]. By the same reason it shifts p_1^* to higher pressures.
- The A-site Ba^{2+} hinders the suppression of the off-centering for both A-site and B-site cations at high pressures.

- The A-site Ba^{2+} enhances the elastic response of the B-site cations and triggers structural alteration that affects the macroscopic strain even before the decoupling of adjacent A-site and B-site dipoles. Moreover, A-site Ba^{2+} inhibits the hardening of the B-cation subsystem at high pressures, likely driving the reduction of the bulk modulus at the MPB.
- The intrinsic chemical pressures associated with the A-site Ba^{2+} suppress the BO_6 tilt order at ambient pressure, but these Ba-related local stresses can be overcome by an external high pressure, leading to BO_6 tilt order.

To summarize, although the substitution of larger-size Ba^{2+} for smaller-size Na^{+} and Bi^{3+} generates local stresses, at the MPB the incorporation of Ba into the structure softens the material, mainly due to enhanced elastic response of the B-cation subsystem.

Acknowledgements

The authors thank Dr. Alexander Kurnosov, Universität Bayreuth, for help with DAC loading and XRD experiments as well as Dr. Semën Gorfman, Tel Aviv University, for providing the samples. Financial support by the Deutsche Forschungsgemeinschaft (MI 1127/12-1 and BO 2550/10-1) is gratefully acknowledged.

[1] A. S. Bhalla, R. Guo, and R. Roy, The perovskite structure - a review of its role in ceramic science and technology, Mater. Res. Innovations **4**, 3 (2000).

[2] A. M. Glazer, P. A. Thomas, K. Z. Baba-Kishi, G. K. H. Pang, and C. W. Tai, Influence of short-range and long-range order on the evolution of the morphotropic phase boundary in $Pb(Zr_{1-x}Ti_x)O_3$, Phys. Rev. B **70**, 184123 (2004).

[3] T. Takenaka, H. Nagata, and Y. Hiruma, Phase transition temperatures and piezoelectric properties of $(Bi_{1/2}Na_{1/2})TiO_3$- and $(Bi_{1/2}K_{1/2})TiO_3$-based bismuth perovskite lead-free ferroelectric ceramics, IEEE Trans. Ultrason. Ferroelectr. Freq. Control **56**, 1595 (2009).

[4] M. Acosta, N. Novak, V. Rojas, S. Patel, R. Vaish, J. Koruza, G. A. Rossetti, and J. Rödel, $BaTiO_3$-based piezoelectrics: Fundamentals, current status, and perspectives, Appl. Phys. Rev. **4**, 41305 (2017).

[5] R. Beanland and P. A. Thomas, Imaging planar tetragonal sheets in rhombohedral $Na_{0.5}Bi_{0.5}TiO_3$ using transmission electron microscopy, Scr. Mater. **65**, 440 (2011).

[6] F. Pforr, M. Major, W. Donner, U. Stuhr, and B. Roessli, Influence of tetragonal platelets on the dielectric permittivity of $0.964Na_{1/2}Bi_{1/2}TiO_3–0.036BaTiO_3$, Phys. Rev. B **94**, 14105 (2016).

[7] D. Maurya, M. Murayama, A. Pramanick, W. T. Reynolds, K. An, and S. Priya, Origin of high piezoelectric response in A-site disordered morphotropic phase boundary composition of lead-free piezoelectric $0.93(Na_{0.5}Bi_{0.5})TiO_3–0.07BaTiO_3$, J. Appl. Phys. **113**, 114101 (2013).

[8] I. Levin and I. M. Reaney, Nano- and Mesoscale Structure of $Na_{1/2}Bi_{1/2}TiO_3$: A TEM Perspective, Adv. Funct. Mater. **22**, 3445 (2012).
[9] T. Takenaka, K. Maruyama, and K. Sakata, $(Bi_{0.5}Na_{0.5})TiO_3$-$BaTiO_3$ System for Lead-Free Piezoelectric Ceramics, Jpn. J. Appl. Phys. **30**, 2236 (1991).
[10] W. Ge, H. Cao, C. Devreugd, J. Li, and D. Viehland, Influence of $BaTiO_3$ Content on the Structure and Properties of $Na_{0.5}Bi_{0.5}TiO_3$ Crystals, J. Am. Ceram. Soc. **94**, 3084 (2011).
[11] Y. Hiruma, K. Yoshii, H. Nagata, and T. Takenaka, Investigation of Phase Transition Temperatures on $(Bi_{1/2}Na_{1/2})TiO_3$-$(Bi_{1/2}K_{1/2})TiO_3$ and $(Bi_{1/2}\ Na_{1/2})TiO_3$-$BaTiO_3$ Lead-free Piezoelectric Ceramics by Electrical Measurements, Ferroelectrics **346**, 114 (2007).
[12] H. Lidjici, B. Lagoun, M. Berrahal, M. Rguitti, M. A. Hentatti, and H. Khemakhem, XRD, Raman and electrical studies on the $(1-x)(Na_{0.5}Bi_{0.5})TiO_3-xBaTiO_3$ lead free ceramics, J. Alloys Compd. **618**, 643 (2015).
[13] W. Ge, C. Luo, C. P. Devreugd, Q. Zhang, Y. Ren, J. Li, H. Luo, and D. Viehland, Direct evidence of correlations between relaxor behavior and polar nano-regions in relaxor ferroelectrics: A case study of lead-free piezoelectrics $Na_{0.5}\ Bi_{0.5}TiO_3$-x%$BaTiO_3$, Appl. Phys. Lett. **103**, 241914 (2013).
[14] W. Ge, C. P. Devreugd, D. Phelan, Q. Zhang, M. Ahart, J. Li, H. Luo, L. A. Boatner, D. Viehland, and P. M. Gehring, Lead-free and lead-based ABO_3 perovskite relaxors with mixed-valence *A*-site and *B*-site disorder: Comparative neutron scattering structural study of $(Na_{1/2}Bi_{1/2})TiO_3$ and $Pb(Mg_{1/3}Nb_{2/3})O_3$, Phys. Rev. B **88**, 174115 (2013).
[15] W. Jo, S. Schaab, E. Sapper, L. A. Schmitt, H.-J. Kleebe, A. J. Bell, and J. Rödel, On the phase identity and its thermal evolution of lead free $(Bi_{1/2}Na_{1/2})TiO_3$-6 mol% $BaTiO_3$, J. Appl. Phys. **110**, 74106 (2011).
[16] C. Ma, X. Tan, E. Dul'kin, and M. Roth, Domain structure-dielectric property relationship in lead-free $(1-x)(Bi_{1/2}Na_{1/2})TiO_3$-$xBaTiO_3$ ceramics, J. Appl. Phys. **108**, 104105 (2010).
[17] G. de La Flor, T. Malcherek, S. Gorfman, and B. Mihailova, Structural transformations in $(1-x)Na_{0.5}Bi_{0.5}TiO_3-xBaTiO_3$ single crystals studied by Raman spectroscopy, Phys. Rev. B **96**, 214102 (2017).
[18] G. de La Flor and B. Mihailova, Tuning the temperature-induced local-dipole coupling in $(1-x)Na_{0.5}Bi_{0.5}TiO_3$-$xBaTiO_3$ via electric field, J. Appl. Phys. **127**, 194103 (2020).
[19] J. Kreisel, P. Bouvier, B. Dkhil, P. A. Thomas, A. M. Glazer, T. R. Welberry, B. Chaabane, and M. Mezouar, High-pressure x-ray scattering of oxides with a nanoscale local structure: Application to $Na_{1/2}Bi_{1/2}TiO_3$, Phys. Rev. B **68**, 14113 (2003).
[20] M. Gröting, S. Hayn, and K. Albe, Chemical order and local structure of the lead-free relaxor ferroelectric $Na_{1/2}Bi_{1/2}\ TiO_3$, J. Solid State Chem. **184**, 2041 (2011).
[21] M. Gröting, I. Kornev, B. Dkhil, and K. Albe, Pressure-induced phase transitions and structure of chemically ordered nanoregions in the lead-free relaxor ferroelectric $Na_{1/2}Bi_{1/2}\ TiO_3$, Phys. Rev. B **86**, 134118 (2012).
[22] Y. Yoneda, H. Nagata, and T. Takenaka, Local structure analysis of $Bi_{0.5}Na_{0.5}TiO_3$, J. Korean Phys. Soc. **66**, 1339 (2015).
[23] K. Datta, R. B. Neder, A. Richter, M. Göbbels, J. C. Neuefeind, and B. Mihailova, Adaptive strain prompting a pseudo-morphotropic phase boundary in ferroelectric $(1-x)Na_{0.5}Bi_{0.5}TiO_3-xBaTiO_3$, Phys. Rev. B **97**, 184101 (2018).
[24] G. O. Jones and P. A. Thomas, Investigation of the structure and phase transitions in the novel A-site substituted distorted perovskite compound $Na_{0.5}Bi_{0.5}TiO_3$, Acta Crystallogr., Sect. B: Struct. Sci. **58**, 168 (2002).

[25]A.-M. Welsch, B. J. Maier, J. M. Engel, B. Mihailova, R. J. Angel, C. Paulmann, M. Gospodinov, A. Friedrich, R. Stosch, and B. Güttler *et al.*, Effect of Ba incorporation on pressure-induced structural changes in the relaxor ferroelectric $PbSc_{0.5}Ta_{0.5}O_3$, Phys. Rev. B **80**, 104118 (2009).
[26]J. Yao, L. Yan, W. Ge, L. Luo, J. Li, D. Viehland, Q. Zhang, and H. Luo, Evolution of domain structures in $Na_{1/2}Bi_{1/2}TiO_3$ single crystals with $BaTiO_3$, Phys. Rev. B **83**, 54107 (2011).
[27]J. Yao, N. Monsegue, M. Murayama, W. Leng, W. T. Reynolds, Q. Zhang, H. Luo, J. Li, W. Ge, and D. Viehland, Role of coexisting tetragonal regions in the rhombohedral phase of $Na_{0.5}Bi_{0.5}TiO_3$-xat.%$BaTiO_3$ crystals on enhanced piezoelectric properties on approaching the morphotropic phase boundary, Appl. Phys. Lett. **100**, 12901 (2012).
[28]B. N. Rao and R. Ranjan, Electric-field-driven monoclinic-to-rhombohedral transformation in $Na_{1/2}Bi_{1/2}TiO_3$, Phys. Rev. B **86**, 134103 (2012).
[29]S. Gorfman and P. A. Thomas, Evidence for a non-rhombohedral average structure in the lead-free piezoelectric material $Na_{0.5}Bi_{0.5}TiO_3$, J. Appl. Crystallogr. **43**, 1409 (2010).
[30]A. M. Glazer, The classification of tilted octahedra in perovskites, Acta Crystallogr., Sect. B **28**, 3384 (1972).
[31]C. Ma, H. Guo, and X. Tan, A New Phase Boundary in $(Bi_{1/2}Na_{1/2})TiO_3$−$BaTiO_3$ Revealed via a Novel Method of Electron Diffraction Analysis, Adv. Funct. Mater. **23**, 5261 (2013).
[32]Q. Zhang, X. Zhao, R. Sun, and H. Luo, Crystal growth and electric properties of lead-free NBT-BT at compositions near the morphotropic phase boundary, Phys. Status Solidi A **208**, 1012 (2011).
[33]S.-J. L. Kang, J.-H. Park, S.-Y. Ko., and H.-Y. Lee, Solid-State Conversion of Single Crystals: The Principle and the State-of-the-Art, J. Am. Ceram. Soc. **98**, 347 (2015).
[34]R. Ranjan and A. Dviwedi, Structure and dielectric properties of $(Na_{0.50}Bi_{0.50})1-xBa_xTiO_3$: 0≤x≤0.10, Solid State Commun. **135**, 394 (2005).
[35]G. de La Flor, S. Gorfman, and B. Mihailova, Local-scale structural response of (1-*x*)$Na_{0.5}Bi_{0.5}TiO_3$-*x*$BaTiO_3$ to external electric fields, Appl. Phys. Lett. **114**, 42901 (2019).
[36]H. Zhang, G. Deng, A. J. Studer, X. Li, X. Zhao, and H. Luo, Neutron diffuse scattering of (1-*x*)$(Na_{0.5}Bi_{0.5})TiO_3$-*x*$BaTiO_3$ relaxor ferroelectric single crystals, Scr. Mater. **86**, 5 (2014).
[37]S. Zhang, R. Xia, and T. R. Shrout, Lead-free piezoelectric ceramics vs. PZT?, J. Electroceram. **19**, 251 (2007).
[38]B. Mihailova, M. Gospodinov, B. Güttler, R. Stosch, and U. Bismayer, Ferroic clustering and phonon anomalies in Pb-based perovskite-type relaxors, J. Phys.: Condens. Matter **19**, 275205 (2007).
[39]P. Fan, K. Liu, W. Ma, H. Tan, Q. Zhang, L. Zhang, C. Zhou, D. Salamon, S.-T. Zhang, and Y. Zhang *et al.*, Progress and perspective of high strain NBT-based lead-free piezoceramics and multilayer actuators, J. Materiomics **7**, 508 (2021).
[40]B. Mihailova, R. J. Angel, B. J. Maier, A.-M. Welsch, J. Zhao, M. Gospodinov, and U. Bismayer, The structural state of lead-based relaxor ferroelectrics under pressure, IEEE Trans. Ultrason. Ferroelectr. Freq. Control **58**, 1905 (2011).
[41]B. Mihailova, N. Waeselmann, B. J. Maier, R. J. Angel, T. Prüßmann, C. Paulmann, M. Gospodinov, and U. Bismayer, Chemically induced renormalization phenomena in Pb-based relaxor ferroelectrics under high pressure, J. Phys.: Condens. Matter **25**, 115403 (2013).

[42]N. Waeselmann, B. Mihailova, M. Gospodinov, and U. Bismayer, In situ high-temperature high-pressure Raman spectroscopy on single-crystal relaxor ferroelectrics $PbSc_{1/2}Ta_{1/2}O_3$ and $PbSc_{1/2}Nb_{1/2}O_3$, J. Phys.: Condens. Matter **25**, 155902 (2013).
[43]B. J. Maier, N. Waeselmann, B. Mihailova, R. J. Angel, C. Ederer, C. Paulmann, M. Gospodinov, A. Friedrich, and U. Bismayer, Structural state of relaxor ferroelectrics $PbSc_{0.5}Ta_{0.5}O_3$ and $PbSc_{0.5}Nb_{.5}O_3$ at high pressures up to 30 GPa, Phys. Rev. B **84**, 174104 (2011).
[44]B. Mihailova, B. J. Maier, T. Steilmann, E. Dul'kin, and M. Roth, Electric-field-induced local structural phenomena in Pb-based ABO_3-type relaxor ferroelectrics, IEEE Trans. Ultrason. Ferroelectr. Freq. Control **62**, 7 (2015).
[45]B. Mihailova, N. Waeselmann, B. J. Maier, A.-M. Welsch, R. J. Angel, and U. Bismayer, Pressure-induced structural transformations in advanced ferroelectrics with relaxor behaviour, High Pressure Res. **33**, 595 (2013).
[46]N. Waeselmann, B. J. Maier, B. Mihailova, R. J. Angel, J. Zhao, M. Gospodinov, C. Paulmann, N. Ross, and U. Bismayer, Pressure-induced structural transformations in pure and Ru-doped $0.9PbZn_{1/3}Nb_{2/3}O_3$-$0.1PbTiO_3$ near the morphotropic phase boundary, Phys. Rev. B **85**, 14106 (2012).
[47]P. B. Groszewicz, M. Gröting, H. Breitzke, W. Jo, K. Albe, G. Buntkowsky, and J. Rödel, Reconciling Local Structure Disorder and the Relaxor State in $(Bi_{1/2}Na_{1/2})TiO_3$-$BaTiO_3$, Sci. Rep. **6**, 31739 (2016).
[48]G. O. Jones, Investigation of the Structure and Phase Transitions in the Novel A-site Substituted Perovskite Series $(Na_{1-x}K_x)_{0.5}Bi_{0.5}TiO_3$, PhD Thesis, University of Warwick (2001).
[49]P. A. Thomas, J. Kreisel, A. M. Glazer, P. Bouvier, Q. Jiang, and R. Smith, The high-pressure structural phase transitions of sodium bismuth titanate, Z. Kristallogr. Cryst. Mater. **220**, 717 (2005).
[50]J. Kreisel, A. M. Glazer, P. Bouvier, and G. Lucazeau, High-pressure Raman study of a relaxor ferroelectric: The $Na_{0.5}Bi_{0.5}TiO_3$ perovskite, Phys. Rev. B **63**, 174106 (2001).
[51]C. Xu, D. He, H. Wang, C. Liu, S. Yin, K. Wang, J. Guan, F. Peng, and Z. Kou, High pressure in situ differential thermal analysis of $Na_{0.5}Bi_{0.5}TiO_3$ phase transitions up to 5GPa, J. Alloys Compd. **533**, 9 (2012).
[52]S. Trujillo, J. Kreisel, Q. Jiang, J. H. Smith, P. A. Thomas, P. Bouvier, and F. Weiss, The high-pressure behaviour of Ba-doped $Na_{1/2}Bi_{1/2}TiO_3$ investigated by Raman spectroscopy, J. Phys.: Condens. Matter **17**, 6587 (2005).
[53]Q. Zheng, Q. Li, S. Xue, Y. Wu, L. Wang, Q. Zhang, X. Qin, X. Zhao, F. Wang, and W. Yang, Pressure Driven Structural Evolutions of $0.935(Na_{0.5}Bi_{0.5})TiO_3$-$0.065BaTiO_3$ Lead-Free Ferroelectric Single Crystal through Raman Spectroscopy, Chin. Phys. Lett. **38**, 26102 (2021).
[54]D. Schütz, M. Deluca, W. Krauss, A. Feteira, T. Jackson, and K. Reichmann, Lone-Pair-Induced Covalency as the Cause of Temperature- and Field-Induced Instabilities in Bismuth Sodium Titanate, Adv. Funct. Mater. **22**, 2285 (2012).
[55]S. Klotz, J.-C. Chervin, P. Munsch, and G. Le Marchand, Hydrostatic limits of 11 pressure transmitting media, J. Phys. D. **42**, 75413 (2009).
[56]K. Takemura, Hydrostaticity in high pressure experiments: some general observations and guidelines for high pressure experimenters, High Pressure Res. **41**, 155 (2021).

[57]M. Woll, M. Burianek, D. Klimm, S. Gorfman, and M. Mühlberg, Characterization of $(Bi_{0.5}Na_{0.5})_{1-x}BaxTiO_3$ grown by the TSSG method, J. Cryst. Growth **401**, 351 (2014).
[58]R. Boehler and K. de Hantsetters, New anvil designs in diamond-cells, High Pressure Res. **24**, 391 (2004).
[59]G. Shen, Y. Wang, A. Dewaele, C. Wu, D. E. Fratanduono, J. Eggert, S. Klotz, K. F. Dziubek, P. Loubeyre, and O. V. Fat'yanov *et al.*, Toward an international practical pressure scale: A proposal for an IPPS ruby gauge (IPPS-Ruby2020), High Pressure Res. **40**, 299 (2020).
[60]H. Kuzmany, Solid-State Spectroscopy (Springer Berlin Heidelberg, Berlin, Heidelberg, 2009).
[61]B. Mihailova, N. Waeselmann, C. Stangarone, R. J. Angel, M. Prencipe, and M. Alvaro, The pressure-induced phase transition(s) of $ZrSiO_4$: revised, Phys. Chem . Miner. **46**, 807 (2019).
[62]OriginPro, Version 2021. OriginLab Corporation, Northampton, MA, USA.
[63]I. Kantor, V. Prakapenka, A. Kantor, P. Dera, A. Kurnosov, S. Sinogeikin, N. Dubrovinskaia, and L. Dubrovinsky, BX90: a new diamond anvil cell design for X-ray diffraction and optical measurements, Rev. Sci. Instrum. **83**, 125102 (2012).
[64]R. J. Angel, M. Bujak, J. Zhao, G. D. Gatta, and S. D. Jacobsen, Effective hydrostatic limits of pressure media for high-pressure crystallographic studies, J. Appl. Crystallogr. **40**, 26 (2007).
[65]K. S. Scheidl, A. Kurnosov, D. M. Trots, T. Boffa Ballaran, R. J. Angel, and R. Miletich, Extending the single-crystal quartz pressure gauge up to hydrostatic pressure of 19 GPa, J. Appl. Crystallogr. **49**, 2129 (2016).
[66]D. M. Trots, A. Kurnosov, L. Vasylechko, M. Berkowski, T. Boffa Ballaran, and D. J. Frost, Elasticity and equation of state of $Li_2B_4O_7$, Phys. Chem . Miner. **38**, 561 (2011).
[67]R. J. Angel and L. W. Finger, *SINGLE*: a program to control single-crystal diffractometers, J. Appl. Crystallogr. **44**, 247 (2011).
[68]R. L. Ralph and L. W. Finger, A computer program for refinement of crystal orientation matrix and lattice constants from diffractometer data with lattice symmetry constraints, J. Appl. Crystallogr. **15**, 537 (1982).
[69]H. E. King and L. W. Finger, Diffracted beam crystal centering and its application to high-pressure crystallography, J. Appl. Crystallogr. **12**, 374 (1979).
[70]K. Datta, A. Richter, M. Göbbels, R. B. Neder, and B. Mihailova, Atomistic origin of huge response functions at the morphotropic phase boundary of $(1-x)Na_{0.5}Bi_{0.5}TiO_3-xBaTiO_3$, Phys. Rev. B **90**, 64112 (2014).
[71]See Supplemental Material at [URL] for additional figures and tables.
[72]J. Kreisel, A. M. Glazer, G. O. Jones, P. A. Thomas, L. Abello, and G. Lucazeau, An x-ray diffraction and Raman spectroscopy investigation of A-site substituted perovskite compounds: the $(Na_{1-x}K_x)_{0.5}Bi_{0.5}TiO_3$ ($0\leq x\leq 1$) solid solution, J. Phys.: Condens. Matter **12**, 3267 (2000).
[73]B. Mihailova, R. J. Angel, A.-M. Welsch, J. Zhao, J. Engel, C. Paulmann, M. Gospodinov, H. Ahsbahs, R. Stosch, and B. Güttler *et al.*, Pressure-induced phase transition in $PbSc_{0.5}Ta_{0.5}O_3$ as a model Pb-based perovksite-type relaxor ferroelectric, Phys. Rev. Lett. **101**, 17602 (2008).
[74]D. S. Keeble, E. R. Barney, D. A. Keen, M. G. Tucker, J. Kreisel, and P. A. Thomas, Bifurcated Polarization Rotation in Bismuth-Based Piezoelectrics, Adv. Funct. Mater. **23**, 185 (2013).

[75]B. Mihailova, U. Bismayer, B. Güttler, M. Gospodinov, and L. Konstantinov, Local structure and dynamics in relaxor-ferroelectric $PbSc_{1/2}Nb_{1/2}O_3$ and $PbSc_{1/2}Ta_{1/2}O_3$ single crystals, J. Phys.: Condens. Matter **14**, 1091 (2002).
[76]A.-M. Welsch, B. J. Maier, B. Mihailova, R. J. Angel, J. Zhao, C. Paulmann, J. M. Engel, M. Gospodinov, V. Marinova, and U. Bismayer, Transformation processes in relaxor ferroelectric $PbSc_{0.5}Ta_{0.5}O_3$ heavily doped with Nb and Sn, Z. Kristallogr. **226**, 126 (2011).
[77]K. Datta, A. Richter, M. Göbbels, R. B. Neder, and B. Mihailova, Mesoscopic-scale structrue and dynamics near the morphotropic phase boundary of (1-*x*)$PbTiO_3$-*x*$BiScO_3$, Phys. Rev. B **92**, 24107 (2015).
[78]A.-M. Welsch, B. Mihailova, M. Gospodinov, R. Stosch, B. Güttler, and U. Bismayer, High pressure Raman spectroscopic study on the relaxor ferroelectric $PbSc_{0.5}Nb_{0.5}O_3$, J. Phys.: Condens. Matter **21**, 235901 (2009).
[79]U. Bismayer, Hard mode Raman spectroscopy and its application to ferroelastic and ferroelectric phase transitions, Phase Transitions **27**, 211 (1990).
[80]F. A. Pina Binvignat, T. Malcherek, R. J. Angel, C. Paulmann, J. Schlüter, and B. Mihailova, Radiation-damaged zircon under high pressures, Phys. Chem . Miner. **45**, 981 (2018).
[81]B. J. Maier, A.-M. Welsch, R. J. Angel, B. Mihailova, J. Zhao, J. M. Engel, L. A. Schmitt, C. Paulmann, M. Gospodinov, and A. Friedrich *et al.*, A-site doping-induced renormalization of structural transformations in the $PbSc_{0.5}Nb_{0.5}O_3$ relaxor ferroelectric under high pressure, Phys. Rev. B **81**, 174116 (2010).
[82]A. Neagu and C.-W. Tai, Investigation of local structural phase transitions in $95Na_{0.5}Bi_{0.5}TiO_3$-$5BaTiO_3$ piezoceramics by means of *in-situ* transmission electron microscopy, J. Appl. Phys. **123**, 244105 (2018).
[83]A.-K. Fetzer, A. Wohninsland, K. V. Lalitha, and H.-J. Kleebe, Nanoscale polar regions embedded within ferroelectric domains in $Na_{1/2}Bi_{1/2}TiO_3$–$BaTiO_3$, Phys. Rev. Materials **6**, 64409 (2022).
[84]H. T. Stokes, E. H. Kisi, D. M. Hatch, and C. J. Howard, Group-theoretical analysis of octahedral tilting in ferroelectric perovskites, Acta Crystallogr., Sect. B: Struct. Sci. **58**, 934 (2002).
[85]R. J. Angel, "Equations of state", in *High-Temperature and High-Pressure Crystal Chemistry* (Rev. Mineral. Geochem., Vol. 41) R. M. Hazen and R. T. Downs, Eds., Chantilly, VA: Mineralogical Society of America, 2000, p. 35–59.
[86]J. Suchanicz, Elastic constants of $Na_{0.5}Bi_{0.5}TiO_3$ single crystal, J. Mater. Sci. **37**, 489 (2002).
[87]H.-Y. Zhang, Z.-Y. Zeng, Y.-Q. Zhao, Q. Lu, and Y. Cheng, First-Principles Study of Lattice Dynamics, Structural Phase Transition, and Thermodynamic Properties of Barium Titanate, Z. Naturforsch. **71**, 759 (2016).
[88]M. Ahart, R. E. Cohen, V. Struzhkin, E. Gregoryanz, D. Rytz, S. A. Prosandeev, H. Mao, and R. J. Hemley, High-pressure Raman scattering and x-ray diffraction of the relaxor ferroelectric $0.96Pb(Zn_{1/3}Nb_{2/3})O_3$–$0.04PbTiO_3$, Phys. Rev. B **71**, 144102 (2005).
[89]G. Fraysse, A. Al-Zein, J. Haines, J. Rouquette, V. Bornand, P. Papet, C. Bogicevic, and S. Hull, Competing order parameters in the $Pb(Zr_{1-x}Ti_x)O_3$ solid solution at high pressure, Phys. Rev. B **84**, 144110 (2011).
[90]R. D. Shannon, Revised effective ionic radii and systematic studies of interatomic distances in halides and chalcogenides, Acta Crystallogr., Sect. A **32**, 751 (1976).

Pressure-induced structural transformations in (1-*x*)$Na_{0.5}Bi_{0.5}TiO_3$-*x*$BaTiO_3$ at the morphotropic phase boundary

Constanze Rösche[1,*], Tiziana Boffa Ballaran[2], Boriana Mihailova[1]

[1]*Department of Earth System Sciences, Universität Hamburg, Grindelallee 48, 20146 Hamburg, Germany*

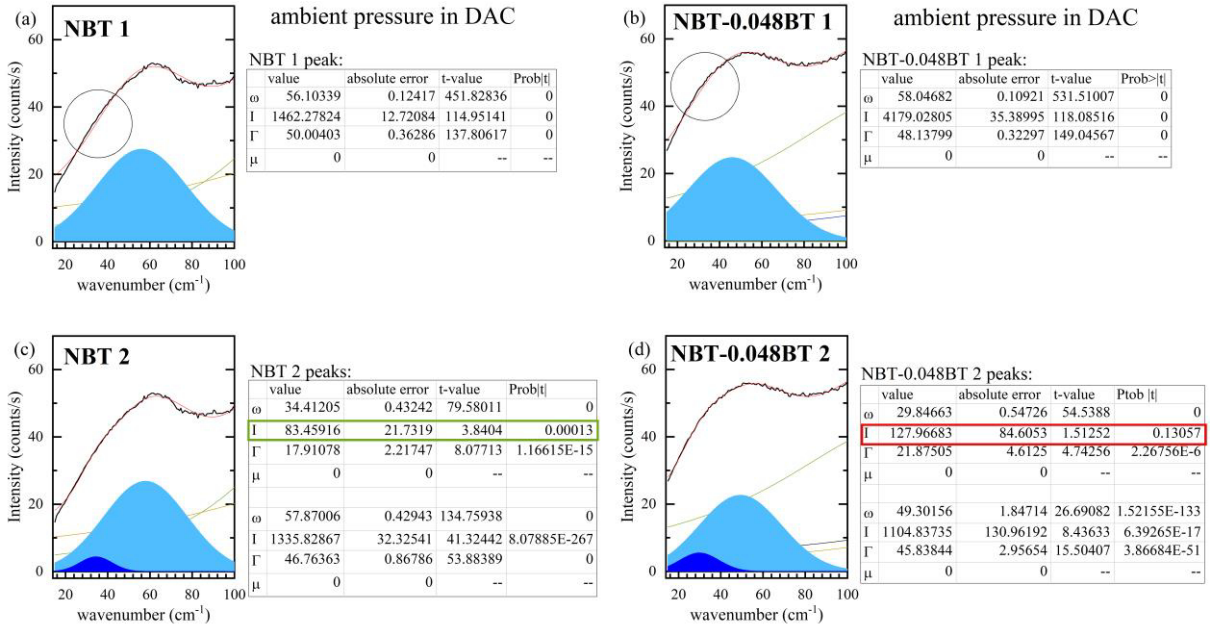
[2]*Bayerisches Geoinstitut, Universität Bayreuth, Universitätsstraße 30, 95440 Bayreuth, Germany*

SUPPLEMENTAL MATERIAL

TEXT SI.

A considerably smaller number of peaks than those expected from group-theory analysis [1] could be resolved in the Raman spectra of pure NBT and NBT-0.048BT. The spectra were therefore fitted using pseudo-Voigt functions within the OriginPro 2021 software package [2] following the procedure presented by de la Flor *et al.* [3]. At each pressure step the number of pseudo-Voigt peaks chosen was justified by the standard criteria for goodness of fit: adjusted R^2, reduced χ^2, and the relative uncertainties of each fitted parameter. We pay particular attention to these relative errors, because they correspond to the t-value (= fitted value/error) and the related prob|t| value, giving the probability of a certain parameter to exist or not. Following the requirements of the null-hypothesis significance testing, if prob|t| < 0.05 (the stronger criterion is <0.005), then the corresponding parameter should exist; if prob|t| for a certain fitting parameter is >0.05, then this parameter should be removed. We routinely apply this rule in particular to the peak integrated intensity: usually if the error in the integrated intensity ΔI for a certain peak is larger than a half of its magnitude I, prob|t| is well above 0.05 and we remove this peak from the fitting model. In the case when R-square or chi-square or a simple visual inspection of the spectrum indicates that an additional peak might be required, we always double check the relative errors of integrated intensities and the prob|t| values for all peaks. Moreover, before changing the number of fitting peak functions, we try several fitting models before proceeding further. To illustrate this procedure, we show how the number of peaks to describe the wavenumber region between 15 and 100 cm^{-1} were chosen (Fig. S1. For the NTB sample, the mathematical criteria described above, i.e. $\Delta I/I = 0.26$ and prob|t| = 0.00013, suggest that two peaks need to be used instead of one (Figure S1, left). This choice has

been further supported by the fact that the peak at ~34 cm^{-1} is enhanced at high-pressures. On the contrary, if we include a component near 34 cm^{-1} in the spectrum of NBT-0.048 BT (Fig. S1, right), the relative error in the intensity is $\Delta I/I$ = 0.66 and prob|t| = 0.13, which is well above 0.05 required by the null-hypothesis significance.



NBT 1 peak:	value	absolute error	t-value	Prob|t|
ω	56.10339	0.12417	451.82836	0
I	1462.27824	12.72084	114.95141	0
Γ	50.00403	0.36286	137.80617	0
μ	0	0	--	--

NBT-0.048BT 1 peak:	value	absolute error	t-value	Prob>|t|
ω	58.04682	0.10921	531.51007	0
I	4179.02805	35.38995	118.08516	0
Γ	48.13799	0.32297	149.04567	0
μ	0	0	--	--

NBT 2 peaks:	value	absolute error	t-value	Prob|t|
ω	34.41205	0.43242	79.58011	0
I	83.45916	21.7319	3.8404	0.00013
Γ	17.91078	2.21747	8.07713	1.16615E-15
μ	0	0	--	--
ω	57.87006	0.42943	134.75938	0
I	1335.82867	32.32541	41.32442	8.07885E-267
Γ	46.76363	0.86786	53.88389	0
μ	0	0	--	--

NBT-0.048BT 2 peaks:	value	absolute error	t-value	Ptob |t|
ω	29.84663	0.54726	54.5388	0
I	127.96683	84.6053	1.51252	0.13057
Γ	21.87505	4.6125	4.74256	2.26756E-6
μ	0	0	--	--
ω	49.30156	1.84714	26.69082	1.52155E-133
I	1104.83735	130.96192	8.43633	6.39265E-17
Γ	45.83844	2.95654	15.50407	3.86684E-51
μ	0	0	--	--

FIG. S1. Pseudo-Voigt function fittings for the A-cation localized mode in pure NBT (a and c) and NBT-0.048BT (b and d) using one peak (a and b) or two peaks (c and d), along with the values of the Raman peak positions ω, FWHMs Γ, integrated intensities I, and the Lorentzian contribution μ to the peak-shape function (μ was initially released to vary between 0 and 1 and fixed to the resultant value only at the final step of fitting, after reaching the final values of all fitting parameters) as well as the corresponding absolute errors, t-values and prob|t| values.

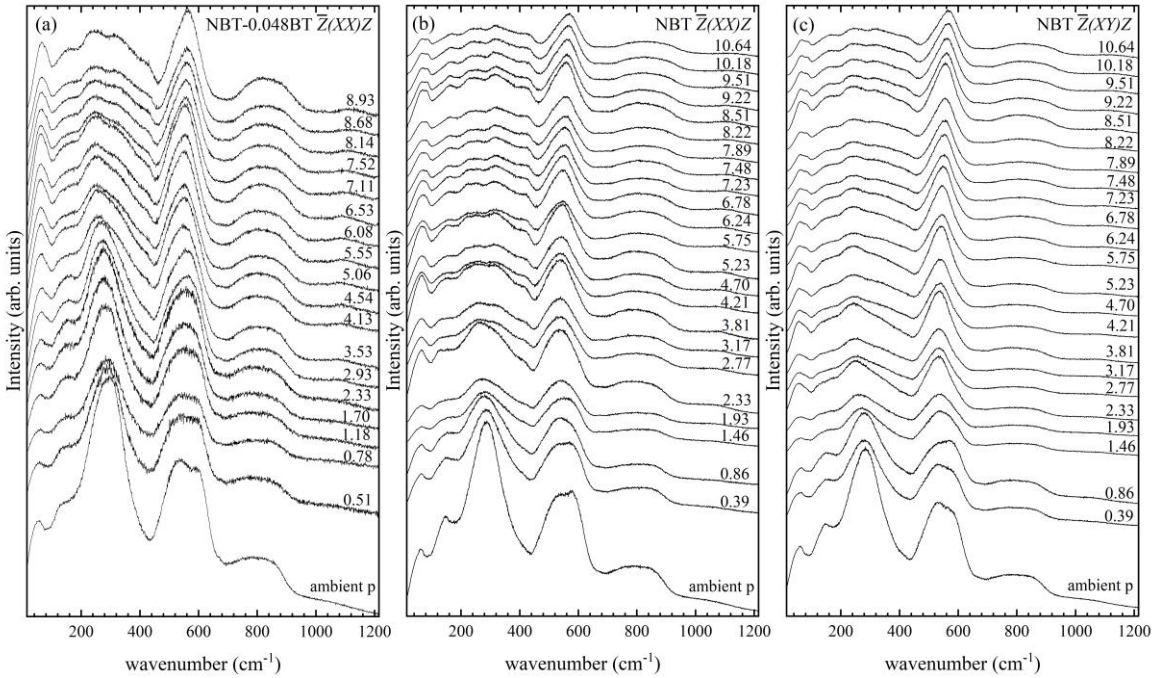


FIG. S2. Comprehensive set of polarized Raman spectra of NBT-0.048BT $\bar{Z}(XX)Z$ (a), NBT $\bar{Z}(XX)Z$ (b) and NBT $\bar{Z}(XY)Z$ (c).

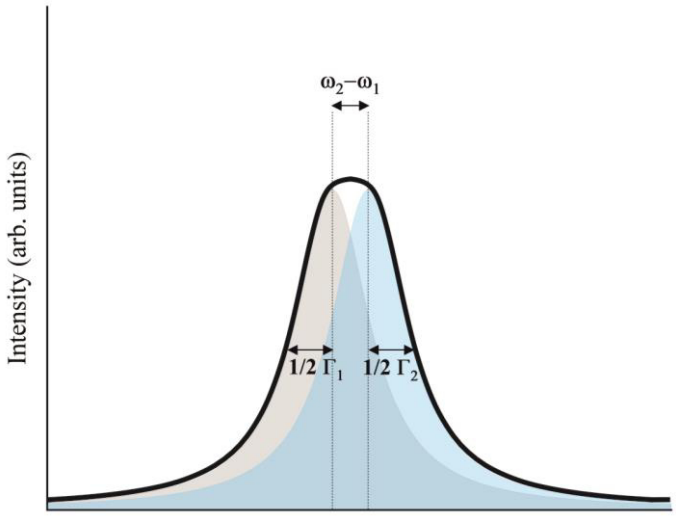


FIG. S3. Effective FWHM $\Gamma_{1,2} = (\omega_2 - \omega_1) + \frac{\Gamma_1+\Gamma_2}{2}$.

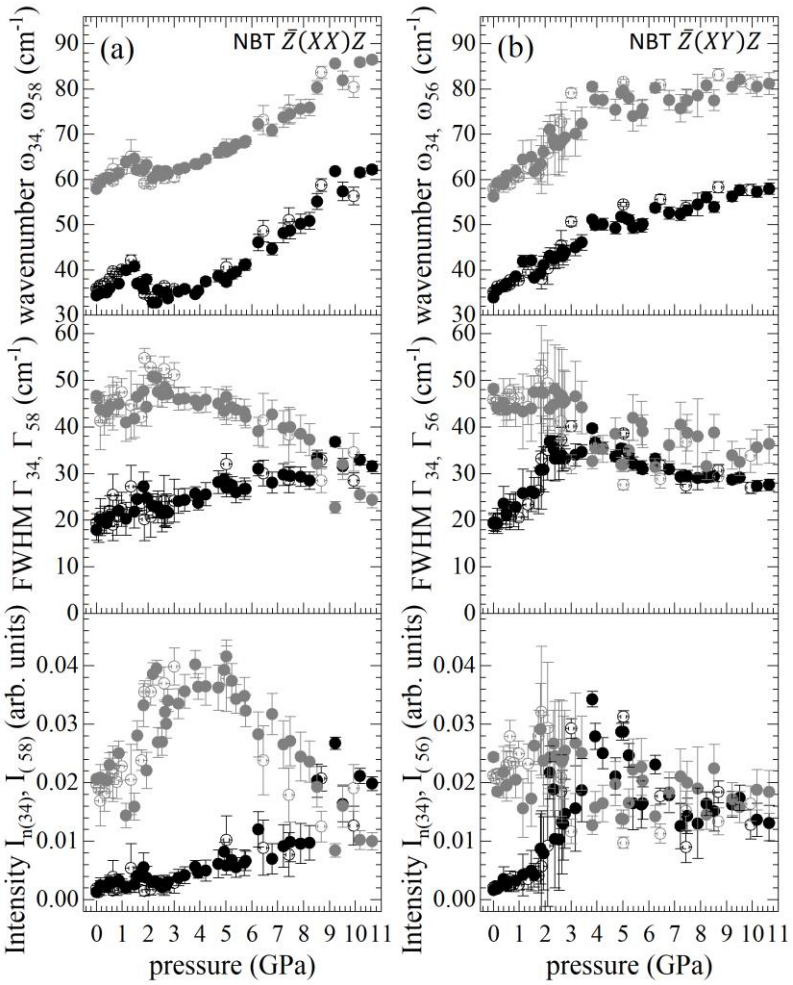


FIG. S4. Pressure dependence of the Raman peak positions ω, FWHMs Γ and fractional intensities I_n of the two A-cation localized modes measured for NBT in parallel polarized spectra of NBT (a) and cross polarized spectra of NBT (b). Open symbols correspond to data measured on decompression.

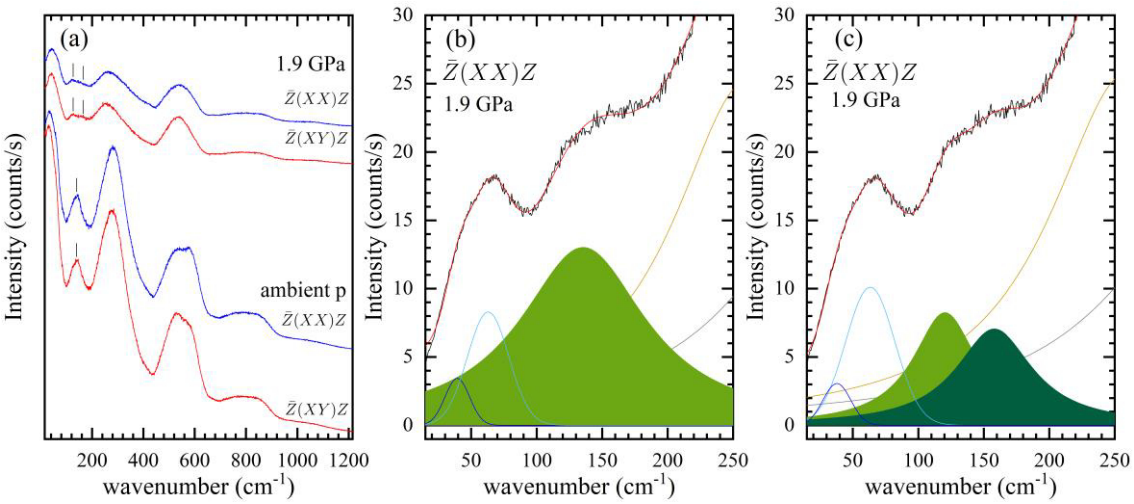


FIG. S5. As-measured spectra of NBT, clearly showing the splitting of the mode near 135 cm^{-1} at elevated pressures (a); a fit of the corresponding parallel polarized T-reduced spectrum, using one peak only for the scattering near 135 cm^{-1} (b); a fit of the corresponding parallel polarized T-reduced spectrum, using two peaks for the scattering near 135 cm^{-1} (c).

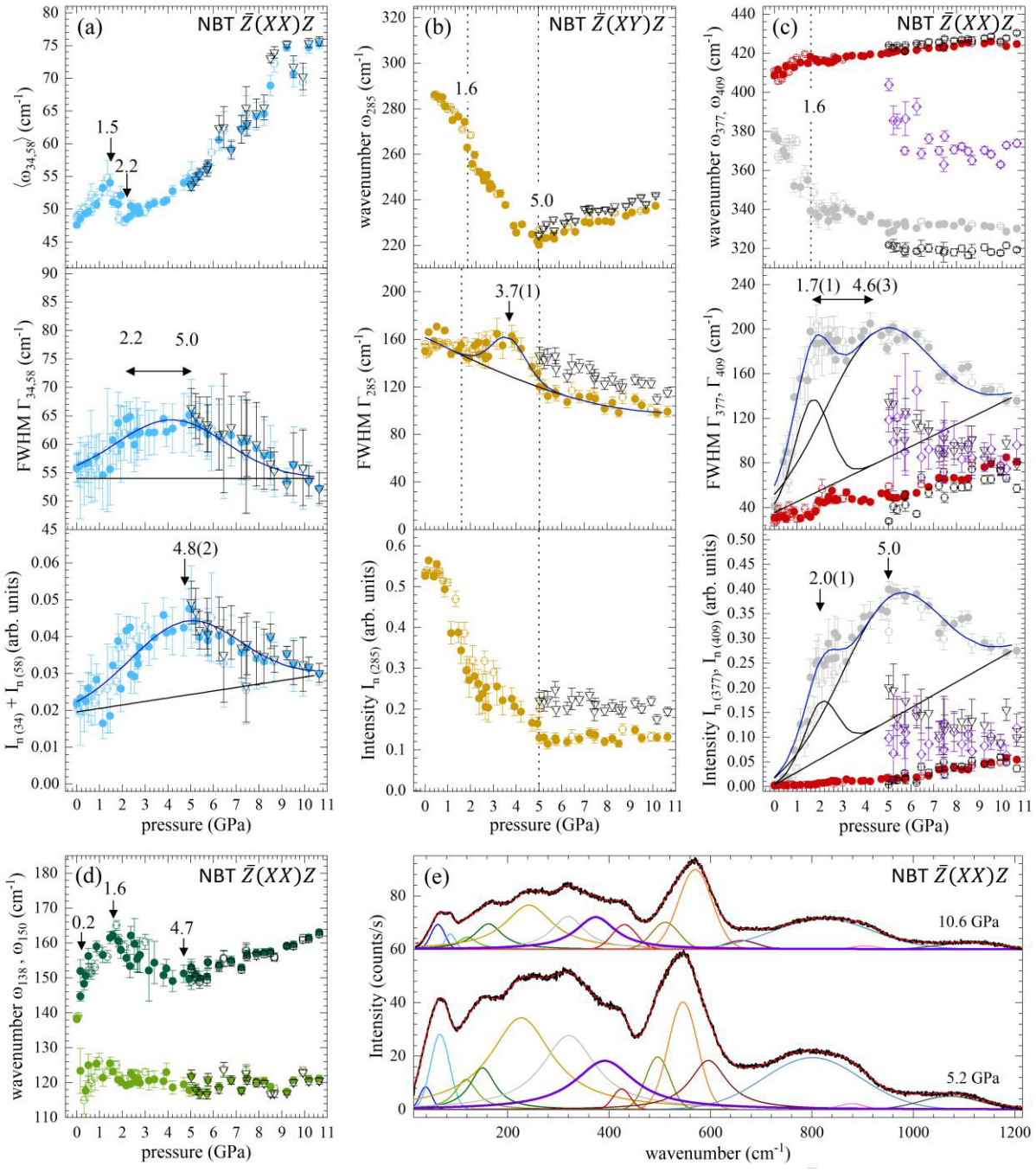


FIG. S6. Pressure dependence of the Raman peak positions ω, FWHMs Γ and fractional intensities I_n of the A-cation (a) and B-cation (b) localized mode, the BO_6 tilting mode (c) and of the peak positions ω of the A-BO_3 translation mode (d) in NBT derived from the parallel polarized spectra. Pseudo-Voigt function fits of Raman spectra of pure NBT at 5.2 GPa and 10.6 GPa with an additional peak near 400 cm^{-1} are shown in (e). The blue, yellow, grey, red and green symbols correspond to the trends as shown in Figs. 3, 5, 6, and 7, whereby open symbols correspond to pressure points measured on decompression. The black open symbols correspond to ω, Γ and I_n as derived from the fittings with an additional peak near 400 cm^{-1} above 5 GPa, which itself is highlighted in purple.

TABLE SI. Raman peak positions ω derived from pseudo-Voigt function fits of the parallel polarized Raman spectra of pure NBT.

	NBT $\bar{Z}(XX)Z$							
Pressure (GPa)	ω_{34}	ω_{58}	$\langle\omega_{34,58}\rangle$	ω_{138}	ω_{145}	ω_{286}	ω_{377}	ω_{409}
0.00010 (1)	34.4 (4)	57.9 (4)	47.6 (4)	138.2 (1)	-	286.1 (1)	377.4 (2.6)	408.5 (1.2)
*0.00010 (1)	35.9 (4)	59.0 (6)	48.9 (5)	138.9 (2)	-	285.3 (1)	379.5 (2.2)	410.8 (1.0)
*0.08 (5)	35.9 (5)	59.5 (5)	49.1 (5)	139.2 (2)	-	286.3 (1)	377.2 (1.3)	409.6 (9)
*0.16 (5)	36.6 (9)	59.6 (1.2)	49.5 (1.1)	105.9 (3.6)	144.7 (1.3)	284.9 (2)	367.0 (3.3)	405.9 (1.7)
0.16 (5)	34.8 (5)	59.2 (8)	48.6 (7)	123.4 (6.4)	152.0 (3.2)	285.5 (1)	375.6 (2.1)	411.7 (1.3)
*0.31 (5)	37.0 (6)	60.2 (1.0)	50.0 (8)	115.0 (3.9)	148.3 (1.8)	283.0 (1)	367.1 (1.4)	406.6 (9)
0.39 (5)	35.0 (5)	60.4 (5)	49.3 (5)	117.7 (2.8)	150.6 (1.8)	285.0 (3)	370.1 (2.9)	409.1 (1.0)
*0.51 (5)	38.0 (5)	60.9 (1.2)	50.8 (9)	119.1 (3.0)	152.1 (1.9)	281.6 (2)	374.3 (2.1)	413.5 (1.0)
0.51 (5)	36 (4)	60.3 (8)	49.7 (6)	125.0 (3.2)	156.3 (2.2)	281.0 (4)	367.4 (1.7)	413.1 (9)
*0.63 (5)	39.7 (7)	62.3 (2.4)	52.2 (1.7)	120.0 (2.5)	151.4 (1.9)	279.9 (3)	374.2 (3.9)	413.9 (1.4)
*0.63 (5)	37.1 (4)	59.7 (7)	49.7 (6)	120.8 (4.6)	151.9 (2.3)	279.9 (2)	366.5 (2.4)	410.5 (1.4)
*0.78 (5)	39.1 (5)	61.3 (1.1)	51.4 (8)	121.4 (3.5)	153.1 (1.9)	280.8 (3)	374.7 (3.4)	416.2 (1.0)
0.86 (5)	37.0 (4)	61.5 (8)	50.7 (7)	125.5 (1.8)	159.0 (1.6)	275.0 (1.0)	352.1 (3.3)	412.8 (1.0)
*0.98 (5)	40 (5)	62.1 (1.1)	52.3 (8)	126.2 (2.2)	157.9 (1.4)	278.5 (4)	374.9 (2.3)	417.6 (7)
1.14 (5)	39.9 (9)	63.9 (1.3)	53.3 (1.1)	121.5 (2.5)	156.6 (2.2)	276.6 (1.2)	351.4 (5.0)	415.2 (7)
*1.34 (5)	42.1 (1.2)	65.1 (3.7)	54.8 (2.7)	122.9 (1.6)	156.1 (1.7)	271.0 (7)	358.5 (3.9)	419.6 (9)
1.46 (5)	40.8 (1.0)	64.6 (1.6)	54.0 (1.3)	125.6 (1.8)	161.5 (1.8)	274.3 (1.2)	355.1 (3.7)	414.9 (7)
1.58 (5)	37.0 (5)	62.2 (1.1)	51.1 (8)	123.2 (8)	162.3 (1.2)	262.9 (1.2)	339.4 (5.6)	418.2 (6)
*1.73 (5)	37.4 (7)	63.2 (7)	51.9 (7)	125.1 (1.2)	165.0 (1.4)	268.4 (1.1)	348.8 (4.2)	416.3 (7)
1.81 (5)	35.9 (8)	62.1 (1.4)	50.7 (1.1)	120.9 (7)	160.7 (1.8)	255.8 (1.0)	337.7 (3.7)	416.9 (5)
*1.85 (5)	34.7 (8)	59.2 (7)	48.5 (7)	122.2 (6)	160.6 (1.4)	254.4 (1.1)	337.9 (5.5)	416.4 (8)
1.93 (5)	37.9 (1.1)	63.3 (1.6)	52.1 (1.4)	120.3 (1.2)	158.0 (2.4)	259.7 (1.6)	336.5 (5.8)	415.5 (9)
*2.09 (5)	33.9 (7)	59.0 (5)	48.1 (7)	121.1 (7)	159.0 (1.6)	252.4 (1.3)	341.2 (3.7)	416.3 (1.9)
2.17 (5)	32.8 (3)	60.3 (5)	48.5 (4)	119.2 (7)	155.7 (2.3)	252.4 (1.1)	340.2 (3.2)	416.0 (6)
2.33 (5)	32.8 (4)	60.9 (4)	48.9 (4)	119.6 (7)	153.4 (3.4)	250.8 (1.3)	338.5 (3.5)	415.9 (5)
2.37 (5)	35.6 (6)	62.0 (9)	50.5 (8)	122.7 (1.2)	162.1 (2.6)	248.6 (1.6)	334.1 (4.5)	415.1 (9)
2.53 (5)	35.1 (7)	60.8 (8)	49.6 (7)	121.5 (2.1)	159.8 (7.3)	250.8 (1.6)	339.7 (3.8)	415.4 (9)
*2.61 (5)	36.4 (7)	60.3 (1.1)	49.8 (1.0)	122.7 (6)	159.8 (1.0)	247.4 (1.0)	345.5 (2.9)	418.2 (8)
2.65 (5)	34.8 (5)	61.8 (6)	50.2 (6)	120.2 (1.0)	155.4 (3.6)	244.9 (1.2)	336.4 (2.8)	416.1 (6)
2.69 (5)	35.0 (6)	61.9 (7)	50.3 (7)	121.3 (1.8)	155.9 (4.4)	246.9 (1.5)	340.5 (2.4)	417.6 (6)
2.77 (5)	33.7 (5)	61.3 (5)	49.5 (5)	120.0 (1.6)	156.6 (5.0)	245.6 (1.3)	336.2 (3.1)	417.2 (5)
*3.01 (5)	35.8 (5)	60.5 (1.0)	49.7 (8)	123.1 (9)	160.4 (2.2)	242.5 (1.0)	342.2 (2.5)	416.8 (7)
3.17 (5)	35.2 (7)	62.2 (7)	50.6 (7)	120.6 (2.7)	152.2 (8.7)	242.8 (1.6)	340.0 (2.4)	418.4 (6)
3.41 (5)	35.8 (7)	62.6 (7)	51.0 (7)	121.0 (2.4)	154.4 (6.1)	237.8 (1.2)	338.4 (2.4)	418.8 (5)
3.81 (5)	34.6 (6)	63.4 (5)	51.1 (5)	120.4 (2.3)	150.8 (3.2)	228.6 (1.0)	335.1 (1.8)	418.6 (4)
3.93 (5)	35.4 (6)	63.4 (4)	51.4 (5)	123.0 (2.7)	152.7 (2.7)	225.6 (1.0)	334.0 (1.7)	418.4 (4)
4.21 (5)	37.5 (8)	64.5 (9)	52.8 (8)	118.6 (1.9)	149.1 (3.0)	229.2 (1.0)	336.9 (2.1)	419.4 (5)
4.70 (5)	38.7 (1.3)	65.9 (1.1)	54.0 (1.2)	119.5 (1.9)	151.2 (2.5)	224.9 (9)	333.1 (1.4)	419.4 (5)
4.94 (5)	38.0 (1.0)	67.1 (6)	54.5 (7)	117.8 (1.7)	149.7 (2.0)	221.8 (8)	332.6 (8)	420.2 (3)
*5.02 (5)	40.6 (1.9)	67.1 (1.8)	55.4 (1.8)	117.8 (1.6)	149.1 (2.4)	226.9 (8)	333.3 (1.2)	420.1 (5)
5.02 (5)	37.4 (8)	66.1 (7)	53.7 (7)	121.9 (1.8)	153.1 (2.3)	220.2 (9)	328.1 (1.0)	420.0 (3)
5.23 (5)	39.0 (1.0)	66.7 (8)	54.7 (8)	118.3 (1.5)	150.9 (1.9)	223.1 (8)	329.1 (1.1)	420.6 (4)
5.39 (5)	39.6 (1.0)	67.8 (8)	55.5 (9)	117.1 (1.4)	150.0 (2.0)	223.3 (9)	332.4 (8)	421.1 (4)
5.71 (5)	41.1 (1.2)	68.2 (1.0)	56.3 (1.0)	117.0 (1.4)	150.4 (1.8)	224.7 (8)	333.7 (9)	421.0 (4)
5.75 (5)	41.2 (1.1)	68.6 (8)	56.6 (9)	120.6 (1.7)	154.4 (1.7)	222.9 (8)	331.6 (9)	421.1 (4)
6.24 (5)	46.1 (1.8)	72.3 (1.6)	60.6 (1.6)	118.9 (1.2)	153.6 (1.5)	226.0 (7)	330.5 (9)	421.6 (4)
*6.45 (5)	48.6 (2.4)	73.2 (3.2)	62.1 (2.8)	123.9 (2.0)	155.8 (2.3)	228.0 (8)	334.0 (1.1)	423.2 (5)
6.78 (5)	44.7 (1.4)	70.9 (1.4)	59.2 (1.3)	120.7 (1.2)	155.0 (1.3)	225.9 (7)	332.3 (7)	422.6 (3)
7.23 (5)	48.2 (2.2)	73.7 (2.2)	62.3 (2.1)	117.8 (1.0)	153.0 (9)	230.3 (7)	332.3 (6)	422.9 (4)
*7.43 (5)	51.1 (2.6)	75.4 (3.2)	64.4 (2.9)	123.4 (1.9)	158.1 (2.0)	232.4 (8)	332.7 (9)	422.7 (5)
7.48 (5)	48.7 (1.9)	74.5 (2.0)	62.9 (1.9)	121.3 (1.2)	156.8 (1.2)	229.8 (7)	332.6 (6)	423.2 (4)
7.89 (5)	50.2 (2.2)	75.6 (2.1)	64.2 (2.1)	120.3 (1.2)	157.2 (1.1)	230.5 (7)	331.7 (6)	423.5 (3)
8.22 (5)	50.8 (1.9)	75.9 (1.8)	64.6 (1.8)	120.6 (1.0)	157.4 (1.0)	230.7 (7)	333.7 (7)	425.0 (3)
8.51 (5)	55.1 (1.8)	80.4 (1.5)	68.9 (1.6)	118.9 (9)	157.6 (9)	230.3 (5)	330.3 (6)	425.4 (3)
*8.68 (5)	58.8 (1.4)	83.7 (1.4)	72.3 (1.4)	118.3 (1.0)	156.1 (1.1)	234.3 (7)	332.3 (8)	425.2 (7)
9.22 (5)	61.8 (7)	85.6 (0.5)	74.7 (6)	117.5 (7)	159.3 (7)	233.0 (6)	331.6 (6)	425.0 (4)
9.51 (5)	57.4 (2.1)	81.9 (2.1)	70.7 (2.0)	120.7 (1.0)	159.6 (9)	234.5 (6)	331.1 (6)	425.9 (5)
*9.93 (5)	56.3 (1.9)	80.5 (2.3)	69.5 (2.1)	123.5 (1.0)	161.5 (9)	235.1 (6)	331.6 (7)	425.3 (5)
10.18 (5)	61.5 (9)	85.9 (9)	74.7 (9)	121.1 (1.0)	161.6 (9)	235.4 (5)	328.7 (6)	423.6 (6)
10.64 (5)	62.2 (9)	86.5 (8)	75.3 (8)	121.2 (1.0)	163.1 (9)	237.3 (6)	330.2 (6)	424.8 (6)

*decompression

TABLE SII. Raman peak positions ω derived from pseudo-Voigt function fits of the cross polarized Raman spectra of pure NBT.

NBT $\bar{Z}(XY)Z$								
Pressure (GPa)	ω_{34}	ω_{56}	$\langle\omega_{34,56}\rangle$	ω_{138}	ω_{150}	ω_{283}	ω_{374}	ω_{410}
0.00010 (1)	33.9 (4)	56.2 (5)	46.4 (4)	137.8 (1)		282.8 (1)	374.4 (1.3)	410.3 (8)
*0.00010 (1)	35.1 (3)	58.0 (5)	48.0 (4)	139.0 (1)		284.2 (1)	379.7 (2.1)	412.2 (9)
*0.08 (5)	35.5 (3)	58.3 (6)	48.3 (6)	139.3 (2)		284.0 (1)	372.2 (5.2)	406.7 (1.9)
*0.16 (5)	36.4 (4)	59.0 (7)	49.0 (7)	139.8 (2)		283.4 (1)	379.1 (3.3)	412.6 (1.2)
0.16 (5)	35.6 (4)	59.3 (6)	48.9 (5)	139.2 (2)		286.1 (1)	381.5 (2.7)	412.1 (1.2)
*0.31 (5)	36.6 (4)	59.8 (7)	49.6 (6)	139.6 (2)		282.2 (2)	373.0 (2.4)	410.4 (1.0)
0.39 (5)	36.4 (4)	58.9 (1.8)	48.9 (1.2)	118.5 (5.1)	150.2 (2.4)	279.4 (1)	365.6 (2.4)	409.6 (2.0)
*0.51 (5)	36.4 (4)	60.4 (8)	49.9 (6)	119.8 (2.6)	152.5 (1.7)	280.9 (2)	369.5 (2.5)	411.6 (1.2)
0.51 (5)	37.0 (5)	60.8 (9)	50.3 (7)	118.2 (2.9)	150.8 (1.6)	282.8 (2)	375.5 (2.5)	413.4 (1.0)
*0.63 (5)	37.8 (4)	60.9 (1.1)	50.7 (1.1)	122.4 (2.5)	154.6 (2.0)	279.2 (3)	365.4 (3.4)	413.7 (1.8)
*0.63 (5)	36.8 (4)	59.0 (9)	49.2 (8)	126.0 (3.8)	156.4 (2.3)	276.3 (4)	364.1 (1.7)	409.3 (8)
*0.78 (5)	37.7 (4)	60.5 (1.2)	50.4 (1.0)	128.4 (2.9)	160.3 (1.8)	277.5 (5)	365.7 (2.4)	415.3 (1.5)
0.86 (5)	38.6 (5)	61.9 (1.4)	51.5 (1.0)	121.0 (2.4)	153.3 (1.6)	279.1 (3)	368.5 (2.9)	410.9 (1.2)
*0.98 (5)	37.8 (3)	60.6 (8)	50.5 (7)	129.7 (2.3)	162.9 (1.6)	275.0 (7)	357.6 (3.0)	416.5 (9)
1.14 (5)	41.9 (1.3)	64.4 (4.2)	54.4 (2.8)	123.7 (2.4)	156.3 (2.0)	271.8 (1.1)	354.4 (7.8)	417.2 (1.3)
*1.34 (5)	39.5 (6)	62.7 (1.4)	52.4 (1.1)	124.7 (2.1)	159.7 (2.1)	269.2 (1.0)	348.8 (3.8)	415.0 (1.3)
1.46 (5)	42.1 (1.1)	65.0 (3.8)	54.8 (2.6)	126.3 (1.8)	160.3 (1.7)	267.4 (8)	353.8 (5.2)	420.2 (1.2)
1.58 (5)	38.3 (4)	61.8 (1.5)	51.4 (1.1)	122.2 (8)	159.4 (1.0)	267.1 (5)	363.9 (2.5)	417.1 (8)
*1.73 (5)	39.2 (5)	61.2 (2.2)	51.4 (1.9)	125.4 (1.1)	163.4 (1.2)	262.8 (9)	347.3 (4.4)	419.3 (1.2)
1.81 (5)	39.3 (1.3)	63.5 (4.0)	52.8 (2.7)	122.2 (7)	161.1 (1.0)	255.4 (8)	342.9 (6.0)	417.5 (8)
*1.85 (5)	38.1 (2.3)	63.3 (6.4)	52.2 (4.3)	121.0 (8)	158.3 (2.0)	248.8 (8)	319.2 (5.4)	414.9 (1.0)
1.93 (5)	41.1 (1.9)	66.1 (5.1)	55.0 (3.4)	123.3 (9)	160.2 (1.5)	256.0 (1.3)	338.9 (6.3)	415.6 (1.5)
*2.09 (5)	40.3 (3.5)	65.8 (7.0)	54.6 (4.6)	121.2 (9)	154.6 (4.1)	245.7 (8)	331.3 (2.9)	418.9 (6)
2.17 (5)	43.1 (1.7)	71.1 (3.0)	58.8 (2.2)	121.8 (6)	159.4 (1.5)	246.0 (5)	337.4 (3.3)	420.3 (9)
2.33 (5)	42.5 (1.5)	68.9 (3.0)	57.3 (2.4)	123.9 (7)	161.9 (1.2)	243.4 (5)	340.4 (3.0)	420.8 (1.0)
2.37 (5)	42.5 (2.3)	67.7 (6.6)	56.5 (4.2)	122.3 (8)	159.0 (1.7)	245.6 (8)	333.2 (4.4)	417.2 (2.9)
2.53 (5)	43.1 (2.6)	67.6 (6.8)	56.7 (4.3)	124.3 (9)	162.2 (2.0)	245.2 (7)	340.8 (3.7)	418.2 (1.6)
*2.61 (5)	45.4 (3.3)	72.7 (4.3)	60.6 (3.2)	121.9 (7)	157.8 (3.4)	242.4 (8)	335.0 (2.6)	418.1 (5)
2.65 (5)	44.1 (2.3)	68.6 (6.9)	57.6 (4.4)	125.0 (1.0)	162.5 (2.1)	244.4 (6)	344.7 (3.0)	419.7 (1.6)
2.69 (5)	43.2 (2.1)	68.9 (4.5)	57.5 (3.0)	124.4 (9)	163.9 (2.0)	244.5 (7)	337.3 (4.0)	414.9 (1.5)
2.77 (5)	43.8 (1.7)	69.3 (4.2)	58.0 (2.7)	123.4 (8)	158.7 (1.9)	243.8 (7)	346.6 (3.3)	418.9 (9)
*3.01 (5)	50.7 (1.0)	79.1 (1.1)	66.5 (1.0)	122.6 (1.1)	161.1 (3.3)	239.7 (7)	337.8 (2.5)	419.0 (9)
3.17 (5)	44.9 (1.8)	70.2 (5.0)	58.9 (3.2)	125.5 (9)	161.3 (2.2)	242.3 (7)	347.2 (1.8)	419.0 (1.5)
3.41 (5)	46.1 (1.7)	72.4 (3.6)	60.7 (2.4)	124.6 (8)	160.5 (2.1)	241.1 (8)	345.1 (1.8)	421.0 (1.8)
3.81 (5)	51.2 (6)	80.5 (9)	67.5 (7)	124.8 (9)	162.6 (1.5)	237.7 (7)	338.0 (2.8)	419.1 (1.8)
3.93 (5)	49.9 (1.1)	77.7 (1.7)	65.3 (1.2)	126.6 (1.2)	163.7 (2.2)	238.7 (7)	346.5 (1.6)	423.9 (1.8)
4.21 (5)	50.1 (1.3)	77.6 (1.8)	65.3 (1.3)	123.8 (1.2)	159.1 (2.7)	237.1 (8)	337.6 (4.7)	420.6 (2.8)
4.70 (5)	49.3 (1.4)	75.4 (2.3)	63.7 (1.7)	127.8 (1.6)	162.3 (3.0)	235.1 (8)	335.3 (3.8)	419.4 (2.7)
4.94 (5)	51.8 (7)	79.1 (1.0)	66.9 (8)	130.4 (1.3)	167.0 (1.5)	234.8 (7)	334.6 (5.5)	416.0 (3.9)
*5.02 (5)	54.5 (5)	81.5 (5)	69.3 (7)	125.1 (2.0)	159.9 (3.0)	230.6 (7)	339.8 (1.5)	420.3 (6)
5.02 (5)	51.7 (7)	79.6 (1.0)	67.1 (8)	130.3 (1.5)	167.0 (1.8)	235.7 (6)	333.8 (4.6)	420.0 (3.3)
5.23 (5)	51.2 (1.0)	78.1 (1.5)	66.0 (1.1)	128.7 (1.9)	163.4 (3.1)	236.2 (8)	331.6 (3.9)	417.5 (3.3)
5.39 (5)	49.5 (1.4)	74.0 (3.3)	63.0 (2.2)	131.2 (1.4)	167.4 (2.4)	236.0 (9)	333.4 (5.5)	419.3 (4.7)
5.71 (5)	49.7 (1.4)	74.7 (2.8)	63.4 (2.1)	127.8 (2.0)	159.9 (4.2)	233.7 (1.0)	327.7 (4.0)	415.4 (3.8)
5.75 (5)	50.2 (1.2)	75.6 (2.1)	64.2 (1.7)	127.5 (1.4)	160.2 (2.5)	235.4 (8)	340.4 (2.2)	420.8 (1.5)
6.24 (5)	53.7 (9)	80.2 (1.1)	68.3 (1.4)	126.6 (2.0)	160.1 (2.7)	234.7 (7)	332.4 (3.2)	418.8 (2.4)
*6.45 (5)	55.6 (1.0)	81.0 (1.2)	69.4 (1.6)	124.8 (2.8)	156.7 (3.1)	232.1 (8)	341.5 (1.2)	419.3 (5)
6.78 (5)	52.6 (1.4)	77.5 (2.2)	66.3 (1.8)	127.2 (1.9)	159.4 (3.0)	235.3 (7)	336.0 (3.2)	418.5 (2.1)
7.23 (5)	52.3 (1.3)	75.7 (3.0)	65.1 (2.7)	132.3 (2.6)	164.2 (4.1)	237.5 (8)	333 (2.6)	418.1 (2.1)
*7.43 (5)	53.7 (1.6)	77.3 (2.6)	66.6 (2.6)	127.6 (2.6)	158.5 (3.0)	233.0 (8)	336.6 (9)	419.2 (5)
7.48 (5)	53.2 (1.2)	77.4 (2.3)	66.4 (2.1)	130.4 (1.8)	163.2 (2.5)	236.1 (8)	328.2 (2.8)	415.6 (2.9)
7.89 (5)	54.5 (2.5)	78.6 (4.7)	67.6 (3.6)	125.9 (2.1)	157.4 (3.4)	234.5 (1.2)	334.3 (2.6)	421.4 (1.8)
8.22 (5)	56.1 (1.2)	80.9 (1.6)	69.6 (1.7)	123.4 (1.5)	157.5 (1.9)	236.5 (7)	332.1 (1.9)	419.2 (1.7)
8.51 (5)	53.9 (1.1)	77.5 (2.3)	66.8 (2.0)	126.6 (1.4)	158.7 (1.9)	234.6 (6)	330.5 (1.7)	419.9 (1.6)
*8.68 (5)	58.3 (1.2)	83.2 (1.4)	71.8 (1.4)	121.5 (1.1)	156.3 (1.5)	234.5 (6)	335.4 (8)	419.8 (6)
9.22 (5)	56.2 (1.1)	80.6 (1.7)	69.5 (1.2)	125.7 (1.5)	159.1 (1.9)	236.4 (7)	328.2 (1.7)	417.3 (1.7)
9.51 (5)	57.6 (1.2)	82.1 (1.7)	71.0 (1.8)	125.8 (1.3)	159.9 (1.7)	237.4 (7)	326.7 (1.4)	418.1 (1.7)
*9.93 (5)	57.7 (1.3)	81.1 (2.0)	70.4 (2.0)	126.7 (1.3)	160.4 (1.6)	237.2 (7)	335.1 (1.1)	419.0 (9)
10.18 (5)	57.3 (1.2)	80.5 (2.2)	69.9 (1.6)	127.6 (1.2)	161.5 (1.5)	237.4 (7)	328.0 (1.4)	419.1 (1.4)
10.64 (5)	58 (1.3)	81.2 (2.4)	70.6 (1.7)	128.5 (1.2)	163.1 (1.4)	240.4 (7)	323.5 (1.0)	415.3 (1.7)

*decompression

TABLE SIII. Raman peak positions ω derived from pseudo-Voigt function fits of the parallel polarized Raman spectra of NBT-0.048BT.

NBT-0.048BT $\bar{Z}(XX)Z$							
Pressure (GPa)	ω_{46}	ω_{125}	ω_{150}	ω_{250}	ω_{310}	ω_{328}	ω_{416}
0.00010 (1)	46.0 (1)	125.2 (4)		249.9 (8)	310.5 (5)		
*0.00010 (1)	49.4 (2)	130.2 (4)		246.4 (1.6)	305.1 (7)		
0.20 (5)	47.6 (2)	131.7 (3)		248.0 (1.1)	302.7 (7)		
0.27 (5)	47.7 (4)	130.2 (7)		249.8 (3.3)	303.8 (1.5)		
*0.28 (5)	50.7 (2)	132.3 (3)		241.4 (1.1)	299.8 (5)		
0.31 (5)	48.1 (3)	131.3 (6)		246.2 (1.6)	302.6 (1.0)		
0.31 (5)	47.9 (2)	132.0 (3)		245.3 (1.1)	299.8 (7)		
0.39 (5)	48.4 (3)	131.6 (6)		248.1 (1.9)	302.5 (1.1)		
*0.43 (5)	52.1 (2)	132.9 (3)		238.8 (1.3)	296.7 (5)		
*0.47 (5)	52.2 (1)	133.7 (2)		239.1 (1.2)	294.9 (5)		
0.51 (5)	49.4 (3)	133.4 (6)		238.5 (2.0)	296.0 (1.1)		
0.59 (5)	50.1 (2)	133.2 (3)		239.5 (1.1)	292.0 (6)		
0.75 (5)	51.0 (2)	134.1 (3)		239.5 (1.0)	291.4 (7)		
0.78 (5)	51.2 (4)	134.4 (7)		238.5 (1.8)	292.3 (1.3)		
*0.86 (5)	54.2 (2)	134.0 (3)		240.3 (1.3)	292.2 (5)		
1.14 (5)	53.0 (4)	119.9 (3.6)	150.8 (2.0)		281.7 (1)		
1.18 (5)	53.4 (3)	132.6 (5)			283.3 (2)		
*1.26 (5)	55.9 (4)	121.4 (2.6)	152.7 (1.7)		286.8 (1)		
*1.66 (5)	58.1 (3)	121.2 (1.3)	153.4 (1.0)		284.6 (1)		
1.70 (5)	54.3 (5)	121.7 (2.9)	154.4 (2.0)		277.2 (2)		
1.73 (5)	56.2 (4)	122.1 (2.0)	152.8 (1.3)		278.5 (1)		
1.85 (5)	54.8 (6)	119.5 (2.7)	152.2 (1.7)		276.7 (2)		
*1.89 (5)	58.6 (3)	123.6 (1.2)	154.9 (9)		282.4 (1)		
2.01 (5)	56.5 (3)	123.2 (1.4)	154.8 (1.0)		276.2 (1)		
*2.09 (5)	58.7 (3)	123.6 (1.2)	154.5 (9)		280.7 (1)		
2.13 (5)	56.9 (5)	124.3 (1.7)	155.7 (1.2)		276.2 (2)		
2.33 (5)	57.8 (5)	121.1 (1.8)	153.1 (1.3)		277.7 (2)		
2.61 (5)	57.1 (6)	121.7 (3.5)	156.3 (2.5)		266.3 (1.2)		
*2.65 (5)	58.2 (3)	124.0 (1.8)	158.2 (1.5)		264.6 (1.0)	328.5 (5.5)	
2.69 (5)	57.2 (3)	126.3 (1.8)	159.8 (1.3)		264.0 (1.1)	326.4 (5.5)	
2.89 (5)	56.7 (3)	124.2 (2.3)	159.7 (1.5)		259.2 (8)	329.7 (5.8)	
2.93 (5)	58.2 (4)	122.9 (2.2)	157.7 (1.7)		262.3 (1.1)	322.1 (6.2)	
3.17 (5)	57.7 (5)	123.8 (3.1)	160.8 (2.2)		258.9 (1.1)	328.5 (8.3)	
3.33 (5)	57.3 (6)	118.8 (3.5)	155.5 (2.7)		256.2 (1.3)	324.2 (8.9)	
3.53 (5)	59.2 (3)	125.1 (1.5)	160.2 (1.3)		259.3 (8)	331.6 (5.3)	
3.65 (5)	58.1 (4)	124.1 (2.4)	160.5 (1.9)		253.3 (7)	323.5 (5.4)	
3.93 (5)	57.3 (3)	126.0 (1.7)	164.4 (1.4)		250.1 (6)	332.6 (3.9)	
*4.01 (5)	57.8 (2)	123.1 (1.1)	158.6 (2.1)		248.5 (8)	340.5 (1.9)	416.2 (4)
4.13 (5)	57.8 (3)	128.2 (1.4)	166.6 (1.2)		247.3 (1.3)	334.8 (2.8)	413.0 (1.0)
4.13 (5)	57.9 (3)	123.6 (1.4)	161.2 (2.3)		248.4 (1.1)	334.5 (2.4)	411.8 (7)
4.49 (5)	58.0 (3)	124.3 (1.8)	162.9 (1.9)		243.8 (1.2)	331.2 (3.2)	411.2 (9)
4.54 (5)	58.4 (2)	123.0 (1.7)	159.1 (3.2)		247.7 (1.0)	339.2 (2.4)	415.0 (5)
*4.94 (5)	58.9 (2)	125.5 (1.5)	161.4 (2.7)		245.2 (8)	344.1 (1.3)	417.1 (3)
5.06 (5)	58.9 (2)	125.5 (1.3)	164.4 (1.9)		243.0 (9)	338.3 (2.0)	415.8 (5)
5.55 (5)	59.2 (2)	126.2 (1.2)	164.4 (1.6)		243.3 (9)	343.8 (1.7)	417.7 (5)
*5.92 (5)	60.0 (2)	125.0 (1.7)	159.0 (3.3)		241.0 (9)	343.1 (1.4)	418.7 (3)
6.08 (5)	60.0 (2)	123.7 (1.8)	160.8 (2.5)		238.8 (8)	339.3 (1.8)	417.9 (5)
6.53 (5)	60.4 (2)	121.7 (2.0)	157.9 (3.2)		238.4 (8)	341.2 (1.6)	420.0 (4)
6.82 (5)	60.3 (2)	121.2 (2.2)	158.4 (3.4)		237.8 (9)	340.4 (1.8)	419.1 (5)
7.11 (5)	60.9 (2)	122.4 (2.1)	159.7 (2.9)		238.8 (9)	340.6 (1.6)	418.8 (5)
*7.15 (5)	62.0 (2)	121.6 (2.2)	153.9 (3.3)		236.6 (9)	341.5 (1.4)	421.5 (3)
7.52 (5)	61.8 (2)	122.3 (2.5)	158.1 (3.7)		237.3 (9)	340.4 (1.7)	419.8 (5)
7.77 (5)	62.1 (2)	121.5 (2.1)	157.5 (3.0)		236.4 (8)	339.2 (1.5)	421.7 (6)
*7.89 (5)	63.1 (2)	121.5 (2.0)	154.9 (2.6)		234.6 (8)	340.1 (1.4)	423.1 (4)
8.14 (5)	62.8 (2)	120.8 (2.0)	156.9 (2.9)		236.2 (9)	340.0 (1.5)	420.4 (6)
8.43 (5)	63.3 (2)	123.3 (1.8)	159.7 (2.5)		237.1 (8)	339.8 (1.3)	421.6 (5)
8.68 (5)	63.8 (2)	122.9 (1.9)	158.8 (2.6)		236.5 (9)	338.7 (1.3)	420.7 (6)
8.93 (5)	64.2 (2)	121.0 (1.7)	155.8 (2.2)		234.6 (7)	338.1 (1.2)	422.5 (5)

*decompression

TABLE SIV. Pressure dependence of the pseudocubic unit cell parameter and volume for NBT-0.048BT.

NBT-0.048BT					
1st run			2nd run		
p (GPa)	*a* (Å)	*V* (Å)	*p* (GPa)	*a* (Å)	*V* (Å)
0.00010 (1)	3.89975 (11)	59.307 (5)	0.00010 (1)	3.90004 (12)	59.321(5)
0.117 (17)	3.89852 (18)	59.251 (8)			
			0.228 (4)	3.89642 (13)	59.156 (6)
			0.314 (4)	3.89524 (14)	59.102 (7)
			0.509 (4)	3.89239 (19)	58.973 (8)
0.557 (13)	3.89171 (15)	58.942 (7)	0.543 (4)	3.89245 (21)	58.975 (10)
			*0.810 (5)	3.88757 (21)	58.754 (10)
			0.852 (4)	3.88752 (14)	58.751 (7)
			*0.853 (6)	3.88739 (17)	58.746 (8)
			*0.879 (4)	3.88642 (17)	58.701 (8)
0.955 (42)	3.88496 (18)	58.635 (8)			
			1.223 (4)	3.88247 (16)	58.523 (7)
1.322 (81)	3.88092 (09)	58.453 (4)			
			1.646 (5)	3.87684 (18)	58.268 (8)
1.662 (87)	3.87659 (10)	58.257 (4)			
2.522 (24)	3.86661 (08)	57.809 (4)			
3.282 (41)	3.85700 (16)	57.379 (7)			
4.029 (139)	3.84819 (19)	56.986 (8)			
5.399 (41)	3.83352 (33)	56.337 (15)			

*decompression

[1] K. Datta, A. Richter, M. Göbbels, R. B. Neder, and B. Mihailova, Atomistic origin of huge response functions at the morphotropic phase boundary of (1−*x*)$Na_{0.5}Bi_{0.5}TiO_3$−*x*$BaTiO_3$, Phys. Rev. B **90**, 64112 (2014).

[2] OriginPro, Version 2021. OriginLab Corporation, Northampton, MA, USA.

[3] G. de La Flor, T. Malcherek, S. Gorfman, and B. Mihailova, Structural transformations in (1−*x*)$Na_{0.5}Bi_{0.5}TiO_3$−*x*$BaTiO_3$ single crystals studied by Raman spectroscopy, Phys. Rev. B **96**, 214102 (2017).

The high-pressure structure of (1-x)$Na_{0.5}Bi_{0.5}TiO_3$-$x$$BaTiO_3$ at the morphotropic phase boundary

Constanze Rösche[1,*], Tiziana Boffa Ballaran[2], Thomas Malcherek[1], Carsten Paulmann[1], Ross John Angel[3], Semën Gorfman[4], and Boriana Mihailova[1]

[1]Department of Earth System Sciences, Universität Hamburg, Grindelallee 48, 20146 Hamburg, Germany
[2]Bayerisches Geoinstitut, Universität Bayreuth, Universitätsstraße 30, 95447 Bayreuth, Germany
[3]Istituto di Geoscienze e Georisorse, CNR, Corso Stati Uniti 4, 35127 Padova, Italy
[4]Department of Materials Science and Engineering, Tel Aviv University, Wolfson Building for Mechanical Engineering, Tel Aviv 6997801, Israel
[*]constanze.roesche@uni-hamburg.de

ABSTRACT

The pressure-induced structural changes in the perovskite-type (ABO_3) ferroelectric solid solution (1-x)$Na_{0.5}Bi_{0.5}TiO_3$-$x$$BaTiO_3$ (NBT-xBT) at the morphotropic phase boundary (MPB) ($x_{MPB} = 0.048$) have been analyzed up to 12.3 GPa by single-crystal x-ray diffraction with synchrotron radiation. A pressure-induced phase transition takes place between 4.4 and 5.0 GPa, where the pseudocubic low-pressure phase transforms into an orthorhombic high-pressure phase with space group *Pnma*. The high-pressure phase is comprised of mixed BO_6 tilts and anti-polar A-cation displacements, without exhibiting coherent off-centered shifts of the B-site Ti^{4+} cations that can be detected by synchrotron x-ray diffraction. Our results reveal that at ambient pressure and room temperature the NBT-x_{MPB}BT structure possesses anti-phase BO_6 tilts with a relatively large correlation length and the same type of polar distortions as those present in pure NBT, but with strongly violated correlation length due to Ba^{2+}-induced local elastic-stress fields. For x_{MPB} the effect of Ba on the mesoscopic-scale structure is compensated by a mild external pressure of only 0.7 GPa, resulting in structural features resembling those of pure NBT at ambient conditions.

Introduction

The perovskite-type (ABO_3) solid solution (1-x)$Na_{0.5}Bi_{0.5}TiO_3$-$x$$BaTiO_3$ (NBT-xBT) is among the potential environmentally friendly alternatives to Pb-based ferroelectric materials. Single-crystal NBT-xBT exhibits a morphotropic phase boundary (MPB) at $x_{MPB} \sim 0.05$, across which the symmetry changes from rhombohedral to tetragonal and the material properties are enhanced[1].

The determination of the actual symmetry at the MPB is hindered by abundant nanoscale structural heterogeneities, which have been described as polar and/or antipolar nanoregions dispersed in a matrix of different symmetry[2,3] or as coexisting nanodomains of different symmetries[3,4], resulting in an overall cubic-like appearance of NBT-x_{MPB}BT[5,6]. The local structural distortions comprise off-centered shifts of A- and B-site cations[7] as well as octahedral tilts of rhombohedral and tetragonal type[4] ($a^-a^-a^-$ and $a^0a^0c^+$, Glazer notation[8]). Refinements to powder x-ray diffraction (XRD) data suggest that the symmetry of NBT-xBT ceramic samples at the MPB is $R3m$[9]. However, refinement parameters for $P4mm$ were almost equally good[9], and there is no single-crystal x-ray/neutron diffraction study confirming or refuting the proposed $R3m$ symmetry. Therefore, the symmetry of the NBT-xBT structure at the MPB is still an open question.

Structural distortions that correlate only on the mesoscopic scale can be analyzed via x-ray, neutron or electron diffuse scattering (DS). At ambient conditions the DS of NBT-xBT changes with composition. According to XRD analyses pure NBT exhibits two types of DS: L-shaped and ellipsoidal-like/T-shaped, both along the primitive cubic (pc) $\langle 100 \rangle_{pc}$ direction[10,11]. Considering an $hk0$ reciprocal-lattice layer, the L-shaped DS appears around $hk0$ Bragg reflections with both h and k nonzero, whereas the ellipsoidal-like/T-shaped DS appears around reflections with h or k equal to zero, i.e., $h00$, $0k0$. The DS extending along $\langle 100 \rangle_{pc}$ has been interpreted as being due to the existence of subordinate platelet-like tetragonal ($P4bm$) regions within the monoclinic/pseudorhombohedral (Cc/$R3c$) matrix[11–13]. The asymmetry of the DS has been attributed to the different charge environments of Bi^{3+} and Na^{+}[10], which, similar to the atomic size effect in disordered alloys, transfers DS intensity from one side of a Bragg peak to another, as a result of the large difference in scattering power of the two types of atoms and low degree of chemical order[14,15].

By increasing x up to $\sim$0.05[16] the L-shaped DS changes to ellipses elongated along the $\langle 110\rangle_{pc}$ directions, implying a change in the direction of mesoscopic-scale correlated cation shifts[11,17]. The same can be deduced from the x-induced transformation of the DS along $\langle 100\rangle_{pc}$ around $h00$ reflections into a butterfly-type with streaks along the $\langle 110\rangle_{pc}$ directions[2,11,16], indicating local-scale deviations from the average structure correlating within the $\{110\}_{pc}$ planes[18]. For $x \geq 0.11$ all types of DS are strongly reduced in intensity, as the whole structure adopts symmetry $P4mm$[11,12].

The Bragg-diffraction pattern of NBT-xBT with $x < 0.11$ is further characterized by the presence of superstructure reflections, indicating that the unit cell is actually doubled. In terms of a double perovskite cell, the superstructure reflections occur at h,k,l all odd (ooo) and/or two odd and one even (oee) and throughout this article we will use the Bragg-peak indices in a double perovskite cell. However, for better understanding of the origin of the superstructure reflections we will consider the first Brillouin zone of a standard single perovskite cell ($Pm\bar{3}m$): the ooo reflections are characteristic of distortions triggered by R-point phonon modes, whereas the ooe reflections correspond to distortions driven by M-point phonon modes[19]. In NBT-xBT these superstructure reflections are associated with the co-existence of alternating anti-phase $a^-a^-a^-$ and in-phase $a^0a^0c^+$ octahedral tilts[20] or with continuous mixed $a^-a^-c^+$ tilts having different coherence lengths of the out-of-phase and in-phase components[21]. For $x < x_{MPB}$ the dominant tilt pattern is anti-phase around all three fundamental crystallographic directions, while for $x > x_{MPB}$ in-phase tilting around only one direction prevails[11].

Analyzing the crystal structure at non-ambient conditions may help to better reveal the competing local distortions and consequently, to better understand the structure at ambient pressure and room temperature. In particular, XRD analyses under high pressure are challenging, but have been successfully performed on various ferroelectric and antiferroelectric materials[10,18,22–25]. Based on the results of previous studies on Pb-based relaxors, one may expect that the application of external pressure to perovskite-type ferroelectric solid solutions may enhance the octahedral tilting and antipolar displacements of A-site cations, while suppressing the B-cation off-centred shifts and dynamical disorder[26].

X-ray[10] and neutron diffraction[27] on pure NBT have shown that pressure induces a phase transition to an orthorhombic ($Pnma$) phase, which starts developing at 1.6 GPa, in coexistence with the low-pressure $R3c$ (or Cc) phase. Only above $\sim$4.0 GPa does the entire structure adopt the $Pnma$ symmetry, which is characterized by anti-polar order of A-cation displacements and mixed $a^-b^+a^-$ octahedral tilting (equivalent to $a^-a^-c^+$, but the in-phase tilting is along the **b** axis).

High-pressure Raman spectroscopy on NBT-0.048BT single crystals has revealed that between 1.0 and 4.8 GPa multi-step local-scale structural changes take place, which involve rearrangements of A-cations and the development of an octahedral tilt pattern with unequal tilts[28]. In-house XRD confirmed the occurrence of significant structural transformations above 4 GPa also on a long-range scale, but failed to resolve a symmetry lower than cubic at any pressure up to 6.1 GPa[28].

Thus, to elucidate the MPB structure of NBT-xBT, here we report the results of single-crystal synchrotron XRD at pressures from ambient up to 12.3 GPa. We show that a reversible phase transition from the pseudocubic low-pressure phase to an orthorhombic $Pnma$ high-pressure phase takes place at p_c = 4.6(1) GPa, with orthorhombic **a** and **c** axes along $\langle 110\rangle_{pc}$ and orthorhombic **b** axis $\parallel [001]_{pc}$. Similar to NBT, the high-pressure phase of NBT-x_{MPB}BT consists of mixed $a^-b^+a^-$ BO_6 tilting and antipolar order of A-cation shifts. The pressure dependence of x-ray DS (XDS) and superstructure Bragg-diffraction peaks demonstrates that at ambient conditions the NBT-x_{MPB}BT structure consists of the same type of polar distortions as those present in pure NBT, but their correlation length is strongly reduced by the Ba^{2+}-induced local elastic-stress fields, and that anti-phase $a^-a^-a^-$ BO_6-tilt order is the dominant tilt pattern at ambient and low pressures ($< p_c$).

Methods

Chemically homogeneous single crystals of (1-x)$Na_{0.5}Bi_{0.5}TiO_3$-$x$$BaTiO_3$ with $x = 0.048$ were synthesized by the top-seeded-solution-growth method[29]. The chemical composition was determined by wavelength-dispersive x-ray emission spectroscopy with uncertainty in x of ± 0.002[5]. The sample appears pseudocubic under in-house XRD examination with $a = b = c \approx$ 3.9 Å[5,28]. For the high-pressure experiments two specimens with a size of $\sim 90 \times 95 \times 40$ and $\sim 100 \times 110 \times 40$ µm cut parallel to one of the pseudocubic $\{100\}$ planes were used for two separate runs: up to 2.3 and 7.9 GPa, respectively. The samples were loaded in Boehler-Almax diamond anvil cells[30] (DACs) with a culet diameter of 600 µm using 200 and 390 µm thick rhenium gaskets with diameter of the drilled hole of 300 µm and a 4:1 methanol:ethanol mixture as a pressure transmitting medium . In addition, a specimen sized $\sim 40 \times 40 \times 30$ µm was loaded in a BX90 DAC with a culet diameter = 300 µm, using He as a pressure transmitting medium to ensure hydrostatic pressure in experiments above 10 GPa. The pressure in the sample chamber was determined using the ruby-line luminescence method[31].

To verify the reversibility of the pressure-induced structural changes the specimen subjected to 7.9 GPa was subsequently measured in air and compared with the data collected from a pristine crystal.

Synchrotron single-crystal XRD experiments were conducted at beamline P24/EH1 at DESY using a Huber four circle Kappa diffractometer equipped with a Pilatus 1M CdTe detector. The experiments were performed with a radiation wavelength of λ = 0.35424 Å and a sample-to-detector distance of 200 mm. For NBT-xBT the use of this high-energy beam (35 keV) ensures an absorption coefficient of $\sim$7 mm^{-1} and corresponding penetration depth of $\sim$140 µm so that the entire bulk of the

sample was probed. At each pressure three identical 70° phi scans were collected with a step width of 0.5° per frame and an exposure time of 3 s per frame, which was double-checked to be sufficient to avoid oversaturation of the strongest Bragg peaks. Intensities from the three scans were summed up in order to improve the signal-to-noise ratio and better reveal the XDS. The data were evaluated with the CrysAlisPro software package[32]. The structure of the high-pressure phase was refined using Jana2006[33].

Results and discussion

Due to the presence of superstructure reflections the Bragg peaks of the NBT-0.048BT crystal were indexed using a double cubic perovskite cell with the unit-cell parameter at atmospheric pressure $a_0 = 7.7997(4)$. Reconstructed $hk0$ and $hk1$ reciprocal-space layers of NBT-0.048BT at selected pressures up to 7.9 GPa are shown in Figs. 1 and 2. As pointed out above, the XDS scattering in the $hk0$ and $hk1$ layers is indicative of intermediate-range order of cationic off-center displacements and of octahedral tilts, respectively.

At ambient pressure the XDS around $hk0$ reflections with $h,k \neq 0$ has an ellipsoidal shape elongated along $\langle 110 \rangle_{pc}$ rather than an L-type shape as for pure NBT[10], while that around $h00$ and $0k0$ Bragg peaks exhibits a butterfly shape instead of ellipsoidal-like/T-shape along $\langle 100 \rangle_{pc}$. Thus, at ambient conditions XDS of NBT-0.048BT exhibits the same features as those observed for NBT-0.05BT[16] as well as for NBT-0.056BT[2], and resembles the XDS typical of Pb-based relaxor ferroelectrics[34]. This indicates that the presence of Ba with MPB concentrations ($x \sim 0.05$) results in nanoregions with cationic polar shifts correlated within $\{110\}_{pc}$ planes[34], which are surrounded by a pseudocubic polarizable matrix, in contrast to pure NBT, which has small platelets with correlated $\langle 100 \rangle_{pc}$ A-cation displacements dispersed in a rhombohedral/pseudorhombohedral matrix[10,11,35]. However, in the vicinity of {220} reflections there are satellite reflections along $\langle 100 \rangle$, which both have a similar intensity and are offset by ~0.3 and ~0.6 reciprocal lattice units (r.l.u.). Most probably those satellite reflections are due to an incommensurate modulated structure on a length scale of approximately three times the double cubic structure (~24 Å); similar modulated structures with a different periodicity have been also observed for pure NBT and NBT-0.04BT[36,37].

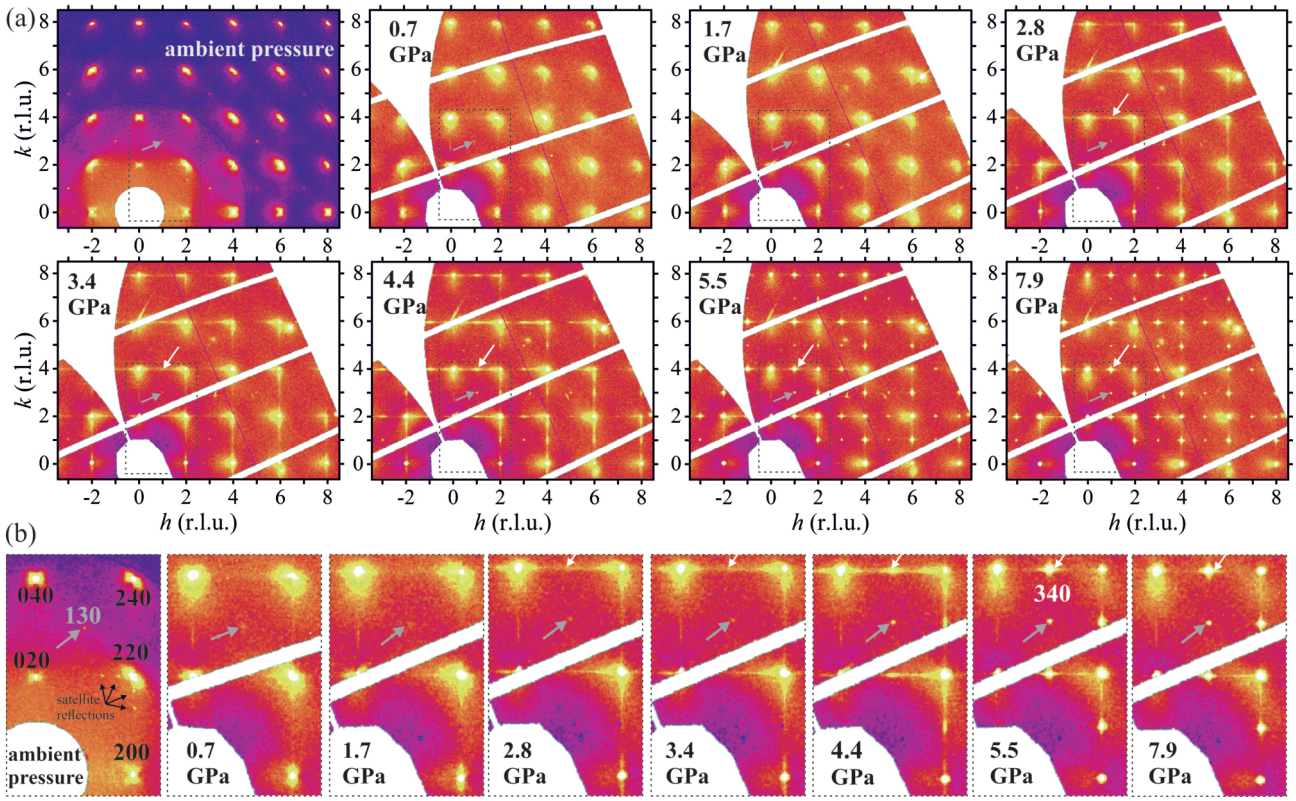


Figure 1. $hk0$ reciprocal space layers of NBT-0.048BT at selected pressures from ambient pressure to 7.9 GPa. The areas marked with a dashed rectangle in (**a**) are shown enlarged in (**b**). The reflections are indexed in a doubled cubic perovskite cell. The grey and white arrows mark representative *ooe* and *oee* reflections, respectively, while the black arrows point to the satellite reflections visible around {220} reflections in the data measured at ambient pressure in air.

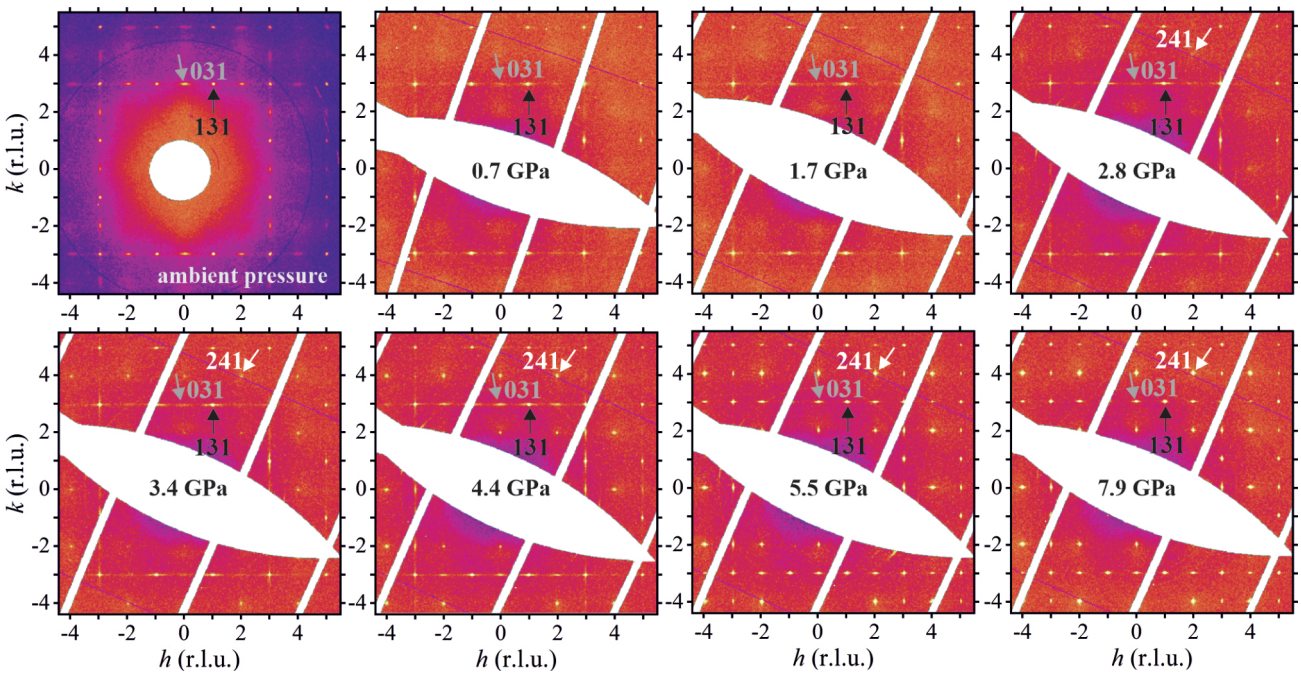


Figure 2. *hk*1 reciprocal space layers of NBT-0.048BT at selected pressures from ambient pressure to 7.9 GPa. The reflections are indexed in a doubled cubic perovskite cell. The black, grey and white arrows mark representative *ooo*, *ooe* and *oee* reflections, respectively.

Upon pressure increase the XDS in the *hk*0 layer changes, and at moderate pressures between 0.7 and 2.8 GPa it resembles that of pure NBT at atmospheric pressure and room temperature. This shows that external hydrostatic pressure reverses the effect of chemically-induced internal local-stress fields related to the incorporation of large-size Ba^{2+} at the A site[38]. The XDS of pure NBT originates from planar nanoregions with correlated $\langle 100 \rangle_{pc}$ shifts of A-site Na^{+} and Bi^{3+} cations within the pseudorhombohedral matrix, analogous to Guinier-Preston zones[10,37]. Apparently, moderate external hydrostatic pressure reinforces this structural state also in NBT-0.048BT, overcoming the chemical effect of embedded Ba^{2+} cations. This suggests how Ba doping modifies the NBT-*x*BT structure at ambient conditions. Since the applied external pressure is isotropic, it seems unlikely to be able to change the preferred direction of polar cationic shifts within the nanodomains, while at the same time suppressing the polar long-range order in the matrix. A more plausible scenario is that at MPB concentrations barium enters both the pseudorhombohedral matrix and tetragonal nanoregions, disturbing the correlation length of coherent cationic shifts in both the pseudorhombohedral matrix and tetragonal-type platelet zones. This results in a pseudocubic matrix of uncorrelated polar distortions, which can mutually align under an externally applied electric field[37,39] , i.e. at the MPB the matrix is polarizable, as in the case of Pb-based relaxor ferroelectrics[40–42]. Remnants of pseudorhombohedral regions, stemming from the matrix, are still preserved, which give rise to the $\langle 110 \rangle_{pc}$ oval-shape XDS. Due to the shrinking volume, external pressure overcomes the internal local elastic stresses in the vicinity of the A-site Ba^{2+}, leading to an increase in the correlation length between tetragonal-type off-center shifts as well as between local distortions of pseudorhombohedral type, which is shown by the increasing intensity and sharpness of the diffuse scattering (Figs. 1 and 2).

The satellite reflections arising from modulated structures are not observed at elevated pressures. Unfortunately it is unclear whether they are suppressed by pressure or they are just too weak to be measured inside a DAC.

At 3.4-4.4 GPa the diffuse scattering streaks in the *hk*0 layers of NBT-0.048BT have reached their maximum length and strong but still diffuse scattering appears between adjacent *ee*0 Bragg reflections (see white arrows in Fig. 1a and b), which is a precursor of new *oee* Bragg reflections that appear above 5 GPa. At 5.5 GPa the XDS is strongly reduced. However, there are still remnants of the $\langle 100 \rangle_{pc}$ streaks, indicating that on a mesoscopic scale there is still a small fraction of tetragonal-type nanoregions that differ from the average high-pressure phase. The broad diffuse scattering at the lower-θ-angle side of *eee* reflections (see e.g. 040 in Fig. 1), which results from the unequal scattering power of chemically disordered A-site Bi^{3+} and Na^{1+} cations[10,14,15], is better seen at high pressures due to the suppression of the L-shaped XDS; this type of XDS persists at all pressures due to its chemical origin.

The pressure dependence of the superstructure reflections gives information on the evolution of the octahedral tilt pattern. The *R*-point reflections (*ooo*) are systematically stronger than the *M*-point reflections (*ooe*); they appear clear and sharp, and

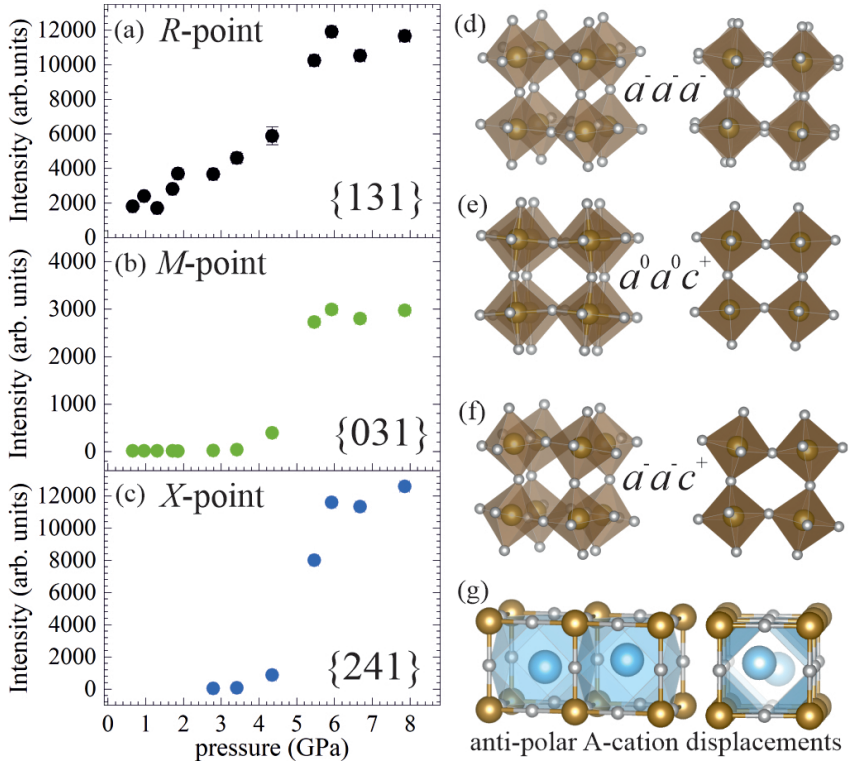


Figure 3. Pressure dependence of the integrated intensities of representative *ooo* (**a**), *ooe* (**b**) and *oee* (**c**) reflections. The intensities are averaged over all peaks, which are symmetry-equivalent with the indices referring to the doubled pseudocubic unit cell. The octahedral tilting patterns relevant for NBT-0.48BT are shown in (**d**)-(**f**): pure anti-phase BO_6 tilting ($a^-a^-a^-$), in-phase tilting around one axis ($a^0a^0c^+$) and mixed tilting ($a^-a^-c^+$); right-hand-side plots are viewed along $[001]_{pc}$. A sketch of anti-polar A-cation displacements is shown in (**g**); for the sake of clarity the magnitude of the displacements is exaggerated. Figures (**d**)-(**g**) were prepared using VESTA[43].

increase in intensity in the whole pressure range measured (Fig. 3a). In contrast, the *M*-point reflections appear as diffuse short streaks that are elongated in ⟨100⟩ directions and have a very low intensity up to 3.4 GPa, just above $3\sigma(I)$, where $\sigma(I)$ is the estimated uncertainty of the integrated intensity. Only above 4.4 GPa does the intensity of the diffraction around the *M*-point increase strongly in intensity (Fig. 3b). These observations unambiguously confirm the dominance of the anti-phase $a^-a^-a^-$ octahedral tilt pattern (Fig. 3d) over in-phase $a^0a^0c^+$ tilting (Fig. 3e) at ambient and low pressure, which above 4 GPa evolves into a pattern of unequal BO_6 tilts, as suggested on the basis of Raman scattering analyses[28]. Precursor *oee* signals are observed already above 2.8 GPa, but they evolve into strong and sharp Bragg diffraction peaks only at 5.5 GPa (Fig. 3c). Bragg reflections of *oee* type are characteristic of distortions triggered by *X*-point phonons of the primitive cubic cell. The *oee* Bragg-diffraction maxima are significantly stronger than the *ooe* peaks, indicating that the *X*-point distortion involves A-site cationic off-centered displacements[19,44]. Hence, the co-appearance of *M*- and *X*-point reflections, along with the pre-existing *R*-point reflections, reveals a change in the octahedral tilt pattern from anti-phase to mixed (Figs. 3d, f), accompanied by the development of antipolar long-range order of A-cation shifts (Fig. 3g)[19,44].

Even though no splitting of any of the cubic Bragg peaks is observed, the additional reflections and the disappearance of most of the diffuse scattering at 5.5 GPa clearly show that a phase transition has taken place. The set of data collected in He (at 5.0, 8.1 and 12.3 GPa) indicates that at 5.0 GPa the phase transition has already occurred, and there are no further phase transitions detected up to 12.3 GPa, as no additional peaks appear at 8.1 and 12.3 GPa (see Supplementary Fig. S3 online). However, due to smaller crystal size and different experimental conditions the integrated intensities of the He data set are not included in Fig. 3.

Structure refinements of the high-pressure phase are consistent with the orthorhombic space group *Pnma* (see Fig. 4), which was also found to be the symmetry to develop in pure NBT above ~2 GPa[27]. The intensities used for the refinements with Jana2006[33] were integrated with CrysAlisPro[32] using the doubled cubic unit cell, since the orthorhombic distortion of the crystal is very small. A detailed description of the refinement details is given in the supplementary material. The unit

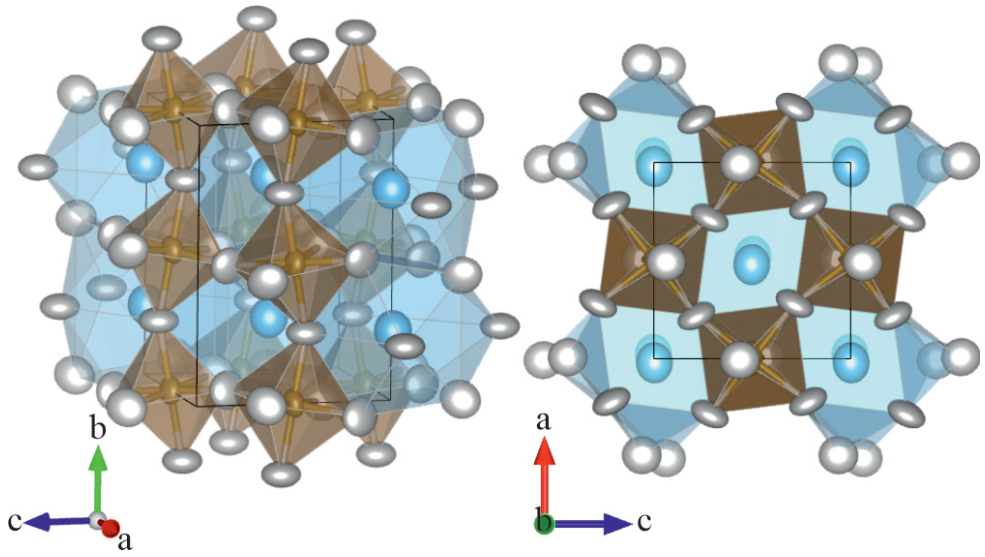


Figure 4. The high-pressure structure of NBT-0.048BT at 7.9 GPa refined in orthorhombic space group *Pnma*. AO_{12} polyhedra are shown in blue, BO_6 octahedra in brown and oxygen atoms in white. All atoms are displayed as displacement ellipsoids. The corresponding refinement results are listed in Supplementary Table S3-S5 online. This figure was prepared using VESTA[43].

cell and refinement parameters of NBT-0.048T at 4.4-8.1 GPa are listed in Supplementary Table S3 online. At 12.3 GPa no successful structure refinement could be achieved due to poor data quality. However, the reconstructed *hkl* layers indicate that the symmetry should still be the same (see Supplementary Fig. S3 online). The higher *R*-value ($R > 5\%$) and goodness of fit (GoF = 1.26) for the refinements at 4.4 GPa show that the structure has not fully adopted the *Pnma* symmetry yet. This is also seen in the high U_{eq} values of Bi/Na and O1 atoms, which indicate that the symmetry imposed during refinement prevents the atomic positions from being determined correctly. Also the presence of strong diffuse scattering in the reconstructed layers of the reciprocal space at 4.4 GPa (see Fig. 1 and 2) shows that the phase transition has not been completed yet. The same is seen when considering the pressure dependence of the integrated intensities (Fig. 3a-c), which shows an abrupt increase in intensity between 4.4 and 5.5 GPa. The structure refinements in *Pnma* for the data sets collected below 4.4 GPa only yielded unsatisfactory *R*-values. Hence, the low-pressure phase is pseudocubic although its structural features include octahedral tilts and A-cation polar shifts correlated at the mesoscopic scale. The unit cell parameters of the low pressure data are reported in Supplementary Table S2 online.

Figure 5a shows the pressure dependence of the off-centering of the AO_{12} polyhedra, calculated as the difference between the cation coordinates and the averaged oxygen coordinates $\vec{\delta}_A = \vec{r}_A - \frac{1}{12} \times \sum_{i=1}^{12} \vec{r}_{iO}$[45], where $\vec{r}$ refers to the corresponding position vector. In the *Pnma* phase the A-cations are only allowed to be off-set along **a** and **c** and the results show that above the phase-transition pressure the A-cation off-centering along the **a** axis significantly exceeds that along the **c** axis (Fig. 5a). The pressure dependence of the squared octahedral tilting angles $\varphi^2 = [(180 - \angle B' - O - B'')/2]^2$ calculated from the refined atomic structures above 4 GPa is shown in Fig. 5b . A simplified model using a Boltzmann growth function to fit the $\vec{\delta}_A(p)$ and $\varphi^2(p)$ data points reveals an inflection point of 4.6(1) GPa, suggesting that this is the phase transition pressure (p_c). However the subtle but steady increase of $\vec{\delta}_A$ and φ^2 above ~5.0 GPa indicates that pressure continues to enhance the tilting of BO_6 octahedra and off-centering of A-cations. It should be noted that in *Pnma* the Ti^{4+} cations are constrained to the centre of BO_6 octahedra. On the other hand, the Raman scattering analysis of NBT-0.048BT indicates that the B-site off-centered shifts, although reduced, persist up to ~9 GPa[28]. Therefore, the high-pressure phase of NBT-0.048BT should still comprise Ti^{4+} polar displacements, which however are uncorrelated and therefore, undetectable by XRD.

On decompression the pressure-induced structural changes in NBT-0.048BT reverse, but the XRD pattern typical of the NBT-x_{MPB}BT structural state at ambient conditions was reestablished only after a prolonged period of time (at least a few hours). Given that the *in situ* high-pressure Raman-scattering experiments indicate that the local-scale structure recovers immediately[28], this suggests that the dominant phase-transition mechanism is order-disorder rather than displacive, as the system needs a prolonged relaxation time to reach a thermodynamic equilibrium after the pressure release, with a structural state comprising abundant uncorrelated local ferroic distortions.

Structure data for the high-pressure phase of pure NBT at 4.0-9.7 GPa have been published by Thomas et al. 2005[27]. Within

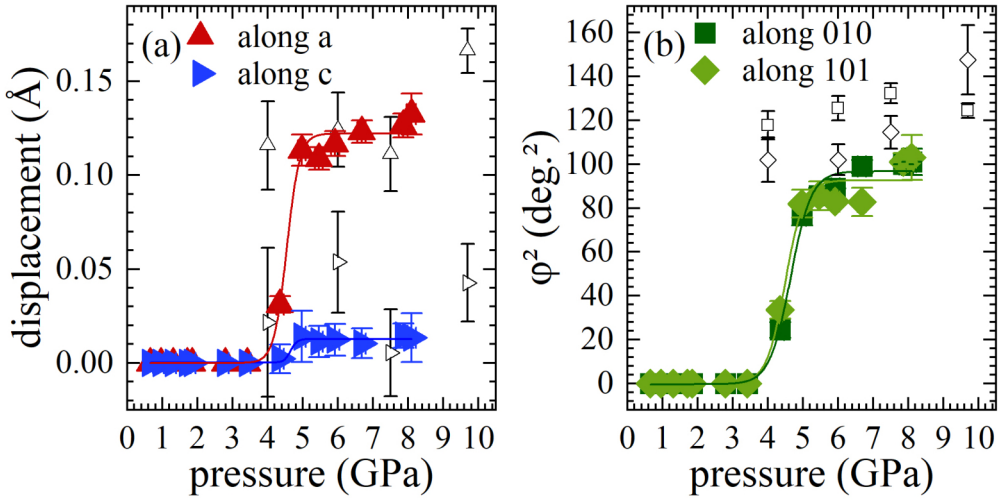


Figure 5. A-cation off-centering displacements $\vec{\delta}_A$ (**a**) and squared octahedral tilting angles φ^2 (**b**). Filled symbols represent data on NBT-0.048BT from this study, assuming cubic structure below 4.4 GPa; lines are Boltzmann growth-function fits to the data points. Open symbols represent data derived from structure refinements on pure NBT by Thomas et al. 2005[27].

uncertainties, there is no clear difference between the calculated $\vec{\delta}_A$ for the high-pressure phase of NBT and NBT-0.048BT (Fig. 5a). The equivalent isotropic atomic displacement parameters (U_{eq}) of the Bi/Na-atoms for pure NBT are lower at all reported pressures than those we obtained from our structure refinements for NBT-0.048BT (0.019(1)-0.010(1) Å^2 vs. 0.032(1)-0.026(1) Å^2) (see Supplementary Table S4 online). The U_{eq} parameters of Ti are in the same order of magnitude (0.006(1)-0.015(1) for $x = 0$ vs. 0.012(3)-0.013(4) Å^2 for $x = 0.048$), indicating that the different A-cation U_{eq} should not be due to different experimental conditions. The increased A-cation U_{eq} in NBT-0.048BT can be explained by substitutional disorder induced by Ba^{2+} cations, which have a larger ionic radius than Bi^{3+} and Na^+ cations (1.61 Å vs. 1.45 and 1.39 Å). In addition, the larger U_{eq} may imply that not only the fraction of off-centered A-cations is increased in the Ba-doped compound (as indicated by Raman spectroscopy[28]), but also the dynamical disorder, i.e. the amplitude of atomic vector displacements of the off-centered A-site cations is higher compared to pure NBT. The octahedral tilt angle φ of the high-pressure phase of pure NBT[27] tends to be higher than that of NBT-0.048BT (Fig. 5b). This indicates that the presence of large-sized Ba cations restrains the tilting of BO_6 octahedra not only in terms of the correlation length as at low pressure, but also in terms of the degree of tilting in the high-pressure phase.

Conclusions

Under hydrostatic pressure, the MPB-compound NBT-0.048BT undergoes a reversible phase transition at $p_c = 4.6(1)$ GPa, with a predominantly order-disorder character. The high-pressure phase is orthorhombic *Pnma* and comprises anti-polar A-cation displacements predominantly along the *a*-axis (corresponding to the $[110]_{pc}$ direction), mixed BO_6 tilts of type $a^-b^+a^-$, (the **b**-axis corresponding to the $[001]_{pc}$ direction), and uncorrelated, reduced in magnitude, polar B-cation shifts.

The pressure evolution of the XDS below p_c indicates that at MPB levels of Ba concentration, the Ba^{2+} cations are embedded in both the pseudorhombohedral matrix and tetragonal-like nanoregions, which violates the correlation length of coherent A-site cations in both the matrix and nanoregions and results in a pseudocubic polarizable matrix with remnants of rhombohedral-like polar clusters. Our data indicate that for $x = x_{MPB}$, the effect of chemically-induced local internal stress fields due to the incorporation of Ba^{2+} cations can be overcome by a mild external hydrostatic pressure of 0.7 GPa.

The relative intensities of the superstructure diffraction scattering below p_c reveals that the anti-phase $a^-a^-a^-$ BO_6-tilt order is the dominant tilt pattern at ambient pressure and room temperature.

Data availability

Crystallographic Information Files (CIFs) are included as supplementary. All other datasets generated and analysed during this study are available from the corresponding author on reasonable request.

References

1. Zhang, Q., Zhao, X., Sun, R. & Luo, H. Crystal growth and electric properties of lead–free NBT–BT at compositions near the morphotropic phase boundary. *Phys. Status Solidi (a)* **208**, 1012–1020, DOI: 10.1002/pssa.201000052 (2011).
2. Ge, W. *et al.* Direct evidence of correlations between relaxor behavior and polar nano-regions in relaxor ferroelectrics: A case study of lead-free piezoelectrics $Na_{0.5}Bi_{0.5}TiO_3 - x\%BaTiO_3$. *Appl. Phys. Lett.* **103**, DOI: 10.1063/1.4846655 (2013).
3. Liu, H., Zhang, Q., Luo, H. & Zhu, J. Direct observations of electric-field-induced domain switching and phase transition in $0.95Na_{0.5}Bi_{0.5}TiO_3$-$0.05BaTiO_3$ single crystals using in situ transmission electron microscopy. *Appl. Phys. Lett.* **120**, DOI: 10.1063/5.0083165 (2022).
4. Ma, C., Tan, X., Dul'kin, E. & Roth, M. Domain structure-dielectric property relationship in lead-free $(1-x)(Bi_{1/2}Na_{1/2})TiO_3 - xBaTiO_3$ ceramics. *J. Appl. Phys.* **108**, DOI: 10.1063/1.3514093 (2010).
5. de La Flor, G., Malcherek, T., Gorfman, S. & Mihailova, B. Structural transformations in $(1-x)Na_{0.5}Bi_{0.5}TiO_3 - xBaTiO_3$ single crystals studied by Raman spectroscopy. *Phys. Rev. B* **96**, DOI: 10.1103/PhysRevB.96.214102 (2017).
6. Ranjan, R. & Dviwedi, A. Structure and dielectric properties of $(Na_{0.50}Bi_{0.50})_{1-x}Ba_xTiO_3$: $0 \leq x \leq 0.10$. *Solid State Commun.* **135**, 394–399, DOI: 10.1016/j.ssc.2005.03.053 (2005).
7. Jones, G. O. & Thomas, P. A. Investigation of the structure and phase transitions in the novel A-site substituted distorted perovskite compound $Na_{0.5}Bi_{0.5}TiO_3$. *Acta Crystallogr. Sect. B, Struct. Sci.* **58**, 168–178, DOI: 10.1107/S0108768101020845 (2002).
8. Glazer, A. M. The classification of tilted octahedra in perovskites. *Acta Crystallogr. Sect. B Struct. Crystallogr. Cryst. Chem.* **28**, 3384–3392, DOI: 10.1107/S0567740872007976 (1972).
9. Jo, W. *et al.* Evolving morphotropic phase boundary in lead-free $(Bi_{1/2}Na_{1/2})TiO_3$-$BaTiO_3$ piezoceramics. *J. Appl. Phys.* **109**, DOI: 10.1063/1.3530737 (2011).
10. Kreisel, J. *et al.* High-pressure x-ray scattering of oxides with a nanoscale local structure: Application to $Na_{0.5}Bi_{0.5}TiO_3$. *Phys. Rev. B* **68**, DOI: 10.1103/PhysRevB.68.014113 (2003).
11. Tung, P. K., Major, M., Hudspeth, J. & Daniels, J. E. Compositional dependence of disordered structures in $Na_{1/2}Bi_{1/2}TiO_3$-$BaTiO_3$ solid solutions. *Mater. Res. Bull.* **106**, 301–306, DOI: 10.1016/j.materresbull.2018.06.019 (2018).
12. Thomas, P. A., Trujillo, S., Boudard, M., Gorfman, S. & Kreisel, J. Diffuse X-ray scattering in the lead-free piezoelectric crystals $Na_{1/2}Bi_{1/2}TiO_3$ and Ba-doped $Na_{1/2}Bi_{1/2}TiO_3$. *Solid State Sci.* **12**, 311–317, DOI: 10.1016/j.solidstatesciences.2009.06.008 (2010).
13. Beanland, R. & Thomas, P. A. Imaging planar tetragonal sheets in rhombohedral $Na_{0.5}Bi_{0.5}TiO_3$ using transmission electron microscopy. *Scripta Materialia* **65**, 440–443, DOI: 10.1016/j.scriptamat.2011.05.031 (2011).
14. Warren, B. E., Averbach, B. L. & Roberts, B. W. Atomic size effect in the x-ray scattering by alloys. *J. Appl. Phys.* **22**, 1493–1496, DOI: 10.1063/1.1699898 (1951).
15. Welberry, T. R. Multi-site correlations and the atomic size effect. *J. Appl. Crystallogr.* **19**, 382–389, DOI: 10.1107/S0021889886089185 (1986).
16. Luo, C. *et al.* Neutron and x-ray scattering study of phonon dispersion and diffuse scattering in $(Na,Bi)TiO_3 - xBaTiO_3$ single crystals near the morphotropic phase boundary. *Phys. Rev. B* **96**, DOI: 10.1103/PhysRevB.96.174108 (2017).
17. Zhang, H. *et al.* Neutron diffuse scattering of $(1-x)(Na_{0.5}Bi_{0.5})TiO_3 - xBaTiO_3$ relaxor ferroelectric single crystals. *Scripta Materialia* **86**, 5–8, DOI: 10.1016/j.scriptamat.2014.04.011 (2014).
18. Chaabane, B., Kreisel, J., Dkhil, B., Bouvier, P. & Mezouar, M. Pressure-induced suppression of the diffuse scattering in the model relaxor ferroelectric $PbMg_{1/3}Nb_{2/3}O_3$. *Phys. Rev. Lett.* **90**, 257601, DOI: 10.1103/PhysRevLett.90.257601 (2003).
19. Maier, B. J. *et al.* Structural state of relaxor ferroelectrics $PbSc_{0.5}Ta_{0.5}O_3$ and $PbSc_{0.5}Nb_{0.5}O_3$ at high pressures up to 30 GPa. *Phys. Rev. B* **84**, DOI: 10.1103/PhysRevB.84.174104 (2011).
20. Dorcet, V. & Trolliard, G. A transmission electron microscopy study of the A-site disordered perovskite $Na_{0.5}Bi_{0.5}TiO_3$. *Acta Materialia* **56**, 1753–1761, DOI: 10.1016/j.actamat.2007.12.027 (2008).
21. Levin, I. & Reaney, I. M. Nano– and mesoscale structure of $Na_{0.5}Bi_{0.5}TiO_3$: A TEM perspective. *Adv. Funct. Mater.* **22**, 3445–3452, DOI: 10.1002/adfm.201200282 (2012).
22. Ravy, S., Itié, J.-P., Polian, A. & Hanfland, M. High-pressure study of x-ray diffuse scattering in ferroelectric perovskites. *Phys. Rev. Lett.* **99**, 117601, DOI: 10.1103/PhysRevLett.99.117601 (2007).

23. Knyazeva, M. A. *et al.* Phase transitions in lead hafnate under high pressure. *Phys. Solid State* **61**, 1759–1765, DOI: 10.1134/S1063783419100202 (2019).

24. Kobayashi, Y. *et al.* X-ray diffraction and dielectric measurements on $PbZrO_3$ at high pressure: a phase transformation study. *J. Phys. Chem. Solids* **60**, 57–64, DOI: 10.1016/S0022-3697(98)00240-6 (1999).

25. Ahart, M. *et al.* Structural transitions in $Pb(In_{1/2}Nb_{1/2})O_3$ under pressure. *J. Adv. Dielectr.* **05**, 1550033, DOI: 10.1142/S2010135X15500332 (2015).

26. Mihailova, B. *et al.* The structural state of lead-based relaxor ferroelectrics under pressure. *IEEE Transactions on Ultrason. Ferroelectr. Freq. Control.* **58**, 1905–1913, DOI: 10.1109/TUFFC.2011.2030 (2011).

27. Thomas, P. A. *et al.* The high-pressure structural phase transitions of sodium bismuth titanate. *Zeitschrift für Kristallographie - Cryst. Mater.* **220**, 717–725, DOI: 10.1524/zkri.220.8.717.67071 (2005).

28. Rösche, C., Boffa-Ballaran, T. & Mihailova, B. Pressure-induced structural transformations in (1-x)$Na_{0.5}Bi_{0.5}TiO_3$−$xBaTiO_3$ at the morphotropic phase boundary. *Phys. Rev. B* **108**, DOI: 10.1103/PhysRevB.108.094110 (2023).

29. Woll, M., Burianek, M., Klimm, D., Gorfman, S. & Mühlberg, M. Characterization of $(Bi_{0.5}Na_{0.5})_{1-x}BaTiO_3$ grown by the TSSG method. *J. Cryst. Growth* **401**, 351–354, DOI: 10.1016/j.jcrysgro.2013.11.102 (2014).

30. Boehler, R. & de Hantsetters, K. New anvil designs in diamond-cells. *High Press. Res.* **24**, 391–396, DOI: 10.1080/08957950412331323924 (2004).

31. Shen, G. *et al.* Toward an international practical pressure scale: A proposal for an IPPS ruby gauge (IPPS-ruby2020). *High Press. Res.* **40**, 299–314, DOI: 10.1080/08957959.2020.1791107 (2020).

32. Agilent. *CrysAlis PRO*, Agilent Technologies Ltd, Yarnton, Oxfordshire, England (2014).

33. Petříček, V., Dušek, M. & Palatinus, L. Crystallographic computing system JANA2006: General features. *Zeitschrift für Kristallographie - Cryst. Mater.* **229**, 345–352, DOI: 10.1515/zkri-2014-1737 (2014).

34. Paściak, M., Wołcyrz, M. & Pietraszko, A. Interpretation of the diffuse scattering in Pb-based relaxor ferroelectrics in terms of three-dimensional nanodomains of the ⟨110⟩-directed relative interdomain atomic shifts. *Phys. Rev. B* **76**, DOI: 10.1103/PhysRevB.76.014117 (2007).

35. Gorfman, S., Keeble, D. S., Bombardi, A. & Thomas, P. A. Topology and temperature dependence of the diffuse X-ray scattering in $Na_{0.5}Bi_{0.5}TiO_3$ ferroelectric single crystals. *J. Appl. Crystallogr.* **48**, 1543–1550, DOI: 10.1107/S160057671501571X (2015).

36. Balagurov, A. M. *et al.* The rhombohedral phase with incommensurate modulation in $Na_{1/2}Bi_{1/2}TiO_3$. *Phase Transitions* **79**, 163–173, DOI: 10.1080/01411590500496238 (2006).

37. Daniels, J. E., Jo, W. & Donner, W. High-energy synchrotron x-ray diffraction for in situ diffuse scattering studies of bulk single crystals. *JOM* **64**, 174–180, DOI: 10.1007/s11837-011-0230-z (2012).

38. Welsch, A.-M. *et al.* Effect of Ba incorporation on pressure-induced structural changes in the relaxor ferroelectric $PbSc_{0.5}Ta_{0.5}O_3$. *Phys. Rev. B* **80**, DOI: 10.1103/PhysRevB.80.104118 (2009).

39. de La Flor, G., Gorfman, S. & Mihailova, B. Local-scale structural response of (1-x)$Na_{0.5}Bi_{0.5}TiO_3 - xBaTiO_3$ to external electric fields. *Appl. Phys. Lett.* **114**, DOI: 10.1063/1.5070118 (2019).

40. Blinc, R. *et al.* ^{207}Pb NMR study of the relaxor behavior in $PbMg_{1/3}Nb_{2/3}O_3$. *Phys. Rev. B* **63**, DOI: 10.1103/PhysRevB.63.024104 (2000).

41. Bokov, A. A. & YE, Z.-G. Dielectric relaxation in relaxor ferroelectrics. *J. Adv. Dielectr.* **2**, 1241010, DOI: 10.1142/S2010135X1241010X (2012).

42. Mihailova, B., Maier, B. J., Steilmann, T., Dul'kin, E. & Roth, M. Electric-field-induced local structural phenomena in Pb-based ABO_3-type relaxor ferroelectrics. *IEEE Transactions on Ultrason. Ferroelectr. Freq. Control.* **62**, 7–17, DOI: 10.1109/tuffc.2014.006669 (2015).

43. Momma, K. & Izumi, F. Vesta 3 for three-dimensional visualization of crystal, volumetric and morphology data. *J. Appl. Crystallogr.* **44**, 1272–1276, DOI: 10.1107/S0021889811038970 (2011).

44. Woodward, D. I. & Reaney, I. M. Electron diffraction of tilted perovskites. *Acta Crystallogr. Sect. B, Struct. Sci.* **61**, 387–399, DOI: 10.1107/S0108768105015521 (2005).

45. Datta, K., Margaritescu, I., Keen, D. A. & Mihailova, B. Stochastic polarization instability in $PbTiO_3$. *Phys. Rev. Lett.* **121**, 137602, DOI: 10.1103/PhysRevLett.121.137602 (2018).

Acknowledgements

The authors thank Dr. Alexander Kurnosov, Bayerisches Geoinstitut, Universität Bayreuth, for help with DAC loading. Financial support by the Deutsche Forschungsgemeinschaft (No. MI 1127/12-1 and No. BO 2550/10-1) is gratefully acknowledged. We acknowledge DESY (Hamburg, Germany), a member of the Helmholtz Association HGF, for the provision of experimental facilities. Experiments were carried out at PETRA III using beamline P24 (beamtime allocated to project I-20220769); pressure was measured using the facilities at the P02.2 beamline.

Author contributions statement

B.M. and T.B. developed the original project. S.G. provided the single crystals. C.R., T.B., T.M., C.P., R.J.A. and B.M. carried out the single-crystal X-ray diffraction experiments. C.R. evaluated the data. C.R. and B.M. wrote the manuscript. All authors reviewed and edited the manuscript.

Funding

Open Access funding enabled and organized by Projekt DEAL. We acknowledge financial support from the Open Access Publication Fund of Universität Hamburg.

Competing interests

The authors declare no competing interests.

Supplementary Material for The high-pressure structure of (1-x)$Na_{0.5}Bi_{0.5}TiO_3$-$x$$BaTiO_3$ at the morphotropic phase boundary

Constanze Rösche[1,*], Tiziana Boffa Ballaran[2], Thomas Malcherek[1], Carsten Paulmann[1], Ross John Angel[3], Semën Gorfman[4], and Boriana Mihailova[1]

[1]Department of Earth System Sciences, Universität Hamburg, Grindelallee 48, 20146 Hamburg, Germany
[2]Bayerisches Geoinstitut, Universität Bayreuth, Universitätsstraße 30, 95447 Bayreuth, Germany
[3]Istituto di Geoscienze e Georisorse, CNR, Corso Stati Uniti 4, 35127 Padova, Italy
[4]Department of Materials Science and Engineering, Tel Aviv University, Wolfson Building for Mechanical Engineering, Tel Aviv 6997801, Israel
*constanze.roesche@uni-hamburg.de

Technical details of the structure refinement

The intensities used for the refinements with Jana2006[1] were integrated with CrysAlisPro[2] using the doubled cubic unit cell. The entire diffraction pattern could be indexed with a single orientation matrix. The refinements are based on the squared structure factor F^2. It was taken into account that the crystal actually consists of twin domains of lower symmetry, which all contribute with an intensity proportional to their fraction to the resulting pseudocubic diffraction pattern. Therefore 6 twin domains are included in the refinement model (see Table S1), which matches the number of possible ferroic domains due to centrosymmetrical distortion of the cubic perovskite cell along $\langle 110 \rangle$. Unit cell parameters and statistical values are reported in Table S3. The site occupation factor of Bi and Na has been fixed to 0.5 and both atoms have been restricted to have the same coordinates and anisotropic displacement parameters (ADPs). The contribution of A-site Ba has been neglected due to its small fraction in the structure (x=0.048). At 5.9-7.9 GPa the displacement parameters were refined anisotropic for all atoms. The fractional atomic coordinates and isotropic displacement parameters equivalent to the refined ADPs, U_{eq}, are reported in Table S4. At 4.4 GPa the displacement parameter of Ti had to be restrained to be isotropic in order to obtain a reasonable value. For the He data set also the oxygen atoms were refined as isotropic at 5.0 and 8.1 GPa due to poorer quality of data.

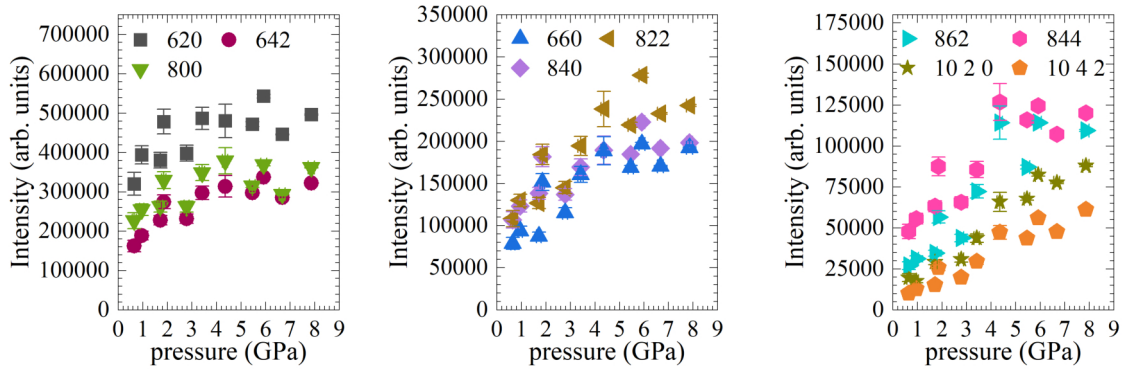


Figure S1. Pressure dependence of the integrated intensities of *eee* reflections of type $h+k+l=4n$. The intensities are averaged over all peaks, which are symmetry-equivalent with the indices referring to the doubled pseudocubic unit cell.

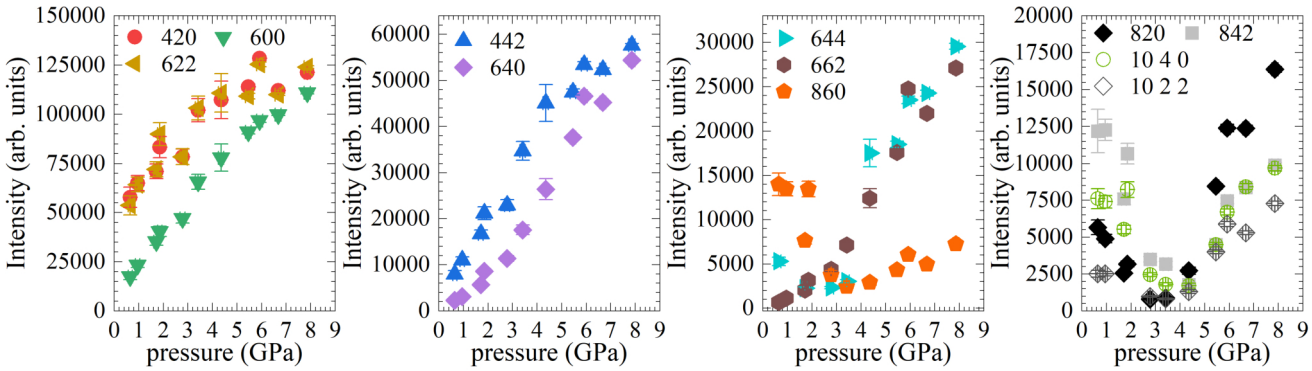


Figure S2. Pressure dependence of the integrated intensities of representative *eee* reflections of type $h+k+l = 4n+2$. The intensities are averaged over all peaks, which are symmetry-equivalent with the indices referring to the doubled pseudocubic unit cell.

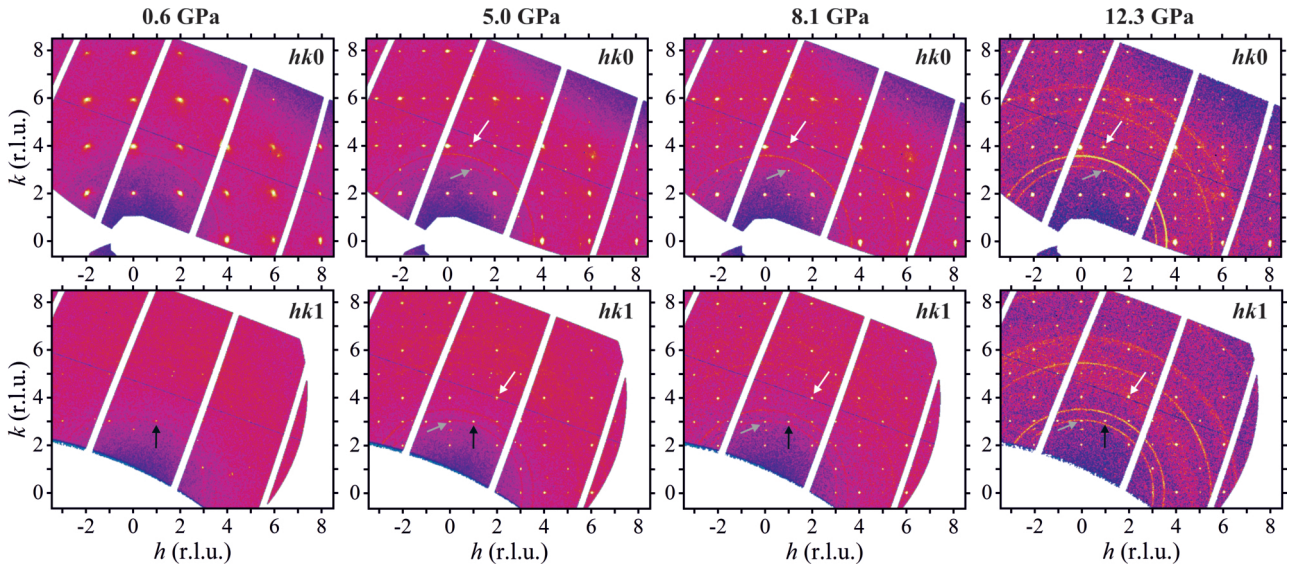


Figure S3. *hk*0 and *hk*1 reciprocal space layers of NBT-0.048BT from the data set measured in Helium at 0.6 to 12.3 GPa. The reflections are indexed in a doubled cubic perovskite cell. The black, grey and white arrows mark representative *ooo*, *ooe* and *oee* reflections, respectively.

Table S1. Twin domains used for the structure refinements at 4.4-8.1 GPa. The rotation axes of the twinning operations in the orthorhombic symmetry are parallel to the edge and the body diagonals of a cubic unit cell. The volume fractions of the twins composing the sample stem from the refinements in Jana2006[1]. The uncertainty for the main twin (tw1) is calculated as $\sigma(\text{tw1vol}) = \sqrt{\sigma(\text{tw2vol})^2 + \sigma(\text{tw3vol})^2 + \sigma(\text{tw4vol})^2 + \sigma(\text{tw5vol})^2 + \sigma(\text{tw6vol})^2}$.

	tw1	tw2	tw3	tw4	tw5	tw6
		2-fold rotation around $(\bar{1},0,1)$ $(\|\|[100]_c)$	3-fold rotation around $[\bar{2},1,0]$ $(\|\|[\bar{1}1\bar{1}]_c)$	3-fold rotation around [2,1,0] $(\|\|[111]_c)$	3-fold rotation around [0,1,2] $(\|\|[\bar{1}11]_c)$	3-fold rotation around $[\bar{2},\bar{1},0]$ $(\|\|[\bar{1}\bar{1}\bar{1}]_c)$
Pressure (GPa)			fraction			
4.35(11)	0.148(19)	0.146(9)	0.177(9)	0.178(8)	0.167(9)	0.184(9)
4.97(12)	0.199(17)	0.169(11)	0.199(7)	0.257(7)	0.027(6)	0.149(5)
5.46(12)	0.168(10)	0.147(4)	0.134(4)	0.106(3)	0.218(5)	0.227(5)
5.92(12)	0.170(9)	0.152(4)	0.227(5)	0.230(5)	0.115(3)	0.105(3)
6.67(13)	0.239(8)	0.242(5)	0.098(3)	0.112(3)	0.165(4)	0.144(3)
7.86(13)	0.166(9)	0.153(4)	0.112(3)	0.102(3)	0.235(5)	0.232(5)
8.09(13)	0.181(18)	0.193(12)	0.250(7)	0.211(7)	0.144(5)	0.021(6)

Table S2. Unit cell parameters of the doubled pseudocubic perovskite unit cell of the low pressure phase of NBT-0.048BT up to 3.4 GPa derived from profile fitting with CrysAlisPro[2].

Pressure	a (Å)
0.00010(1) GPa	7.7997(4)
0.65(9) GPa	7.7712(8)
0.95(9) GPa	7.7620(7)
1.30(9) GPa	7.7530(6)
1.71(10) GPa	7.7424(10)
1.85(10) GPa	7.7415(8)
2.79(11) GPa	7.7184(8)
3.41(11) GPa	7.7052(7)

Table S3. Results of the structure refinements in space group *Pnma* of the single-crystal XRD data of NBT-0.048BT above 4.4 GPa. The parameter b stems from the unit cell refinement with CrysAlisPro[2] using a doubled pseudocubic perovskite cell, while a and c stem from the transformation of the cubic to an orthorhombic unit cell with $a = c = b/\sqrt{2}$ and uncertainties $\Delta a = \Delta c = \Delta b/\sqrt{2}$.

Pressure	4.4 GPa	5.0 GPa	5.5 GPa	5.9 GPa	6.7 GPa	7.9 GPa	8.1 GPa
Unit cell parameters (Å)	$a = 5.4309(4)$ $b = 7.6804(5)$ $c = 5.4309(4)$	$a = 5.4163(3)$ $b = 7.6598(4)$, $a = 5.4163(3)$	$a = 5.4159(2)$, $b = 7.6592(3)$, $c = 5.4159(2)$	$a = 5.4092(2)$, $b = 7.6498(3)$, $c = 5.4092(2)$	$a = 5.3964(2)$, $b = 7.6316(3)$ $c = 5.3964(2)$	$a = 5.3855(2)$ $b = 7.6163(3)$ $c = 5.3855(2)$	$a = 5.3818(3)$, $b = 7.6110(4)$, $a = 5.3818(3)$
R (obs/all)	0.0579/0.0630	0.0471/0.0584	0.0437/0.0448	0.0427/0.0440	0.0407/0.0423	0.0355/0.0364	0.0522/0.0652
GoF (obs/all)	1.26/1.05	1.13/1.00	1.09/1.05	1.08/1.02	1.06/1.00	1.04/0.99	1.16/0.99
Number of reflections (obs/all)	239/362	226/351	406/460	404/460	392/447	399/445	217/351
Variables refined	28	20	33	33	33	33	20

Table S4. Fractional atomic coordinates *x*, *y* and *z* and equivalent isotropic displacement parameters U_{eq} (Å^2) from structure refinements in *Pnma*.

4.4 GPa	*x*	*y*	*z*	U_{eq}[1]
Bi/Na	-0.5054(1)	0.75	0.5004(4)	0.050(1)
Ti	0.5	0.5	0	0.016(1)
O1	-0.7574(8)	-0.0191(15)	0.2377(5)	0.057(3)
O2	-0.5011(5)	0.25	1.036(2)	0.023(3)
5.0 GPa	*x*	*y*	*z*	U_{eq}[2]
Bi/Na	-0.5189(2)	0.75	0.4981(3)	0.031(1)
Ti	0.5	0.5	0	0.014(1)
O1	-0.7781(13)	-0.0266(9)	0.2226(13)	0.021(2)
O2	-0.5061(14)	0.25	1.056(2)	0.025(2)
5.5 GPa	*x*	*y*	*z*	U_{eq}[3]
Bi/Na	-0.5176(2)	0.75	0.4979(2)	0.032(1)
Ti	0.5	0.5	0	0.013(2)
O1	-0.7787(9)	-0.0286(8)	0.2208(10)	0.022(2)
O2	-0.5076(10)	0.25	1.057(2)	0.024(3)
5.9 GPa	*x*	*y*	*z*	U_{eq}[3]
Bi/Na	-0.5192(2)	0.75	0.4977(2)	0.029(1)
Ti	0.5	0.5	0	0.013(3)
O1	-0.7786(11)	-0.0289(7)	0.219(1)	0.021(2)
O2	-0.5073(10)	0.25	1.056(2)	0.021(3)
6.7 GPa	*x*	*y*	*z*	U_{eq}[3]
Bi/Na	-0.5201(2)	0.75	0.4981(2)	0.027(1)
Ti	0.5	0.5	0	0.012(3)
O1	-0.7814(9)	-0.0311(6)	0.2197(9)	0.018(2)
O2	-0.5082(10)	0.25	1.056(2)	0.020(3)
7.9 GPa	*x*	*y*	*z*	U_{eq}[3]
Bi/Na	-0.5209(2)	0.75	0.4973(2)	0.026(1)
Ti	0.5	0.5	0	0.013(4)
O1	-0.7817(10)	-0.0293(5)	0.216(1)	0.020(2)
O2	-0.5077(10)	0.25	1.0623(10)	0.020(2)
8.1 GPa	*x*	*y*	*z*	U_{eq}[2]
Bi/Na	-0.5222(2)	0.75	0.4975(3)	0.023(1)
Ti	0.5	0.5	0	0.009(1)
O1	-0.7838(18)	-0.0289(12)	0.2167(17)	0.017(2)
O2	-0.5073(19)	0.25	1.063(3)	0.025(3)

[1]data set measured in methanol:ethanol 4:1; refinement: displacement parameters Bi/Na and O anisotropic, Ti isotropic
[2]data set measured in Helium; refinement: displacement parameters Bi/Na anisotropic, Ti and O isotropic
[3]data set measured in methanol:ethanol 4:1; refinement: displacement parameters of all atoms anisotropic

Table S5. Anisotropic displacement parameters from structure refinements in *Pnma* at 4.4-8.1 GPa.

4.4 GPa	U_{11}	U_{22}	U_{33}	U_{12}	U_{13}	U_{23}
Bi/Na	0.0566(14)	0.0581(16)	0.0338(11)	0	0.00044(12)	0
O1	0.073(6)	0.066(5)	0.031(3)	0.0114(17)	0.034(3)	0.0047(13)
O2	0.032(5)	0.010(4)	0.025(5)	0	0.0025(11)	0
5.0 GPa	U_{11}	U_{22}	U_{33}	U_{12}	U_{13}	U_{23}
Bi/Na	0.0279(9)	0.0360(13)	0.0303(13)	0	0.0001(3)	0
5.5 GPa	U_{11}	U_{22}	U_{33}	U_{12}	U_{13}	U_{23}
Bi/Na	0.0328(8)	0.0359(7)	0.0277(12)	0	−0.00003(14)	0
Ti	0.007(4)	0.012(4)	0.022(4)	0.0009(2)	0.0003(4)	0.0008(4)
O1	0.017(3)	0.0256(16)	0.025(3)	−0.0036(18)	0.0121(10)	−0.0032(17)
O2	0.025(6)	0.016(4)	0.029(5)	0	−0.0017(16)	0
5.9 GPa	U_{11}	U_{22}	U_{33}	U_{12}	U_{13}	U_{23}
Bi/Na	0.0310(8)	0.0321(6)	0.0241(11)	0	0.00013(14)	0
Ti	0.009(5)	0.015(4)	0.014(5)	0.0006(2)	−0.0004(6)	0.0011(4)
O1	0.013(3)	0.0239(17)	0.027(3)	−0.004(2)	0.0074(13)	−0.004(2)
O2	0.018(6)	0.009(3)	0.035(5)	0	0.0002(16)	0
6.7 GPa	U_{11}	U_{22}	U_{33}	U_{12}	U_{13}	U_{23}
Bi/Na	0.0278(8)	0.0277(6)	0.0240(11)	0	0.00036(15)	0
Ti	0.012(6)	0.015(3)	0.010(6)	0.0005(3)	0.0004(5)	0.0013(4)
O1	0.011(2)	0.0193(15)	0.025(3)	−0.0057(17)	0.0075(11)	−0.0008(18)
O2	0.012(6)	0.009(3)	0.037(6)	0	−0.0020(16)	0
7.9 GPa	U_{11}	U_{22}	U_{33}	U_{12}	U_{13}	U_{23}
Bi/Na	0.0281(8)	0.0261(6)	0.0225(11)	0	0.00023(11)	0
Ti	0.020(8)	0.013(4)	0.007(6)	0.0003(3)	−0.0004(4)	0.0006(3)
O1	0.014(2)	0.0232(17)	0.024(3)	−0.0042(17)	0.0069(10)	−0.0006(18)
O2	0.024(6)	0.010(3)	0.026(4)	0	−0.0003(15)	0
8.1 GPa	U_{11}	U_{22}	U_{33}	U_{12}	U_{13}	U_{23}
Bi/Na	0.0202(9)	0.0244(12)	0.0237(13)	0	0.0005(3)	0

References

1. Petříček, V., Dušek, M. & Palatinus, L. Crystallographic computing system JANA2006: General features. *Zeitschrift für Kristallographie - Cryst. Mater.* **229**, 345–352, DOI: 10.1515/zkri-2014-1737 (2014).
2. Agilent. *CrysAlis PRO*, Agilent Technologies Ltd, Yarnton, Oxfordshire, England (2014).

Structural transformations in the (1-x)$Na_{0.5}Bi_{0.5}TiO_3$-$xBaTiO_3$ solid solution under high pressure: comparison between x below and above the morphotropic phase boundary

Constanze Rösche,[1,*] Thomas Malcherek,[1] Tiziana Boffa Ballaran,[2] Carsten Paulmann,[1] Ross John Angel,[3] Semën Gorfman,[4] and Boriana Mihailova[1,†]

[1] *Department of Earth System Sciences, Universität Hamburg, Grindelallee 48, 20146 Hamburg, Germany*
[2] *Bayerisches Geoinstitut, Universität Bayreuth, Universitätsstraße 30, 95447 Bayreuth, Germany*
[3] *Istituto di Geoscienze e Georisorse, CNR, Corso Stati Uniti 4, 35127 Padova, Italy*
[4] *Department of Materials Science and Engineering, Tel Aviv University, Wolfson Building for Mechanical Engineering, Tel Aviv 6997801, Israel*

Single crystals of (1-x)$Na_{0.5}Bi_{0.5}TiO_3$-$xBaTiO_3$ (NBT-xBT) with a composition below (x = 0.013) and above (x = 0.074) the morphotropic phase boundary (MPB) were studied by *in situ* high-pressure x-ray diffraction with synchrotron radiation and Raman spectroscopy. We show that both compounds undergo a reversible pressure-induced phase transition to structures with *Pnma* symmetry, regardless of their symmetry at ambient conditions. The high-pressure phase resembles that recently reported for $x_{MPB} = 0.048$ [1], as the critical pressure p_c gradually increases with x. However, the pathway of developing the high-pressure phase varies with the composition, revealing distinct ways of Ba incorporation into the NBT matrix for the pseudorhombohedral ($x = 0.013$) and tetragonal ($x = 0.074$) phases. For $x < x_{MPB}$ the Ba^{2+} cations are preferentially accommodated in the tetragonal-type nanodomains existing in the dominant pseudorhombohedral NBT matrix, whereas for $x > x_{MPB}$ Ba^{2+} is dispersed in both the rhombohedral nanodomains and the dominant tetragonal matrix. Furthermore, for $x = 0.074$ there are incommensurate structural modulations at ambient pressure, which up to p_c remain unaffected by pressure, but vanish above p_c.

I. INTRODUCTION

Ferroelectrics have a wide range of applications due to many useful properties such as piezo- and pyroelectricity. Despite years of global efforts to reduce the use of lead, which is toxic to humans and the environment, the market for ferroelectric materials is still dominated by lead-based compounds like $Pb(Zr_xTi_{1-x})O_3$ (PZT) because of their superb properties. The perovskite-type (ABX_3) solid solution (1-x)$Na_{0.5}Bi_{0.5}TiO_3$-$xBaTiO_3$ (NBT-xBT) is a promising environmentally friendly alternative, particularly suitable for use in actuators [2] and ultrasonic transducers [3] or for energy storage applications [4, 5]. However, its properties still need to be improved to become competitive with the lead-based compounds currently in use. The macroscopic properties strongly depend on the nanoscale structure, which in turn varies with the chemical composition. Thus a better understanding of the relation between the chemical composition, the nanoscale structural heterogeneity and the properties of NBT-xBT is required.

With the increase of x the average symmetry of NBT-xBT transforms from monoclinic ($0 \le x \le 0.03$) to rhombohedral ($0.03 \le x \le 0.05$) to tetragonal ($x > 0.06$) [6, 7]. At $x = 0.05 - 0.06$ NBT-xBT exhibits a morphotropic phase boundary (MPB), that is, a composition x_{MPB} across which the symmetry of the ferroelectric phase changes and the material properties are significantly enhanced. The deviations from cubic symmetry are quite small and therefore the structure is mostly discussed in terms of cubic metrics.

NBT-xBT with $x \le 0.11$ is characterized by tilting of the BO_6 octahedra, whose pattern changes upon increasing x until the tilting finally vanishes for x above 0.11. The description of the tilt pattern has been a matter of long-term debate [8, 9], but it is accepted that for $x \le x_{MPB}$ the dominant tilt pattern is anti-phase around all three crystallographic axes ($a^-a^-c^-$ or $a^-a^-a^-$, Glazer notation [10]) and for $x > x_{MPB}$ the prevailing tilt pattern consists of in-phase tilts around only one axis ($a^0a^0c^+$) [11]. Anti-phase and in-phase octahedral tilting correspond to distortions at the R-point and M-point of the first Brillouin zone of the primitive cubic perovskite cell ($Pm\bar{3}m$, $a \approx 3.9$Å), which produce x-ray and neutron diffraction superstructure reflections at $\frac{1}{2}(ooo)$ and $\frac{1}{2}(ooe)$ [12], respectively, where o and e stand for *odd* and *even* indices. Thus, octahedral tilting leads to doubling of the unit cell, and therefore it is convenient to discuss the NBT-xBT structure in terms of a doubled cubic perovskite cell with $a \approx 7.8$Å.

At ambient conditions NBT-xBT shows relaxor behavior, i.e. a frequency dispersion of the dielectric-permittivity features, for $0 \le x \le 0.02$ and $0.05 \le x \le 0.1$, whereas compounds with $0.03 \le x \le 0.04$ and $x \ge 0.11$ behave as

* constanze.roesche@uni-hamburg.de
† boriana.mihaylova@uni-hamburg.de

normal ferroelectrics [13]. The relaxor properties can be explained by the existence of dynamic nanoscale polar and/or antipolar regions, the structure of which deviates from the surrounding matrix [14]. Such mesoscopically correlated structural fluctuations can be revealed by single-crystal x-ray, neutron or electron diffuse scattering (DS). For $x < 0.05$ asymmetric DS extends along pseudocubic $\langle 100\rangle^*_{\rm pc}$ directions, which has been attributed to thin platelet-like tetragonal ($P4bm$) nanoregions inside the (pseudo)rhombohedral matrix [11, 15, 16]. For $0.05 \leq x \leq 0.11$ the extension direction of DS changes to $\langle 110\rangle^*_{\rm pc}$, which suggests that for this compositional range the structural state of NBT-xBT may be described as a pseudocubic or tetragonal matrix including rhombohedral-like nanoregions [11, 14, 17], i.e. with the A-site cation off-centered shifts predominantly along $\langle 111\rangle_{\rm pc}$ [18].

In spite of the extensive studies on the composition-induced changes of NBT-xBT, it still remains unclear how exactly Ba^{2+} cations are incorporated into the NBT structure and in particular, if they cluster or they are homogeneously distributed over the dominant matrix and the intrinsically existing nanoregions. High-pressure structural analyses can help to elucidate this issue, because external hydrostatic pressure can enhance subtle antiferrodistortive order that may exist at ambient conditions and thus can better reveal the inherent nanoscale structural inhomogeneities [19].

High-pressure (HP) experiments on pure NBT [15, 20] and NBT-0.048BT [1] have revealed that the symmetry of the HP structure is orthorhombic $Pnma$. The $Pnma$ phase is characterized by anti-polar order of A-site cationic displacements and a mixed BO_6 tilt pattern of type $a^-b^+a^-$. The orthorhombic unit cell is rotated by 45° with respect to the cubic perovskite cell so that the orthorhombic **a** axis is oriented parallel to the cubic [110] direction and the orthorhombic **b** axis corresponds to the cubic [001] direction. The A-site cations are shifted from the centers of the AO_{12} polyhedra predominantly along **a** [1]. Off-centering of the B cations is not allowed by symmetry. However, Raman spectroscopic HP experiments have shown that on a local scale polar B-cation shifts persist with a reduced magnitude [21]. The Ba-induced intrinsic local elastic stresses smear out the phase transition and increase the critical pressure p_c [1, 21]. At ambient conditions the bulk modulus of NBT-$x_{\rm MPB}$BT is smaller than that of pure NBT, most probably due to the Ba-enhanced elastic response of the B-cation subsystem upon mild pressures [21].

Here we report the results of our HP study on NBT-xBT single crystals with $x = 0.013$ and $x = 0.074$, which are on the pseudorhombohedral and tetragonal side of the MPB, respectively. By combining HP synchrotron x-ray diffraction (XRD) and Raman scattering experiments, we have gained a comprehensive picture of the pressure-induced structural transformations from the long-range to the short-range scale in both compounds. We compare these results to our previous work on NBT-xBT at the MPB (x=0.048) [1, 21]. The high-pressure phase of all three compounds has orthorhombic $Pnma$ symmetry, but the pressures of the phase transition and preceding structural transformations depend on the Ba content.

II. EXPERIMENTAL DETAILS

Single crystals of (1-x)$Na_{0.5}Bi_{0.5}TiO_3$-$xBaTiO_3$ with Ba contents (in atoms per formula unit (apfu)) of $x = 0.013(2)$ and $x = 0.074(7)$ were synthesized by the top-seeded-solution-growth method [22]. The chemical composition was determined by wavelength-dispersive x-ray emission spectroscopy [23]. According to in-house XRD analysis, the NBT-0.013BT sample is pseudorhombohedral with $90° - \alpha_{rh} = 0.085(10)$ and $a = b = c \approx 3.888(1)$ Å, whereas the NBT-0.074BT sample is pseudocubic with $a = b = c \approx 3.901(1)$ Å [23].

High-pressure experiments up to ∼10 GPa were conducted on $\{100\}_{\rm cubic}$ slices with a thickness of ∼40 μm, using Boehler-Almax diamond anvil cells [24] with a culet diameter of 600 µm, rhenium or stainless steel gaskets with diameter of the drilled hole of 300 µm, and a methanol:ethanol 4:1 mixture as a pressure transmitting medium to ensure hydrostatic conditions. The pressure in the sample chamber was determined using the ruby-line luminescence method [25].

A. Synchrotron XRD

Synchrotron single-crystal XRD experiments were conducted at beamline P24/EH1 at DESY with a radiation wavelength of $\lambda = 0.3542$ Å, corresponding to ∼35 keV. The absorption coefficient of NBT-xBT at the high photon energy is ∼7 mm^{-1}, resulting in a penetration depth of ∼140 µm and ensuring that the entire bulk of the samples was probed.

The measurements were carried out using a Huber four circle Kappa diffractometer equipped with a Pilatus 1M CdTe detector and a sample-to-detector distance of 200 mm. At each pressure step three identical 70° phi scan data collections with a step width of 0.5° per frame were performed. The exposure time was 3 s per frame, which was checked and confirmed to prevent oversaturation of the strongest Bragg reflections. The intensities of the three scans were combined to enhance the signal-to-noise ratio and improve the visibility of x-ray diffuse scattering (XDS).

For NBT-0.013BT a specimen sized $\sim 75 \times 80 \times 40$ µm was measured upon compression up to 4.8 GPa. Two additional data sets were collected upon decompression and a full data collection was performed in air on the recovered sample and an additional pristine crystal to verify the reversibility of the pressure-induced structural changes.

For NBT-0.074BT three different runs up to 3.3, 4.0 and 4.5 GPa were conducted using specimens with a size of approximately $\sim 100 \times 100 \times 40$ µm. A further NBT-0.074BT specimen sized $\sim 40 \times 40 \times 30$ µm was loaded in a BX90 DAC [26] with a culet diameter of 300 µm and data were collected up to 12.2 GPa using helium (He) as pressure transmitting medium. A full data collection was performed in air on the recovered sample from the HP run up to 4.5 GPa and on an additional virgin crystal.

The data were processed with the CrysAlisPro software package [27] and refinements of the high-pressure structure were performed using Jana2006 [28]. Details are described in the Supplemental Material [29].

B. Raman spectroscopy

High-pressure Raman scattering experiments were performed using a Horiba Jobin-Yvon T64000 triple-grating spectrometer and the 514.532-nm line of an Ar^+ laser. The experimental set-up ensured a spectral resolution of ∼2 cm^{-1} and peak position accuracy of 0.35 cm^{-1}. Polarized Raman spectra were collected in the range 15-1215 cm^{-1} in scattering geometries $\bar{Z}(XX)Z$ and $\bar{Z}(XY)Z$ (Porto's notation) with X, Y, Z parallel to the three pseudocubic ⟨100⟩ directions. We always started from an orientation for which the difference between the $\bar{Z}(XX)Z$ and $\bar{Z}(XY)Z$ spectra was most pronounced. The subsequent analyses revealed that the depolarization ratio $I_{\bar{Z}(XY)Z}/I_{\bar{Z}(XX)Z}$ did not change with pressure.

Single crystals of NBT-0.013BT ($\sim 90 \times 60 \times 40$ µm) and NBT-0.074BT ($\sim 80 \times 70 \times 40$ µm) were loaded in DACs as described above, and the pressure was increased in steps < 0.5 GPa up to 9.8 GPa and 10.6 GPa, respectively. Additional data were collected on decompression after reaching the highest pressure. Raman spectra were measured focusing the laser at least at two different areas of the crystals at every pressure to verify reproducibility of the data and a background spectrum from an area adjacent to the sample was measured under identical experimental conditions. For both compounds additional Raman scattering experiments were conducted on different sample specimens that verified the reproducibility of the pressure-induced structural changes.

The data were evaluated with the OriginPro 2024b software package [30]. To correct the Raman spectra for the contribution from the DAC and the pressure transmitting medium the background spectra were normalized to the height of the Raman peaks of the pressure transmitting medium in the sample spectra and then subtracted. The subtracted spectra were consequently normalized to the Bose-Einstein phonon occupation factor to remove the temperature effects on the Raman intensities (see Fig. S5 in the Supplemental Material [29]). The corrected Raman spectra were fitted with pseudo-Voigt functions, following the procedure described in the Supplemental Material of [21], to determine the phonon wavenumbers (ω), full widths at half maximum (FWHMs, Γ) and integrated intensities (I).

III. RESULTS

A. Synchrotron XRD

Previous powder diffraction studies at atmospheric pressure have indicated that the symmetries of the room-temperature structure of NBT-xBT with $x = 0.013$ and $x = 0.074$ are monoclinic Cc [6, 7] and tetragonal $P4bm$ [6, 31], respectively. However, the monoclinic and tetragonal distortions from cubic symmetry are small and the occurrence of twin domains leads to pseudocubic appearance of the NBT-xBT crystals [23, 32].

Structure refinements to our own ambient pressure synchrotron XRD data on single crystals were hindered by the presence of strong XDS and yielded too high R-values. Thus, the reflections were indexed in terms of a doubled cubic perovskite cell with $a_{0(x=0.013)} = 7.7841(4)$ Å and $a_{0(x=0.074)} = 7.8172(1)$ Å. Reconstructed $hk0$ and $hk1$ reciprocal-space layers of both compounds at increasing pressures are shown in Fig. 1-4.

At ambient pressure the XDS for NBT-0.013BT extends along the $\langle 100 \rangle^*_{pc}$ reciprocal-space directions (Fig. 1 and 2), similar to that for pure NBT, indicating that the (pseudo)rhombohedral matrix is interspersed with subordinate platelet-like tetragonal nanoregions [16, 33]. However, contrary to the diffraction pattern of pure NBT, there is no sign of x-ray scattering at *ooe*, which is characteristic of distortions driven by M-point phonon modes [34]. This indicates that the correlation length of in-phase BO_6 tilts in the tetragonal platelets, if any, is too small to be detected by XRD. The presence of sharp *ooo* Bragg reflections in the $hk1$ plane (see Fig. 2 and Fig. S1 in the Supplemental Material [29]) shows that the structure is characterized by long-range anti-phase tilt order. Upon increasing pressure the XDS along $\langle 100 \rangle^*_{pc}$ increases in length and intensity around both, *eee* and *ooo* Bragg reflections. At 1.8 GPa there is

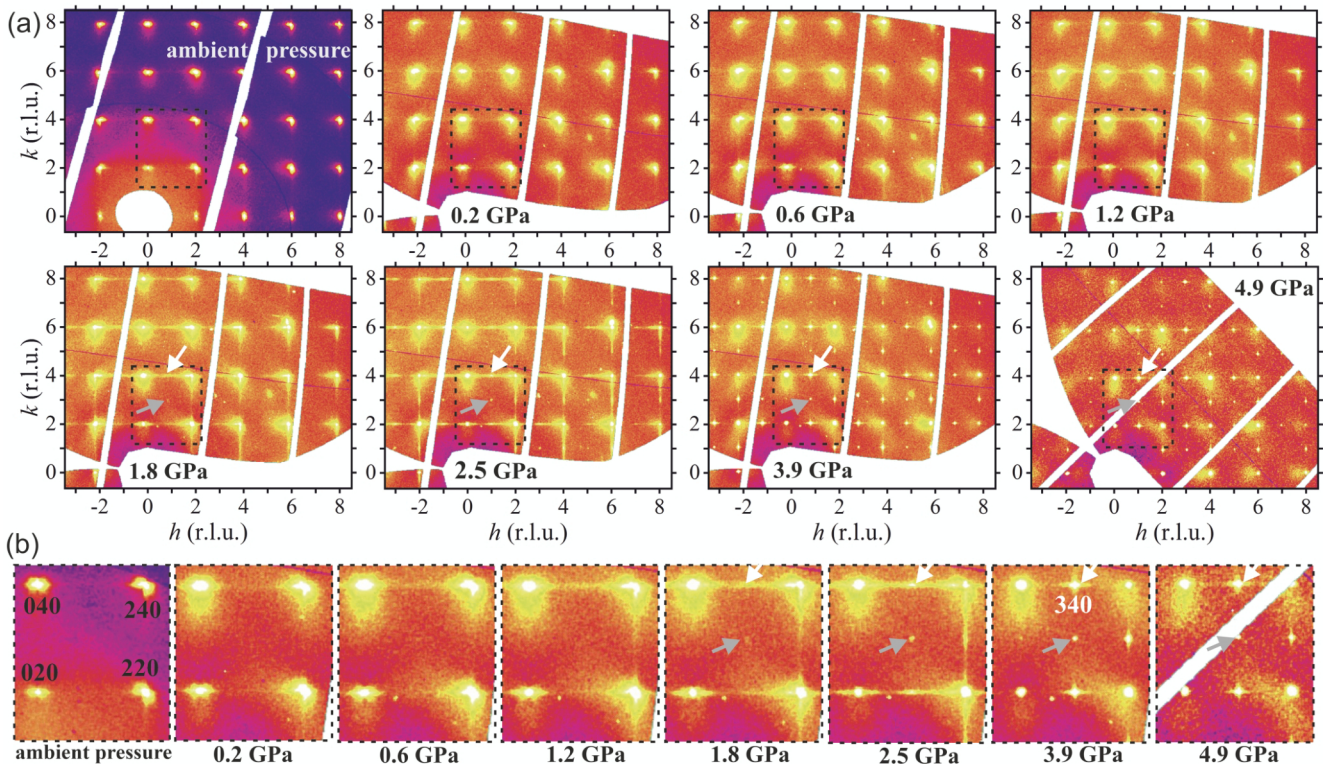


FIG. 1. $hk0$ reciprocal space layers of NBT-0.013BT at pressures from ambient pressure up to 4.9 GPa. The indices refer to a doubled cubic perovskite cell. Magnified images of the areas highlighted with a dashed rectangle in (a) are shown in (b). Representative *ooe* and *oee* reflections are marked by gray and white arrows, respectively.

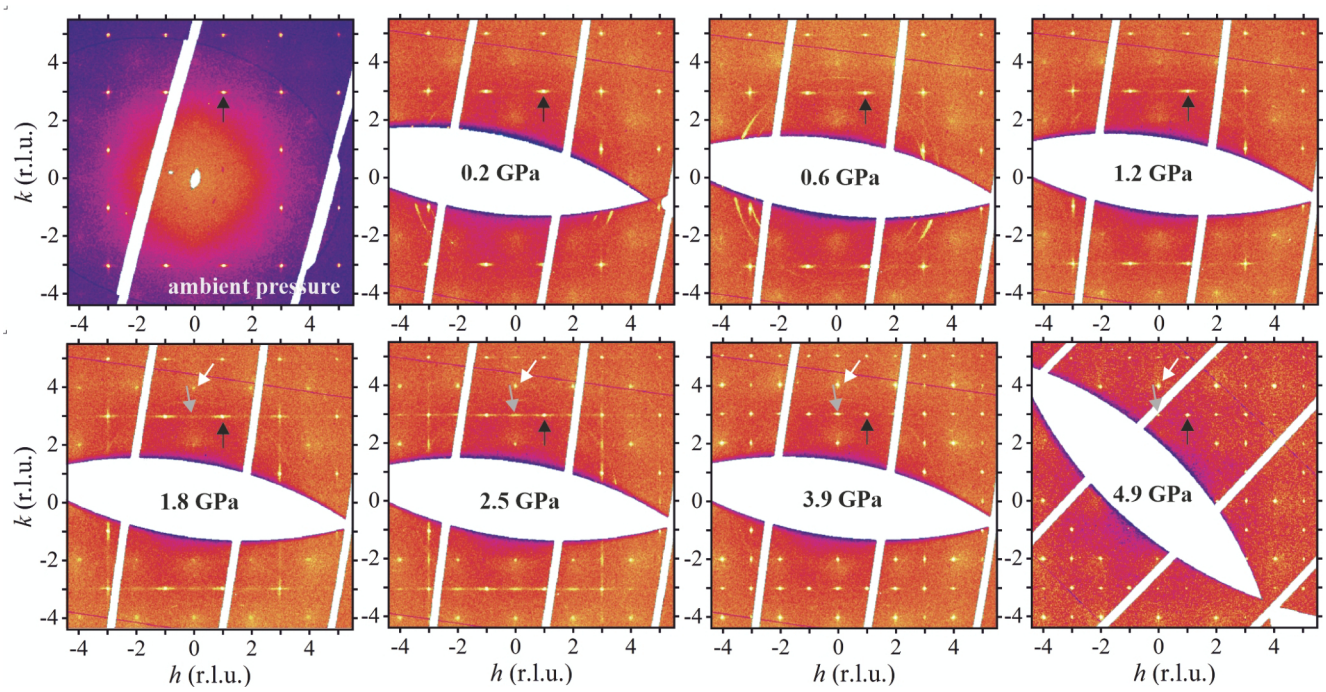


FIG. 2. $hk1$ reciprocal space layers of NBT-0.013BT at pressures from ambient pressure up to 4.9 GPa. The indices refer to a doubled cubic perovskite cell. Representative *ooo*, *ooe* and *oee* reflections are marked by black, gray and white arrows, respectively.

enhanced XDS at *oee* and *ooe* (see white and gray arrows in Fig. 1 and 2), characteristic of distortions activated by X-point and M-point phonons of the aristotype perovskite structure ($Pm\bar{3}m$) [34]. The appearance of XDS at M-points indicates that pressure locally induces in-phase octahedral tilts, disrupting the long-range order of anti-phase octahedral tilts in NBT-0.013BT, a process similar to the structural transformations in $PbZrO_3$ at high temperatures [35]. On the other hand, the evolving Bragg scattering at X-points indicates the development of antipolar shifts of A-cations along with mixed octahedral tilts [12, 34]. With further increase in pressure the M- and X-point precursor reflections increase in intensity and sharpen until the critical phase-transition pressure is reached at $\sim$ 3.9 GPa, at which the XDS related to nanoscale structural inhomogeneities evolves into sharp Bragg diffraction peaks indicating the development of long-range order. For NBT-0.074BT the ambient-pressure XDS extends along $\langle 110\rangle^*_{pc}$ (Fig. 3 and 4), similar to NBT-xBT with x = 0.048-0.075 [1, 14, 17, 18]. Such a shape of XDS is typical of Pb-based relaxors (e.g. [36–38]). For the latter system the $\langle 110\rangle^*_{pc}$-shaped XDS is commonly assumed to be due to dynamical rhombohedral nanoregions with polar cation shifts along $\langle 111\rangle_{pc}$ that correlate within $\{110\}_{pc}$ direct-space planes [36], although thermal diffuse scattering due to phonons as well as Huang scattering due to local lattice distortions also can contribute to this XDS [38]. The polarization in NBT-xBT always occurs along with octahedral tilts and doubling of the unit cell. Rhombohedral-like nanodomains with anti-phase BO_6 tilts have been observed for NBT-xBT with x between 0.05-0.09 (e.g. [39–41]), i.e. for compounds exhibiting $\langle 110\rangle^*_{pc}$-shaped XDS. Thus, the XDS along $\langle 110\rangle^*_{pc}$ we have observed for NBT-xBT is most likely related to rhombohedral-like polar nanoregions with doubled unit cell distributed within a pseudocubic polarizable matrix/ tetragonal polar larger-size domains [1, 14, 17, 18]. There are weak reflections at *ooe* (M-point), which appear as sharp spots in the $hk0$ layer and as diffuse streaks in the $hk1$ plane, that is, both features represent XDS rods along $\langle 100\rangle^*_{pc}$. Even weaker x-ray scattering is observed at *ooo* (R-point) in the $hk1$ layer (see Fig. 4). Accordingly, the dominant BO_6 tilt pattern in NBT-0.074BT is in-phase $a^0a^0c^+$, but there is also subordinate anti-phase octahedral tilting.

With pressure increase, the XDS streaks in the $hk0$ layer of NBT-0.074BT change from parallel to $\langle 110\rangle^*_{pc}$ to parallel to $\langle 100\rangle^*_{pc}$. Furthermore, the *ooo* reflections strongly increase in intensity and above 1.7 GPa they become stronger than the *ooe* reflections (see Fig. S2 in the Supplemental Material [29]). As a result, at 2.3 GPa the diffraction pattern

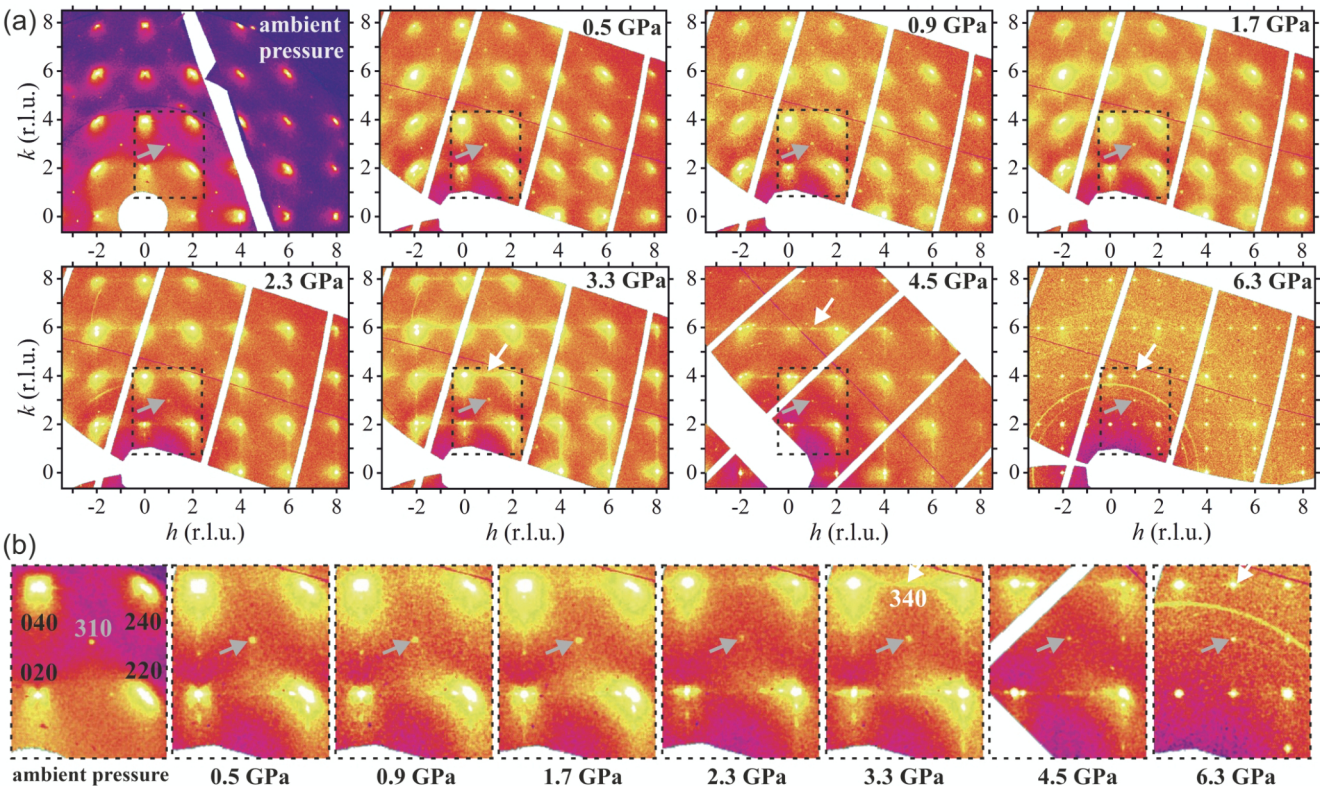


FIG. 3. $hk0$ reciprocal space layers of NBT-0.074BT at pressures from ambient pressure up to 6.3 GPa. The indices refer to a doubled cubic perovskite cell. Magnified images of the areas highlighted with a dashed rectangle in (a) are shown in (b). Representative *ooe* and *oee* reflections are marked by gray and white arrows, respectively. Note that the data at 4.5 GPa and 6.3 GPa were collected from different pieces of the same sample in separate DAC loadings (see section II.A.)

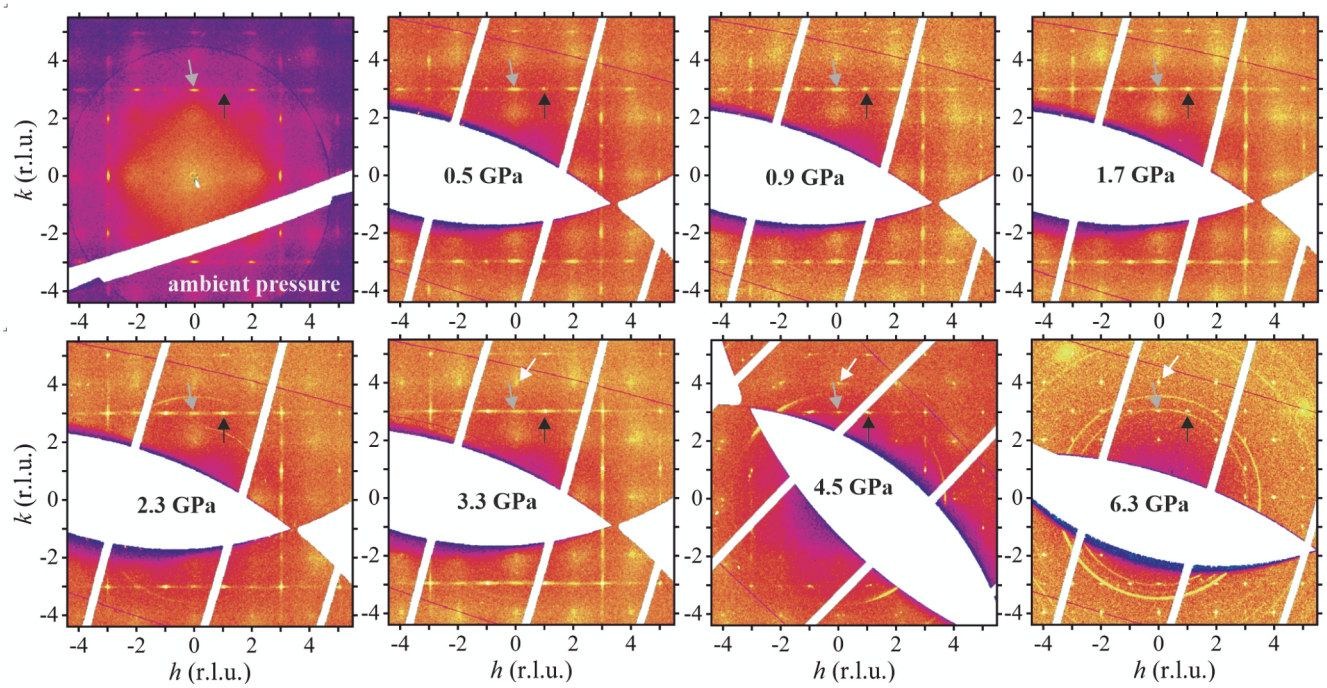


FIG. 4. $hk1$ reciprocal space layers of NBT-0.074BT at pressures from ambient pressure up to 6.3 GPa. The indices refer to a doubled cubic perovskite cell. Representative *ooo*, *ooe* and *oee* reflections are marked by black, gray and white arrows, respectively. Note that the data at 4.5 GPa and 6.3 GPa were collected from different pieces of the same sample in separate DAC loadings (see section II.A.)

of NBT-0.074BT resembles that of pure NBT [11, 15, 33] and NBT-0.013BT at ambient pressure, as well as NBT-0.048BT at 0.7 GPa [1]. Similar to $x = 0.013$ and 0.048 [1], the $\langle 100 \rangle^*_{\mathrm{pc}}$ XDS streaks keep intensifying with pressure for x=0.074 until precursors of *oee* Bragg reflections (X-points) appear at 3.3 GPa. Unfortunately, we could not collect high-quality data between 3.3-6.3 GPa because of twinning of the specimens used in the second and third pressure run. However, data collected at 4.5 GPa clearly show that at this pressure $\langle 100 \rangle^*_{\mathrm{pc}}$ XDS still persists and no phase transition has taken place yet. At 6.3 GPa the XDS has evolved into sharp Bragg peaks (Fig. 3 and 4), indicating that the phase-transition pressure has been crossed, and the diffraction pattern resembles that of the high-pressure phase of NBT-0.013BT (Fig. 1 and 2) and NBT-0.048BT [1]. Data collections on decompression indicate that for both NBT-0.013BT and NBT-0.074BT the pressure-induced phase transition is reversible, but there is a time hysteresis of several hours before the structure of the low-pressure phase is completely recovered. Another peculiarity in the XRD pattern of NBT-0.074BT is the presence of satellite reflections offset from *eee* Bragg reflections towards the lower-angle side along $\langle 100 \rangle^*_{\mathrm{pc}}$, already at ambient pressure. The observed offsets of the satellites from the Bragg peaks are multiples of 0.15 reciprocal lattice units (r.l.u.) (see Fig. S3 in the Supplemental Material [29]), indicating that the NBT-0.074BT structure is incommensurately modulated. Satellite reflections with an offset of ~ 0.3 and ~ 0.6 r.l.u. were observed also for NBT-0.048BT at ambient conditions [1]. However, the satellite peaks are stronger for NBT-0.074BT than for NBT-0.048BT, implying a larger difference between the modulated and non-modulated structure for $x = 0.074$, which is consistent with the observation of higher order satellite peaks (see Fig. S3 in the Supplemental Material [29]). Pure NBT also exhibits a modulated structure at ambient pressure, but at elevated temperatures, between the depoling temperature T_d and the temperature of the dielectric-permittivity maximum T_m [42, 43]. This intermediate state has been considered to be antiferroelectric [44], but recently a weak structural polarity has been demonstrated [42], implying a ferrielectric or canted antiferroelectric state. The structural modulation was suggested to be due to a *Pnma*-type layer comprising mixed tilts of type $a^-b^+a^-$ ($[010]_{Pnma} \parallel [001]_{\mathrm{cubic}}$) in order to reduce the strain in the tilted BO_6 system between two opposite rhombohedral domains with $a^-a^-a^-$ tilts [45]. Alternatively, the existence of self-organized extended defects within the A-sublattice along the four-fold axis of the precursor high-temperature tetragonal phase existing near T_m was proposed to be the reason for the one-dimensional modulation of the NBT polar rhombohedral matrix [46]. In fact the two models are consistent, because orthorhombic *Pnma* contains mixed BO_6 tilts as well as antipolar shifts of A-site cations. That is, the presence of *Pnma*-type layers modulating the perovskite structure along $\langle 100 \rangle^*_{\mathrm{pc}}$ can relax both the tilt system between two *R*3*c*-type domains and the A-sublattice

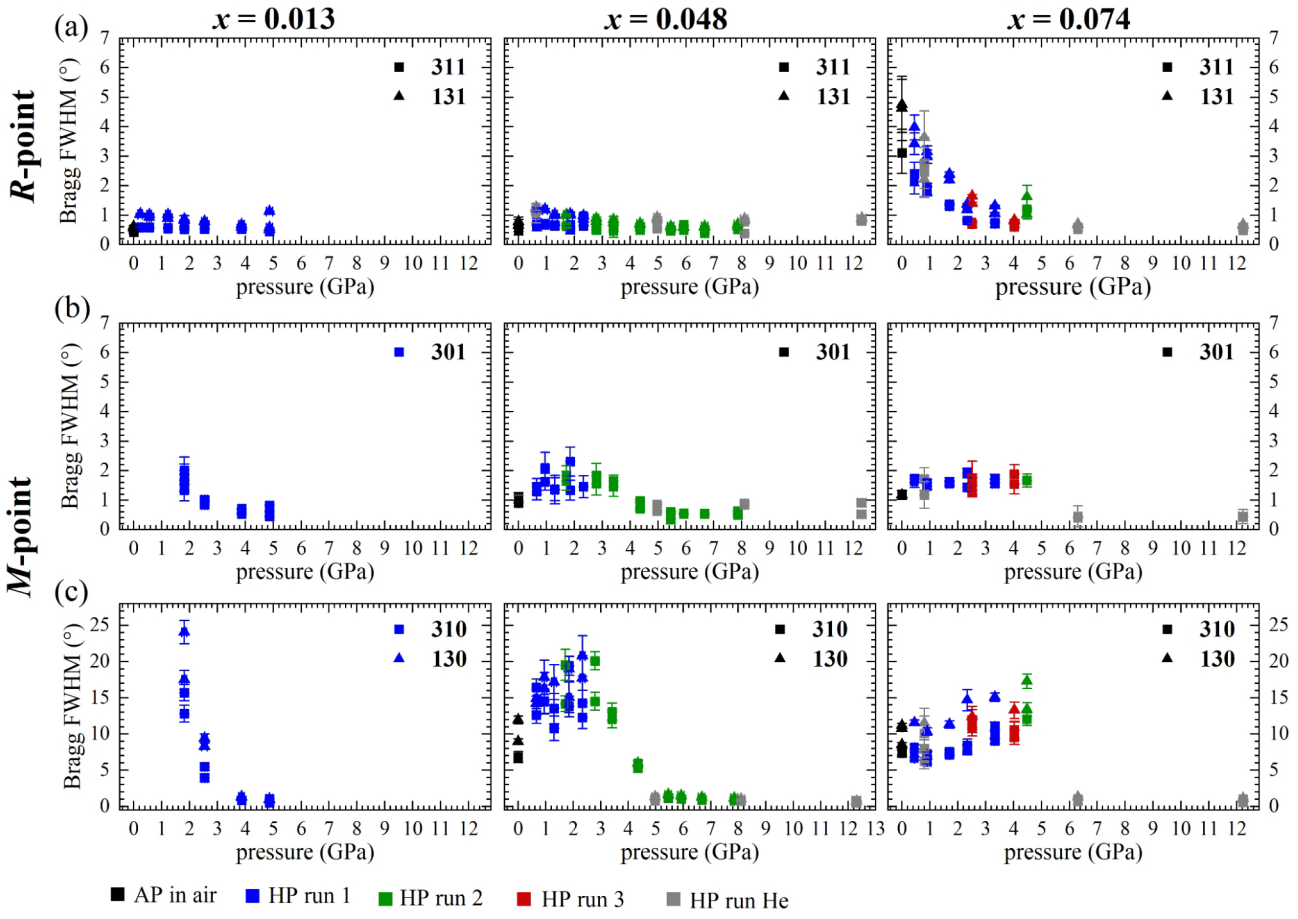


FIG. 5. Bragg peak full widths at half maximum (FWHMs) of representative (a) R-point and (b) and (c) M-point reflections as a function of pressure derived from rocking curves. Please note the different y-axis scales.

between two $P4bm$-type domains. Hence, periodic orthorhombic $Pnma$-like layers that reduce the inherent strain in the perovskite structure may exist at any x, but the temperature range where the modulated structure is stable can vary with the content of Ba, similar to the well-known compositional dependence of T_d [47]. Thus, we suggest that for $x = 0.048$ and 0.074 a modulated structure comprising $Pnma$-like layers is stabilized already at room temperature, giving rise to the observed satellite peaks at ambient conditions. Our high-pressure data on NBT-0.074BT show that the offset as well as the intensity of the satellite peaks from *eee* Bragg reflections remain unchanged, *i.e.*, pressure does not affect the structural modulation on the approach to the critical pressure p_c. Above p_c the satellite peaks disappear as the whole structure switches to $Pnma$. The strong alteration of XDS between ambient pressure and p_c indicates that the structure adapts to the evolving external pressure via rearranging the A-site cation shifts and BO_6 tilts within the domain bulk rather than creating further extended defects of $Pnma$ type.

To elucidate the mechanism of pressure-induced transformation processes in the octahedral tilt systems, we have compared the pressure dependence of the FWHMs of the rocking curves at selected *ooo* and *ooe* for $x = 0.013$, 0.048, and 0.074 (Fig. 5), since they give information on the correlation length of coherent anti-phase and in-phase tilts. The R-point (*ooo*) reflections are almost equally sharp in the low- and high-pressure phase for NBT-0.013BT and NBT-0.048BT, confirming that the anti-phase tilts exhibit long-range order. The R-point reflections in the XRD pattern of NBT-0.074BT are significantly broader at ambient pressure, indicating a relatively short correlation length of anti-phase tilts. However, upon pressure increase these reflections gradually sharpen, showing that the correlation length of anti-phase tilts gradually increases. For all three compounds, the FWHMs of 131 reflections (triangles in Fig. 5a) are nearly the same as those of 311 reflections (squares in Fig. 5a), meaning that the correlation length of anti-phase tilts is similar along the three $\langle 100 \rangle_{\mathrm{pc}}$ crystallographic directions. On the other hand, M-point (*ooe*)

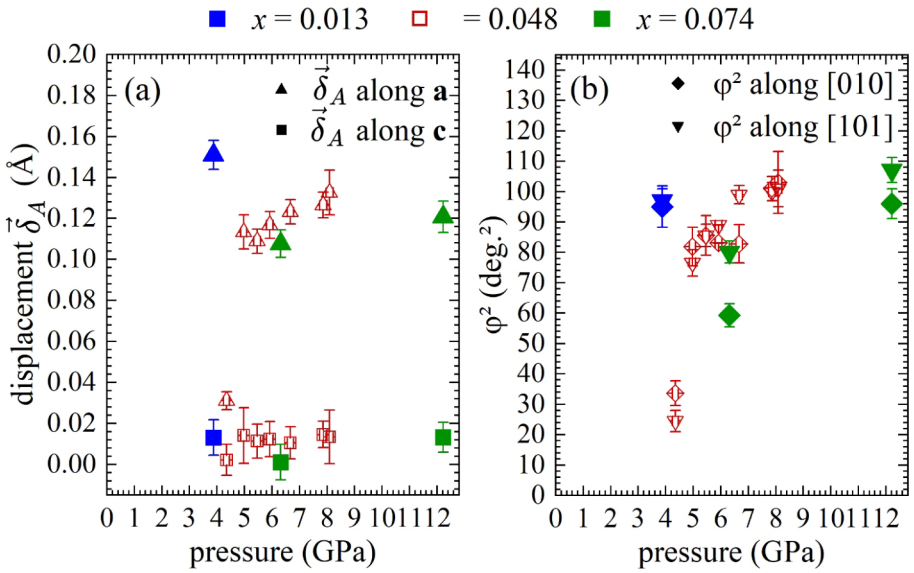


FIG. 6. (a) A-cation off-centering displacements $\vec{\delta}_A$ and (b) squared octahedral tilting angles φ^2 of NBT-xBT with $x = 0.013$ (blue filled symbols), 0.048 [1] (red open symbols) and 0.074 (green filled symbols) in the high-pressure *Pnma* phase.

reflections appear as sharp spots in $hk0$ planes but diffuse streaks in $hk1$ planes, reflecting the rod-shape XDS (Figs. 1-4), which in turn indicates anisotropically correlated in-phase tilts within $(100)_{\mathrm{pc}}$ planes in the direct space, i.e. two-dimensional correlations. As rocking-curve analyses are always performed perpendicular to the $hk0$ and $hk1$ planes, the FWHMs of 301 are quite sharp (<2.5°) and correspond to the thickness of the rods, while 310 and 130 reflections have a FWHM of ≈ 5-25° in the low-pressure phase, which corresponds to the length of the rods. For NBT-0.013BT, no M-point reflections are present at ambient pressure, but such appear above 1.8 GPa with large FWHM, and gradually sharpen up to the phase-transition pressure, at which the streaks transform into sharp reflections with equal widths in all three $\langle 100 \rangle_{\mathrm{pc}}$ directions. For NBT-0.048BT and NBT-0.074BT streaks of XDS at M-points already exist at ambient pressure. They first increase strongly in length (Fig. 5c) and slightly in thickness (Fig. 5b) upon pressure increase, before they sharpen above 2.8 GPa (x=0.048) and 4.5 GPa (x=0.074), and appear as isotropic sharp reflections in the high pressure phase. The maximum of FWHM *versus* pressure for *ooe* and *oeo* reflections indicates that the development of mixed octahedral tilting is predominantly realized via rearrangement of the preexisting $a^0a^0c^+$ in-phase tilt system.

Structure refinements of the high-pressure XRD data, following the procedure that has been applied for NBT-0.048BT [1], revealed that the symmetry of the high-pressure phase of NBT-0.013BT (above 3.9(1) GPa) and NBT-0.074BT (at 6.3(1) GPa) is orthorhombic *Pnma*, similar to pure NBT (above ∼3.3 GPa) [20] and NBT-0.048BT (above 4.6(1) GPa) [1]. Thus, our new data confirm that the high-pressure structure of NBT-xBT, $x \in [0, 0.074]$, consists of antipolar shifts of A-site cations in the plane perpendicular to the orthorhombic **b** axis (parallel to the cubic [001] direction) and a mixed $a^-b^+a^-$ tilt pattern. The details of the refinement, the unit cell parameters, fractional atomic coordinates and atomic displacement parameters for NBT-0.013BT at ∼3.9 GPa and NBT-0.074BT at ∼6.3 and 12.2 GPa are given in Table SI-SIV in the Supplemental Material [29]. Supplemental Crystallographic Information Files (CIFs) are also provided [29].

The off-centering of A-site cations in the high-pressure phase (*Pnma*) of NBT-xBT for $x = 0.013$, 0.048, and 0.074 are compared in Fig. 6a. The off-centering was calculated as $\vec{\delta}_A = \vec{r}_A - \frac{1}{12} \times \sum_{i=1}^{12} \vec{r}_{iO}$ [48], where $\vec{r}_A$ and $\vec{r}_O$ are the position vectors of A-site cations and oxygen atoms. The results show that for all three compounds the A-site cations are predominantly displaced along the orthorhombic **a** axis, with only a minor off-set along the orthorhombic **c** axis (Fig. 6a). Within the uncertainties, NBT-0.074BT (this work) and NBT-0.048BT [1] exhibit the same $\vec{\delta}_A$ along either **a** and **c**. For NBT-0.013BT however, $\vec{\delta}_A$ along **a** is significantly larger, which is in accordance with the previously reported largest non-orthogonality for this NBT-xBT compound at ambient pressure [23] and the higher intensity of R-point reflections (see Fig. S1 and S4 in the Supplemental Material [29]), indicative of anti-phase octahedral tilts, whose presence also promotes anti-polar A-cation shifts.

The degree of octahedral tilting can be represented by the squared octahedral tilting angle $\varphi^2 = [(180 - \angle(B' -$

$O - B''))/2]^2$ (Fig. 6b). As φ^2 increases with pressure for all three compounds, the values cannot be compared unequivocally. However, the corresponding values of the degree of anti-phase octahedral tilting in different directions indicate that a larger content of Ba^{2+} leads to higher anisotropy in the tilt system regarding the tilt angle, whereas increasing pressure has the opposite effect and reduces this anisotropy.

B. Raman spectroscopy

Selected Raman spectra of NBT-0.013BT and NBT-0.074BT at elevated pressures are shown in Fig. 7. Comprehensive sets of Raman spectra for both compounds are shown in Fig. S6 in the Supplemental Material [29]. The ambient-pressure spectra were fitted following the model used by de la Flor *et al.* [23] for NBT-xBT single crystals. Similar to our previous high-pressure study on pure NBT and NBT-0.048BT [21], in the high-pressure spectra peaks were removed if they did not meet the standard goodness-of-fit criteria (e.g. $\Delta I/I < 0.5$, whereby ΔI is the absolute error in the integrated intensity I), and a new peak was only added if the spectral fit was significantly improved as indicated by the statistical criteria.

An unambiguous peak assignment in terms of crystal normal phonon modes is not feasible due to strong peak broadening and consequent overlaps [49, 50]. Since the fitted peaks cannot be associated with specific phonon symmetries, it is most appropriate to analyze the spectra in terms of the dominant type of atomic vibrations that comprise a certain phonon mode. Vibrations of off-centered A-site cations contribute to the NBT-xBT Raman spectrum in the range of 30-60 cm^{-1} [23]. These vibrations are dominated by Bi^{3+} cations, due to their stronger affinity to shift from the centers of AO_{12} polyhedra compared to Na^+ and Ba^{2+} [51] and the higher degree of co-valency of Bi-O bonds compared to Na-O and Ba-O bonds [50]. Raman scattering in the spectral range from 115-160 cm^{-1} is attributed to out-of-phase TiO_3 and Bi^{3+}-cation vibrations [23]. Vibrations of off-centered B-site cations (Ti^{4+}) contribute to the spectral range 240-325 cm^{-1}, whereas BO_6 tilting vibrations contribute to the range 370-420 cm^{-1}. Internal

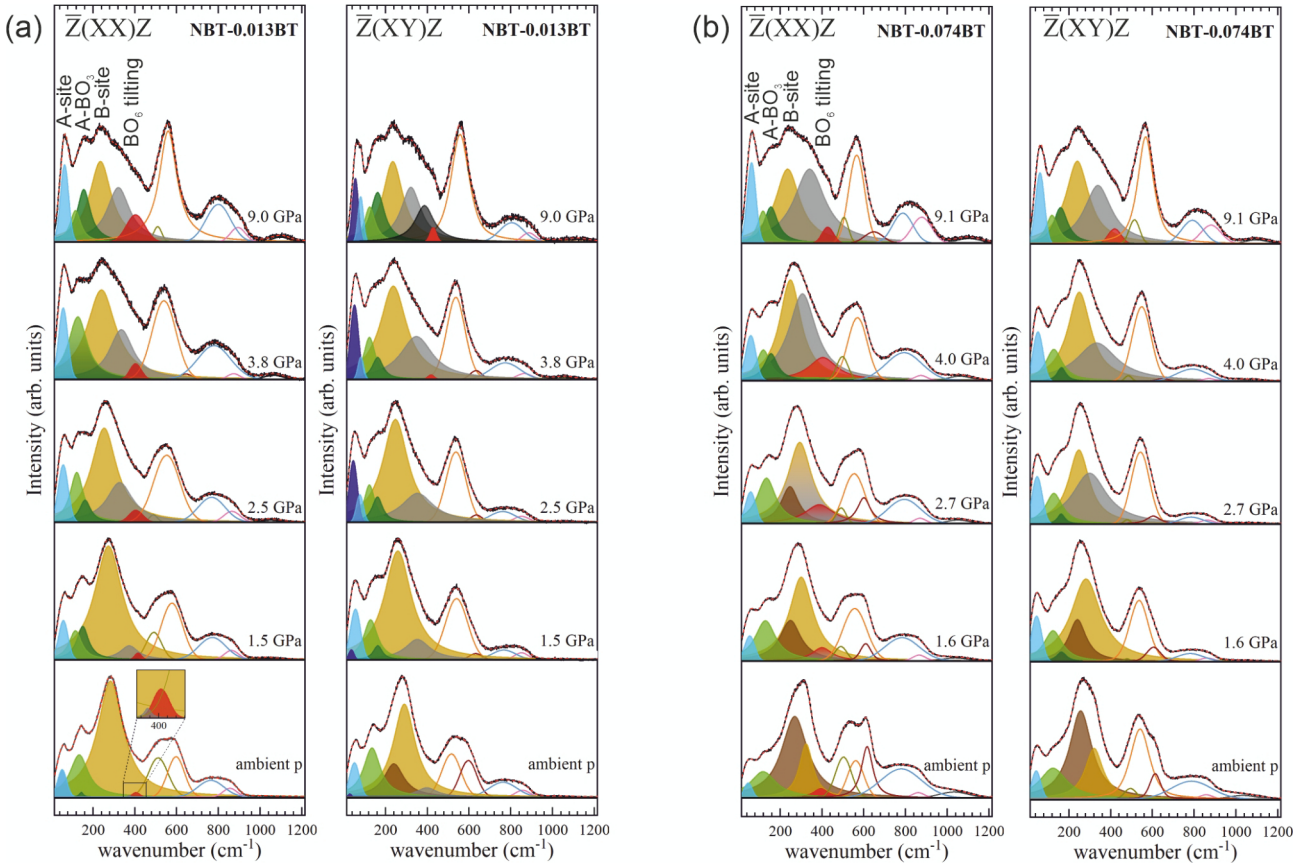


FIG. 7. Selected high-pressure $\bar{Z}(XX)Z$ and $\bar{Z}(XY)Z$ Raman spectra of (a) NBT-0.013BT and (b) NBT-0.074BT (solid black line) along with the fitted pseudo-Voigt functions and the resultant spectrum profiles (red dashed lines).

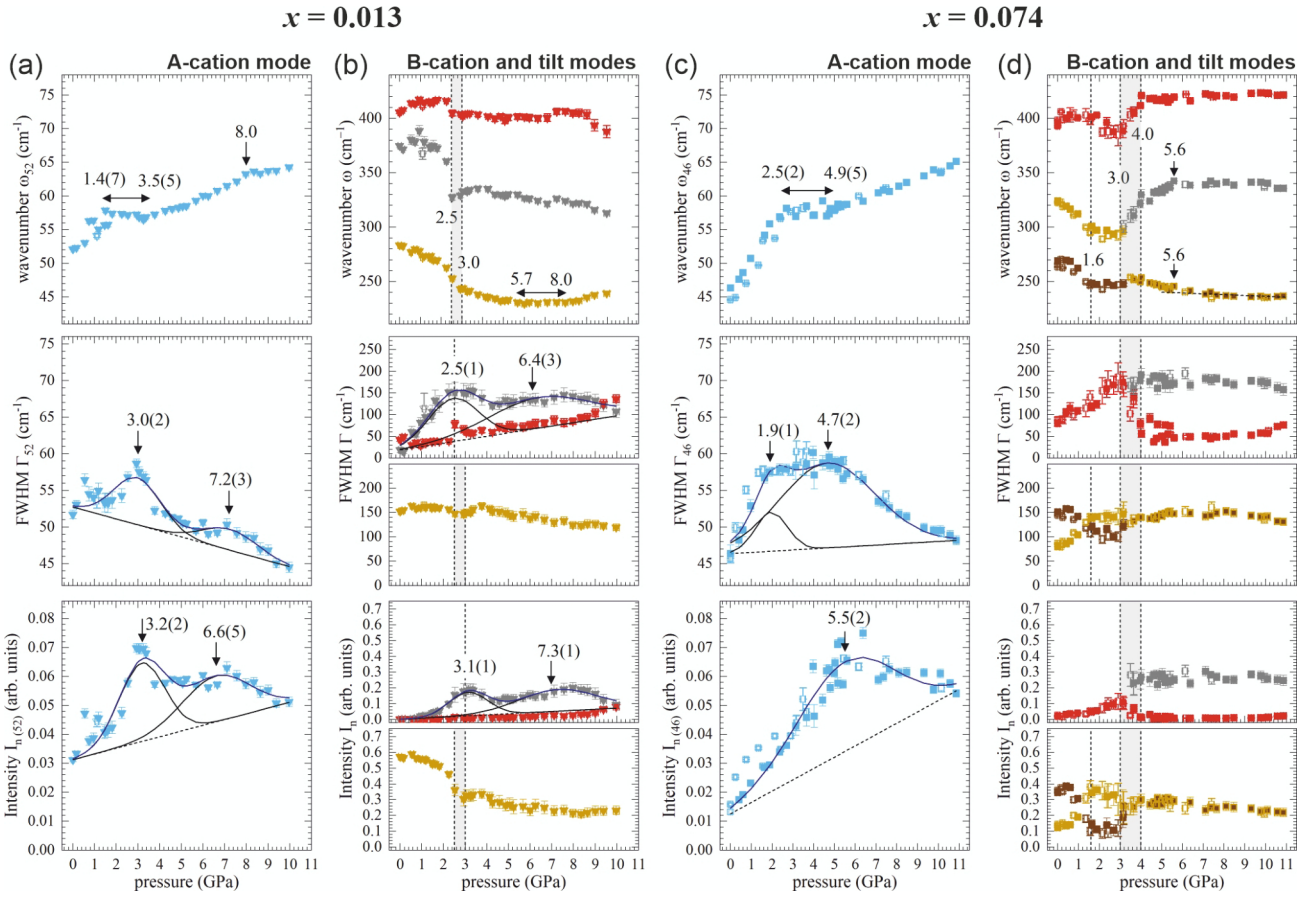


FIG. 8. Pressure dependence of the Raman peak positions (ω), full widths at half maxima (FWHMs; Γ), and fractional intensities (I_n) of selected Raman modes of NBT-xBT with $x = 0.013$ ((a) and (b)) and $x = 0.074$ ((c) and (d)) derived from pseudo-Voigt function fits of $\bar{Z}(XX)Z$ Raman spectra. The pressure dependence of the A-cation localized mode (light blue) is shown in (a) and (c), while that of B-cation localized modes (yellow and brown) and BO_6 tilting modes (red and gray) is shown in (b) and (d). Open symbols correspond to data measured on decompression. The line in the $\omega(p)$ plot in (d) is a linear fit to the data points in the corresponding pressure range. The solid lines in the $\Gamma(p)$ and $I_n(p)$ plots in (a)-(c) are Gaussian fits to the data points with polynomial baselines (dashed lines). The errors in the individual data points stem from the corresponding spectral fit. The errors in the characteristic pressures are derived from Gaussian or linear fits to the data points.

BO_6 vibrations are observed in the range 470-860 cm^{-1} [23]. Lower-energy phonon modes are more sensitive to phase transitions than higher-energy phonon modes which are related to internal vibrations of the primary building units (e.g. [52]). Therefore, in the following we focus on the spectral range <450 cm^{-1}. The pressure dependence of the spectral parameters of the internal BO_6 stretching modes at ~660-860 cm^{-1} are shown in Fig. S7 in the Supplemental Material [29]. The unconstrained fits resulted in a large dispersion of the relative intensities of the Raman scattering in the range 450-650 cm^{-1} for some pressure points and hence, we will not discuss theses trends here.

The pressure dependencies of ω, Γ and $I_n(p)$ derived from $\bar{Z}(XX)Z$ and $\bar{Z}(XY)Z$ spectra are given in Fig. 8 and Fig. S8 in the Supplemental Material [29], respectively. Below, we will mainly discuss the trends obtained by fitting the $\bar{Z}(XX)Z$ spectra because, with a couple of exceptions discussed later in the text, the corresponding trends obtained from ($\bar{Z}(XY)Z$) spectra do not provide significantly different information.

As can be seen in Figs. 7, 8 and S8, $\omega(p)$, $\Gamma(p)$ and $I_n(p)$ show anomalous non-linear behavior, indicating a sequence of pressure-induced structural alterations. The phonon evolution with pressure reveals three types of structural transformations, which resemble those observed for NBT-x_{MPB}BT and/or pure NBT [21]:

1. At ambient pressure the presence of Ba^{2+} induces a local anisotropy of the BO_6 octahedra, resulting in the presence of two distinguishable Raman peaks in the range of off-centered B-cation vibrations (240-325 cm^{-1}). The higher- and lower-wavenumber components are related to B-cation vibrations along the polar axis and within the plane perpendicular to the polar axis, respectively [53]. For NBT-0.013BT the lower-wavenumber component could be clearly distinguished only in the $\bar{Z}(XY)Z$ spectra (Fig. 7a). Upon pressure increase, both the lower and higher

energy component of the B-cation localized mode anomalously soften. The two components become undistinguishable above ∼0.2 GPa for $x = 0.013$ (Fig. 7a and Fig. S8 in the Supplemental Material [29]), ∼1.0 GPa for $x = 0.048$ [21] and ∼3.5GPa for $x = 0.074$ (Fig. 7b and 8d), although there is no obvious reduction of the wavenumber difference, implying that pressure increases mainly the orientation disorder of local B-site dipoles. For $x = 0.048$ and $x = 0.074$ this is preceded by a minimum of $\omega(p)$ of the lower-energy component at ∼0.5 GPa [21] and ∼1.6 GPa (Fig. 8d), respectively, indicating the beginning of rearrangement within the B-site subsystem.

2. In accordance with the XRD data, upon further pressure increase a phase transition takes place, involving the development of anti-polar A-cation order, reduction of polar B-cation displacements, enhancement of octahedral tilts and a change in the tilt pattern. In the Raman spectra these alterations are indicated by several anomalies that take place over a pressure range. The A-cation localized mode shows a plateau-like $\omega(p)$ trend (1.4-3.5 GPa for $x = 0.013$, 1.9-4.3 GPa for x=0.048 [21], 2.5-4.9 GPa for $x = 0.074$), which is accompanied by maxima in $\Gamma(p)$ and $I_n(p)$ (Fig. 8a and c). Within the same pressure ranges, the B-cation localized mode is strongly shifted to lower wavenumbers and decreases in intensity (Fig. 8b and d), as polar B-cation shifts are reduced. The BO_6 tilting modes likewise show peculiar behavior. For NBT-0.013BT two weak BO_6 tilt modes are detectable at ω_{375} and ω_{405} at ambient pressure, which gain intensity and broaden upon pressure increase, as octahedral tilting is enhanced, whereby the I_n and Γ increase of ω_{375} is stronger than that of ω_{405} (Fig. 8b). At 2.5 GPa the tilt modes are abruptly shifted to lower wavenumbers and at the same pressure there is a maximum in $\Gamma(p)$ followed by a maximum of $I_{n(375)}(p)$ at 3.1(1) GPa, indicating that this is the pressure range in which the BO_6 tilt pattern changes. For NBT-0.074BT at ambient pressure only one BO_6 tilt mode can be identified at ω_{398}, which broadens and gains intensity with increasing pressure (Fig. 8d). It is shifted to lower wavenumbers at 1.9-3.0 GPa, where a second tilt mode can be distinguished near 310 cm^{-1}. Upon further pressure increase both BO_6 tilt modes are shifted to higher wavenumbers, until $\omega(p)$ remains constant above 4.0 and 5.6 GPa, respectively. The FWHM and fractional intensity of the newly formed BO_6 tilt mode remain constant up to 10 GPa, while the $\Gamma(p)$ and $I_n(p)$ of the pre-existing mode are strongly reduced. All these developments show that for NBT-0.074BT alterations in the BO_6 tilt pattern take place over the pressure range 1.9-5.6 GPa.

3. In the Raman spectra of NBT-0.013BT a third structural alteration is indicated by a broad minimum of the B-cation mode at 5.7-8.0 GPa and a change in $d\omega/dp$ of the A-cation mode, accompanied by maxima in Γ and I_n of the A-cation and BO_6 tilting modes measured in scattering geometry $\bar{Z}(XX)Z$ (Fig. 8a and b). Furthermore, in the $\bar{Z}(XY)Z$ geometry a third tilt mode becomes distinguishable at 6 GPa at ∼ 391 cm^{-1} (see Fig. 7a and Fig. S9 in the Supplemental Material [29]). A $\omega(p)$ minimum of the B-cation localized mode and the splitting of BO_6 tilt modes has also been observed in pure NBT at 5 GPa [15, 21], and may indicate that from this point onward

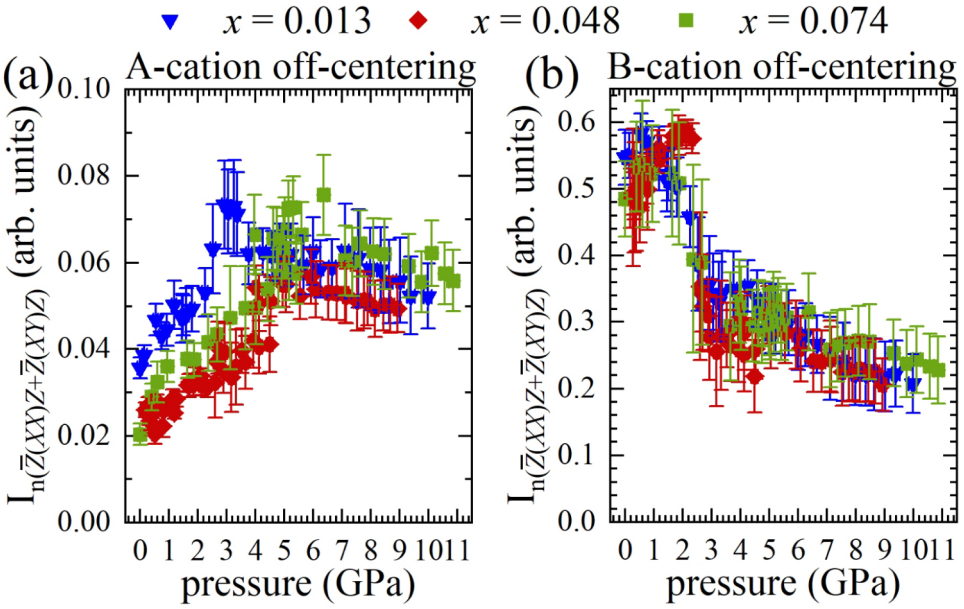


FIG. 9. Pressure dependence of the total fractional intensity $I_{n(XX+XY)}(s) = [I_{XX}(s) + I_{XY}(s)]/\sum_i[I_{XX}(s) + I_{XY}(s)]$ of the (a) A-cation and (b) B-cation localized modes in NBT-xBT with $x = 0.013$ (blue triangles), $x = 0.048$ (red diamonds), x = 0.074 (green squares), where $I_{XX}(s)$ and $I_{XY}(s)$ are the integrated Raman intensities of a phonon mode (s) measured in $\bar{Z}(XX)Z$ and $\bar{Z}(XY)Z$ scattering geometry.

B-cation off-centering displacements are not further reduced with increasing pressure and a further adjustment of the BO_6 tilt pattern takes place [21]. Also for NBT-0.11BT a minimum has been reported to exist at 9-10 GPa [54]. In contrast, no wavenumber minimum of the B-cation localized mode or BO_6 tilt mode splitting is observed for NBT-0.074BT up to 10 GPa. Instead, the B-cation mode anomalously softens with the pressure increase, as in the case of NBT-0.048BT [21]. The softening indicates evolving disorder in the B-cation subsystem and the comparison of $\omega(p)$ slopes ($d\omega/dp = -2.30$ above 4.5 GPa for $x = 0.048$ $d\omega/dp = -0.77$ above 5.6 GPa for $x = 0.074$) reveals that the process is more pronounced for the MPB composition. The Ba-enhanced disorder in the B-site local dipoles at high pressures seems to corroborate the Ba-enhanced relaxor behavior at ambient pressure near and just above the MPB [13]. The fraction of the off-centered A- and B-cations can be estimated by considering the fractional intensity I_n at the corresponding wavenumbers. Since I_n of a mode is not the same when measured in different scattering geometries, the sum of fractional intensities measured at a certain wavenumber in both the parallel polarized ($\bar{Z}(XX)Z$) and cross polarized ($\bar{Z}(XY)Z$) spectra has to be considered. The total fractional intensity was calculated as $I_{n(XX+XY)}(s) = [I_{XX}(s)+I_{XY}(s)]/\sum_i[I_{XX}(s)+I_{XY}(s)]$, where $I_{XX}(s)$ and $I_{XY}(s)$ are the integrated Raman intensities of a phonon mode (s) measured in $\bar{Z}(XX)Z$ and $\bar{Z}(XY)Z$ scattering geometry. The fraction of off-centered B-cations seems to be the same within uncertainties in the low- and high-pressure phase, independent of the Ba content (Fig. 9). The same observation is made for the fraction of off-centered A-site cations in the high-pressure phase, however, in the low-pressure phase it is significantly higher for NBT-0.013BT, which again is in accordance with the large non-orthogonality measured for this compound by XRD at ambient pressure [23]. Compared to pure NBT [21], the fraction of off-centered A- and B-cations in the high-pressure phase is larger for NBT-xBT with $x \in [0.013, 0.074]$.

IV. DISCUSSION

Weak x-ray diffraction peaks at *ooe*, indicative of $a^0a^0c^+$ octahedral tilting, are observed for pure NBT and NBT-xBT with $x = 0.04 - 0.09$ [1, 11, 14, 17, 55] at ambient pressure, but none are present for NBT-0.013BT. The question whether there are no in-phase BO_6 tilts, or whether it is only a matter of correlation length, is answered by Raman spectroscopy. In the $\bar{Z}(XX)Z$ ambient pressure spectra of NBT-0.013BT two peaks are distinguishable at ω_{375} and ω_{405} (Fig. 7a and 8b) in the spectral range where octahedral tilting vibrations are observed. The existence of two octahedral tilt phonon modes indicates the existence of tilts with unequal magnitudes [34]. Our combined XRD and Raman-scattering analyses of all three NBT-xBT compounds indicates that the higher-energy tilt mode is related to in-phase tilting and the lower-energy tilt mode to anti-phase tilting, due to the following arguments:

1. At ambient pressure the dominant BO_6 tilt pattern in NBT-0.074BT is in-phase ($a^0a^0c^+$) (see Fig. 4 and Supplemental Figs. S1, S2 and S4 [29]) and one Raman-active tilt mode is detected at 398 cm^{-1} (Fig. 7 and 8d). Only at higher pressures, when the XRD data reveal that anti-phase tilting becomes dominant, a second Raman-active octahedral tilt mode can be resolved near 320 cm^{-1}.

2. In the Raman spectra of NBT-0.048BT below the phase transition pressure, where anti-phase octahedral tilting is dominant, only the lower-energy tilt mode is detectable [21].

3. For all three compounds ($x = 0.013$, 0.048 and 0.074) the high-pressure phase comprises a mixed octahedral tilt pattern ($a^-b^+a^-$) and the R-point Bragg peaks, which are characteristic of the anti-phase octahedral tilt component, have a higher intensity than the M-point Bragg peaks, which are indicative of the in-phase octahedral tilt component (Supplemental Figs. S2 and S4 [29] and [1]). At the same time, above p_c the lower-energy Raman peak (near 375 cm^{-1}) is stronger than the higher-energy Raman peak (near 398 cm^{-1}) for all three compounds (see Fig. 7 and 8b and d).

We were not able to resolve any BO_6 tilt mode up to 2.7 GPa in the Raman spectra of NBT-0.048BT [21], although XRD data reveal the existence of BO_6 tilts in this compound [1] already at ambient pressure. This is most likely due to the enhanced degree of local tilt disorder at the MPB [13] and the consequent broadening of the corresponding Raman signal as well as the strong overlap with the Raman peaks generated by B-cation localized modes (see Fig. 7). Therefore, the fact that BO_6-tilt Raman peaks could not be resolved in NBT-0.048BT at low pressures does not contradict the proposed assignment of the Raman peaks near 320-375 cm^{-1} and 390-410 cm^{-1} to anti- and in-phase octahedral tilting, respectively.

In pure NBT both tilt modes can be resolved already at ambient pressure [21], corroborating the presence of nanoregions with in-phase tilted octahedra inside a pseudorhombohedral matrix containing anti-phase octahedral tilts [16]. An in-phase tilt mode could be resolved also in the ambient-pressure Raman spectrum of NBT-0.013BT, indicating a short length of correlation, insufficient to be detected in XRD experiments.

The disturbance of the correlation length of $a^0a^0c^+$ BO_6 tilts in the tetragonal type platelets existing in the NBT structure upon adding $x = 0.013$ $BaTiO_3$ indicates that the Ba^{2+} cations preferentially accumulate in these platelets. $BaTiO_3$ is tetragonal, therefore it is convenient for Ba^{2+} cations to be incorporated where there are already tetragonal

TABLE I. Isothermal phonon Grüneisen parameters γ_T of NBT-xBT ($\gamma_T = \frac{\beta_\omega}{\beta_V}$, $\beta_\omega = \frac{1}{\omega_0}\frac{d\omega}{dp}$, $\beta_V = -\frac{1}{V}\frac{dV}{dp} = \frac{1}{K_T}$, where β_ω is the phonon compressibility, β_V is the volume compressibility and K_T is the isothermal bulk modulus). The phonon compressibility β_ω is derived from linear fits of $\omega(p)$ in scattering geometry $\bar{Z}(XX)Z$. For the A-cation and B-cation modes the linear fits are applied between ambient p and the first pressure at which $(\frac{d\omega}{dp})_T$ changes; for the internal BO_6 stretching modes the linear fits are applied between ambient pressure and p_c. The corresponding data on $x = 0$ and $x = 0.048$ are published in Rösche *et al.* [21]. The bulk moduli K_T used are 95.2 GPa for pure $x = 0$ [57] and 83.5(1.7) GPa for $x = 0.048$ [21]. For $x = 0.013$ and $x = 0.074$, K_T is estimated to be 92.1 and 77.3 GPa, respectively, based on a simplified linear extrapolation to data for $x = 0$ and 0.048, which is characteristic of $K(x)$ dependence of solid solutions [58].

$x = 0$		$x = 0.013$		$x = 0.048$		$x = 0.074$		
ω_0	γ_T	ω_0	γ_T	ω_0	γ_T	ω_0	γ_T	mode assignment
47.6(4)	**8.1(8)**	52.1(1)	**6.0(1.0)**	46.0(1)	**10.9(7)**	46.4(2)	**8.2(5)**	A-cation localized mode
286.1(1)	**-2.5(5)**	283.5(1)	**-2.4(3)**	310.5(5)	**-6.1(2)**	324.3(3)	**-3.2(1)**	B-cation localized mode
788.1(1.3)	**0.2(1)**	763.9(2.2)	**0.3(1)**	777.3(1.3)	**0.5(1)**	781.7(2.2)	**0.4(1)**	internal BO_6 stretching mode
861.7(7)	**0.2(1)**	855.1(1.0)	**0.4(1)**	859.9(7)	**0.2(1)**	861.7(1.0)	**0.3(1)**	internal BO_6 stretching mode

type defects within the pseudorhombohedral NBT structure.

For NBT-0.074BT the amount of Ba^{2+} cations in the structure is high enough for the material to be dominated by tetragonal structural features. However, the rod-like XDS at the M-points (*ooe*) indicates a two-dimensional correlation of in-phase tilting. This may be due to the persistence of regions in the structure with anti-phase BO_6 tilts as well as due to the existence of tilt-free regions, which emerge with increasing $BaTiO_3$ content [39].

It is interesting to compare also the isothermal phonon Grüneisen parameters γ_t across the MPB (Table I). We have considered only a few phonon modes, which exhibited a linear $\omega(p)$ trend below p_c. In general, phonon Grüneisen parameters of optical modes vary between 0 and 1 in a stable solid-state phase [56]. As can be seen in Table I, the internal BO_6 stretching modes at ∼770 and ∼850 cm^{-1} show phonon Grüneisen parameters of low values, near 0.35 on average, and no specific dependence on the amount of Ba, that is, BO_6 stretching vibrations are not involved in the pressure-induced phase transition, nor in the x-induced structural crossover at ambient conditions. In strong contrast, the phonon Grüneisen parameters of the A-cation mode near 47 cm^{-1} are much larger than unity, while those of the B-cation mode near 300 cm^{-1} are negative. The latter underlines the strong instability of correlated polar shifts of B-site cations upon pressure increase. The largest magnitude of the phonon Grüneisen parameter for the A-cation mode emphasizes that the atomic dynamics of off-centered A-site cations is the microscopic driving force of the phase transition upon pressure. Moreover, for both A-cation and B-cation-localized modes γ_t in absolute value is largest for x_{MPB}. This reveals that the response of both the subsystems of off-centered A-site cations and of off-centered B-site cations to external elastic stimuli is strongest at the MPB.

V. SUMMARY AND CONCLUSIONS

The high-pressure phase of NBT-xBT with $x = 0 - 0.074$ is orthorhombic $Pnma$, independent of the symmetry of the low-pressure structure; a pressure-composition diagram is given in Fig. 10. The critical phase transition pressure p_c as well as the pressure ranges of structural transformations preceding the phase transition vary with x_{Ba} (Table II). The suppression of the B-cation off-center displacements is a precondition for the development of anti-polar A-cation shifts and a mixed octahedral tilt pattern. Since the presence of Ba^{2+} in the structure stabilizes B-cation polar shifts at high pressure compared to pure NBT [21], this may be one reason for the Ba-induced shift of p_c to higher pressure. Moreover, our data indicate that the development of mixed octahedral tilting is predominantly realized via rearrangements of the $a^0a^0c^+$ in-phase tilts.

Furthermore, novel conclusions can be drawn on how Ba^{2+} cations are incorporated in the NBT structure: for a very low amount ($x = 0.013$), the Ba^{2+} cations predominantly accumulate in the preexisting tetragonal nanoregions (see the sketch in Fig. 11a) and disturb the correlation length of the in-phase tilts, while the (pseudo)rhombohedral matrix remains mostly unchanged. The exceptionally large unit-cell non-orthogonality of this compound [23], may be explained by an increased displacement and higher fraction of off-centered A-cations.

For NBT-0.048BT (x_{MPB}) Ba^{2+} cations are randomly dispersed in both tetragonal nanoregions and the rhombohedral matrix, disturbing the correlation length in both tetragonal nanoregions and the rhombohedral matrix. This results in rhombohedral nanodomains inside a pseudocubic matrix [1] (Fig. 11b).

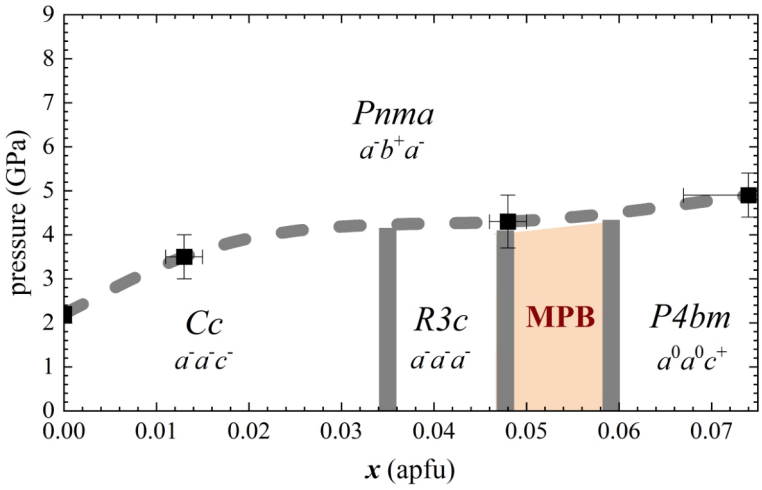


FIG. 10. Pressure-composition phase diagram of NBT-xBT for $x \in [0; 0.074]$. The phase-transition pressures are determined by combining XRD data and the $\omega(p)$ minimum (upper limit of the plateau-like minimum) of the Raman-active A-cation phonon modes (this work, Rösche et al. [21], [1] and Kreisel *et al.* [15]). The dashed line is a spline interpolation to data points, and is merely a guide for the eye. The vertical solid lines denote the compositions at which structural alterations occur at ambient conditions, after Ma *et al.* 2013 [9].

TABLE II. Pressure-induced structural transformations and the corresponding characteristic pressures for NBT-xBT with $0 \leq x \leq 0.074$. Please note that for $x = 0.074$ no XRD data were collected between 4.5-6.3 GPa.

$x = 0$		$x = 0.013$		$x = 0.048$		$x = 0.074$		
Raman[a]	XRD[b]	Raman	XRD	Raman[a]	XRD[c]	Raman	XRD	Structural transformation
-	-	-	-	0.5-1.0		1.6-3.2		rearrangements of the B-site cations, suppression of the Ba-induced uniaxial local BO_6 anisotropy
-	-	-	-		0.7		1.7-2.3	similar structural state as pure NBT at ambient p
1.5-2.2	1.6-3.7	1.4-3.5	1.8-3.9	1.9-4.3	2.8-5.0	2.5-4.9	3.3-6.3	development of antipolar order of A-cation off-center shifts
1.6-2.2	1.6-3.7	1.3-3.2	1.2-3.9	2.7-4.5	2.8-5.0	1.9-2.9 2.9-5.6	0.5-2.3	development of mixed BO_6-tilt pattern
3.7	2.8-3.7	3.0	2.5-3.9	4.8	4.4-5.0	4.7	4.5-6.3	Suppression of the directional dispersion of A-cation off-center shifts and increasing of the length of coherence of correlated anti-phase A-cation shifts
2.2(1)	**2.0**	**3.5(5)**	**3.9**	**4.3(6)**	**4.6(1)**	**4.9(5)**	**4.5-6.3**	**phase transition pressure** p_c
5.0	-	5.7-8.0	-	4.5	-	5.6	-	slowdown of the suppression of B-cation off-centering
5.0	-	5.7-8.0	-	-	-	-	-	further alteration of BO_6-tilt pattern

[a]Rösche *et al.* [21], [b]Kreisel *et al.* [15], [c]Rösche *et al.* [1]

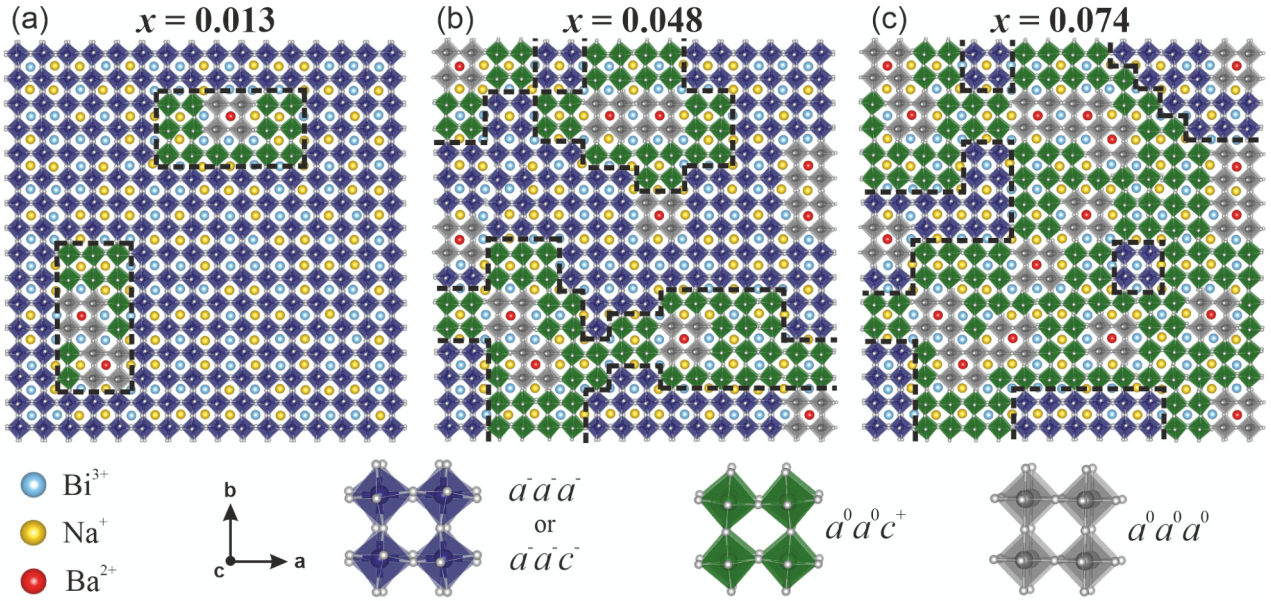


FIG. 11. Sketch of the octahedral tilt patterns and Ba^{2+} cation distribution in NBT-xBT with x (a) below ($x = 0.013$), (b) at ($x = 0.048$) and (c) above ($x = 0.074$) the morphotropic phase boundary at ambient pressure and room temperature. A-site Ba^{2+} is assumed to locally suppress the BO_6 titling [39, 59]. The **a**, **b** and **c** axes correspond to cubic symmetry.

For NBT-0.074BT Ba^{2+} are likewise dispersed in both the rhombohedral and tetragonal fractions. This is evident from the fact that at high pressure, but below p_c, the structural state of NBT-0.074BT resembles that of pure NBT at ambient pressure, as a result of the opposing effect of external pressure (favoring anti-phase tilting and the rhombohedral structure) to the effect of Ba-induced local "chemical pressures" (favoring the tetragonal structure). The Ba-induced tetragonal-type defects in the rhombohedral fraction facilitate the expansion of tetragonal distortions, leading to the formation of a dominant tetragonal matrix with in-phase tilts ($P4bm$). However, the structure is still heterogeneous due to remnants of the rhombohedral matrix and Ba-induced tilt-free regions (see Fig. 11c).

For $x = 0.074$ and $x = 0.048$ periodically arranged layers modulating the structure exist already at room temperature and ambient pressure. Our data on NBT-0.074BT show that the structural modulation does not change when the pressure approaches p_c from below and disappears above p_c, when the structure adopts $Pnma$ symmetry. The latter supports the previously proposed model that the modulating layers are of $Pnma$ type [45], with mixed octahedral tilts and antipolar A-cation shifts, which can relax the strain in both the tilt system and the A-sublattice.

ACKNOWLEDGMENTS

The authors thank Dr. Alexander Kurnosov, Universität Bayreuth, for help with DAC loading. Financial support by the Deutsche Forschungsgemeinschaft (No. MI 1127/12-1 and No. BO 2550/10-1) is gratefully acknowledged. We acknowledge DESY (Hamburg, Germany), a member of the Helmholtz Association HGF, for the provision of experimental facilities. Experiments were carried out at PETRA III using beamline P24 (beamtime allocated to project I-20220769); pressure was measured using the facilities at the P02.2 beamline.

[1] C. Rösche, T. Boffa Ballaran, T. Malcherek, C. Paulmann, R. J. Angel, S. Gorfman, and B. Mihailova, The high-pressure structure of (1-x)$Na_{0.5}Bi_{0.5}TiO_3$ -x$BaTiO_3$ at the morphotropic phase boundary, Scientific reports **14**, 18799 (2024).
[2] P. Fan, K. Liu, W. Ma, H. Tan, Q. Zhang, L. Zhang, C. Zhou, D. Salamon, S.-T. Zhang, Y. Zhang, B. Nan, and H. Zhang, Progress and perspective of high strain NBT-based lead-free piezoceramics and multilayer actuators, Journal of Materiomics **7**, 508 (2021).
[3] D. Zhou, K. H. Lam, Y. Chen, Q. Zhang, Y. C. Chiu, H. Luo, J. Dai, and H. L. W. Chan, Lead-free piezoelectric single crystal based 1–3 composites for ultrasonic transducer applications, Sensors and Actuators A: Physical **182**, 95 (2012).

[4] X. Lu, J. Xu, L. Yang, C. Zhou, Y. Zhao, C. Yuan, Q. Li, G. Chen, and H. Wang, Energy storage properties of $(Bi_{0.5}Na_{0.5})_{0.93}Ba_{0.07}TiO_3$ lead-free ceramics modified by La and Zr co-doping, Journal of Materiomics **2**, 87 (2016).

[5] E. Lee and J. Y. Son, Energy storage and ferroelectric properties of flexible 1-x$(Na_{0.5}Bi_{0.5}TiO_3)$-x$BaTiO_3$ thin films on Pt/mica substrates, Journal of Energy Storage **77**, 109945 (2024).

[6] C. Ma, X. Tan, E. Dul'kin, and M. Roth, Domain structure-dielectric property relationship in lead-free (1-x)$(Bi_{1/2}Na_{1/2})TiO_3 - x BaTiO_3$ ceramics, Journal of Applied Physics **108**, 10.1063/1.3514093 (2010).

[7] G. Das Adhikary, G. J. Muleta, and R. Ranjan, Composition–electric field phase diagram of the Pb-free piezoelectric system $Na_{0.5}Bi_{0.5}TiO_3 - BaTiO_3$, Physical Review B **108**, 10.1103/PhysRevB.108.224105 (2023).

[8] I. Levin and I. M. Reaney, Nano– and mesoscale structure of $Na_{0.5}Bi_{0.5}TiO_3$: A TEM perspective, Advanced Functional Materials **22**, 3445 (2012).

[9] C. Ma, H. Guo, and X. Tan, A new phase boundary in $(Bi_{1/2}Na_{1/2})TiO_3$ - $BaTiO_3$ revealed via a novel method of electron diffraction analysis, Advanced Functional Materials **23**, 5261 (2013).

[10] A. M. Glazer, The classification of tilted octahedra in perovskites, Acta Crystallographica Section B Structural Crystallography and Crystal Chemistry **28**, 3384 (1972).

[11] P. K. Tung, M. Major, J. Hudspeth, and J. E. Daniels, Compositional dependence of disordered structures in $Na_{1/2}Bi_{1/2}TiO_3$-$BaTiO_3$ solid solutions, Materials Research Bulletin **106**, 301 (2018).

[12] D. I. Woodward and I. M. Reaney, Electron diffraction of tilted perovskites, Acta Crystallographica. Section B, Structural Science **61**, 387 (2005).

[13] P. B. Groszewicz, M. Gröting, H. Breitzke, W. Jo, K. Albe, G. Buntkowsky, and J. Rödel, Reconciling local structure disorder and the relaxor state in $(Bi_{1/2}Na_{1/2})TiO_3$ -$BaTiO_3$, Scientific Reports **6**, 31739 (2016).

[14] W. Ge, C. Luo, C. P. Devreugd, Q. Zhang, Y. Ren, J. Li, H. Luo, and D. Viehland, Direct evidence of correlations between relaxor behavior and polar nano-regions in relaxor ferroelectrics: A case study of lead-free piezoelectrics $Na_{0.5}Bi_{0.5}TiO_3 - x\%BaTiO_3$, Applied Physics Letters **103**, 10.1063/1.4846655 (2013).

[15] J. Kreisel, P. Bouvier, B. Dkhil, P. A. Thomas, A. M. Glazer, T. R. Welberry, B. Chaabane, and M. Mezouar, High-pressure x-ray scattering of oxides with a nanoscale local structure: Application to $Na_{0.5}Bi_{0.5}TiO_3$, Physical Review B **68**, 10.1103/PhysRevB.68.014113 (2003).

[16] R. Beanland and P. A. Thomas, Imaging planar tetragonal sheets in rhombohedral $Na_{0.5}Bi_{0.5}TiO_3$ using transmission electron microscopy, Scripta Materialia **65**, 440 (2011).

[17] C. Luo, D. Bansal, J. Li, D. Viehland, B. Winn, Y. Ren, X. Li, H. Luo, and O. Delaire, Neutron and x-ray scattering study of phonon dispersion and diffuse scattering in $(Na,Bi)TiO_3 - xBaTiO_3$ single crystals near the morphotropic phase boundary, Physical Review B **96**, 10.1103/PhysRevB.96.174108 (2017).

[18] H. Zhang, G. Deng, A. J. Studer, X. Li, X. Zhao, and H. Luo, Neutron diffuse scattering of (1-x)$(Na_{0.5}Bi_{0.5})TiO_3 - xBaTiO_3$ relaxor ferroelectric single crystals, Scripta Materialia **86**, 5 (2014).

[19] B. Mihailova, R. J. Angel, B. J. Maier, A.-M. Welsch, J. Zhao, M. Gospodinov, and U. Bismayer, The structural state of lead-based relaxor ferroelectrics under pressure, IEEE Transactions on Ultrasonics, Ferroelectrics, and Frequency Control **58**, 1905 (2011).

[20] P. A. Thomas, J. Kreisel, A. M. Glazer, P. Bouvier, Q. Jiang, and R. Smith, The high-pressure structural phase transitions of sodium bismuth titanate, Zeitschrift für Kristallographie - Crystalline Materials **220**, 717 (2005).

[21] C. Rösche, T. Boffa-Ballaran, and B. Mihailova, Pressure-induced structural transformations in (1-x)$Na_{0.5}Bi_{0.5}TiO_3 - xBaTiO_3$ at the morphotropic phase boundary, Physical Review B **108**, 10.1103/PhysRevB.108.094110 (2023).

[22] M. Woll, M. Burianek, D. Klimm, S. Gorfman, and M. Mühlberg, Characterization of $(Bi_{0.5}Na_{0.5})_{1-x}BaTiO_3$ grown by the TSSG method, Journal of Crystal Growth **401**, 351 (2014).

[23] G. de La Flor, T. Malcherek, S. Gorfman, and B. Mihailova, Structural transformations in (1-x)$Na_{0.5}Bi_{0.5}TiO_3 - xBaTiO_3$ single crystals studied by Raman spectroscopy, Physical Review B **96**, 10.1103/PhysRevB.96.214102 (2017).

[24] R. Boehler and K. de Hantsetters, New anvil designs in diamond-cells, High Pressure Research **24**, 391 (2004).

[25] G. Shen, Y. Wang, A. Dewaele, C. Wu, D. E. Fratanduono, J. Eggert, S. Klotz, K. F. Dziubek, P. Loubeyre, O. V. Fat'yanov, P. D. Asimow, T. Mashimo, and R. M. M. Wentzcovitch, Toward an international practical pressure scale: A proposal for an IPPS ruby gauge (IPPS-ruby2020), High Pressure Research **40**, 299 (2020).

[26] I. Kantor, V. Prakapenka, A. Kantor, P. Dera, A. Kurnosov, S. Sinogeikin, N. Dubrovinskaia, and L. Dubrovinsky, BX90: a new diamond anvil cell design for X-ray diffraction and optical measurements, The Review of Scientific Instruments **83**, 125102 (2012).

[27] Agilent, *CrysAlis PRO*, Agilent Technologies Ltd, Yarnton, Oxfordshire, England (2014).

[28] V. Petříček, M. Dušek, and L. Palatinus, Crystallographic computing system JANA2006: General features, Zeitschrift für Kristallographie - Crystalline Materials **229**, 345 (2014).

[29] See Supplemental Material at [url] for additional XRD and Raman-scattering data, details on structure refinements, and crystallographic information files., .

[30] OriginLab Corporation, OriginPro, Version 2024b, Northampton, MA, USA (2024).

[31] Y. Kitanaka, M. Ogino, K. Hirano, Y. Noguchi, M. Miyayama, Y. Kagawa, C. Moriyoshi, Y. Kuroiwa, S. Torii, and T. Kamiyama, Crystal structural analyses of ferrielectric tetragonal $(Bi_{1/2}Na_{1/2})TiO_3$ –7%$BaTiO_3$ powders and single crystals, Japanese Journal of Applied Physics **52**, 09KD01 (2013).

[32] S. Gorfman and P. A. Thomas, Evidence for a non-rhombohedral average structure in the lead-free piezoelectric material $Na_{0.5}Bi_{0.5}TiO_3$, Journal of Applied Crystallography **43**, 1409 (2010).

[33] P. A. Thomas, S. Trujillo, M. Boudard, S. Gorfman, and J. Kreisel, Diffuse X-ray scattering in the lead-free piezoelectric

crystals $Na_{1/2}Bi_{1/2}TiO_3$ and Ba-doped $Na_{1/2}Bi_{1/2}TiO_3$, Solid State Sciences **12**, 311 (2010).
[34] B. J. Maier, N. Waeselmann, B. Mihailova, R. J. Angel, C. Ederer, C. Paulmann, M. Gospodinov, A. Friedrich, and U. Bismayer, Structural state of relaxor ferroelectrics $PbSc_{0.5}Ta_{0.5}O_3$ and $PbSc_{0.5}Nb_{0.5}O_3$ at high pressures up to 30 GPa, Physical Review B **84**, 10.1103/PhysRevB.84.174104 (2011).
[35] N. Zhang, M. Paściak, A. M. Glazer, J. Hlinka, M. Gutmann, H. A. Sparkes, T. R. Welberry, A. Majchrowski, K. Roleder, Y. Xie, and Z.-G. Ye, A neutron diffuse scattering study of $PbZrO_3$ and Zr-rich $PbZr_{1-x}Ti_xO_3$, Journal of Applied Crystallography **48**, 1637 (2015).
[36] M. Paściak, M. Wołcyrz, and A. Pietraszko, Interpretation of the diffuse scattering in Pb-based relaxor ferroelectrics in terms of three-dimensional nanodomains of the ⟨110⟩-directed relative interdomain atomic shifts, Physical Review B **76**, 10.1103/PhysRevB.76.014117 (2007).
[37] G. Xu, Z. Zhong, H. Hiraka, and G. Shirane, Three-dimensional mapping of diffuse scattering in $Pb(Zn_{1/3}Nb_{2/3})O_3 - xPbTiO_3$, Physical Review B **70**, 10.1103/PhysRevB.70.174109 (2004).
[38] A. Bosak, D. Chernyshov, S. Vakhrushev, and M. Krisch, Diffuse scattering in relaxor ferroelectrics: true three-dimensional mapping, experimental artefacts and modelling, Acta Crystallographica Section A **68**, 117 (2012).
[39] A.-K. Fetzer, A. Wohninsland, K. V. Lalitha, and H.-J. Kleebe, Nanoscale polar regions embedded within ferroelectric domains in $Na_{1/2}Bi_{1/2}TiO_3$−$BaTiO_3$, Physical Review Materials **6**, 10.1103/PhysRevMaterials.6.064409 (2022).
[40] H. Liu, Q. Zhang, H. Luo, and J. Zhu, Direct observations of electric-field-induced domain switching and phase transition in $0.95Na_{0.5}Bi_{0.5}TiO_3$-$0.05BaTiO_3$ single crystals using in situ transmission electron microscopy, Applied Physics Letters **120**, 10.1063/5.0083165 (2022).
[41] A. Neagu and C.-W. Tai, Investigation of local structural phase transitions in $95Na_{0.5}Bi_{0.5}TiO_3$-$5BaTiO_3$ piezoceramics by means of in-situ transmission electron microscopy, Journal of Applied Physics **123**, 244105 (2018).
[42] O. Aktas, J. R. Duclère, S. Quignon, G. Trolliard, and E. K. H. Salje, Polarity of modulated $Na_{0.5}Bi_{0.5}TiO_3$ and its slow structural relaxation, Applied Physics Letters **113**, 032901 (2018).
[43] G. Trolliard and V. Dorcet, Reinvestigation of phase transitions in $Na_{0.5}Bi_{0.5}TiO_3$ by TEM. Part II: Second order orthorhombic to tetragonal phase transition, Chemistry of Materials **20**, 5074 (2008).
[44] L. Luo, W. Ge, J. Li, D. Viehland, C. Farley, R. Bondnar, Q. Zhang, and H. Luo, Raman spectroscopic study of $Na_{1/2}Bi_{1/2}TiO_3$-x%$BaTiO_3$ single crystals as a function of temperature and composition, Journal of Applied Physics **109**, 113507 (2011).
[45] V. Dorcet, G. Trolliard, and P. Boullay, Reinvestigation of phase transitions in $Na_{0.5}Bi_{0.5}TiO_3$ by TEM. Part I: First order rhombohedral to orthorhombic phase transition, Chemistry of Materials **20**, 5061 (2008).
[46] A. M. Balagurov, E. Y. Koroleva, A. A. Naberezhnov, V. P. Sakhnenko, B. N. Savenko, N. V. Ter-Oganessian, and S. B. Vakhrushev, The rhombohedral phase with incommensurate modulation in $Na_{1/2}Bi_{1/2}TiO_3$, Phase Transitions **79**, 163 (2006).
[47] U. Lewczuk-Jodłowiec, J. Suchanicz, D. Sitko, and K. K. and, Thermal properties of NBT-BT systems, Phase Transitions **90**, 818 (2017).
[48] K. Datta, I. Margaritescu, D. A. Keen, and B. Mihailova, Stochastic polarization instability in $PbTiO_3$, Physical Review Letters **121**, 137602 (2018).
[49] M. K. Niranjan, T. Karthik, S. Asthana, J. Pan, and U. V. Waghmare, Theoretical and experimental investigation of Raman modes, ferroelectric and dielectric properties of relaxor $Na_{0.5}Bi_{0.5}TiO_3$, Journal of Applied Physics **113**, 10.1063/1.4804940 (2013).
[50] K. Datta, A. Richter, M. Göbbels, R. B. Neder, and B. Mihailova, Atomistic origin of huge response functions at the morphotropic phase boundary of $(1-x)Na_{0.5}Bi_{0.5}TiO_3-xBaTiO_3$, Physical Review B **90**, 10.1103/PhysRevB.90.064112 (2014).
[51] D. S. Keeble, E. R. Barney, D. A. Keen, M. G. Tucker, J. Kreisel, and P. A. Thomas, Bifurcated polarization rotation in bismuth-based piezoelectrics, Advanced Functional Materials **23**, 185 (2013).
[52] E. Husson, Raman spectroscopy applied to the study of phase transitions, Key Engineering Materials **155-156**, 1 (1998).
[53] G. de La Flor, S. Gorfman, and B. Mihailova, Local-scale structural response of $(1-x)Na_{0.5}Bi_{0.5}TiO_3-xBaTiO_3$ to external electric fields, Applied Physics Letters **114**, 10.1063/1.5070118 (2019).
[54] S. Trujillo, J. Kreisel, Q. Jiang, J. H. Smith, P. A. Thomas, P. Bouvier, and F. Weiss, The high-pressure behaviour of Ba-doped $Na_{1/2}Bi_{1/2}TiO_3$ investigated by Raman spectroscopy, Journal of Physics: Condensed Matter **17**, 6587 (2005).
[55] J. E. Daniels, W. Jo, and W. Donner, High-energy synchrotron x-ray diffraction for in situ diffuse scattering studies of bulk single crystals, Journal of The Minerals, Metals & Materials Society **64**, 174 (2012).
[56] N. W. Ashcroft and N. D. Mermin, *Solid state physics*, international ed. (Saunders College Publ, Philadelphia, 1976).
[57] J. Suchanicz, Elastic constants of $Na_{0.5}Bi_{0.5}TiO_3$ single crystal, Journal of Materials Science **37**, 489 (2002).
[58] F. Béjina, M. Bystricky, N. Tercé, M. L. Whitaker, and H. Chen, Bulk modulus of Fe-rich olivines corrected for non-hydrostaticity, Comptes Rendus Géoscience **351**, 86 (2019).
[59] G. Das Adhikary, B. Mahale, B. N. Rao, A. Senyshyn, and R. Ranjan, Depoling phenomena in $Na_{0.5}Bi_{0.5}TiO_3$-$BaTiO_3$: A structural perspective, Physical Review B **103**, 184106 (2021).

Supplemental Material for Structural transformations in the (1-x)$Na_{0.5}Bi_{0.5}TiO_3$-$x$$BaTiO_3$ solid solution under high pressure: comparison between x below and above the morphotropic phase boundary

Constanze Rösche,[1,*] Thomas Malcherek,[1] Tiziana Boffa Ballaran,[2] Carsten Paulmann,[1] Ross John Angel,[3] Semën Gorfman,[4] and Boriana Mihailova[1,†]

[1] *Department of Earth System Sciences, Universität Hamburg, Grindelallee 48, 20146 Hamburg, Germany*
[2] *Bayerisches Geoinstitut, Universität Bayreuth, Universitätsstraße 30, 95447 Bayreuth, Germany*
[3] *Istituto di Geoscienze e Georisorse, CNR, Corso Stati Uniti 4, 35127 Padova, Italy*
[4] *Department of Materials Science and Engineering, Tel Aviv University, Wolfson Building for Mechanical Engineering, Tel Aviv 6997801, Israel*

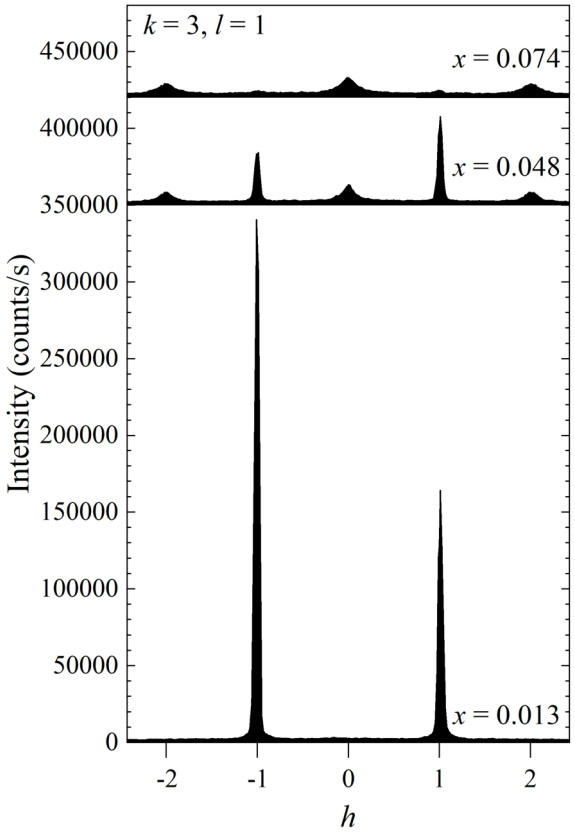


FIG. S1. Combined line scans through h31, h-31, 3k1 and -3k1 in reconstructed reciprocal space layers of NBT-xBT with x = 0.013, 0.048 and 0.074 from synchrotron XRD measurements at ambient pressure in air.

* constanze.roesche@uni-hamburg.de
† boriana.mihaylova@uni-hamburg.de

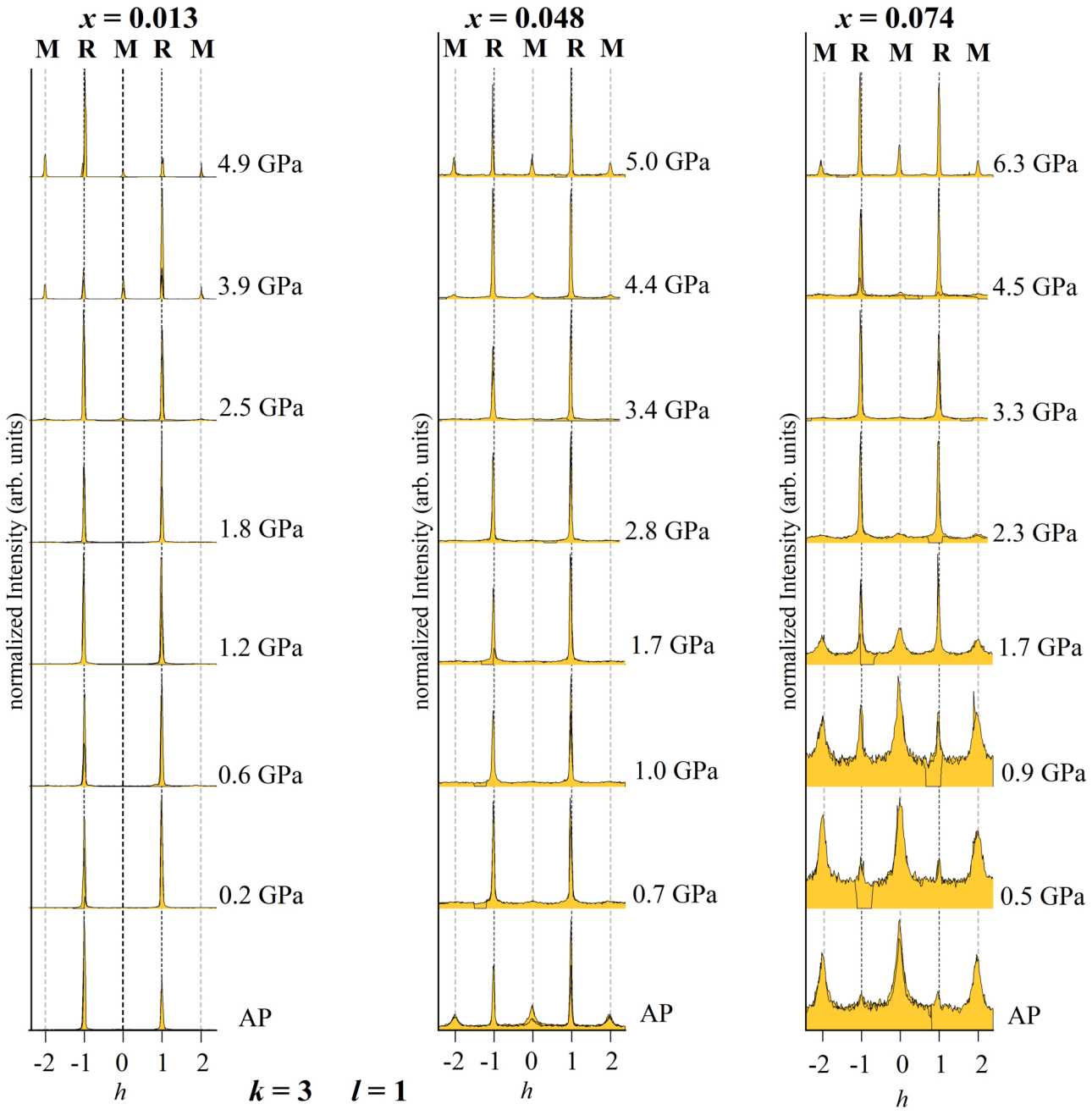


FIG. S2. Combined line scans through $h31$, h-31, $3k1$ and -$3k1$ in reconstructed reciprocal space layers at increasing pressure. The intensities were normalized to the strongest peak in every scan to better reveal the pressure dependence of the ratio between *ooo*- and *ooe*-type reflections for NBT-xBT with x = 0.013, 0.048 and 0.074.

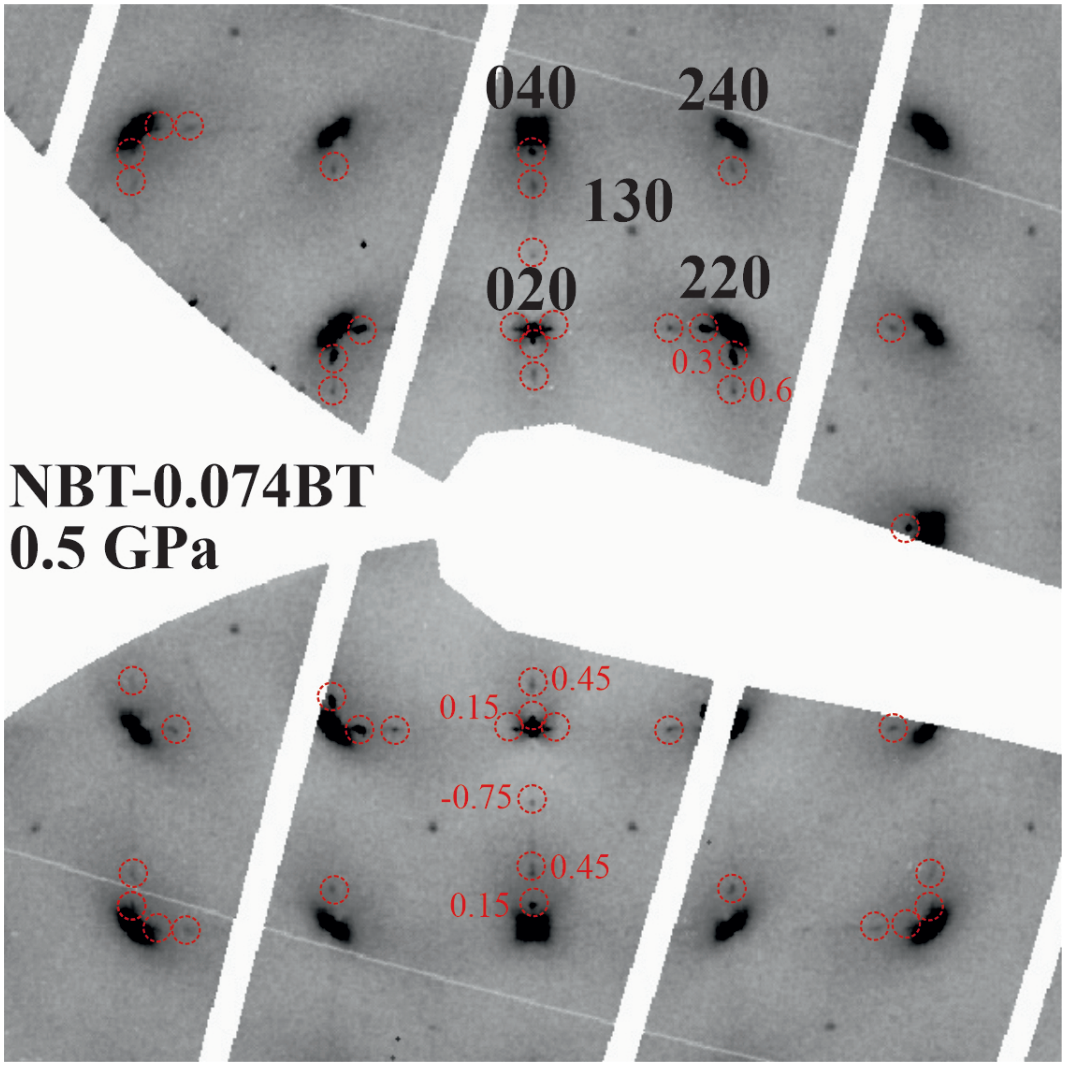


FIG. S3. $hk0$ reciprocal space layer of NBT-0.074BT at 0.5 GPa. The indices refer to a doubled cubic unit cell. Satellite peaks, which are displaced by ∼0.15, 0.3, 0.45, 0.6 and 0.75 r.l.u. towards the lower angle side of *eee* Bragg reflections, are marked by red dashed circles.

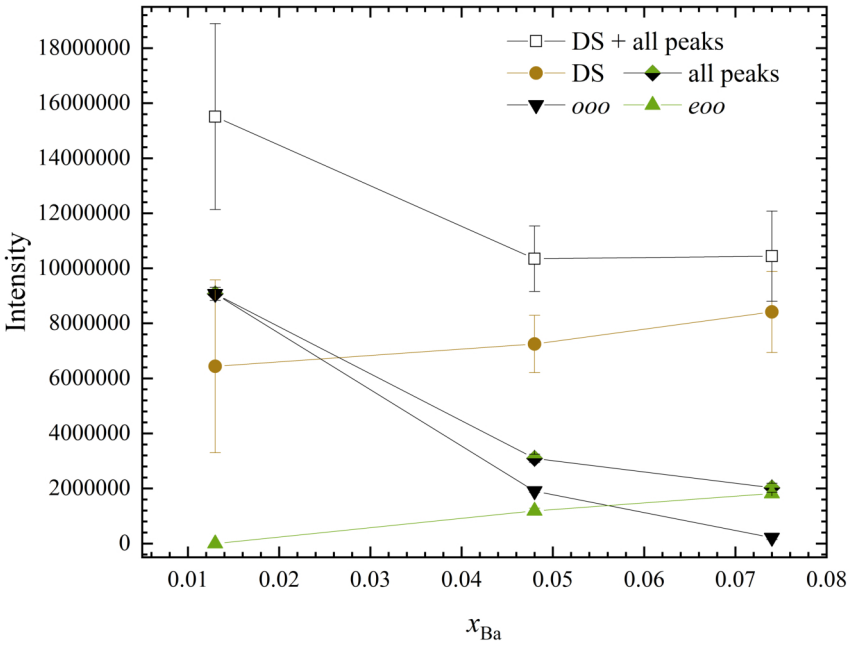


FIG. S4. Comparison of the intensities of the diffuse scattering (DS) and Bragg reflections in the $hk1$ layer at ambient pressure derived from pseudo-Voigt function fits of the line scans through $h31$, h-31, $3k1$ and -$3k1$ in reconstructed reciprocal space layers. The lines are merely a guide to the eye.

TECHNICAL DETAILS OF THE STRUCTURE REFINEMENT

The pixel intensities of the Bragg reflections were integrated with CrysAlisPro [1] using a doubled cubic unit cell. The entire diffraction pattern could be indexed with a single orientation matrix. The structure of the high-pressure phase was refined using Jana2006 [2] based on the squared structure factor F^2. The criterion for convergence was max(change/s.u.) ≤ 0.005 in two consecutive cycles. Further refinement details can be found in the supplemental crystallographic information files (CIFs). The NBT-xBT single crystals actually consist of twin domains of lower symmetry, which all contribute to the resulting pseudocubic diffraction pattern with an intensity proportional to their volume fraction. Six twin domains are included in the refinement model (see Table SI). This matches the number of possible ferroic domains generated by the centrosymmetric distortion of the cubic perovskite cell along ⟨110⟩. The maximum angular difference for a twin overlap was set to 0.1°. The unit cell parameters and statistical values are reported in Table SII. The site occupancy factor of Bi and Na has been fixed to 0.5 and both atoms have been restricted to have the same coordinates and anisotropic displacement parameters (ADPs). The contribution of A-site Ba has been neglected due to its small fraction in the structure ($x = 0.013$ and 0.074 in atoms per formula units). The fractional atomic coordinates and isotropic displacement parameters equivalent to the refined ADPs, U_{eq}, are reported in Table SIII. The displacement parameters of Bi/Na could always be refined as anisotropic (see Table SIV), while the displacement parameters of Ti had to be restrained to be isotropic in order to obtain a reasonable value. The displacement parameters of oxygen atoms were refined as anisotropic for the NBT-0.013BT data set measured in methanol: ethanol 4:1, whereas for the NBT-0.074BT data set measured in He, the oxygen atoms had to be restrained to be isotropic to obtain a reasonable value.

TABLE SI. Twin domains used for the structure refinements of the high-pressure phase of NBT-xBT. The rotation axis of the twinning operations in the orthorhombic symmetry are parallel to the edge and the body diagonals of a cubic unit cell. The volume fractions of the twins composing the sample stem from the refinements in Jana2006 [2]. The uncertainty for the main twin (tw1) is calculated as $\sigma(\text{tw1vol}) = \sqrt{\sigma(\text{tw2vol})^2 + \sigma(\text{tw3vol})^2 + \sigma(\text{tw4vol})^2 + \sigma(\text{tw5vol})^2 + \sigma(\text{tw6vol})^2}$.

		tw1	tw2	tw3	tw4	tw5	tw6
			2-fold rotation around $(\bar{1},0,1)$ ($\|\|[100]_c$)	3-fold rotation around $[\bar{2},1,0]$ ($\|\|[\bar{1}1\bar{1}]_c$)	3-fold rotation around $[2,1,0]$ ($\|\|[111]_c$)	3-fold rotation around $[0,1,2]$ ($\|\|[\bar{1}11]_c$)	3-fold rotation around $[\bar{2},\bar{1},0]$ ($\|\|[\bar{1}\bar{1}\bar{1}]_c$)
	Pressure						
$x =$	(GPa)			fraction			
0.013	3.87(11)	0.504(12)	0.199(9)	0.073(3)	0.067(3)	0.072(5)	0.084(4)
0.074	6.31(12)	0.103(14)	0.115(4)	0.185(5)	0.191(5)	0.178(9)	0.227(7)
0.074	12.22(16)	0.189(12)	0.216(7)	0.168(4)	0.166(5)	0.114(5)	0.147(5)

TABLE SII. Results of the high-pressure structure refinements in space group $Pnma$ of the single-crystal XRD data of NBT-xBT. The parameter b stems from the unit cell refinement with CrysAlisPro [1] using a doubled pseudocubic perovskite cell, while a and c stem from the transformation of the cubic to an orthorhombic unit cell with $a = c = b/\sqrt{2}$ and uncertainties $\Delta a = \Delta c = \Delta b/\sqrt{(}2)$. The R_{int} values refer to orthorhombic symmetry.

$x =$	0.013	0.074	0.074
Pressure (GPa)	3.87(11)	6.31(12)	12.22(16)
Unit cell	$a = 5.4205(2)$,	$a = 5.4019(3)$,	$a = 5.3441(3)$,
parameters (Å)	$b = 7.6658(3)$,	$b = 7.6395(4)$,	$b = 7.5577(4)$,
	$c = 5.4205(2)$	$c = 5.4019(3)$	$c = 5.3441(3)$
R_{int}	0.0189	0.0037	0.0064
R (obs/all)	0.0540/0.0565	0.0520/0.0572	0.0419/0.0457
GoF (obs/all)	1.55/1.43	1.19/1.06	0.98/0.95
Number of reflections (obs/all)	293/351	273/368	292/355
Variables refined	28	20	20

TABLE SIII. Fractional atomic coordinates x, y and z and equivalent isotropic atomic displacement parameters U_{eq} (Å^2) from structure refinements in *Pnma*.

x = 0.013

3.87(11) GPa	x	y	z	U_{eq} [a]
Bi/Na	-0.5245(3)	0.75	0.4976(2)	0.031(1)
Ti	0.5	0.5	0	0.014(1)
O1	-0.7820(9)	-0.0293(7)	0.2178(11)	0.020(2)
O2	-0.5101(12)	0.25	1.060(2)	0.017(2)

x = 0.074

6.31(12) GPa	x	y	z	U_{eq} [b]
Bi/Na	-0.5181(2)	0.75	0.4998(3)	0.024(1)
Ti	0.5	0.5	0	0.006(1)
O1	-0.7781(11)	-0.0279(7)	0.2227(12)	0.017(1)
O2	-0.5056(10)	0.25	1.047(2)	0.011(2)

12.22(16) GPa	x	y	z	U_{eq} [b]
Bi/Na	-0.5203(2)	0.75	0.4975(2)	0.015(1)
Ti	0.5	0.5	0	0.005(1)
O1	-0.7846(12)	-0.0308(5)	0.2174(13)	0.015(1)
O2	-0.5069(13)	0.25	1.0607(13)	0.011(2)

[a]data set measured in methanol:ethanol 4:1, Bi/Na and O displacement parameters refined anisotropic, Ti displacement parameters refined isotropic

[b]data set measured in Helium, Bi/Na displacement parameters refined anisotropic, Ti and O displacement parameters refined isotropic

TABLE SIV. Anisotropic displacement parameters from structure refinements in *Pnma*.

x= 0.013

3.87(11) GPa	U_{11}	U_{22}	U_{33}	U_{12}	U_{13}	U_{23}
Bi/Na	0.0355(12)	0.0360(8)	0.0209(13)	0	-0.0005(2)	0
O1	0.009(2)	0.0215(15)	0.028(4)	-0.006(2)	0.0071(13)	0.0002(18)
O2	0.013(4)	0.014(3)	0.023(4)	0	0.003(2)	0

x= 0.074

6.31(12) GPa	U_{11}	U_{22}	U_{33}	U_{12}	U_{13}	U_{23}
Bi/Na	0.0262(8)	0.0287(10)	0.0174(10)	0	0.0012(2)	0

12.22(16) GPa	U_{11}	U_{22}	U_{33}	U_{12}	U_{13}	U_{23}
Bi/Na	0.0165(7)	0.0160(8)	0.0113(11)	0	0.00097(10)	0

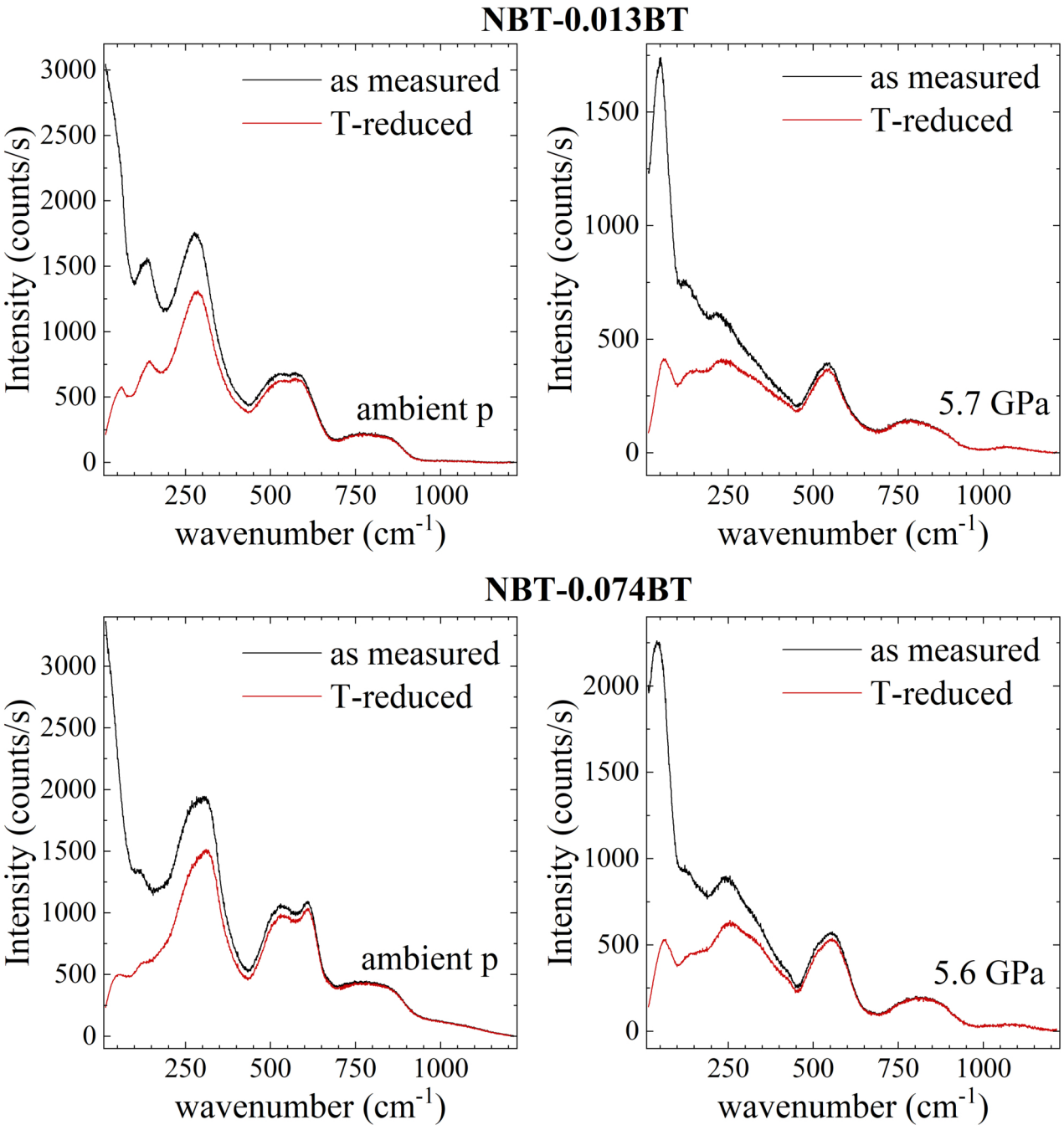


FIG. S5. As-measured Raman spectra (black) of NBT-0.013BT and NBT-0.074BT at ambient pressure and above p_c vs spectra normalized to the Bose-Einstein phonon occupation factor (red) to remove the temperature effects on the Raman intensities.

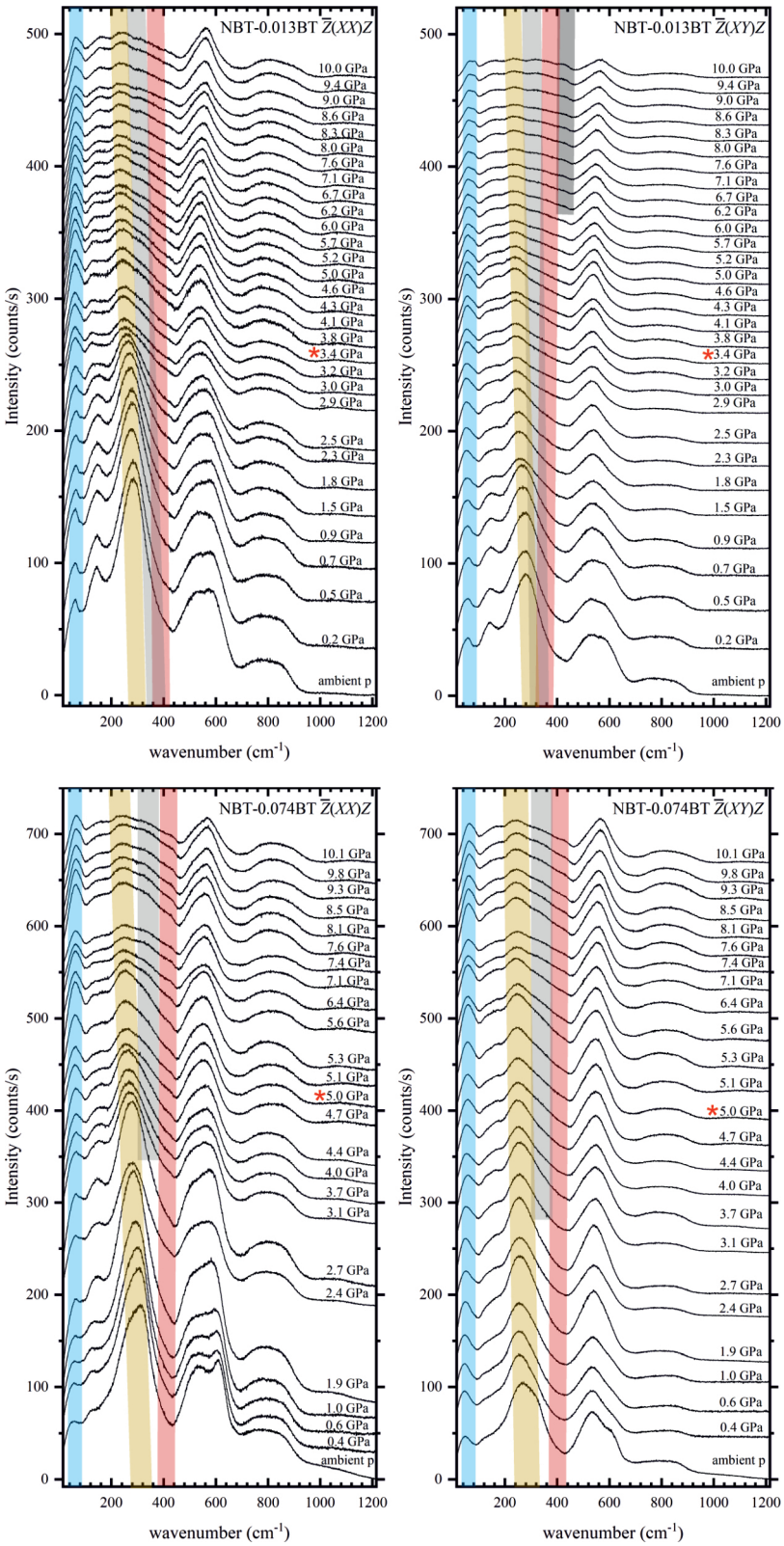


FIG. S6. Comprehensive set of $\bar{Z}(XX)Z$ and $\bar{Z}(XY)Z$ Raman spectra of NBT-0.013BT and NBT-0.074BT at pressures up to 10 GPa. The phase transition pressure p_c is marked by a red asterisk (*). The spectral range where A-cation localized modes are observed is highlighted in blue, that of B-cation localized modes in yellow and the spectral range of octahedral tilting vibrations is marked with gray and red.

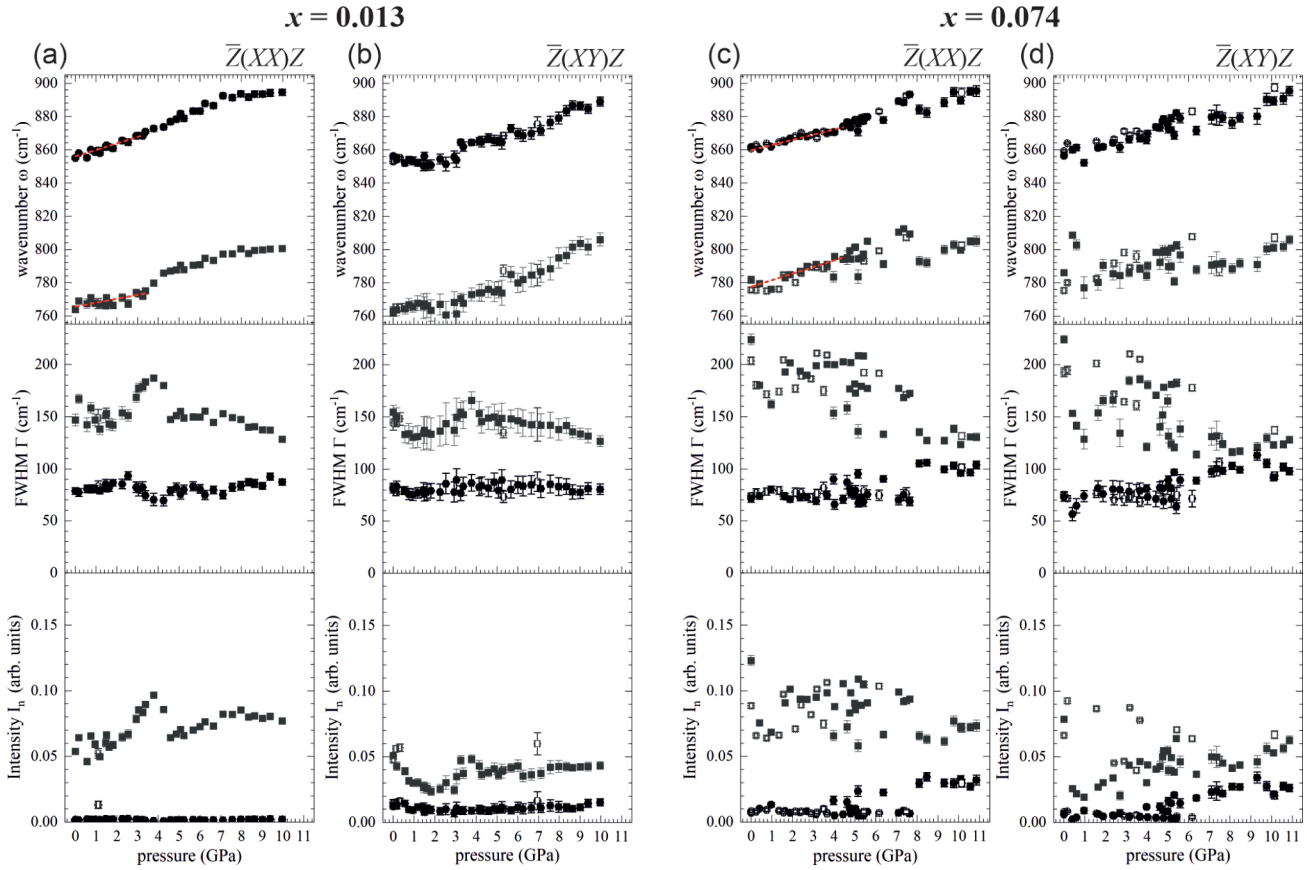


FIG. S7. Pressure dependence of the Raman peak positions (ω), full widths at half maxima (FWHMs; Γ), and fractional intensities (I_n) of Raman modes in the range 760-860 cm^{-1} of NBT-xBT with $x = 0.013$ ((a) and (b)) and $x = 0.074$ ((c) and (d)) derived from pseudo-Voigt function fits of $\bar{Z}(XX)Z$ and $\bar{Z}(XY)Z$ Raman spectra. Open symbols correspond to data points measured on decompression. The errors in the individual data points stem from the corresponding spectral fit. The red dashed lines in (a) and (c) are linear fits to $\omega(p)$ below p_c.

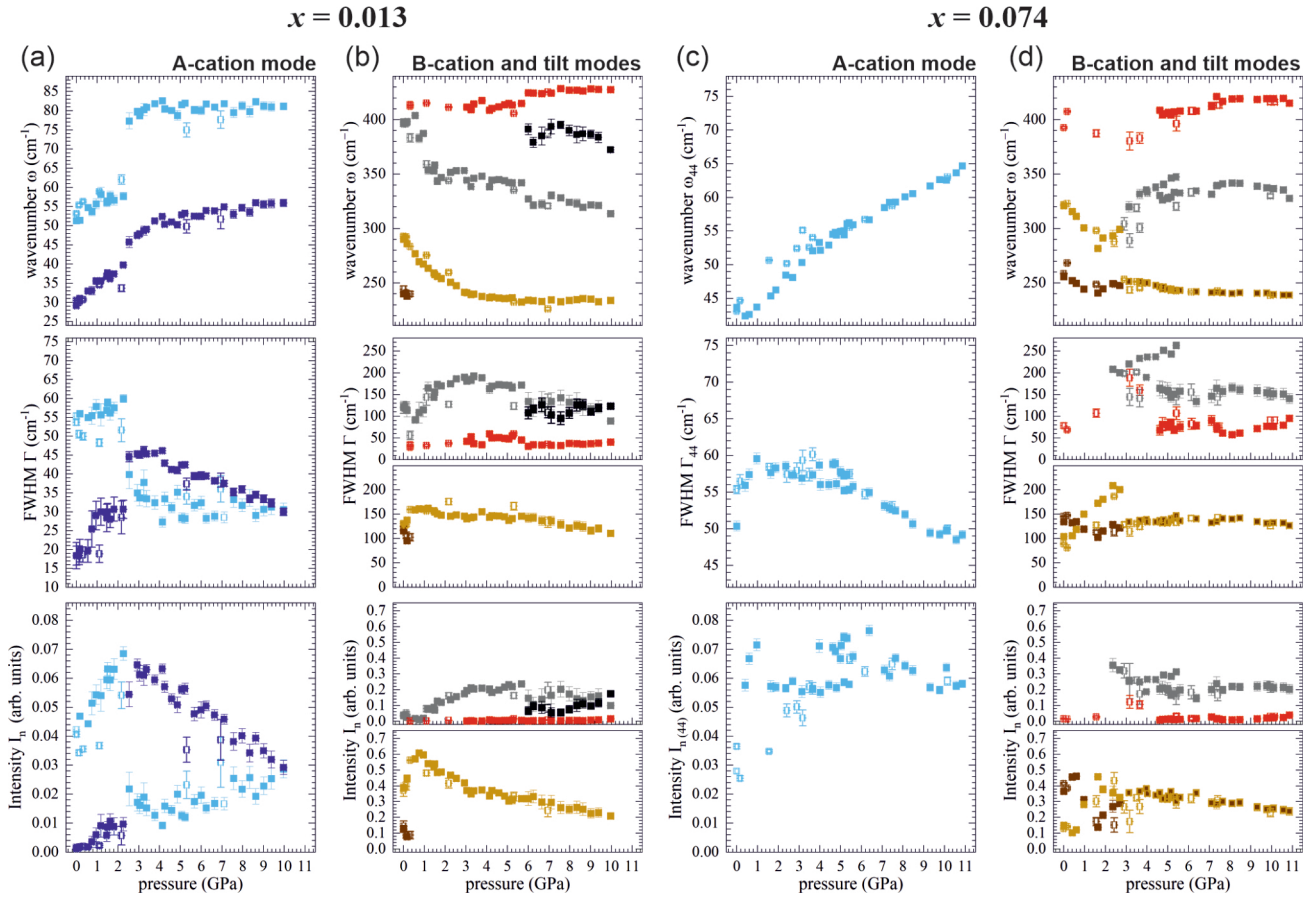


FIG. S8. Pressure dependence of the Raman peak positions (ω), full widths at half maxima (FWHMs; Γ), and fractional intensities (I_n) of selected Raman modes of NBT-xBT with $x = 0.013$ ((a) and (b)) and $x = 0.074$ ((c) and (d)) derived from pseudo-Voigt function fits of $\bar{Z}(XY)Z$ Raman spectra. The pressure dependence of the A-cation localized modes (blue) is shown in (a) and (c), while that of B-cation localized modes (yellow and brown) and BO_6 tilting modes (red, gray and black) is shown in (b) and (d). Open symbols correspond to data points measured on decompression. The errors in the individual data points stem from the corresponding spectral fit.

[1] Agilent, *CrysAlis PRO*, Agilent Technologies Ltd, Yarnton, Oxfordshire, England (2014).
[2] V. Petříček, M. Dušek, and L. Palatinus, Crystallographic computing system JANA2006: General features, Zeitschrift für Kristallographie - Crystalline Materials **229**, 345 (2014).

Eidesstattliche Versicherung

Hiermit erkläre ich an Eides statt, dass ich die vorliegende Dissertationsschrift selbst verfasst und keine anderen als die angegebenen Quellen und Hilfsmittel benutzt habe. Sofern im Zuge der Erstellung der vorliegenden Dissertationsschrift generative Künstliche Intelligenz (gKI) basierte elektronische Hilfsmittel verwendet wurden, versichere ich, dass meine eigene Leistung im Vordergrund stand und dass eine vollständige Dokumentation aller verwendeten Hilfsmittel gemäß der Guten wissenschaftlichen Praxis vorliegt. Ich trage die Verantwortung für eventuell durch die gKI generierte fehlerhafte oder verzerrte Inhalte, fehlerhafte Referenzen, Verstöße gegen das Datenschutz- und Urheberrecht oder Plagiate.



Hamburg, den 15.09.2026 Unterschrift